University of Oxford.

The development and application of novel magnetic resonance spectroscopic and imaging techniques to assess cardiac energetics and substrate handling in the human heart.

RADCLIFFE DEPARTMENT OF MEDICINE.

&

DEPARTMENT OF PHYSIOLOGY ANATOMY AND GENETICS.

Thesis Submitted for the Degree of Doctor of Philosophy.

Candidate:

Dr. Andrew Apps BMBCh, MRCP, BSc.

Supervisors:

Professor Oliver Rider D.Phil, BMBCh, FRCP

Professor Damian Tyler, PhD, MSci



Table of Contents

Declaration 6
Abstract 7
Abbreviations 10
Index of Figures 13
Index of Tables 15
Acknowledgements 16
Chapter 1: Introduction 17
1.1 Preface; why metabolism? 17
1.2 Cardiac Energy Metabolism and its homeostasis 18
1.2.1 ΔG_{ATP}; the free energy of ATP hydrolysis 18
1.2.2 Substrate modulation 19
1.2.3 Oxidative phosphorylation and its control 21
1.2.4 The phosphotransfer hypothesis 24
1.2.5 Problems with the phosphotransfer model 29
1.2.6 Energy metabolism and this work 29
1.3 Physics for magnetic resonance spectroscopy 31
1.4 Assessment of myocardial substrate handling 33
1.4.1 Hyperpolarised MR allows real time cardiac substrate preference analysis 33
1.4.2 Substrate handling in heart failure and diabetes 36
1.5 Myocardial energetics and the high energy phosphate pool 38
1.5.1 ^{31}P-Phosphorus spectroscopy for the study of myocardial energetics 38
1.5.2 Phosphate metabolism in diabetes and heart failure 40
1.5.3 Why measure Pi; ΔG_{ATP}, Pi/PCr and pH 41
1.5.4 Challenges and solutions to measuring Pi using ^{31}P-MRS 45
1.6 Assessment of myocardial lipid content 46
1.7 Toward imaging metabolism using hyperpolarised MR 48
1.8 Aims of this work 49
Chapter 2 (methodology) 51
2.1 General ethical considerations 51
2.2 Hyperpolarised magnetic resonance 51
2.2.1 Production of hyperpolarised [1-^{13}C]pyruvate 51
2.2.2 Quality control of hyperpolarised [1-^{13}C]pyruvate solution 53
2.2.3 Clinical Hyperpolarised MRS protocol 54
2.3 Phosphorus spectroscopy 55

2.3.1 ^{31}P-MRS STEAM sequence theory and design 55
2.3.2 ^{31}P-MRS Protocol at 7T 58
2.3.3 ^{31}P-MRS protocol at 3T 62
2.4 Other techniques and interventions 65
2.4.1 ^{1}H-MRS 65
2.4.2 ^{1}H MRI – Left ventricular ejection fraction and mass 66
2.4.3 Late gadolinium enhancement to assess for myocardial infarction 67
2.4.4 Echocardiography 67
2.4.5 Dobutamine Infusion Protocol 68
2.5.6 Other clinical measurements 69
2.5 Summary of techniques used. 70
Chapter 3. Optimal preparation strategy for hyperpolarised MR experiments 72
3.1 Introduction 73
3.1.1 Cardiac energy metabolism and the Randle cycle 73
3.1.2 Techniques for in-vivo metabolic assessment 74
3.1.3 Hyperpolarised MRS using [1-^{13}C]pyruvate 75
3.1.4 Subject preparation for hyperpolarised MRS 76
3.2 Methods 77
3.2.1 Ethical considerations 77
3.2.2 Animal handling and preparation 78
3.2.3 Streptozotocin high fat diet diabetic model 79
3.2.4 Intravenous glucose tolerance testing 79
3.2.5 Hyperpolarised [1-^{13}C]pyruvate production and MRS protocol 80
3.2.6 Data handling and statistical analysis 81
3.2.7 Statistical methodology 82
3.3 Results 83
3.3.1 Validating the STZ diabetic model 83
3.3.2 In-vivo metabolic data. 84
3.3.3 The impact of Animal preparation strategy on metabolic Flux changes. 86
3.3.4 Overcoming pathological PDH flux with intravenous glucose 87
3.3.5 Preparation strategy and variability in metabolic flux between animals 89
3.4 Discussion 92
3.4.1 Effect of glucose administration on cardiac metabolism 92
3.4.2 Metabolic variation is likely multifactorial 93
3.4.3 Confounding factors in the present study 94

3.4.4 Implications for human translation 95
3.5 Conclusion 96
Chapter 4. Substrate handling in the human diabetic heart; a multi-nuclear approach to diabetic cardiac metabolism 98
4.1 Introduction 99
4.1.1 Substrate handling in the diabetic heart 99
4.1.2 Hyperpolarised MRS offers mechanistic insight into substrate selection 100
4.2.3 Hyperpolarised MRS to assess the Randle cycle in real time 101
4.2 Methods 102
4.2.1 Ethical considerations 102
4.2.2 Eligibility criteria 102
4.2.3 Study population 103
4.2.4 Study visit 103
4.2.5 Data and statistical analysis 105
4.3 Results 107
4.3.1 Baseline population characteristics 107
4.3.2 Baseline structural characteristics and MRS 108
4.3.3 Injected [1-^{13}C]pyruvate specifications, and population injected 112
4.3.4 Hyperpolarised ^{13}C MRS 114
4.3.5 Substrate metabolism, energetics, insulin resistance and LV characteristics 119
4.3.6 Effect size and power comparisons 122
4.4 Discussion 122
4.4.1 The Randle cycle in the healthy and diabetic heart 123
4.4.2 Confirmation of glucose optimisation protocol 124
4.4.3 Lactate dehydrogenase and alanine aminotransferase flux 126
4.4.4 Impact of insulin resistance on global cardiac metabolism 127
4.4.5 Difficulties in human translation of hyperpolarised MR, limitations of the present study 129
4.5 Conclusions and future perspectives 131
Chapter 5. Quantifying the effect of stress on myocardial Pi and pH in healthy volunteers; ^{31}P-MRS at 7T. 132
5.1 Introduction 133
5.1.1 Myocardial ΔG_{ATP} requires measurement of [Pi] 134
5.1.2 Techniques to measure cardiac Pi 136
5.1.3 Pi and the control of oxidative phosphorylation 139
5.1.4 STEAM-^{31}P-MRS at high field strength for myocardial Pi 139

5.2 Methods 140
5.2.1 Ethical considerations 140
5.2.2 Eligibility criteria 140
5.2.3 Study population and visit 141
5.2.5 MRS analysis 143
5.2.6 Statistical analysis 145
5.2.7 Signal to noise (SNR) changes during stress; dealing with unpaired results 145
5.3 Results 146
5.3.1 Repeatability 146
5.3.2 Resting myocardial energetics and pH in healthy controls 148
5.3.2 Dobutamine stress in healthy controls 149
5.3.4 Effect of dobutamine on myocardial Pi/PCr and pH 152
5.4 Discussion 154
5.4.1 Resting energetics and pH 154
5.4.2 Resolution of Pi with STEAM-^{31}P-MRS 154
5.4.3 Stress Pi/PCr, and the control of oxidative respiration 156
5.4.4 Myocardial pH during dobutamine stress 158
5.4.5 Pi, CK flux and glucose metabolism 158
5.4.6 Comparison with other techniques and limitations 159
5.6 Conclusion 161
Chapter 6. Investigating Pi metabolism in the diabetic and cardiomyopathic heart; a step closer to ΔG_{ATP} 162
6.1 Introduction 163
6.1.1 The emergence of diabetic cardiomyopathy 164
6.1.2 Progression toward cardiomyopathy is likely multifactorial 164
6.1.3 Impaired energetics and diabetic cardiomyopathy 165
6.1.4 Impairment of CK flux in DCM, and the potential impact on Pi and ΔG_{ATP} 167
6.2 Methods 168
6.2.1 Ethical considerations 168
6.2.2 Eligibility criteria 168
6.2.3 Study population and visits 169
6.2.4 Data analysis 171
6.2.5 Statistical analysis 171
6.3 Results 171
6.3.1 Baseline population characteristics 171
6.3.2 Resting Energetics and resting pH 173

6.3.3 Dobutamine stress at 7T in a patient population 174
6.3.4 Pi/PCr during dobutamine stress in DCM and diabetes 175
6.3.5 Intracellular pH during dobutamine stress in DCM and diabetes 177
6.3.7 Energetics and Structural heart disease in dilated cardiomyopathy 179
6.4 Discussion 180
6.4.1 Pi/PCr in the diabetic heart 181
6.4.2 Pi/PCr and its relation to diastolic function 184
6.4.3 Pi/PCr and pH in DCM 185
6.4.4 Energetic consequences of the changes in Pi seen 187
6.4.6 Limitations of the present study 188
6.5 Conclusion and future perspectives 189
Chapter 7. Imaging myocardial ischaemic metabolism using hyperpolarised MR 191
7.1 Introduction 192
7.2 Methods 194
7.2.1 Ethical considerations 194
7.2.2 Human ^{13}C Hybrid-Shot Spiral for hyperpolarised Imaging 195
7.2.3 Pilot work; ischaemia study design and eligibility 196
7.2.4 Pilot work; viability study design and eligibility 197
7.3 Results 198
7.4 Discussion 200
Chapter 8. Conclusions and further work. 203
8.1 Summary of main findings 203
8.2 Subject preparation prior to hyperpolarised studies 204
8.3 Hyperpolarised MRS to assess disease progression 205
8.4 Hyperpolarised imaging for diagnosis and treatment planning in coronary disease 206
8.5 Hyperpolarised imaging for regional cardiac pH assessment 207
8.6 Measuring ΔG_{ATP} in the human heart and its pathological alterations 208
8.5 Post face narrative 209
Chapter 9. Appendix 211
9.1 Data handling chapter 5 211
9.2 Data handling chapter 6 212
9.3 General MR exclusion criteria 214
References. 216

Declaration

This thesis is my own work. It has not been submitted, either wholly or substantially for another degree at this University or any other institution. I have proportionately acknowledged the assistance of colleagues where relevant. Publications containing data presented in this thesis are given on the title page of each chapter.

Abstract

Myocardial energy homeostasis requires an interplay between three stages of energy transduction; the choice of substrate oxidised, the rate of mitochondrial oxidative phosphorylation, and finally transfer of adenosine triphosphate (ATP) to sites of disposal via the intermediate phosphocreatine (PCr). Whilst all three elements are fundamental, until recently, non-invasive assessment was limited to ^{31}Phosphorus magnetic resonance spectroscopy (^{31}P-MRS) assessment of the PCr/ATP ratio. This thesis aims to gain a deeper understanding of pathologic energy metabolism by using two novel MRS techniques. Firstly ^{31}P-MRS at the ultra-high field strength of 7T to assess myocardial Pi, and secondly the first in man clinical translation of hyperpolarised ^{13}C MRS, which offers the ability to quantify in real time the metabolism of an administered hyperpolarised ^{13}C containing substrate into downstream ^{13}C containing products. Using these techniques, a more comprehensive assessment of energy metabolism either side of the mitochondria was made in both the diabetic and failing heart.

The pyruvate dehydrogenase complex (PDH) catalyses the irreversible decarboxylation of glycolytically derived pyruvate to Acetyl CoA (Coenzyme A). Flux through this enzyme determines the prevailing rate of glucose oxidation and is highly regulated. Using a hyperpolarised and ^{13}C labelled version of its substrate ([1-^{13}C]pyruvate), PDH flux can be recorded using MRS by monitoring production of [^{13}C]bicarbonate. Chapter 3 presents preclinical work to define the optimal preparation strategy prior to recording [1-^{13}C]pyruvate MRS. This was essential prior to translation into human hyperpolarised imaging studies, to both minimise variability and maximise baseline flux through the PDH complex. Chapter 4 is a human multi-nuclear ^{31}P, ^{13}C and ^{1}H study of cardiac metabolism in diabetes. I present the first human cardiac hyperpolarised ^{13}C MRS study, and show, along with elevated cardiac

triglyceride and reduced PCr/ATP, a significant reduction in flux though PDH in diabetes. The switch from fatty acids to glucose oxidation occurring after feeding is also clearly shown in both controls and diabetics, providing the first non-invasive visualisation of the Randle cycle in vivo. The effect size of diabetes on PDH flux is greater than that on PCr/ATP, with only a small group of patients with diabetes needed to show a significant difference, demonstrating the power of the technique, and the magnitude of this physiological metabolic change.

As all cellular energy requiring processes have a unique value for the free energy of ATP hydrolysis (ΔG_{ATP}) above which they halt, measurement of ΔG_{ATP} would be a powerful tool to understand the thermodynamic consequences of pathological substrate metabolism. However, whilst this is routinely performed in animal experiments, the measurement of myocardial inorganic phosphate (Pi) is necessary, which has previously not been achieved due to the presence of blood pool 2,3-diphoshphoglycerate (2,3-DPG) obscuring the Pi resonance within the ^{31}P spectrum. In Chapter 5, I report results from a novel ^{31}P MRS STimulated Echo Acquisition Mode (STEAM) sequence, which allowed suppression of the blood pool signal, and demonstration of Pi free from contamination. Firstly, the robustness of such an approach is proven, following which, gross stability of Pi/PCr, and myocardial pH (which can be computed from the chemical shift of Pi) in a healthy cohort during dobutamine stress is shown. In chapter 6, pathological energy metabolism in the diabetic heart is further investigated; a rise in resting Pi/PCr is shown, but in contrast to decreases in PCr/ATP, no change is seen during dobutamine stress. Finally, focus turns to dilated cardiomyopathy (DCM). Here a significant rise in Pi/PCr during stress is reported, independent of the degree of underlying systolic dysfunction, which has implications for a change in ΔG_{ATP} during physical exertion.

My thesis data chapters conclude with chapter 7, presenting a small amount of metabolic imaging data obtained using a novel hybrid spiral shot ^{13}C sequence and hyperpolarised [1-^{13}C]pyruvate, in which regional variations of PDH flux in the hearts of those with coronary artery disease is shown. This preliminary work confirms the potential for hyperpolarised [^{13}C]bicarbonate production, to be a novel marker of myocardial viability. Collectively, this work uses new MR techniques to study pathological energy metabolism on both sides of mitochondrial oxidative phosphorylation; upstream at the level of the substrate, and downstream in the high energy phosphate pool.

Abbreviations

ΔG_{ATP}	Gibbs free energy of ATP hydrolysis
^{31}P-MRS	^{31}Phosphorus Magnetic Resonance Spectroscopy
2,3-DPG	2,3-diphosphoglycerate
ACC	Acetyl CoA carboxylase
ADP	Adenosine Diphosphate
AMARES	Advanced method for accurate and robust spectral fitting
ANT	Adenine nucleotide transporter
ATP	Adenosine Triphosphate
CK	Creatine kinase
CoA	Coenzyme A
CPT	Carnitine palmitoyltransferase
CSI	Chemical shift imaging
CytCK	Cytosolic creatine kinase
DCA	Dichloroacetate
DCM	Dilated cardiomyopathy
DNP	Dynamic nuclear polarisation
ECG	Electrocardiogram
ELISA	Enzyme-linked immuosorbent assay
FA	Fatty acid
$FADH_2$	Flavin adenine dinucleotide hydroquinone
FDG	Fluorodeoxyglucose
GLUT 4	Glucose transporter type 4

HEP	High energy phosphate
HFpPEF	Heart failure with preserved ejection fraction
HFrEF	Heart failure with reduced ejection fraction
HK	Hexokinase
HOMA-IR	Homeostatic model assessment of insulin resistance
IV	Intravenously
LAD	Left anterior descending artery
LV	Left ventricle
LVEF	Left ventricular ejection fraction
LVEDV	Left ventricular end diastolic volume
LVH	Left ventricular hypertrophy
MHR	Maximum heart rate
MRS	Magnetic Resonance Spectroscopy
MtCK	Mitochondrial creatine kinase
MVO_2	Myocardial oxygen consumption
NADH	Nicotinamide adenine dinucleotide
NMR	Nuclear magnetic resonance
OGTT	Oral glucose tolerance test
PCr	Phosphocreatine
PDH	Pyruvate Dehydrogenase Complex
PDK	PDH kinase
PEP	Phosphoenolpyruvate
PET	Positron emission tomography
Pi	Inorganic phosphate

PK	Pyruvate kinase
PPARα	Peroxisome proliferator activated receptor α
QALY	Quality adjusted life year
REC	Research ethics committee
RPP	Rate pressure product
SC	Subcutaneous
SCD	Sudden cardiac death
SFP	Sterile fluid pathway
SNR	Signal to noise ratio
SR	Sarcoplasmic reticulum
SSFP	Steady state free procession
STEAM	Stimulated echo acquisition mode
STZ	Streptozotocin
TCA	Tricarboxylic acid cycle
T_M	Mixing time
WSVD	Whitened singular value decomposition

Index of Figures

Figure 1: The phosphotransfer system 26
Figure 2: Healthy cardiac energy metabolism 30
Figure 3: Metabolic conversion of ^{13}C substrates in hyperpolarised experiments 34
Figure 4: Pathway of clinical DNP experiments 36
Figure 5: A typical cardiac ^{31}P-MRS spectrum 39
Figure 6: A typical ^{1}H MRS spectrum 47
Figure 7: Typical sterile fluid pathway for human studies 52
Figure 8: The dissolution process and team members 54
Figure 9: Physics of the STEAM sequence 56
Figure 10: STEAM ^{31}P MRS sequence 58
Figure 11: Voltage map of the heart from FID recovery curves 60
Figure 12: CSI grid positioning for PCr/ATP at 7T 61
Figure 13: CSI grid positioning for PCr/ATP at 3T 63
Figure 14: Manual selection of CODS for coil positioning 64
Figure 15: Example myocardial ^{1}H MRS spectrum and fit 65
Figure 16: ^{1}H CMR imaging views of the human heart 66
Figure 17: Assessment of diastolic function using echocardiography 68
Figure 18: The 7T experimental setup for rest/stress STEAM ^{31}P MRS 69
Figure 19: The Randle cycle 74
Figure 20: Rodent preparation 79
Figure 21: The preclinical DNP workflow 80
Figure 22: Summed spectra analysis in JMRUI 81
Figure 23: validating the diabetes rat model 83
Figure 24: IV glucose tolerance testing in diabetic and control rats 84
Figure 25 Typical ^{13}C rat spectra highlighting [1-^{13}C]pyruvate and its metabolites 85
Figure 26: Metabolite ratios in diabetic and control rats 87
Figure 27: PDH flux vs HOMA-IR in all rats 88
Figure 28: Preparation strategy and metabolic flux in diabetic and control rats 91
Figure 29: Diabetes and cardiac metabolism study visit 105
Figure 30: Comprehensive structural and metabolic assessment of diabetes 105
Figure 31: Myocardial PCr/ATP and lipid content in diabetics and controls 109
Figure 32: LV characteristics and relationships to diastolic function and energetics 110
Figure 33: Myocardial lipid content and its relations to insulin sensitivity and LV characteristics 111
Figure 34: Myocardial lipid content, energetics, and diastolic function 112
Figure 35: PCr/ATP and lipid content in [1-^{13}C]pyruvate injected subgroup 114
Figure 36: Representative spectra from healthy and diabetic participants 115
Figure 37: Effect of diabetes and feeding on cardiac metabolic flux 118
Figure 38: Metabolic flux data and PCr/ATP 119
Figure 39: Metabolic flux and its correlations to other structural characteristics 121
Figure 40: Cardiac changes during very low energy diet 129
Figure 41: Box Whisker plot of 300 PCr/ATP recordings from OCMR across groups 134
Figure 42: Comparing recent techniques for the quantification of cardiac Pi 138
Figure 43: Outline of the studies to record Pi using STEAM-^{31}P-MRS in healthy controls 142
Figure 44: Typical STEAM-^{31}P-MRS spectra showing PCr (A) and Pi (B) interleaves 144
Figure 45: Bland Altman plots for repeatability of Pi/PCr and pH 147

Figure 46: Pair of STEAM-^{31}P MRS spectra from the repeatability study 148
Figure 47: Correlation between markers of resting energetics 149
Figure 48: RPP changes during stress in a healthy cohort 151
Figure 49: Typical spectra from stress studies 152
Figure 50: Myocardial Pi/PCr and pH during stress in healthy controls 153
Figure 51: Myocardial Pi/PCr and pH during stress in patients with diabetes and DCM 170
Figure 52: Resting energetics in all participants 174
Figure 53: Changes in RPP during stress at 7T in patients 175
Figure 54: Pi/PCr changes during dobutamine stress 176
Figure 55: Intracellular pH during stress in diabetic and DCM patients 177
Figure 56: Relationship between metrics of rest energetics in diabetics 178
Figure 57: Correlation of diastolic function with energetics in diabetics 179
Figure 58: Energetics and stress response according to baseline LVEF in DCM 180
Figure 59: Pi/PCr variation with age in healthy controls 189
Figure 60: Ischaemia imaging in the pig heart using Hyperpolarised MR 193
Figure 61: Hybrid-Shot Spiral sequence for hyperpolarised imaging 196
Figure 62: Hyperpolarised imaging in CAD; ischaemia sub-study 197
Figure 63: Hyperpolarised imaging in CAD; viability sub-study 198
Figure 64: Hyperpolarised imaging following STEMI 199
Figure 65: Hyperpolarised imaging following NSTEMI 200

Index of Tables

Table 1: Summary of techniques and interventions undertaken in this work 0
Table 2: Metabolite ratios of control and diabetic rats 86
Table 3: Baseline population characteristics 107
Table 4: Table of baseline structural and MRS characteristics 108
Table 5: Characteristics of the group receiving hyperpolarised MRS 113
Table 6: Integrated ratios for each of the three metabolic products of [1-^{13}C]pyruvate 115
Table 7: Time integrated metabolite ratios for successful scans 117
Table 8: Repeatability results in healthy volunteers 146
Table 9: RPP and HR changes during dobutamine infusion 150
Table 10: Baseline characteristics of DCM and diabetic patients 172
Table 11: Resting energetics in diabetic and DCM patients 173
Table 12: RPP changes during dobutamine stress in patient studies 175
Table 13: Data handling chapter 5 healthy controls 211
Table 14: Data collection dilated cardiomyopathy 212
Table 15: Data collection type two diabetics 213
Table 16: Extended control group chapter 6 214

Acknowledgements

I would firstly like to thank the British Heart Foundation who provided me a Clinical Research Training Fellowship (No. FS/17/18/32449).

I would also like to thank:

- Chapter 3: Dr. Kerstin Timm who managed animal welfare and handling during these experiments. Dr. Jack Miller who helped undertake statistical tests that required R.
- Chapter 4 and 7: The human C-13 team at the University of Oxford; all of whom were required for each study visit. The team consisted of physicists Dr. Jack Miller, Dr. Justin Lau and Professor Damian Tyler, clinicians Dr. Andrew Lewis, Dr. Mark Peterzan and Professor Oliver Rider, and our Qualified Person (QP), Claire Trumper.
- Chapter 4 and 6: Professor Ingo Schmid for development of the STEAM-31P-MRS sequence. I also would like to thank Dr. Ladislav Valkovic and Dr. Jane Ellis for their help in the running of all clinical scans, trouble-shooting spectroscopy and data analysis problems. This work was the first to employ dobutamine stress at 7T and required two people (one of whom is a clinician – myself) to attend every scan.
- My supervisors Professor Oliver Rider and Professor Damian Tyler, as well as Dr. Mark Peterzan and Dr. Justin Lau for providing support and direction throughout.

Finally; thanks to the patients and volunteers who made this possible.

Chapter 1: Introduction

1.1 Preface; why metabolism?

Traditional imaging techniques must be safe, accurate, reproducible, and “diagnostic” in the sense that they allow efficacious medications to be targeted to those who stand to benefit. Although good, testing could likely be improved by combining the contemporary strategy of assessing for the presence of macroscopic phenotypic markers of disease, with an attempt to assess the prevailing metabolic status of the system studied. Technological innovation to improve precision within cardiac imaging may help inform who, when, and how to treat disease. Pathological metabolism often underpins disease appearance and progression, so its addition to the imaging armamentarium may be considered complimentary, increasing the specificity (with a reduction in unnecessary treatment and the associated risks and costs), and sensitivity (reducing the false negative rate and providing reassurance to a population without risk) of disease recognition. As technology is adopted and scaled, the costs of delivery fall, and as such despite the techniques presented in this work being firmly restricted to the research domain, it is important to not lose sight of the bigger picture. It is my hope that themes developed within my thesis will at some point contribute to an evidence base which collectively supports the integration of metabolic assessment into the clinical imaging workflow, reducing the risks and costs of both over and under treatment for millions of patients.

1.2 Cardiac Energy Metabolism and its homeostasis

1.2.1 ΔG_{ATP}; the free energy of ATP hydrolysis

The maintenance of an adequate human circulation requires the two ventricles, working in series, to collectively circulate upwards of 10 tons of blood daily in to circulatory beds with significant resistance profiles. It's perhaps not surprising then, that the heart consumes more energy than any other organ [1]. Energy released during cleavage of the terminal phosphate from ATP – the 'universal energy currency' to form adenosine diphosphate (ADP) and Pi, is used to drive cellular processes involved in myocardial contraction and relaxation. The hydrolysis is given by,

$$MgATP + H_20 \rightarrow MgADP + Pi + H^+$$

All ATP-powered processes require a minimum threshold for the Gibbs free energy released during ATP hydrolysis (ΔG_{ATP}), below which they become thermodynamically unfavourable and hence halt. $\Delta G_{ATP,}$ is in part determined by the cellular phosphorylation potential ([ATP]/[ADP][Pi]), and is given by the equation:

$$\Delta G_{ATP} = \Delta G^{\circ}{}_{ATP} - \mathrm{RT} \ln \frac{[ATP]}{[ADP][Pi]} \qquad \Delta G^{\circ}{}_{ATP} = -59.5\ kjmol^{-1}\ (37^{\circ}\mathrm{C})$$

Where $\Delta G^0{}_{ATP}$ is the standard free energy change of ATP hydrolysis under standard conditions, R is the gas constant, and T is the temperature in Kelvin. Regeneration of ATP and maintenance of a high phosphorylation potential, is thus crucial to keep $|\Delta G_{ATP}|$ large enough to drive essential energy requiring processes.

Human myocardial ATP concentration is estimated at 6.9±1.6 µmol/g wet weight [2], with the organ cycling between 10 and 20 kg every day [3], and completely turning over its ATP content every ~10 seconds [4]. As cardiac work increases, ATP disposal increases 5 to 10 fold from a resting level of 30 µmol per g wet weight min^{-1}, yet, ATP levels hardly change [5]. Maintaining stability of $\Delta G_{ATP,}$ and tight ATP homeostasis in the face of both physiological variation in the prevailing cardiac workload and the bioavailability of different catabolic substrates, and of course during pathological insults such as myocardial infarction, requires the integration of three processes which taken together define healthy cardiac energy metabolism. Firstly, at the level of the catabolic substrate oxidised, secondly at mitochondrial oxidative phosphorylation and the production of ATP itself, and finally phosphotransfer mediated by the creatine kinase (CK) system. CK ensures [ATP] local to the ATPases is maintained by transferring a phosphate group from the energy reserve compound PCr to ADP, at a rate far exceeding the rate of ATP production from oxidative phosphorylation. Each of these will be introduced in turn, in a style to contextualise the research hypothesis tested.

1.2.2 Substrate modulation

As there is considerable variation in the underlying bioavailability of substrates, the prevailing energy requirements, and the oxygen supply, the heart displays great flexibility in its catabolic substrates acting as a "metabolic omnivore". In 1953 Hans Adolf Krebs was awarded the Nobel Prize in physiology or medicine for his discovery of the tricarboxylic acid (TCA) cycle. Carbon from various substrates enters this, most often as Acetyl-CoA (Fritz Albert Litman was jointly awarded the 1953 award for his discovery of co-enzyme A) derived from either carbohydrates, fatty acids [FAs] or ketone bodies. Electrons are passed to nicotinamide dinucleotide (NAD+) and Flavin adenine dinucleotide (FAD+), thus generating the reduced

equivalents NADH and $FADH_2$ which in turn power oxidative phosphorylation. Maintaining a steady state in the face of great variation in ATP hydrolysis (at ATPases) requires feedback control of energy metabolism.

In 1929, Visscher and colleagues observed that glucose utilization did not account for the observed oxygen consumption in an ex-vivo heart lung preparation [6], suggesting the predominant oxidation of a non-carbohydrate substrate. Subsequent in-vivo observations made via measurement of trans-myocardial substrate extraction in human subjects suggested this substrate was likely FAs [7], confirming that the predominant source of ATP in the healthy heart is derived from the β-oxidation of these within the mitochondria [4]. FAs are firstly conjugated to carnitine by carnitine palmitoyl-transferase (CPT) with the resultant fatty acyl carnitine then translocated in to the mitochondria through carnitine acylcarnitine translocase. Subsequent β-oxidation cleaves the long chain fatty acids in to 2 carbon units of Acetyl-CoA which then enter the TCA cycle. On the other hand, glucose contribution to the mitochondrial Acetyl-CoA pool is largely controlled by the activity of the PDH complex which catalyses the irreversible oxidative decarboxylation of pyruvate (the final glycolytic product) to produce Acetyl-CoA.

PDH governs the choice of substrate depending on conditions. In the fasted state, flux through PDH is relatively suppressed due to phosphorylation, with its kinase being activated by an abundance of FA derived Acetyl-CoA. Central to the switch to glucose oxidation and away from FAs after feeding are the downstream targets of insulin signalling. During feeding, insulin stimulates increased cellular uptake of glucose via translocation of glucose transporter type 4 (GLUT 4) to the cell membrane, and PDH phosphatase is activated, thus upregulating PDH activity and releasing the break on glucose oxidation. In parallel fatty acid metabolism switches away from oxidation toward synthesis with insulin activating Acetyl-CoA

carboxylase, increasing malonyl-CoA, which inhibits CPT (and mitochondrial FA translocation), and is itself the building block for FA synthesis. In this way the oxidation of glucose and fatty acids as energy substrates in health are reciprocally regulated, with this shift toward glucose following feeding first described by Randle [8].

1.2.3 Oxidative phosphorylation and its control

The second level of control to maintain ATP homeostasis is oxidative phosphorylation taking place within the mitochondrial matrix. Electrons from reducing equivalents are passed down the electron transport chain to oxygen. This generates an electrochemical proton gradient across the mitochondrial intermembrane space. The release of this gradient through the F0,F1 ATP-ase (complex V of the respiratory chain) is coupled to the synthesis of ATP from ADP and Pi. Under aerobic conditions, 95% of ATP is generated in this way. The reaction can be summarised as:

$$3ADP + 3P_i + NADH + H^+ + \frac{1}{2}0_2 \leftrightarrow 3ATP + NAD^+ + H_20$$

Early observations in isolated mitochondria in the 1950s reported a linear relationship between rates of oxidative phosphorylation and extra mitochondrial concentrations of Pi [9], with large changes in oxidative phosphorylation seen as [Pi] is varied near the cardiac intracellular concentration in isolated preparations. [10]. This work provided a simplistic yet elegant hypothesis, that it is the products of ATP hydrolysis that provide cytosolic feedback of prevailing ATPase activity to the mitochondria, to upregulate the rate of ATP production by oxidative phosphorylation and achieve homeostasis of [ATP]. Such feedback seems intuitive

given the detrimental effect Pi has on $\Delta G_{ATP,}$ limiting the heart's ability to hydrolyse ATP and undertake work. Corroborating this hypothesis, open chest animal models clearly demonstrated Pi markedly increasing with cardiac work from mostly undetectable levels [11, 12, 13]. Such changes are seen however at extreme workloads induced by a combination of catecholamine infusions, intra-cardiac pacing, and uncoupling agents, (in highly un-physiological models), and may represent a pathological loss of the steady state rather than physiological control.

An early ^{31}P-MRS experiment in healthy human controls in which myocardial Pi was estimated semi-quantitatively by assuming any change to the spectral resonance in the region of 2,3-DPG during stress represents a change in Pi, also demonstrated an increase in Pi during stress, of 33% [14]. This study aimed for 100% of the target heart rate with the addition of atropine (to dobutamine) for added chronotropic response, achieving three-fold increases in the recorded rate pressure product (RPP) in these volunteers. It should be stressed however that [Pi] here is inferred and not directly recorded. PCr/ATP was also shown to fall significantly in this study during stress; a finding at odds to the stability of PCr/ATP during dobutamine stress in the healthy control arms of a number of subsequent clinical studies [15, 16, 17]. Indeed, myocardial Pi has been shown to be stable during a threefold increase in oxygen consumption (MVO_2) induced by intra-cardiac pacing in dogs, [18] with more aggressive increases in MVO2 (up to 5 times) during adrenaline infusion needed to demonstrate an increase in Pi. Gross myocardial Pi stability during low grade work may not be un-expected given the reported PCr/ATP stability, and the deleterious impact on ΔG_{ATP} large changes would confer.

In contrast, in tissues with a lower capacity for oxidative ATP production such as in skeletal muscle, an increase in Pi during work is far clearer. The phosphorylation potential is

not maintained over a range of physiological workloads with Pi/PCr increasing linearly within workload [13]. This has led some to suggest that a potential role for Pi and ADP as feedback controllers of oxidative phosphorylation could be restricted to skeletal muscle only. In contrast to skeletal muscle however, which has much lower resting concentrations of Pi and ADP, cardiac mitochondrial free [Pi] and [ADP] are higher; 100 – 1000 μmol and 20 – 60μm respectively [19, 20]. These values are non-saturating to the ATP synthase, and instead represent the concentration at which 50% saturation occurs [21], meaning only small changes in concentration markedly simulates the rate of oxidative phosphorylation [10]. Such small physiological fluctuations capable of modulating oxidative phosphorylation are indeed difficult to detect by contemporary nuclear magnetic resonance (NMR) methods, in a similar way, to difficulty detecting changes of high energy phosphate (HEP) metabolites within the cardiac cycle [22]. Recent in-silico work based on simulated mathematical modelling of cardiac energy metabolism, electrophysiology, and available in-vivo experimental data, do implicate small changes in Pi as a crucial mechanism by which changes in ATP hydrolysis modulate ATP production [23, 24, 25], especially by feedback activation of complex III of the respiratory chain [25]. The gross changes in Pi demonstrated in the animal models outlined above [11, 12, 13], are seen to occur at extreme cardiac workloads and may thus represent the loss of the steady state. Here, due to an inability of both oxidative phosphorylation and phosphotransfer (mediated by Creatine kinase – discussed below) to collectively maintain ATP homeostasis, a marked increase of $|\Delta G_{ATP}|$ occurs. It could be hypothesised that any impairment in either of these two, would bring the point at which the steady state is lost to a lower $MV0_2$.

Any sustained increase in the rate of oxidative phosphorylation and ATP production requires a parallel increase in supply of NADH and $FADH_2$ from the TCA cycle. This is largely

mediated by changes in cytosolic calcium levels as work increases. In the healthy heart cell membrane depolarisation during the action potential opens voltage gated L type calcium channels with subsequent influx of calcium. This 'trigger' calcium then induces a much larger efflux of calcium from the sarcoplasmic reticulum (SR) via type 2 ryanodine receptors in a process termed calcium induced calcium release [26] The increase in cytosolic [Ca2+] which triggers contraction and cross bridge cycling is transient as calcium is pumped back in to the SR by a SERCA2a with subsequent relaxation. These components of the calcium handling machinery are all direct (or indirect in the case of SERCA2a via phospholamban) targets of protein kinase A phosphorylation which is increased during exercise via adrenergic signalling. This results in enhanced SR calcium loading and subsequent calcium release. in response to increased chronotropy or inotropy [27]. Mitochondria are sensitive to these changes in calcium transients since they are in close proximity to sites of calcium release from the SR, and uptake calcium freely via the mitochondrial calcium uniporter protein situated In the inner mitochondrial membrane [28]. Within the matrix, calcium stimulates pyruvate, α-ketoglutarate, and isocitrate dehydrogenases thus stimulating the TCA cycle and increasing the regeneration of NADH and $FADH_2$, in response to increasing cardiac workload [29].

1.2.4 The phosphotransfer hypothesis

The final component required for healthy energy metabolism, is phosphotransfer; the transfer of ATP from the mitochondrial matrix to sites of hydrolysis by facilitated diffusion. This is achieved by the Creatine Kinase (CK) shuttle. CK has two isoforms, a mitochondrial octameric form (MtCK) located in the mitochondrial intermembrane space close to the adenine nucleotide transporter (ANT), and a cytosolic dimeric form located by active ATPases (CytCK). The rate constant varies for each with kinetics in favour of ATP production at the

mitochondria and vice versa in the cytosol [30]. The reaction can be summarised below where Kf and Kr are the forward and reverse reaction rate constants of the CK reaction respectively.

$$PCr^{2-} + MgADP^{-} + H^{+} \underset{Kr}{\overset{Kf}{\leftrightarrow}} Cr + MgATP^{2-}$$

In the cytosol, local to the ATPases, CytCK maintains [ATP]/[ADP] whereas at the mitochondrial matrix with constant ATP production MtCK maintains a relatively low [ATP]/[ADP] by removal of the ATP produced, thus maintaining rates of oxidative phosphorylation by maintaining ADP availability. In this way, a relatively large pool of cytosolic phosphocreatine is maintained, which unlike adenine nucleotides is highly diffusible within the cell [31]. Creatine is constantly being produced in the cytosol which freely diffuses back to the mitochondria to be rephosphorylated into PCr. Thus, it is the reversible interconversion of creatine into PCr that locally regenerates ATP at the myofibril, with the two pools of HEP compounds (mitochondrial and cytosolic) remaining fairly distinct. Phosphotransfer can be summarised as shown in Figure 1.

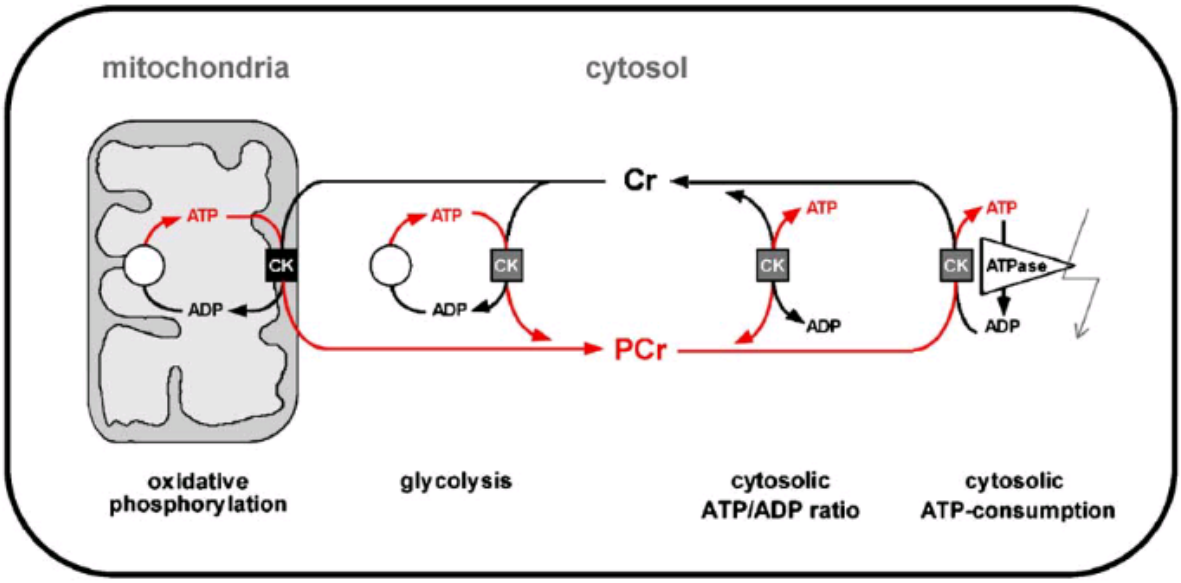


Figure 1: The phosphotransfer system

Creatine kinase serves as a spatial and temporal energy buffer within the myocyte. ATP generated at the inner mitochondrial membrane is quickly removed by MtCK, located within the intermembrane space associated with adenine nucleotide transporters within the inner mitochondrial membrane. ADP is regenerated for ongoing ATP production and a phosphocreatine reservoir builds up a within the cytosol. At sites of ATP usage, cytCK catalyses the reverse reaction with regeneration of ATP, local to sites of hydrolysis. Figure taken from Schlattner et al 2006 [31].

Early work in the 1970s gave rise to the idea of two functionally and geographically distinct pools of CK within the cell. In isolated mitochondria in suspension with fixed [ATP], PCr appearance is linear with time according to the rate of oxidative phosphorylation (varied with oligomycin) suggesting a tight coupling between the mitochondrial ANT translocase and MtCK [32]. Experimental observations noting the effectiveness of exogenous ADP to stimulate oxidative phosphorylation, and its availability for mitochondrial ATP generation provide the bulk of the evidence for this two-compartment hypothesis. In isolated mitochondrial preparations, pyruvate kinase (PK) competes effectively with CK for the ADP produced by the

hexokinase (HK) catalysed production of glucose-6-phosphate from glucose. The rates of these competing reactions can easily be followed from the production of creatine or pyruvate with the suspension containing the substrates PCr and phosphoenolpyruvate (PEP). When repeated in a myofibrillar preparation however pyruvate kinase competes less effectively with CK for ADP suggesting that a significant proportion of the ADP pool is not available to phosphoenolpyruvate, again suggesting separate pools of adenine nucleotides [33]. In a series of ingenious experiments, Yang [34] then went on to directly demonstrate the preference of mitochondrial CK for ATP produced by oxidative phosphorylation using media containing a high concentration of [γ-^{32}P] labelled ATP, but no ADP. Shortly after the addition of creatine, the specific activity of the PCr was small compared to that of ATP suggesting that the major substrate for MtCK mediated PCr production must have been ATP produced by oxidative phosphorylation (synthesized from ADP derived from [γ-^{32}P]ATP and unlabelled Pi).

Even stronger evidence for CK compartmentalisation corroborating the above, comes from experiments probing the stimulatory role of ADP on rates of oxidative phosphorylation in permeabilised muscle cells (retaining only MtCK) [35]. While the addition of ATP alone activated oxygen consumption (via ADP produced by Adenylate kinase and myofibrillar ATPase), the addition of creatine (a substrate for CK) increased this 2-fold by increasing the availability of ADP. Two key observations suggest that this 'additive ADP stimulus' to oxidative phosphorylation is restricted to ADP produced in the mitochondrial intermembrane space by MtCK. Firstly, the stimulatory role of added creatine is largely abolished in CK knock out mice. Secondly, if a cytosolic ADP sink is introduced (in the form of (PEP + PK)), alongside an adenylate kinase inhibitor, the role of cytosolic ADP as a regulator of oxidative phosphorylation should be minimised. Cytosolic ADP is indeed markedly reduced, but creatine still increases VO_2. Thus, ADP produced in the mitochondria intermembrane space

preferentially stimulates VO_2, increased by the addition of creatine, but unaffected by a drop in cytosolic ADP mediated by the addition of PK + PEP. Addition of trypsin, which disrupts sarcomeric and mitochondrial structural integrity renders the ADP sink (PK + PEP) more effective at suppressing VO_2, suggesting that this disruption gives PEP greater access to the total ADP pool [36]. Further ex-vivo data to support the phosphocreatine shuttle hypothesis can be reviewed elsewhere [37].

Evidence for distinct functionality of CK isozymes, that is, a cytosolic pool catalysing ATP regeneration whereas a mitochondrial pool regenerating PCr, is found from ^{31}P NMR saturation transfer experiments which allow the interrogation of flux through CK, by transfer of a magnetisation label. In vivo K_f (PCr→γ-ATP) can be measured with selective saturation of γ-ATP. Measurement of K_R however (ATP→PCr) requires simultaneous saturation of PCr and Pi given ATP – Pi exchange. This is not possible in vivo given the Pi resonance cannot be robustly detected due to blood pool contamination. Ex-vivo using a perfused Langendorff technique however, Pi can be detected and thus saturated. Using a combination of inversion protocols [38], CK kinetics can be shown to be dependent on the subcellular compartment, with CytCK associated with ATPases favouring ATP synthesis (K_f>K_r), and MtCK favouring PCr synthesis (K_r>K_f) [39]. Whether K_f is rate limiting in the healthy human heart is controversial, with some studies demonstrating an increase during stress [40, 41], and others not [42]. CK flux variation within the cardiac cycle may also occur and account for the stability of the HEP pool during the cardiac cycle seen in the human heart [22, 43]; small variations may occur, but again within boundaries undetectable by ^{31}P-MRS in healthy individuals. Indeed changes within the cardiac cycle have been demonstrated in the ex-vivo perfused heart [44, 45].

1.2.5 Problems with the phosphotransfer model

Various observations are problematic for the phosphotransfer hypothesis. Firstly mice deficient in CK (a knockout of the biosynthetic enzyme N-guanidinoacetate N-methyltransferase reducing creatine to undetectable levels) demonstrate normal exercise capacity [46]. Second, in explanted hearts from mice in which MtCK has been knocked out, K_f falls to only 10% of the rate of oxidative phosphorylation suggesting that ATP transfer from the mitochondria to the cytosol has no obligatory requirement for PCr [47]. Do such observations mandate an alternative hypothesis? A competing (but likely complementary) hypothesis for energy distribution within the cell has recently emerged from the study of mitochondrial networks within skeletal muscle, using scanning electron microscopy [48]. Mitochondria are shown to form a single functional reticular network, extending deep in to the muscle such that the proton motive force generated at the mitochondrial matrix can be released to generate ATP local to sites of hydrolysis, thus minimising transfusion distances of both ATP and PCr. In all likelihood, healthy energy transfer from the mitochondria to the ATPase relies on an interplay between all of these systems.

1.2.6 Energy metabolism and this work

The three components of healthy energy metabolism are summarised in Figure 2. The work detailed in this thesis describes a range of experiments interrogating different points in energy metabolism which lie on either side of mitochondrial oxidative phosphorylation. Upstream of the mitochondria at the level of the substrate, I have used hyperpolarised MR to study glucose entry in to the TCA cycle by measuring physiological (Randle cycle changes during feeding) and pathological (in diabetes) changes in flux through the pyruvate dehydrogenase complex. Secondly, now downstream to mitochondrial oxidative

phosphorylation, I have measured myocardial Pi in vivo in the healthy and pathological myocardium (diabetes and dilated cardiomyopathy), at rest and during catecholamine stress using a novel Stimulated Echo Acquisition Mode (STEAM) ^{31}P MRS sequence.

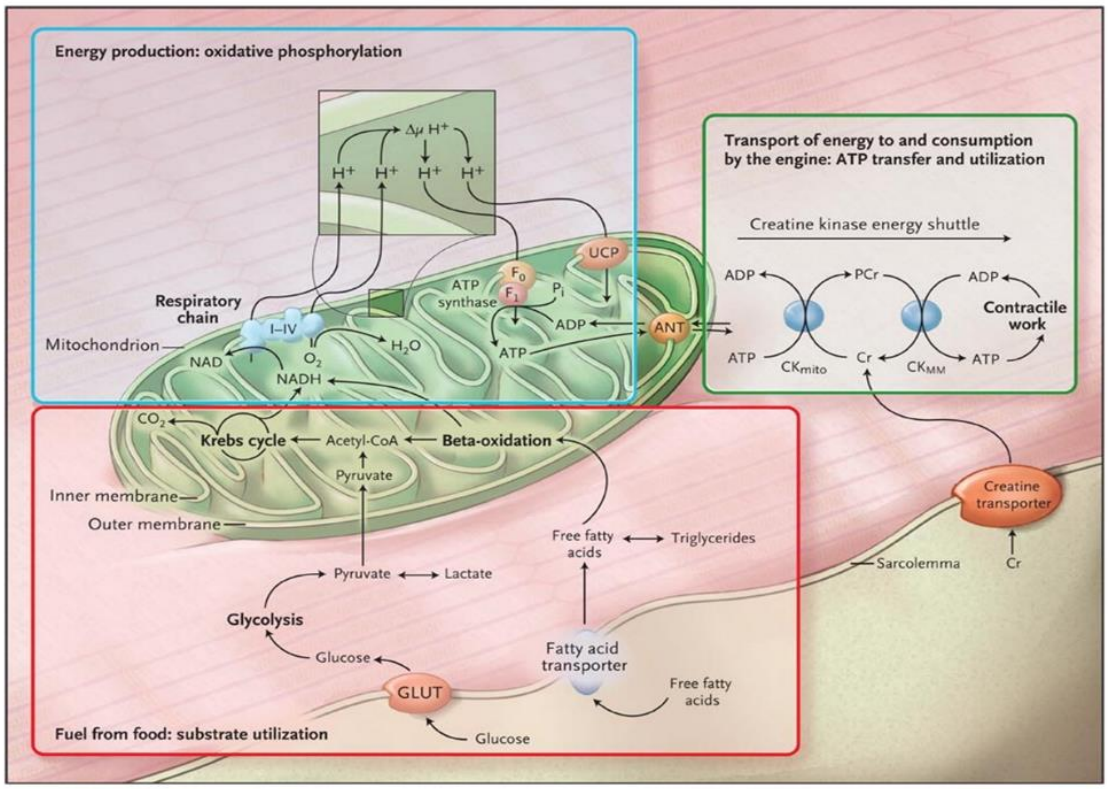


Figure 2: Healthy cardiac energy metabolism

Cardiac metabolic energy homeostasis requires the interconnection of three steps. Firstly, great versatility in substrate preference is seen (red box). Entrance of glycolytic glucose derived carbon in the mitochondria is controlled at the level of PDH and can be studied by using hyperpolarised MR. Following ATP production at the mitochondria (blue box), ATP is shuttled to sites of usage via the intermediate PCr (green box). Changes in the pool of phosphate intermediates can be measured using ^{31}P-MRS techniques. Figure taken from Neubauer et al [1].

Recording Pi/PCr allowed me to begin to gain a deeper understanding of the impaired energetics demonstrated in diabetes [15] and heart failure [49], and how this may impact mechanical function. The CK first order rate constant, $K_{f,}$ has been shown to be depressed in human heart failure [42], and a rise in cytosolic Pi is predicted to accompany this [50]. This can be hypothesised to be exaggerated further at higher workloads, with direct deleterious implications for $\Delta G_{ATP.}$

The MRS techniques used in this work – Hyperpolarised ^{13}C MRS, ^{31}P-MRS, and ^{1}H MRS are explained in more detail in the following sections. Taking each in turn, technical aspects are first discussed, prior to a targeted review of the evidence base pertaining to the segment of energy metabolism which they are principally used to study, and relevant to the research aims. Prior to this, the relevant magnetic resonance physics is briefly discussed.

1.3 Physics for magnetic resonance spectroscopy

Electromagnetic radiation can be regarded to carry discrete packets of energy, quanta, whose magnitude is given by:

$$E = hv$$

Where h is the Planck constant, and v is the frequency of radiation. MR active nuclei possess spin. When a magnetic field is applied, these "spins" behave like bar magnets and either align with or against the applied magnetic field, creating two distinct populations each with slightly different associated energy levels. The difference between these populations, the net magnetisation vector, is determined by the strength of the applied field, and is miniscule at common field strengths (hence the low signal inherent in magnetic resonance spectroscopy

[MRS] experiments). Transitions between these two energy states can be induced by applying radiation at the *resonance* frequency:

$$v = \frac{\gamma B_0}{2\pi}$$

Where γ is the gyromagnetic constant (varies for each MR active nuclei) for the nuclei in questions and B_0 is the strength of the applied magnetic field. The resonance frequency depends on the local field experienced by the nucleus which varies according to its chemical environment. As such, resonant frequencies vary slightly, termed chemical shift, relative to an arbitrary standard.

Paul Lauterbur and Sir Peter Mansfield were recognised as co-recipients of the 2003 Nobel Prize in physiology or medicine for their work in developing clinical MRI. Here, the inherent insensitivity arising from the small size of the net magnetisation to produce clinical quality images is overcome due to the high concentration of hydrogen nuclei (protons ^{1}H) in water. In contrast, even though ^{31}P is the naturally abundant isotope of phosphorus, the low *in vivo* concentration of phosphorus containing compounds makes ^{31}P MRS technically challenging. Despite these challenges, ^{31}P MRS spectra can be acquired *in vivo* and compounds containing ^{31}P can easily be identified based on their different chemical shifts. For carbon-13 MRS, the challenges are even greater because the NMR visible isotope of carbon, ^{13}C, has an extremely low natural abundance of about 1% - ^{13}C NMR experiments are thus largely restricted to steady state assessments of ex-vivo hearts perfused with high concentrations of ^{13}C substrates, with long imaging protocols needed to acquire signal.

Hyperpolarised MR overcomes this with the ingenious principle of Dynamic Nuclear Polarisation (DNP) and is discussed further below.

1.4 Assessment of myocardial substrate handling

1.4.1 Hyperpolarised MR allows real time cardiac substrate preference analysis

The process of Hyperpolarisation brings the net magnetisation vector of a compound transiently away from thermal equilibrium such that metabolic exchange can be measured in real time. Signal amplification by reversible exchange (SABRE) achieves this by utilising the nuclear singlet state of parahyrdrogen as a source of hyperpolarisation, which is transferred to the substrate of interest using a metal centre. Although this process is quick, parahydrogen must be produced by bubbling H_2 gas (an explosive gas) over a charcoal catalyst at liquid nitrogen temperature (77K) before chemically reacting this with the probe of interest. Levels of substrate polarisation are low meaning clinical applicability has not yet been achieved [51]. DNP however, although taking much longer for spin polarisation to build up due to it being transferred from highly polarised free electrons (admittedly at much lower, liquid nitrogen temperatures), gives much higher levels of polarisation making metabolic imaging feasible. The technique allows the ^{13}C nuclei contained within the hyperpolarised tracer whose metabolism is of interest, to be tracked into the downstream metabolic products upon injection into a living system, opening the door to the real time assessment of in-vivo metabolic flux. In the case of [^{13}C]pyruvate, the tracer used in the experiments presented here, varying the position of the ^{13}C nucleus also allows interrogation of different metabolic pathways. In my studies [1-^{13}C]pyruvate was used to interrogate PDH, with the ^{13}C nucleus released as $^{13}CO_2$ as a by-product. Using [2-^{13}C]pyruvate however, the label is passed directly

into acetyl-CoA such that Krebs flux can be assessed with production of [5-^{13}C]glutamate and [1-^{13}C]citrate [52]. This range of possibilities is demonstrated in Figure 3.

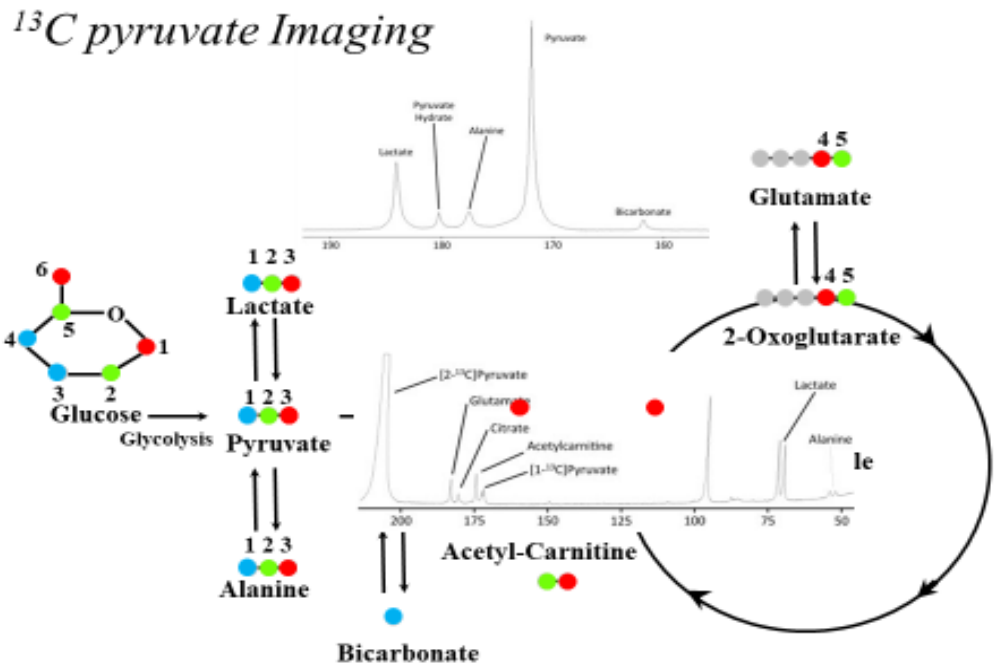


Figure 3: Metabolic conversion of ^{13}C substrates in hyperpolarised experiments

Different metabolic conversions can be followed by varying the position of the ^{13}C nucleus within the administered substrate (in this case pyruvate). Using [1-^{13}C]pyruvate, PDH flux can be measured, whereas [2-^{13}C]pyruvate offers interrogation of TCA flux.

Using DNP the MR signal can be increased by up to 10,000x [53]. This is achieved by transferring the high spin polarisation associated with free electrons at extremely low temperatures (~1K) to the nuclear spins of the biological substrate of interest by microwave irradiation, prior to dissolution and subsequent injection in to a living system [54]. Firstly, the substrate (typically ^{13}C labelled pyruvic acid) is mixed with a source of free electrons (a free radical – that used in my studies was an electron paramagnetic agent - EPA), at very low

temperature (in liquid helium ~1K) at high field strength (typically 3-5T). Under these conditions, electron polarisation approaches 100%. This is transferred to the sample via microwave irradiation (whose frequency depends on the magnetic field strength and tracer). This process takes on the order of two hours and achieves polarisation levels of between 30 and 40% (compared to ~0.0005% at thermal equilibrium). Dissolution to room temperature and injection must be achieved rapidly given that polarisation, and thus signal, decays according to T_1 relaxation processes (T_1 ~45 s in the case of pyruvate). This is achieved by releasing superheated sterile water under pressure through the sample, dissolving it into a receiving chamber containing a base solution (Sodium hydroxide) to neutralize the pH. The free radical is filtered prior to this chamber, with a further filtration step, pH check, and visual inspection (by a qualified person) prior to release for human injection. DNP was undertaken in a General Electric SpinLab system [53] for the human studies undertaken here, and a prototype hyperpolariser for the animal experiments. A summary of the process is shown in Figure 4.

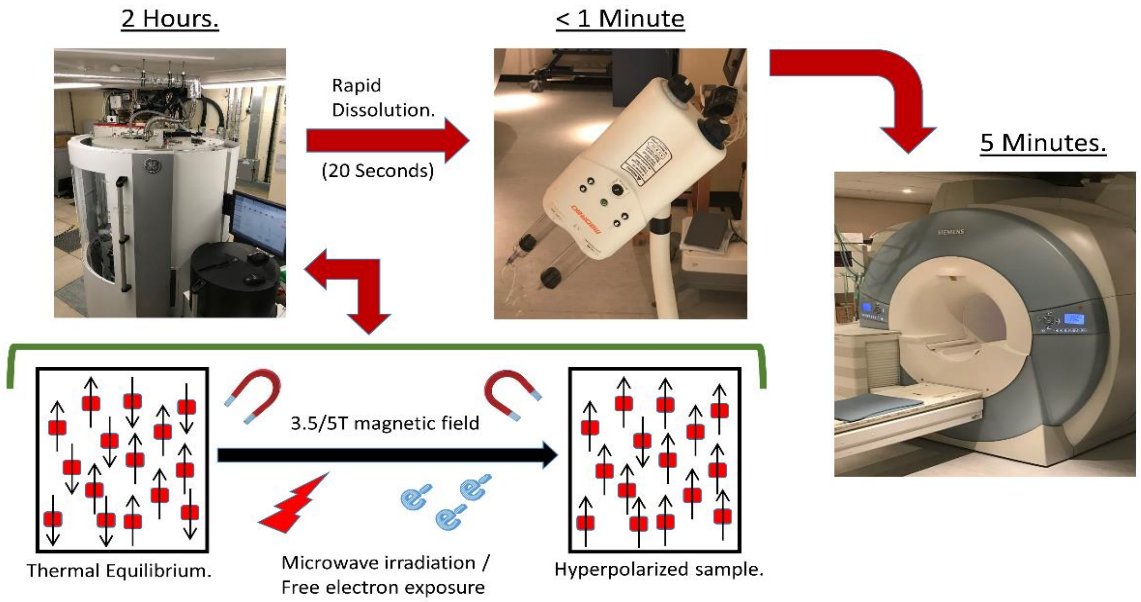


Figure 4: Pathway of clinical DNP experiments

Summary of the DNP process, images are taken from the equipment within OCMR, taken from Apps et al. [55].

1.4.2 Substrate handling in heart failure and diabetes

Pathological substrate handling is consistently seen in heart failure, and extensively reviewed elsewhere [56]. In animal models of heart failure measuring trans-myocardial extraction of isotopically labelled substrates, FA oxidation is decreased with a parallel increase in glucose oxidation [57], findings corroborated in-vivo in humans using positron emission tomography (PET) to quantify uptake in patients with DCM [58]. The early failing heart can thus be regarded as developing a foetal metabolic phenotype [59], this shift toward glucose results in the production of more ATP generated per mole of oxygen consumed, thus promoting myocardial contractile efficiency [60]. This shift has recently been shown to be likely driven by an altered pattern of DNA methylation [61]. As heart failure progresses, these 'adaptations' however give way to reduced glucose uptake [62], and global energy starvation [1], despite an abundance of substrates.

Pre-clinically, hyperpolarised MR has proven utility in studying such pathological changes. For example, with repeated hyperpolarised MR experiments using [1-^{13}C]pyruvate stepwise change during disease progression can be measured, often despite macroscopic phenotypic stability. Such utility is demonstrated in a variety of rodent models of ventricular hypertrophy. In an abdominal aortic banding model, flux through PDH remains stable during hypertrophy development whereas [1-^{13}C]lactate increases [63] suggesting an uncoupling of glucose oxidation at the level of PDH with increased glycolysis. This in-vivo finding corroborates ex-vivo work demonstrating increased glucose oxidation [64], and increased

glycolysis [65] in such animals. More pronounced hypertrophy is seen in the spontaneously hypertensive rat, a genetic model which progresses quickly to failure. Here, increased PDH flux is seen, representing either forced upregulation of glucose oxidation due to the impaired fatty acid oxidation in the model, or, a compensatory mechanism seen as disease progresses [66]. Finally, depression of PDH flux marks metabolic decompensation (accounting for markedly reduced glucose oxidation) occurring at the onset of mechanical dysfunction in a porcine pacing induced heart failure model [67]. Temporal changes in cardiac substrate preference during progression toward a universally energy deplete stage of heart failure is likely disease specific and highly heterogeneous between individuals. The technique could thus be valuable in identifying those in which metabolic therapy to increase glucose oxidation may be beneficial. Such therapy includes trimetazedine to inhibit the β-oxidation of fatty acids, and perhexiilne to inhibit the CPT1 mediated translocation of fatty acids in to the mitochondria, both of which reciprocally increase glucose oxidation and both of which have been shown to improve cardiac performance in those with heart failure [68, 69].

Hyperpolarised MR has the power to detect smaller changes in substrate metabolism such as physiological, Randle cycle based changes in PDH flux that have been discussed in section 1.2.2. These changes have been demonstrated during feeding in mice [70] rats [71] and pigs [72]. Such experiments are discussed in more detail in chapter 4, where I try to observe such changes in the human heart. I also test its ability to identify the pathological changes seen in diabetes, which is characterised by reduced PDH flux in the fasted state and a blunted response to feeding [71] (likely due to PDH kinase [PDK] overexpression [73]). In diabetes, raised FAs leads to myocardial steatosis (measured by ^{1}H magnetic resonance spectroscopy [74]), with upregulation of myocardial peroxisome proliferator activated receptor alpha (PPARα) signalling shifting substrate preference away from glucose towards

FA oxidation [75]. Decreased glucose uptake in the human diabetic heart has been demonstrated with [^{18}F] fluorodeoxyglucose (FDG) PET [76], but oxidation changes cannot be studied with this technique. By measuring PDH flux, the relative contributions glucose (via glycolysis), and by inference FAs (via β-oxidation) are contributing to the acetyl-CoA pool (and thus ATP generation) at the moment of imaging can be assessed. Diabetes is also characterised by progressive energetic impairment with a reduction in PCr/ATP [15], as measured by ^{31}P-MRS (described more fully below). Together [77], steatosis and energetic impairment drive structural changes in the diabetic heart which evolves from impaired relaxation toward a heart failure phenotype – 'diabetic cardiomyopathy' [78], which is discussed in more detail in chapter 6. By measuring all of these parameters in the translational study presented here, I can compare the effect size of diabetes on each.

1.5 Myocardial energetics and the high energy phosphate pool

1.5.1 ^{31}P-Phosphorus spectroscopy for the study of myocardial energetics

Interrogating dynamic changes within the cardiac HEP pool via invasive biopsy techniques is not practical. ^{31}P-MRS, however, is non-invasive, meaning the chemical environment is not disturbed by the biopsy process itself. ^{31}P is a naturally abundant isotope of phosphorus, and within the spectrum all compounds containing ^{31}P (given sufficient concentration) can be identified, with chemical shifts determined by the chemical environment of the ^{31}P nucleus. The human cardiac ^{31}P MRS spectrum contains 5 obvious resonances (peaks). PCr is arbitrarily assigned a chemical shift value of 0ppm, and is readily seen, due to a myocardial concentration in health reported in the range of 20-30mM [2, 20, 79]. Three resonances are seen from ATP (3-7mM [2, 20]) each representing one of the three possible positions of the ^{31}P nucleus within the ATP molecule. These are seen at chemical shifts -2.6 (γ), -7.5 (α) and -

16 (β) ppm. Beta ATP is often incompletely excited however depending on the bandwidth of the excitation pulse used. Two other peaks are commonly seen, corresponding to 2,3-DPG contamination from blood (seen at 7ppm), and phosphodiesters (mainly membrane phospholipids) at 2.5ppm. The inorganic phosphate (Pi) signal is largely buried due to its chemical shift being within the range of that measured for 2,3-DPG. A typical ^{31}P-MRS spectrum can be found in Figure 5. Robust resolution of Pi such that cardiac pH can be computed from its chemical shift relative to PCr (discussed below), and Pi/PCr be calculated (a novel marker of energetic dysfunction), has not been previously achieved in humans and is the subject of the inorganic phosphate chapters (5 and 6) in this work. The first demonstration of quantification of phosphate metabolites in the human heart was by Paul Bottomley using ^{31}P NMR in 1985 [80]. Since then, the technique has been instrumental in studying the energetic status of the human heart under various conditions and pathologies. Signal to noise ratio (SNR) is an ongoing problem, but this can be improved by scanning at the higher field strength of 7T which has recently been described [81, 82].

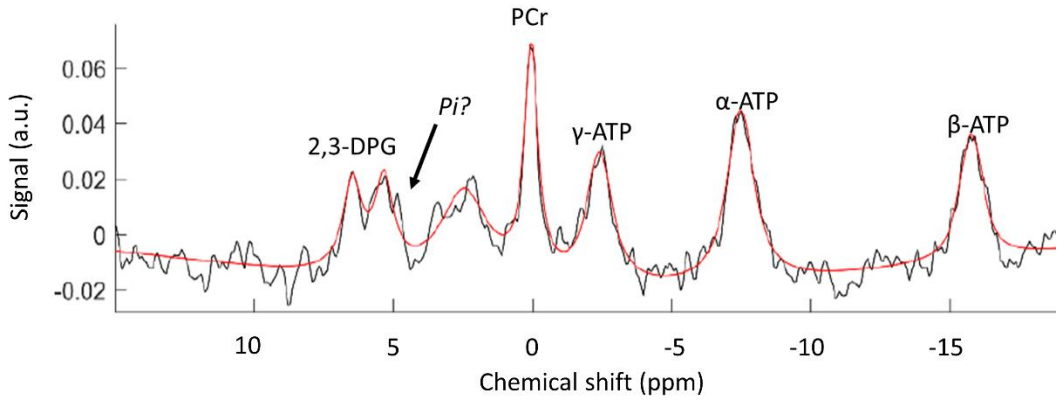


Figure 5: A typical cardiac ^{31}P-MRS spectrum

Typical ^{31}P-MRS cardiac spectrum (patient DM13 from chapter 3) demonstrating all phosphorous resonances seen. PCr and γ- and α-ATP as well as phosphodiesters (PDE) and 2,3-DPG are clearly seen. Pi is not visible, being obscured by the 2,3-DPG peak at around 5ppm.

1.5.2 Phosphate metabolism in diabetes and heart failure

Contemporary human ^{31}P-MRS studies report PCr/ATP as a marker of the prevailing energy status of the cell. PCr is present in concentrations twice that of ATP in the healthy myocardium, providing a PCr/ATP of ~2, and is maintained at a constant value due to co-ordination of ATP utilising and synthesising pathways. This ratio is shown to be depressed in systolic heart failure such as encountered in dilated cardiomyopathy [83, 84], where the finding correlates with New York heart Association (NYHA) class [85], and impacts prognosis independent of left ventricular (LV) function [83]. A fall in PCr/ATP in this context is in part due to myocardial loss of both creatine and purines which can mean the measured ratio does not accurately reflect the degree of energetic impairment, and may indeed underlie normalisation of the ratio in some published heart failure cohorts [86]. This is discussed in more detail below as a key consideration in making the case to quantify Pi/PCr. A reduced PCr/ATP characterises other systemic conditions considered as at risk of developing a cardiomyopathy phenotype such as obesity [16, 77], diabetes [15], left ventricular hypertrophy (with normal systolic function) [87] and hypertrophic cardiomyopathy [17]. Experimentally, interrogating myocardial energetics during stress is important, given evidence that energetic impairment is often exacerbated (or latent deficits revealed) at times of stress, with compromise of the underlying mechanisms which underpin the remarkable homeostasis of the HEP pool exacerbated (or exposed) during an incremental workload [15, 16, 17, 77, 87].

Compounding a reduction in PCr/ATP, derangement in CK flux itself is recognised as a factor driving energetic dysfunction. Using saturation transfer techniques, the CK first order rate constant K_f is shown to be depressed in human heart failure [42, 88]. These non-invasive findings agree with the reduced CK activity demonstrated when directly assayed from endocardial (or papillary muscle) biopsy tissue taken from DCM patients awaiting cardiac transplant [89], or the hearts of those with severe valvular heart disease awaiting cardiac surgery [90]. The failing heart is likened to an engine running low on fuel, and although the energy starvation theory of heart failure is accepted [1], the exact contribution of abnormalities in CK flux, oxidative phosphorylation, substrate handling, and Purine / creatine metabolism to this energy deficient state (or indeed which is primary), is yet to be identified.

1.5.3 Why measure Pi; ΔG_{ATP}, Pi/PCr and pH

Aside from the negative effect [Pi] has on $\Delta G_{ATP,}$ multiple arguments can be made for its measurement. The mechanisms driving the observed fall in PCr/ATP in heart failure may make it an insensitive tool to probe early energetic dysfunction. Phosphocreatine, is a sensitive marker of myocardial energetic dysfunction in the human heart. Myocardial creatine directly assayed from tissue biopsy from the hearts of those with DCM is shown to be reduced by a half [89]. Non-invasively measured by ^{31}P-SLOOP MRS, in the myocardial compartment, [PCr] is reduced by the same amount [91]. Creatine loss with a fall in [PCr] is also demonstrated to occur prior to the onset of frank heart failure, with PCr reduced in those with severe aortic stenosis but preserved ventricular function [91], and also in those with essential hypertension and concentric hypertrophy [88]. Unlike PCr however, conserved ATP homeostasis in the early stages of compensated heart failure make [ATP] an insensitive metric to probe early pathological changes in energy metabolism. As heart failure ensues, ATP is shown to fall by

up to 35% in human DCM [91, 92], likely reflecting a reduction in the total purine pool [93]. Given this parallel fall in PCr and ATP in the later stages of heart failure, a measured PCr/ATP may underestimate energetic dysfunction and may even become pseudo-normal.

Mirroring an early fall in PCr however, a rise in [Pi] is shown in a rodent thoracic aortic banding model of hypertension, in spite of unaltered [ATP] [65]. Pi, as estimated by the difference in the 2,3-DPG resonance, was also shown to be elevated in humans with hypertension and ventricular hypertrophy compared to controls [87]. Pi is a potent stimulator of the glycolytic enzyme phosphofructokinase [94], such that this observation may be adaptive, in part accounting for the increased glucose oxidation and glycolysis observed in early compensated heart failure [1, 58]. Furthermore, during adrenergic stimulation such as during exercise, glucose is mobilised from glycogen stores via activation of glycogen phosphorylase, mediated by PKA phosphorylation through the second messenger cyclic AMP [95]. In a canine model of hypertrophy [12] Pi was shown to significantly increase during intra-cardiac pacing in LVH but not control animals (with PCr/ATP remaining stable in both groups). Pi is a substrate for the active glycogen phosphorylase, and is non-saturating at rest (Km 26mmol/l) [96], as such, higher basal levels and increases during stress would augment glucose mobilisation from glycogen during stress, further increasing the bioavailability of glucose as a substrate. Clearly, small rises would however come at the cost of a rise (albeit tiny) in $\Delta G_{ATP.}$ Such observations again demonstrate the importance of being able to make recordings of Pi at stress to uncover latent deficits in energetics. With the potential of Pi increasing earlier in disease progression and moving reciprocally to PCr, Pi/PCr may offer a more sensitive marker of impaired myocardial energetics than PCr/ATP.

As described in the oxidative phosphorylation section above, Pi along with ADP are considered key feedback modulators of mitochondrial ATP production [23, 24]. Measuring

this non-invasively thus opens up another branch of energy metabolism, especially in conditions where impairment of oxidative phosphorylation, such as hypoxia, occur. In ischaemia, intracellular [Pi] is far more labile than [ATP] and [PCr], rapidly increasing by many orders of magnitude following hypoxia [23] with concentration climbing as the ischaemic time is prolonged [97]. Pi is shown to rise first at the onset of ischaemia, earlier than a smaller rise in [ADP] which occurs at the onset of left ventricular mechanical dysfunction [98]. As such, this rapid increase in [Pi] drives the fall in phosphorylation potential ([ATP]/[ADP]+[Pi]) which may account for the onset of systolic dysfunction; mediated by a failure of various ATP requiring processes such as SERCA2A driven calcium resequestration into the SR (shown to be inhibited by Pi [99]) and failure of cross bridge cycling.

Compounding myocardial loss of purines and creatine during progression toward heart failure, K_f is shown to be depressed in human heart failure [42, 88]. With reduced PCr and CK flux (K_f.[PCr]), the bioavailability of ATP at sites of hydrolysis is dramatically reduced [88, 100]. Due to an inability to define the resonance (and thus saturate) Pi during ^{31}P-MRS experiments, K_r cannot be measured in-vivo using saturation transfer techniques in humans. In silico-modelling along with experimental observations of the consequences of alterations in CK flux on phosphorus metabolites suggest a rise in [Pi] but not [ADP] can be expected with impaired global CK flux, or specifically MtCK [50]. As such Pi may represent a proxy through which an impairment in CK flux can be investigated. Indeed, this hypothesis may account for discrepancies in models investigating Pi as a modulator of control of oxidative phosphorylation. Observations of rises in Pi in healthy hearts in open chest animals exposed to high grades of cardiac stress induced by combinations of pacing, adrenaline, and decoupling agents, may reflect loss of the CK steady state with a consequent explosive rise in Pi [11, 12, 18]. This point may be brought forward, to lower degrees of stress in conditions

such as hypertrophy or heart failure characterised by impairment in basal CK flux [12, 87]. The magnitude of changes in Pi implicated in control of oxidative phosphorylation over a physiological range of work (such as induced by small increases in heart rate alone [18]) are however smaller in magnitude [9], and given low myocardial concentrations, likely much harder to detect in the healthy heart with non-invasive ^{31}P-MRS assessment. Again, exposing a latent impairment of CK flux (by assessing Pi) only manifested during high workloads, requires a protocol acceptable to patients during dobutamine stress.

Intracellular pH homeostasis is achieved by a variety of sarcolemmal and membrane H^+ transport proteins [101]. Despite these mechanisms restricted H^+ diffusion within the cell can lead to cytoplasmic pH gradients, this is mitigated by mobile buffers such as histidyl dipeptides which effectively shuttle H+ between the SR and cytoplasm [101, 102]. Myocardial intracellular pH is tightly regulated with falls in pH below a steady state of 7.2 prompting contractile depression [103] and arrhythmia [104], thus the recording of myocyte pH non-invasively may be clinically desirable. Measurement of Pi with ^{31}P-MRS, provides a mechanism for this and was, first demonstrated by Moon *et al* in red blood cells [105]. At physiological pH Pi exists mainly as HPO_4^{2-} and $H_2PO_4^-$ whose chemical shifts differ by 2.4ppm. These species are in exchange as indicated in the equation below. The acid dissociation constant (pKa) for each reaction is given above each arrow.

$$H_3PO_4 \overset{2.14}{\Longleftrightarrow} H_2PO_4^- + H^+ \overset{6.77}{\Longleftrightarrow} HPO_4^{2-} + H^+ \overset{12.4}{\Longleftrightarrow} PO_4^{3-} + H^+$$

Rapid chemical exchange between hydrogen phosphate and hydrogen diphosphate gives rise to only a single resonance in the ^{31}P spectrum, whose chemical shift is determined by their relative concentrations. The pKa (6.77) for this dissociation is close to physiological pH,

meaning this resonance is extremely sensitive to pH changes within this range (which shifts this equilibrium) [106]. Myocardial pH can be calculated from the shift of Pi relative to PCr, using a modified Henderson-Hasselbalch relationship:

$$\mathrm{pH}(\delta) = 6.77 + \log_{10}\frac{\delta - 3.23}{5.70 - \delta}$$ [107].

Experiments measuring intracellular pH using the chemical shift of deoxyglucose-6-phospate (pH sensitive, but exclusively cytosolic) agree with those of Pi, providing reassurance that the technique measures intracellular, and not mitochondrial pH [107]. pH assessment by ^{31}P NMR quantifies the acidosis associated with ischaemia in ex-vivo models [107, 108]. In-vivo pH quantification by this method maybe of clinical benefit in cardiology beyond localising ischaemia, given falls in cytoplasmic pH occur in various pathological processes and may herald contractile dysfunction and dysrhythmia [101].

1.5.4 Challenges and solutions to measuring Pi using ^{31}P-MRS

These experimental observations of cardiac Pi under various conditions are from the ex-vivo heart, or in-vivo open chest models. These are unconfirmed in the human heart. Data on human cardiac Pi are scarce because overlap from 2,3-DPG has made it challenging to quantify reliably. This is of course compounded by its sub-millimolar concentration. The myocardium forms a comparatively thin wall around the blood-filled ventricle. Resolving blood and heart muscle tissue by localisation techniques is not possible given the voxel size required for adequate ^{31}P-MRS SNR. Various approaches have been suggested for ^{31}P-MRS of cardiac Pi in the presence of contaminating blood pool 2, 3-DPG. Recently, our group showed that using

the higher SNR and spectral dispersion at 7T, cardiac Pi can be quantified in 45 minutes from long T_R chemical shift imaging (CSI) ^{31}P-MRS with adiabatic excitation [109]. However, a 45-minute measurement duration is too long for stress-response studies, and some overlap of 2,3-DPG remains making resolution imprecise. Other approaches have been tried in the past at lower field strengths, including ^{1}H-decoupled ^{31}P-MRS to reduce Pi and 2,3-DPG linewidths in the hope of achieving separated peaks [110, 111]. Signal to noise is still low using this technique however with Pi reported cleanly in only half the healthy subjects, despite a scan time of 30 minutes (again making stress studies not practical). This approach is not feasible at higher field strengths due to regulatory limits on specific absorption rate (SAR) and the restriction on peak B_1^+ for ^{1}H.

We therefore aimed to develop a measurement technique for Pi that provides an adequate SNR within a scan time that allows stress measurements in both controls and patients, and good blood signal suppression, sufficient to allow reliable quantification of Pi amplitude and frequency (pH). Stimulated Echo Acquisition Mode (STEAM) MR has been previously shown to suppress signal from moving spins in blood in ^{1}H-MRI [112, 113], and is also a commonly used and available MRS technique. In contrast to CSI [114], which generates bright blood contrast, STEAM generates dark-blood contrast. In this thesis, I have investigated the potential for a STEAM protocol to demonstrate cardiac Pi without obscurement from 2,3-DPG, in a short enough time frame (14 minutes) that the sequence could practically be used during stress, and in patients.

1.6 Assessment of myocardial lipid content

The elevated plasma FA levels seen in diabetes leads to increased myocardial FA uptake and subsequent steatosis [74, 115], this has an important metabolic consequence for the heart.

PPARα upregulation occurs, [116] which transcriptionally upregulates various enzymes involved in FA metabolism, and reduces glycolytic flux and PDH flux [71, 117, 118]. The effect of this is a loss of metabolic flexibility, with an inability to upregulate glucose oxidation, away from FA oxidation. Myocardial steatosis is also associated with structural changes in diabetic patients, with concentric remodelling [119], and significant diastolic dysfunction [120] occurring en route in some cases to development of diabetic cardiomyopathy [121]. Mechanistic causation between steatosis, abnormal energetics and substrate handling, leading to diastolic impairment and cardiomyopathy is however lacking. With this in mind during the first human study attempting to directly record PDH flux in the human diabetic heart presented in chapter 4, an assessment of myocardial lipid content was also made using ^{1}H MRS.

The proton (^{1}H) is abundant in long chain FAs, and as such SNR in ^{1}H MRS experiments is typically better than for the ^{31}P or ^{13}C nucleus. However, unlike the ^{31}P spectrum the ^{1}H spectrum is complex due to the large number of different chemical environments experienced by protons within FAs. Using water suppression to remove the signal from solvent, the technique is typically used to calculate total triglyceride content – expressed as a percentage relative to the water signal. Examples of spectra can be found in Figure 6.

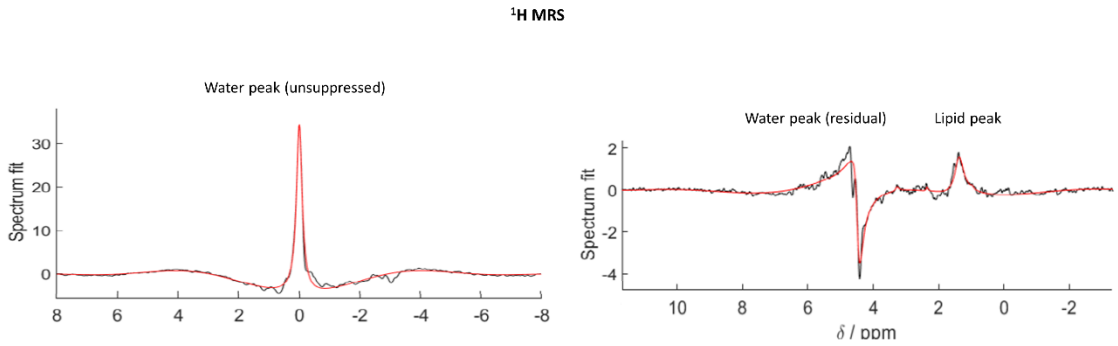


Figure 6: A typical ^{1}H MRS spectrum

^{1}H MRS spectra from a healthy volunteer (chapter 4), lipid spectra (right) are scaled using the unsuppressed water peak (left).

1.7 Toward imaging metabolism using hyperpolarised MR

MRS techniques discussed thus far assess metabolism in the voxel of interest, any assessment of myocardial signal away from the cardiac septum is difficult due to loss of signal around the posterior aspect of the heart, and requires multiple scans. The signal amplification that DNP provides offers the potential to regionally localise variation in metabolism of the administered hyperpolarised tracer within a target tissue or organ.

Hyperpolarised imaging studies in humans have recently begun. Initial work has been focussed on imaging the metabolic hallmark of a number of solid malignancies – the Warburg effect. Here, metabolically reprogrammed cancerous cells upregulate glycolysis even in the presence of adequate oxygenation. A resultant increase in lactate can be imaged using hyperpolarised [1-^{13}C]pyruvate. [1-^{13}C]lactate / [1-^{13}C]pyruvate has been shown to be elevated in areas of biopsy proven human prostate cancer [122], with magnitude correlating with histological Gleason score and expression of the mono-carboxylate 1 transporter [123], the primary pyruvate cellular uptake transporter protein. A high [1-^{13}C]lactate signal has also recently been shown to delineate pancreatic adenocarcinoma from surrounding normal exocrine tissue in two patients with pancreatic cancer [124], and malignant cells from normal brain in a number of cases of primary or secondary neoplasms [125]. The ability to detect this phenomenon non-invasively has not been possible prior to DNP, and not only has diagnostic implications in oncology, but also in measuring treatment response [126].

Significant utility for the technique also lies in cardiology for the detection of ischaemia and its consequences. Compelling evidence suggests that 'ischaemic burden' from

stable coronary artery disease confers risk [127], and that revascularisation with cardiac stenting or bypass restores myocardial contractility to hibernating tissue deemed viable by CMR [128]. However, the clinical impact of revascularisation procedures aimed at these targets is often disappointing, [129, 130]. One explanation for this discrepancy is that the non-invasive testing used as a gatekeeper for access to these is only measuring surrogate markers (flow or perfusion for ischaemia, and an expansion of the extracellular space for viability) rather than the metabolic hallmarks of ischaemia and viability (lactate production and respiration). Preclinical work using porcine models demonstrates that hyperpolarised imaging can delineate ischaemia following coronary artery occlusion, and viable from non-viable myocardium following infarction [131, 132]. Metabolic imaging of the healthy human heart after hyperpolarised [1-^{13}C]pyruvate injection has been described [133]. The final chapter of this work, presents preliminary work using an imaging sequence to demonstrate regional variations in PDH flux consistent with areas of viability and ischaemia in the hearts of those with coronary artery disease.

1.8 Aims of this work

1) To define the optimal preparation regimen for hyperpolarised [1-^{13}C]pyruvate experiments in humans. Using a small animal model, variability and magnitude of PDH flux was compared in fed, and fasted then glucose loaded states, in both control and diabetic animals.

2) The human translation of hyperpolarised MR aimed to quantify with MRS the physiological Randle cycle changes in PDH flux that occur during feeding, and the impact of insulin resistance on this in those with diabetes. By making a multinuclear

assessment of metabolism in this diabetic cohort using ^{31}P and ^{1}H MRS, a comprehensive assessment of the impact of diabetes on metabolism was made.

3) To determine the robustness of using STEAM ^{31}P MRS at high field strength (7T) to record myocardial Pi free from contaminating 2,3-DPG.

4) To test the hypothesis that gross increases in myocardial Pi are required to signal an increasing myocardial work load to the mitochondria and upregulate the rate of mitochondrial respiration.

5) To record myocardial Pi/PCr and pH at rest and during stress in both a diabetic and DCM cohort, and compare results to that seen in a normal healthy cohort.

6) To test whether changes in Pi/PCr at rest, or in its response to pharmacological stress correlated with left ventricular characteristics as recorded by CMR (in DCM) or grade of diastolic dysfunction (in diabetes).

7) In the final chapter prior to beginning clinical studies, I aimed to test the feasibility of using a hybrid shot spiral sequence to image the myocardial metabolic conversion of hyperpolarised [1-^{13}C]pyruvate, and identify local pathological metabolism following myocardial infarction.

Chapter 2 (methodology)

2.1 General ethical considerations

All animal experiments conformed to the Animals (Scientific Procedures) Act (1986), were carried out under project licence number 30/3322 and were approved by a local ethics committee. All volunteers (patients and healthy controls) included in the clinical research studies provided written informed consent prior to participation. Research was carried out in accordance with the principles of Helsinki and Caldicott principles. References to requirements specific to each experiment can be found in the relevant sections. Healthy volunteers and patients were recruited from the outpatient clinics, in-patient wards and diagnostic testing services of Oxford University Hospitals NHS trust, Buckinghamshire NHS trust and Harefield Hospital. This was done from a combination of replies to posters displayed within OUH sites and approaches to patients from members of their regular clinical care teams. All research was locally approved by Oxford University hospitals research and development.

2.2 Hyperpolarised magnetic resonance

2.2.1 Production of hyperpolarised [1-^{13}C]pyruvate

Sterile fluid pathways (SFPs) from which [1-^{13}C]pyruvic acid for human injection is generated were supplied by GE healthcare and filled in-house in a grade A sterile environment by the team at the clinical trials aseptic services unit at the Churchill hospital Oxford, for which I am grateful. These contained 1.47g [1-^{13}C]pyruvate (Sigma Aldrich, Gillingham, UK) and 15mM AH111501 (Syncom, Groningen, Netherlands) as the electron paramagnetic agent (EPA).

These were frozen in a General Electric SpinLab system (GE Healthcare, Chicago, USA) [134] which was used for the process of DNP. Sufficient polarisation levels of 30-40% were achieved after 2-3 hours of microwave irradiation. Dissolution was achieved using 38.5g sterile water heated to 130^{o}C under pressure, released through the pyruvate containing vial into a receiving chamber containing 17.7g of trometamol buffer solution (600 mM NaOH, 333 mM Tris base, and 333 mg/L disodium EDTA [as the chelating agent], Royal Free Hospital UK), and a further 19.5 g of sterile water. The EPA was filtered prior to the receiving chamber, with the final product for injection drawn from the receiving chamber into a 50ml injection syringe (Bayer, Indianola, USA) via a further 0.2µm sterilisation filter (Saint-Gobain, Gaithersburg, USA). The structure of the disposable sterile fluid pathway (SFP) can be seen in Figure 7.

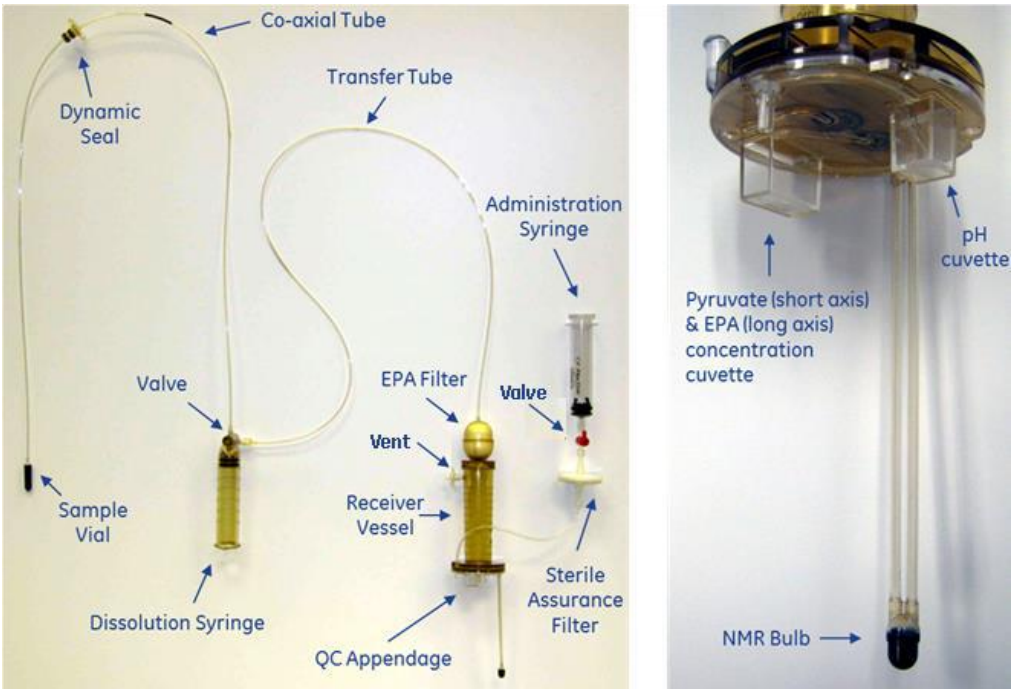


Figure 7: Typical sterile fluid pathway for human studies

The sample vial containing 1-^{13}C[pyruvate] was loaded in to the polariser with sufficient polarisation achieved after between 2 and 3 hours. Dissolution was achieved by releasing super-heated sterile

water under pressure from the dissolution, across the sample vial in to a receiver vessel containing buffer and EDTA.

2.2.2 Quality control of hyperpolarised [1-^{13}C]pyruvate solution

Rigorous quality control of the final filtered sodium [1-^{13}C]pyruvate solution was undertaken prior to human administration. This consisted of both online measurements (pyruvic acid concentration, pH, residual EPA concentration, temperature, polarization, volume) directly from the SpinLab inbuilt QC console, with further 'offline' pH measurement (RQflex 10 from Merck, Darmstadt, Germany), and visual inspection of the product (for sediment / purity), undertaken manually prior to release. Pathways were only released for human injection if the following criteria were met: pH 6.7-8.4, temperature 25.0-37°C, polarisation ≥ 15%, pyruvate 220-280mM, EPA ≤ 3µM, appearance: clear with no visual particulate matter. Pathways not meeting these release criteria were rejected. Hyperpolarised [1-^{13}C]pyruvate solution was administered through an 18G BD venflon™ sited in the left antecubital fossa, at a dose of 0.4ml/kg, followed by a 25ml 0.9% normal saline flush. Injections were undertaken at a rate of 5mls per second using a MEDRAD ® power injector system (Bayer, Berlin, Germany). The experimental setup is summarised in Figure 8.

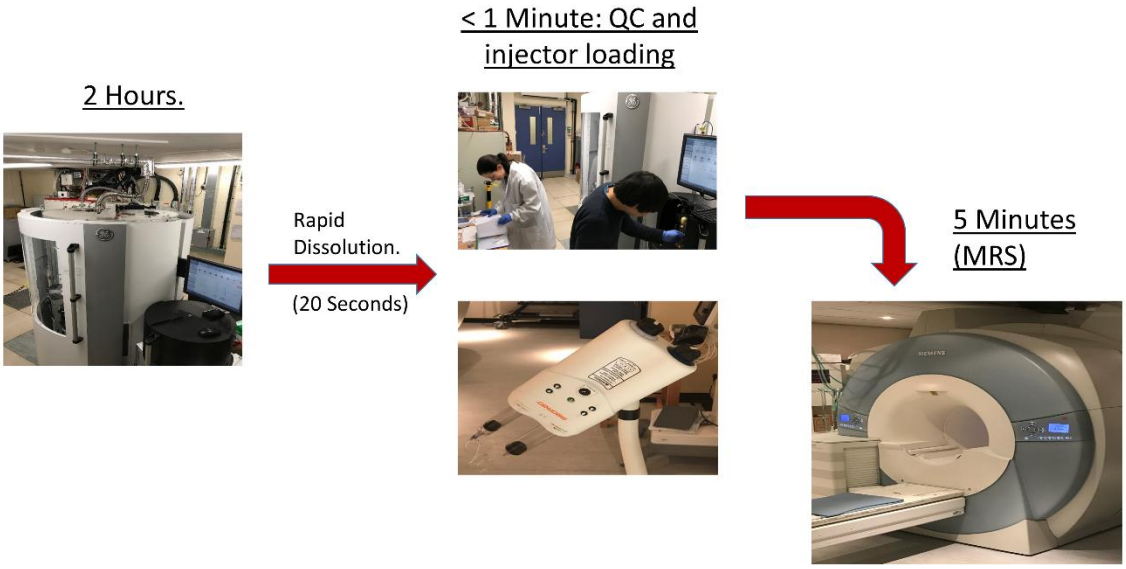


Figure 8: The dissolution process and team members

Quality control requires 2 appropriately trained individuals. The administration syringe is released from the QC unit (left) which gives a set of parameters for the final product. The syringe is passed to the deliverer (myself) into the 3T magnet room through a hatch in the wall. The syringe is loaded in to the power injector by me, while a second clinician (Professor Rider) in the control room, delivers the injection.

2.2.3 Clinical Hyperpolarised MRS protocol

Subjects were scanned supine and free breathing, short axis localisers to plan hyperpolarised data acquisition were acquired using the inbuilt ^{1}H body coil. ^{13}C MR spectra were acquired using a 2 channel transmit, 8 channel surface receive array (Rapid Biomedical, Rimpar, Germany). A [^{13}C]urea fiducial marker strapped on top of the coil was used to calibrate the ^{13}C centre frequency. Thermal equilibrium spectra were acquired prior to hyperpolarised injection and used to subtract the fiducial and background thermal equilibrium fat signals from the hyperpolarised spectra, leaving a pyruvate only signal. Hyperpolarised data were

acquired from a mid-ventricular 10mm axial slice, beginning immediately after delivery of the saline flush.

The MR acquisition was a pulse-acquire spectroscopy sequence with slice selection achieved with a 1.3 ms sinc excitation triggered by ECG-gating to the R-wave. A single excitation and spectroscopic readout was acquired every heartbeat and run for up to four minutes after injection (flip angle 10°, bandwidth 5 kHz, TR 500 ms). Multi-coil data were recombined in MATLAB using the Whitened Singular Value Decomposition algorithm (WSVD) [135], with coil combination weights calculated for spectra with the highest SNR subsequently applied to the entire dataset. Spectra were background-subtracted prior to quantification with the AMARES algorithm [136], with appropriate prior knowledge. Spectral fitting here was checked by Dr Jack Miller. Total integrated metabolite-to-pyruvate ratios, known to linearly correlate with first-order chemical kinetic rate constants [137], were calculated from 60 seconds of data taken after the initial appearance of the pyruvate resonance in the spectrum.

2.3 Phosphorus spectroscopy

2.3.1 ^{31}P-MRS STEAM sequence theory and design

To robustly define Pi without contaminating 2,3-DPG signals, my work employed a STEAM sequence for ^{31}P-MRS, at the higher field strength at 7T to improve SNR. STEAM uses three selective 90° pulses to produce a stimulated echo which is acquired for spectroscopy. The first pulse flips magnetization in to the transverse plane where T_2 relaxation occurs, the second pulse (delivered at TE/2) then flips magnetisation in to the longitudinal plane and dephasing effectively stops. Prior to the third pulse, a pause occurs, known as the mixing time (T_M), which can be chosen by the operator. Theoretically this delay can be tailored to the metabolite of

interest. Since the T1 of Pi is relatively long - recorded recently at 5s [109, 138], it is almost unaffected by extending this pause, while the signal of the moving blood is suppressed if T_M is long enough, thus creating a selective sequence for acquisition of cardiac Pi free from contamination. Finally, the third pulse flips magnetisation back in to the transverse plane, where spins rephase and a stimulated echo is recorded at TE/2. The structure of the STEAM sequence is summarised in Figure 9.

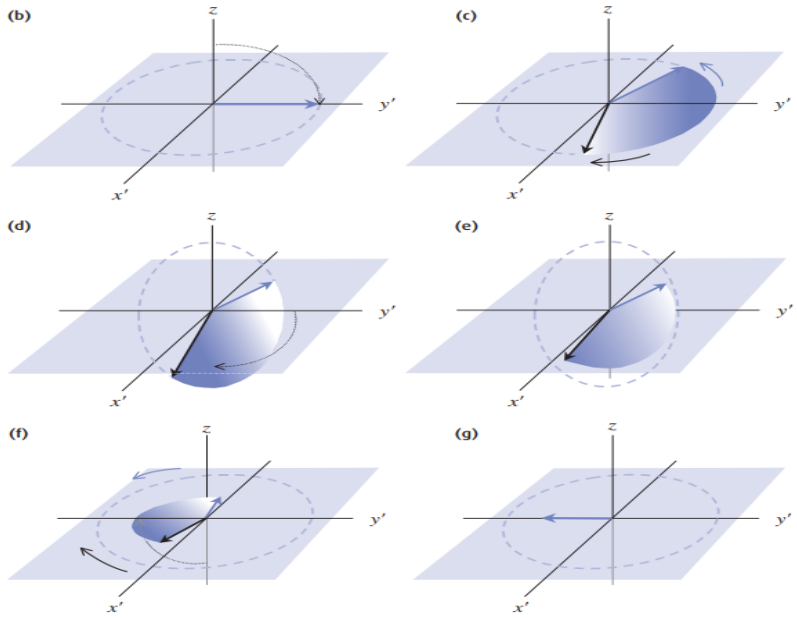


Figure 9: Physics of the STEAM sequence

STEAM used three 90° pulses to produce a stimulated echo used for spectroscopy. First magnetisation is flipped in to the transverse plane where T2 relaxation occurs (b,c), a second pulse flips the spins in to the longitudinal plane where T1 relaxation occurs during T_M (d,e). Finally, a third pulse flips spins back to the transverse plane (f) where they re-phase (g) and a stimulated echo is recorded. (McRobbie 2006).

Unlike the GRE/FLASH-like contrast of the typical CSI sequences used for cardiac ^{31}P-MRS, STEAM ^{1}H cardiac imaging achieves dark blood contrast because incoherent motion of the blood during T_M, will lead to dephasing of the blood signal [112]. Meanwhile, the myocardium is relatively immobile so that myocardial ^{31}P signals are preserved if the T_M is chosen appropriately [113]. The RF coil used in the studies had good receive sensitivity with 16 receive channels but a rather low transmit field (peak B_1^+ was about 10 μT at the depth of the heart), meaning long (4.5ms truncated sinc) pulses were required to obtain the 90^O pulses required by STEAM. Such pulses have small bandwidth and, when compounded by large voxel dimensions, result in significant chemical shift displacement. The experiment was thus split in two, with one excitation centering the RF pulse on the PCr peak in the first scan (0ppm) and a second on Pi thereafter (5ppm). These two were interleaved during T_R. This had the additional advantage that T_E, and in particular T_M, could be set to different values for Pi and PCr. Based on STEAM imaging data [113], a T_M of 60 ms was chosen for Pi, representing a good compromise between blood suppression and sensitivity to diffusion and cardiac motion which caused dephasing and signal loss at T_M>60ms (experiments undertaken by Ingo Schmid, not published). Scalar coupling during the prolonged T_M further helps suppress signals from 2,3-DPG. The shortest possible echo time (T_E = 13 ms) was used to minimise effects of T_2 relaxation on the Pi signal. PCr was acquired with short T_M (7ms). Recording of the stimulated echo for each metabolite was in early systole just following the isovolumetric contraction period [139]; the point of data collection within the cardiac cycle was thus fairly constant despite the heart rate increasing during stress.

A T_R of 3s was used, with the first pulse of the next acquisition delivered on the subsequent R wave. This meant the effective T_R for each metabolite was 2 x (T_R plus an inter-trigger delay time) ≈ 7s. 128 averages were acquired, with scans typically lasting 14 min. The

long effective T_R ensured almost full relaxation between consecutive excitations, improving the detectability of static spins with long T_1, such as cardiac Pi. The sequence diagram is shown in Figure 10. STEAM is a single voxel spectroscopy technique, voxel placement ensured maximal septal coverage and minimal skeletal muscle contamination.

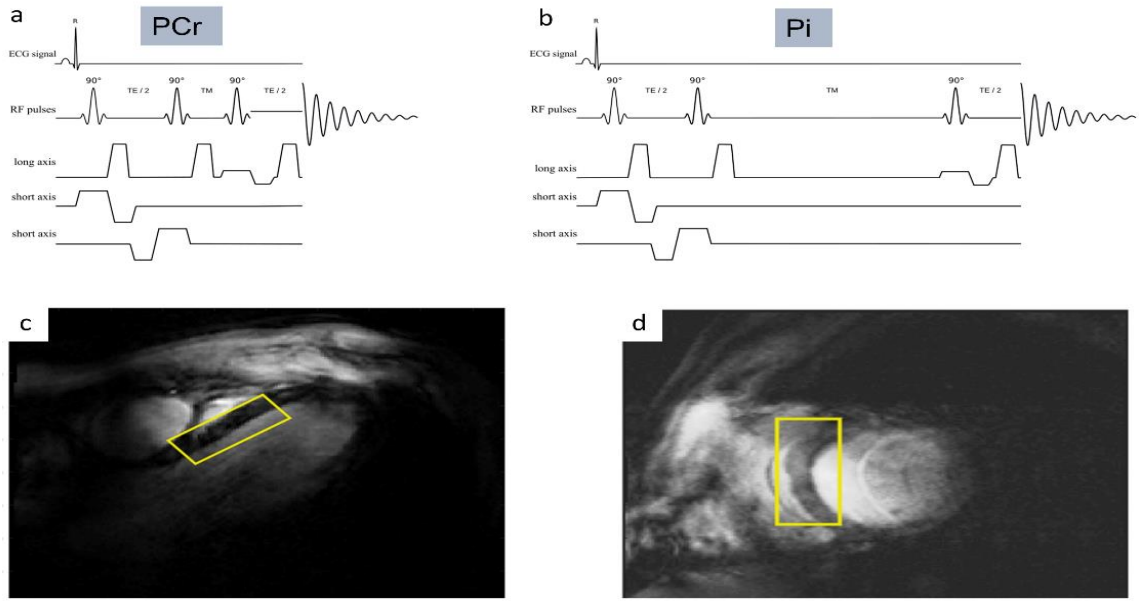


Figure 10: STEAM ^{31}P MRS sequence

STEAM-^{31}P-MRS sequence for interleaved RF excitation centred at PCr (a: RF excitation centred at 0ppm relative to PCr, T_M 7 ms, T_E 13ms) and Pi (b: RF excitation centred at 4.8 ppm relative to PCr, T_M 60 ms, T_E 13ms). Typical STEAM-31P-MRS voxel placement is shown ([c] horizontal long axis view, [d] short axis view), chosen to optimise septal coverage while minimising the potential for skeletal muscle contamination.

2.3.2 ^{31}P-MRS Protocol at 7T

All scanning was performed on a Magnetom whole-body 7T MRI scanner (Siemens, Erlangen, Germany). Using a 10cm ^{1}H transmit/receive loop (Rapid Biomedical, Rimpar, Germany),

localisers were first acquired with 3-lead ECG gating in the main cardiac orientation (HLA / VLA / Short Axis). Subject-specific B_0-shimming (as opposed to the manufacturers tune up shim) was then performed on all subjects, maps were acquired as a stack of 18 dual-echo gradient-recalled echo slices (T_R 314 ms, TE_1 2.4 ms, TE_2 4.3 ms). The standard B_0 map was altered using a Matlab script – here, all pixels with an intensity less than the inferior myocardium were zeroed, with those remaining assigned the value 1. This method ensured that the high intensity of the chest wall was somewhat nullified and did not dominate the shim calculations. It ensured coverage of the whole heart and was recently described in ^{31}P studies at 7T to produce higher quality spectra [82]. The modified map was used in the scanner's shim calculations.

The ^{1}H coil was then removed and swapped for a 16-element array ^{31}P coil (Rapid Biomedical, Rimpar, Germany). This comprised a rigid 27 x 28 cm^2 transmit ^{31}P element, combined with a flexible set of 16, 8 x 5.5 cm^2 receive elements arranged in a 4 x 4 grid. The coil had five fiducial markers each containing phenylphosphonic acid (PPA), and one of two solvents. Four markers at the corners of the coil were used for localisation, each containing the solvent acetone. A marker at the centre of the coil (dissolved in solvent ethanol) was used for calibration of the inversion recovery free induction decays (IR-FIDS). First ^{31}P-FLASH localisers were acquired from the fiducial markers mounted on the coil corners to determine the coil position, then a set of IR-FIDs (13, 1000µs hard inversion pulses, inversion delay 0 – 1500ms) were performed. These were used to calculate the transmit efficiency, such that saturation corrected measurements for PCr/ATP could be calculated from a CSI sequence, as previously described [81]. A voltage reference map of the heart was also generated from these IR-FIDs. This map (Figure 11) allowed me to calculate the voltage required through the coil, to produce the 90° flip angles used in STEAM, in the voxel of interest in the mid ventricular

septum. The map spatially resolves the voltage required for an inversion pulse of 1ms (this was divided by four to give a 90° pulse over 0.5ms). Following the IR-FIDs, an ultra-short-echo–time chemical shift imaging (UTE-CSI) was used to compute PCr/ATP. The CSI sequence was run at rest, free breathing without ECG gating, acquisition weighted (matrix size 8 X 16 X 8; nominal voxel size [25 X 15 X 25mm^3]), with a T_R of 2.2s, and four averages. The CSI grid orientation was cardiac short axis in-plane rotated so the phase encoding direction with the highest resolution was in the anterior-posterior direction to minimise skeletal muscle contamination. The grid was placed to ensure a voxel was appropriate for analysis this was pre-specified and sited at the mid-ventricular level on the first slice when papillary muscle was visible, and in the mid septum Figure 12. Unlike at 3T this not at the most basal level, as usable signal with this sequence at 7T only emerged at the mid cavity level. A single saturation band 25mm thick over the chest wall was used, the voltage of the pulse used was set to the maximum that did not breach specific absorption limits for that subject.

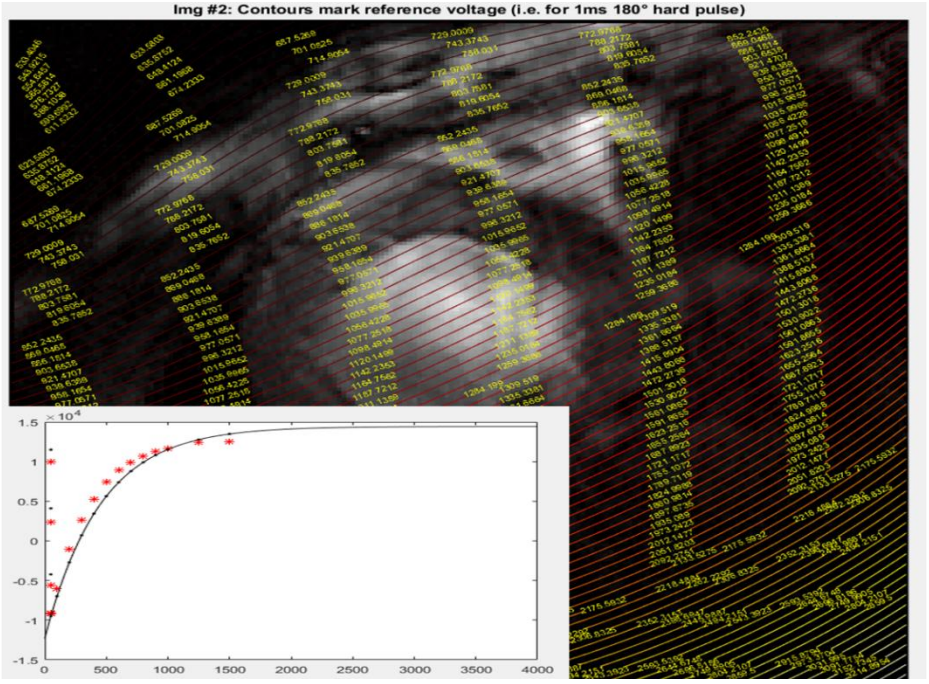


Figure 11: Voltage map of the heart from FID recovery curves

Reference voltage map and FID inversion recovery curve (bottom). Transmit voltages given are those required for an inversion pulse of 1ms duration.

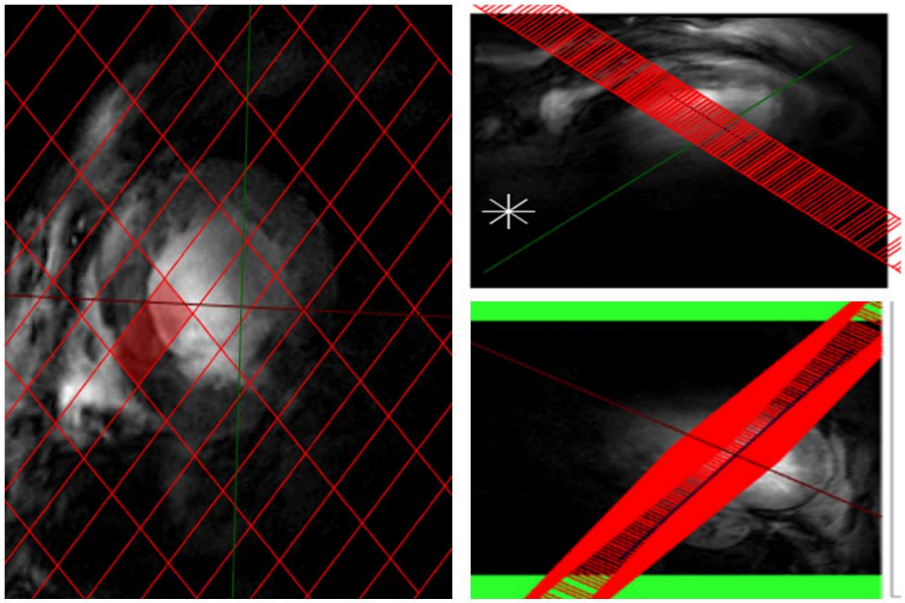


Figure 12: CSI grid positioning for PCr/ATP at 7T

Typical CSI grid orientation for UTE-CSI spectroscopy. The phase encoding direction with highest resolution was in A-P direction minimising skeletal muscle contamination. Grid positioning ensured one voxel was in the mid septum / at the mid ventricular level.

Excitation was with a shaped pulse centred at +300Hz to the right of (lower than the frequency of) PCr [21], such that the excitation band-width covered PCr and γ-ATP and 2,3-DPG. At 7T a longer pulse was used than at 3T to ensure the correct voltage can be transmitted for the required flip angle, this results in a low bandwidth. As such PCr/γ-ATP is reported – the bandwidth is not sufficient to fully excite β-ATP, and α-ATP is contaminated by NADH. This UTE-CSI sequence was recently published [82], and was used here due to its short length (6.5 minutes). Although longer versions of this sequence with more averages reduces uncertainty

in the measurement of PCr/γ-ATP, increases in in-magnet time would likely reduce patient compliance such that the research question answering sections of the protocol (^{31}P-MRS-STEAM) may be compromised.

Next, ECG-triggered, free-breathing STEAM-^{31}P-MRS spectra were acquired with the single voxel covering the basal septum (Figure 10). Firstly, a short scan (48 averages) with a single interleaf centred on PCr was undertaken (3 minutes) to ensure that the excitation frequency was centred exactly on PCr at 0ppm. If necessary, the excitation frequency was changed prior to commencing the full (2 interleaves, 148 averages) scan. During the full scan, shot-to-shot interleaving of acquisitions was undertaken as described. Dobutamine was started (described below) and STEAM-^{31}P-MRS was repeated when 65% of the maximum target heart rate had been achieved.

2.3.3 ^{31}P-MRS protocol at 3T

Scans were performed in the same 3T system (Siemens) as for the hyperpolarised experiments. As previously described in our centre [15, 140], to minimise heart-coil distance, subjects were positioned prone on a dual tuned commercially available ^{31}P (49.8 MHz) /^{1}H (127.7 MHz) surface heart-liver coil (Siemens, Erlangen, Germany). IR-FIDs (ten 1000μs hard inversion pulses, inversion delay 100-3000ms) were acquired, along with the position of PPA fiducials and a cod liver oil phantom. Long and short axis proton localisers were acquired to plan the CSI voxel grid. This was positioned to ensure a voxel of interest contained mid septal myocardium, at the most basal level (Figure 13). Saturation bands were used to minimise signal contamination from skeletal muscle and the liver.

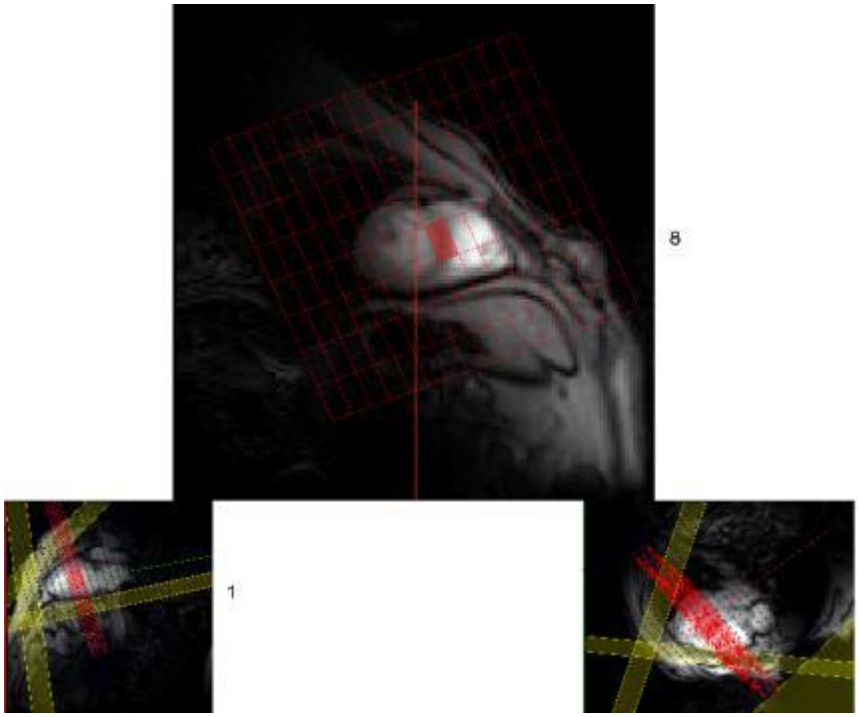


Figure 13: CSI grid positioning for PCr/ATP at 3T

The CSI grid was positioned to ensure the voxel of interest covered the mid-ventricular septum at the most basal slice of the ventricle, defined as being one half voxel shift below the left ventricular outflow tract. Saturation bands (in yellow) covered the liver and skeletal muscle.

PCr/ATP was measured during free breathing using a short echo time (0.3ms) 3D acquisition-weighted (matrix size 16 × 16 × 8, FOV 240 × 240 × 200 mm^3) CSI sequence with 10 averages and T_R 1000ms (nominal voxel size 5.6mls). Excitation with a shaped pulse was centred at -200Hz relative to (lower than the frequency of) PCr (between α and γ ATP) to ensure uniform excitation of all high energy phosphate containing compounds (from β ATP all the way to 2,3-DPG on the other side) [140].

Voxels for analysis were pre-specified, and as is standard practice in our unit at 3T the PCr/average ATP from the two most basal mid septal voxels (separated by a half voxel shift)

were averaged, and results were corrected for blood pool contamination (reducing ATP peaks in proportion to the 2,3-DPG signal) and partial saturations [140]. Apart from anatomical voxel positioning and selection, and visual confirmation of peak fitting, the analysis tool is automated. Inter-observer variability of reported PCr/ATP when analysing the same data using this technique is <5%, similarly low intra-observer variability of 8% is seen on blinded re-analysis of multiple data sets by a single individual [140]. Unlike at 7T the position of the coil has to be fitted manually in Matlab (Figure 14) prior to analysing the data. As at 7T, fitting was undertaken using the Matlab based OXSA open source toolbox to fit the signal with the AMARES algorithm in jMRUI, using a set of prior knowledge of expected chemical shifts and j-couplings of metabolites within the phosphorus spectrum [125].

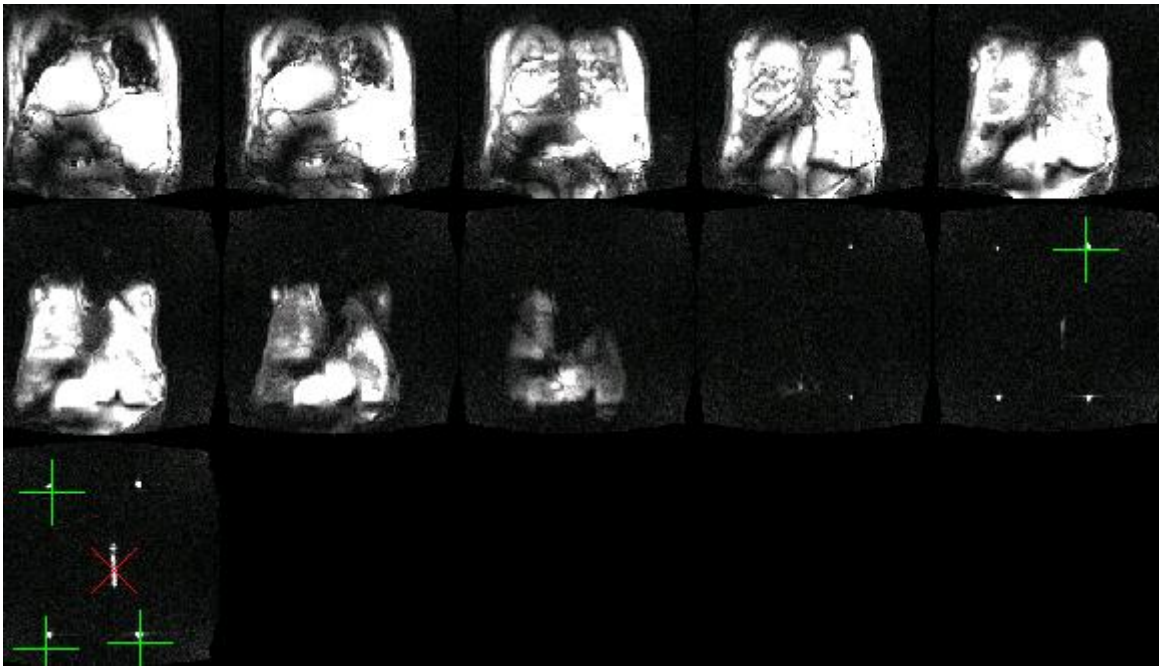


Figure 14: Manual selection of CODS for coil positioning

The manual selection of Cods (green crosses) at the ^{31}P coil corners, and one fiducial (red cross) for coil positioning and the IR-FIDS.

2.4 Other techniques and interventions

2.4.1 ^{1}H-MRS

A suitable mid interventricular septal voxel was firstly selected for analysis from long and short axis cardiac localisers. As previously described [141], myocardial lipid content was measured from a series of five water suppressed, T_1 and B_1 insensitive STEAM spectra (T_E 10ms, T_R 2s, 5 averages), using a 6 channel flexible ^{1}H receive array coil. These were standardised using a single water unsuppressed spectrum. All data were analysed in Matlab using an implementation of the AMARES algorithm in jMRUI using prior knowledge [136]. The myocardial lipid content was calculated as a percentage relative to the water signal. An example spectrum and fitting is shown in Figure 15.

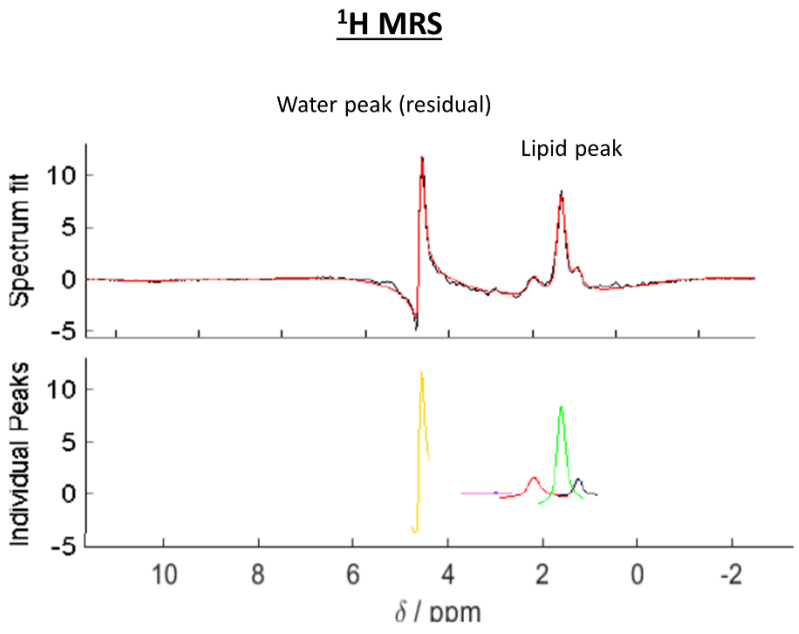


Figure 15: Example myocardial ^{1}H MRS spectrum and fit

Example ^{1}H MRS Spectrum from a healthy volunteer, lipid spectra (top) are scaled using an unsuppressed water peak (not shown). Fitting of peaks (below) is automated within Matlab using the AMARES algorithm.

2.4.2 ^{1}H MRI – Left ventricular ejection fraction and mass

Cardiac magnetic resonance is the gold standard for the assessment of structure and function. Scans were performed in the same 3T system (Siemens) as for the hyperpolarised experiments. A 24-channel spine matrix and 6-channel flexible body receive array coil (Siemens, Germany) were used. Steady-state free precession (SSFP) imaging in the horizontal and vertical long axis, and short axis were acquired as previously described [142], with typical images shown in Figure 16. Typical parameters were T_E 1.5ms, T_R 46ms, FA 50^0, field of view 400mm. Imaging was retrospectively gated during breath holding at the end of expiration.

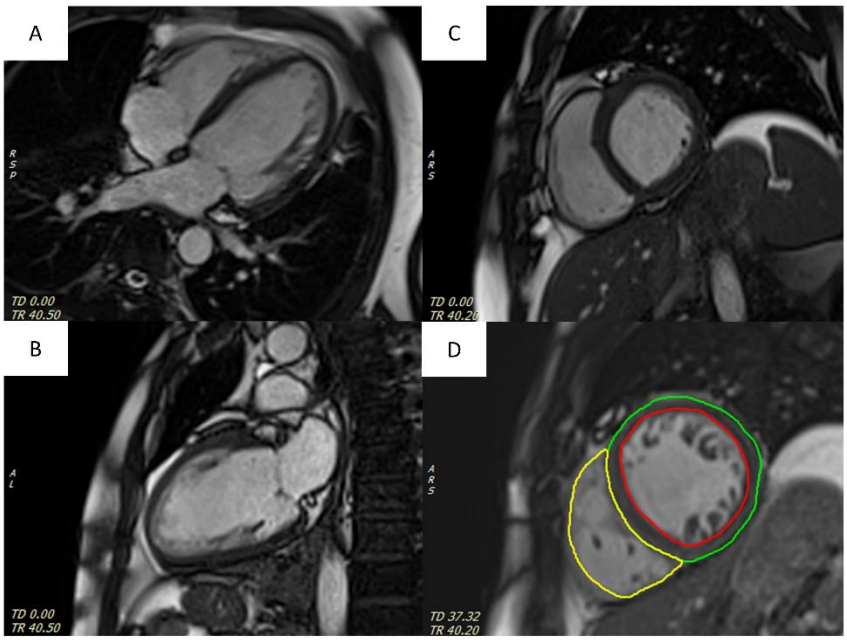


Figure 16: ^{1}H CMR imaging views of the human heart

Imaging was acquired in horizontal (A) and vertical (B) long axis, as well as a short axis stack (C) comprising sequential slices through the ventricle. These were contoured (D, red endocardial, green epicardial, yellow right ventricle) to calculated parameters of ventricular structure and function. Epicardial and endocardial borders were manually contoured for calculation of parameters of

ventricular function and mass, with subsequent analysis performed using cmr42© (Circle Cardiovascular Imaging inc, Canada).

2.4.3 Late gadolinium enhancement to assess for myocardial infarction

Areas of myocardial infarction and their grade (from sub endocardial to transmural) were measured using late gadolinium enhancement imaging. This was undertaken three minutes after a 0.1mmolkg^{-1} dose of Dotarem (Guerbet Laboratories, France), chased by 10ml of normal saline. Images were ECG gated, in the long and short axis planes with breath-holding using a single shot inversion recovery sequence TR / TE / FA / slice thickness (3ms / 7.5ms / 20^{0} / 8mm). Imaging was undertaken at 3T. Areas of enhancement were judged by two experienced certified CMR reporters.

2.4.4 Echocardiography

Standard 2D Transthoracic echocardiographic (TTE) scanning was undertaken on our workhorse machine (CX50 console, Philips, Amsterdam, Netherlands), and analysed offline using Xcelera (Philips, Amsterdam, Netherlands). This was done according to standard guidelines [143] using mitral pulse-wave Doppler inflow at the mitral valve leaflet tips (early E, and atrial A), and peak diastolic mitral annular tissue velocity using tissue Doppler assessment (both medial and lateral, e'). E/A, and average E/e' are presented (Figure 17)

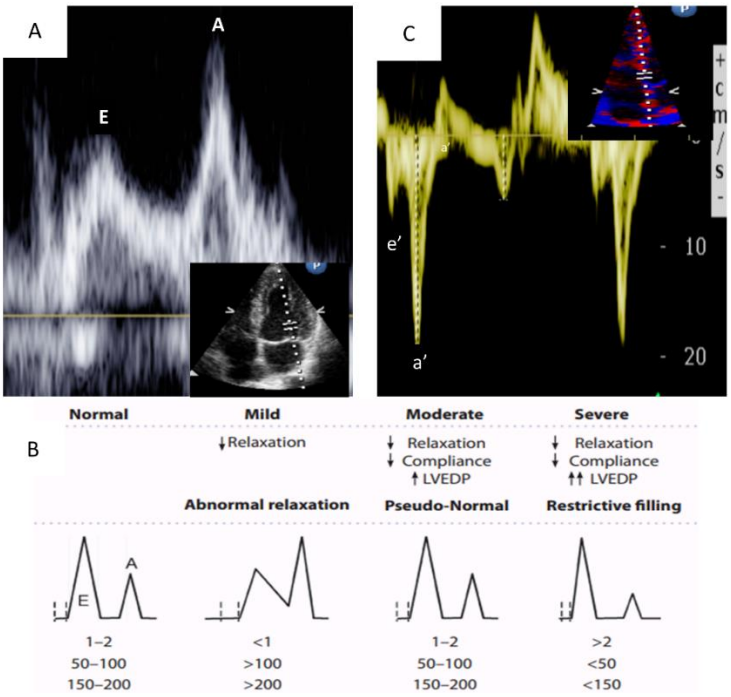


Figure 17: Assessment of diastolic function using echocardiography

Echocardiography was used to assess diastolic dysfunction; inflow across the mitral valve tips (A) was first recorded, whose interpretation is shown (B). Tissue Doppler velocity at the mitral valve annulus was then recorded (C), to calculate E/e'; which increases as ventricular compliance falls.

2.4.5 Dobutamine Infusion Protocol

In my work, I record Pi/PCr and pH at a new steady state during dobutamine stress in healthy controls, and patients with diabetes and dilated cardiomyopathy. Intravenous Dobutamine infusion (GRASEBY ™ 3500 anaesthesia pump, Graseby medical, UK) was started at a dose of 5 µg/kg/min, increasing at regular intervals up to a maximum dose of 40 µg/kg/min to achieve a target heart rate of 65% of the age predicted maximal heart rate [MHR = 207 – (age x 0.7)]. During the infusion, participants had continuous ECG and heart rate monitoring by 3-leads and pulse oximetry, and non-invasive blood pressure monitoring (VICORDER ®, SMT Medical, Germany) every minute (at 7T). Mean rate pressure product (RPP = systolic blood pressure ×

heart rate) was recorded at rest and during stress. Heart rate was maintained at target for the duration of the ^{31}P-MRS-STEAM acquisition. Mine is the first work to undertake stress studies at the 7T field strength, an image of the experimental setup is given in Figure 18.

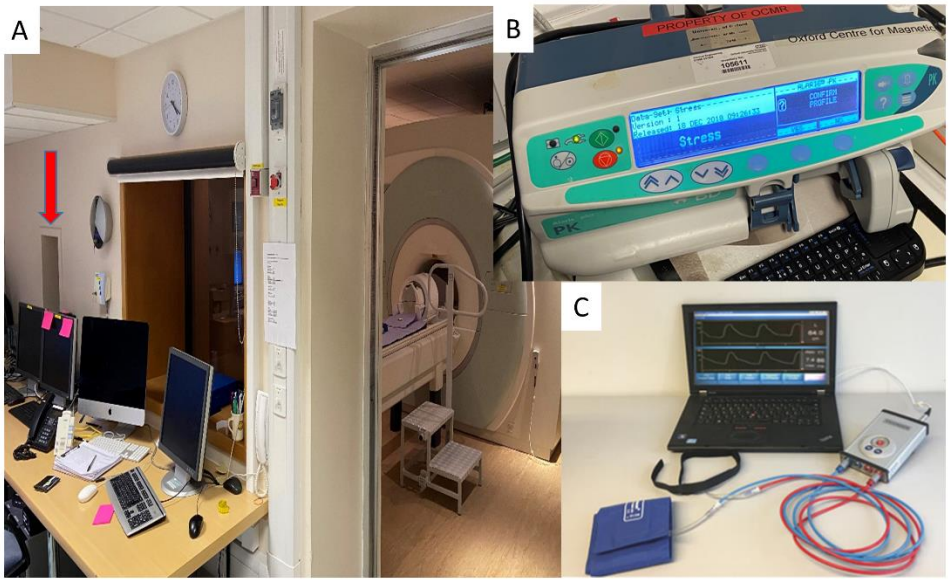


Figure 18: The 7T experimental setup for rest/stress STEAM ^{31}P MRS

The 7T setup (A). Multiple connection lines were needed and passed from the magnet bore through a hatch in the wall (red arrow) to the control room, where they were connected to the dobutamine infusion pump (B) and VICORDER blood pressure recorder (C).

2.5.6 Other clinical measurements

Height (cm) and weight (kg) were recorded using calibrated scales in all participants. Body mass index (BMI) was calculated according to the following equation

$$BMI = \frac{m}{h^2}$$

A 12-lead ECG was recorded in all participants. Venous blood was drawn from an appropriate peripheral vein by an appropriately trained individual, samples were analysed in the laboratories of Oxford University Hospitals NHS laboratories.

2.5 Summary of techniques used.

The techniques used in the human chapters, and measurements taken across this work are summarised in the Table 1.

Study	**ECG**	**Bloods**	**^{1}H CMR**	**^{13}C MRS**	**LGE**	**^{13}C imaging**	**PCr/ATP**	**^{1}H MRS**	**Pi/PCr**	**Echo**	**Dobutamine**
Preclinical Variability (chapter 3)		•	•	•							
Diabetes (chapter 4)	•	•	•	•	•		•	•		•	
Repeatability (STEAM, chapter 5)	•								•		
Stress Pi/PCr (controls, chapter 5)	•						•		•		•
Stress PI/PCr (diabetes, chapter 6)	•						•		•	•	•
Stress Pi/PCr (DCM, chapter 6)	•		•				•		•		•
Viability (pilot work, chapter 7)	•	•	•		•	•					

Table 1: Summary of techniques and interventions undertaken in this work

Chapter 3. Optimal preparation strategy for hyperpolarised MR experiments

The work in this chapter is published in the following journal:

Timm KN, Apps A, Miller JJ, et al. Assessing the optimal preparation strategy to minimize the variability of cardiac pyruvate dehydrogenase flux measurements with hyperpolarised MRS. *NMR in biomedicine* 2018;**31**:e3992.

My contribution to this work was in running the hyperpolarised experiments (managing the preparation of the [1-^{13}C]pyruvate solution and dissolution), processing the ELISA kits to record insulin, and acquiring and analysing the spectral data. The data was written into my transfer of status report which was then used as the first draft of the above paper. I do not hold a home office animal licence and did not undertake the day-to-day care of the rats. Dr Kerstin Timm who holds a home office licence undertook day-to-day animal welfare tasks.

3.1 Introduction

This aims of this chapter were:

1) To investigate whether a strategy of IV glucose administration following fasting reduced variation in, while increasing flux through, the PDH complex, when compared to the fed state.
2) By undertaking experiments in both diabetic and control rats, the chapter also aimed to investigate whether high dose glucose infusion can overcome the pathologically reduced PDH flux that characterises diabetes.

3.1.1 Cardiac energy metabolism and the Randle cycle

The heart reconciles huge variation in prevailing energy requirements, with strict metabolic energy homeostasis, by demonstrating great flexibility in its choice of catabolic substrate. It can thus be described as a veracious "metabolic omnivore" [3] consuming ketone bodies, glucose, and fatty acids, with carbon from each contributing to the acetyl-CoA pool and fuelling the TCA cycle. The relative contributions depend on availability, workload, oxygen supply and a variety of pathologies. In health, the β-oxidation of FAs predominates at rest, and in the fasted state high levels of FA derived acetyl-CoA inhibit PDH allosterically, which is also largely in a phosphorylated and inactive state (catalysed by PDK). A switch to glucose is seen following feeding, predominantly actioned by the hormone insulin, which activates PDH phosphatase (PDP), dephosphorylating and activating PDH and increasing glucose oxidation. Insulin also activates Acetyl-CoA carboxylase (ACC) increasing levels of malonyl-CoA, which is the building block for FA biosynthesis, inhibiting CPT-1 and the translocation of FAs into the mitochondria (reducing β-oxidation). This inverse relationship is termed the Randle cycle [8],

and can be seen in Figure 19. Insulin resistance results in reduced phosphatase activity [144] and an overexpression of PDK [73, 145], which results in reduced flux through PDH.

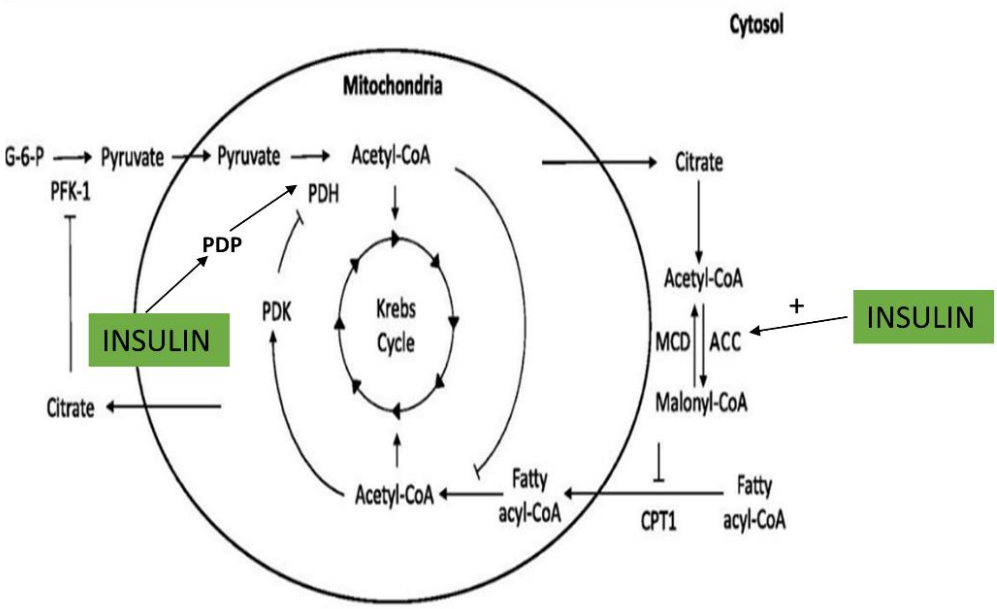


Figure 19: The Randle cycle

The Randle cycle, FA oxidation to the right, and glucose oxidation to the left are reciprocally regulated. A switch to glucose oxidation is seen during feeding mediated by insulin. PDP is activated which dephosphorylates and activates PDH increasing glucose oxidation. On the other hand, β-oxidation is curtailed with reduced translocation of FAs in to the mitochondria due to increased inhibition of CPT-1 by malonyl-CoA (the substrate for FA biosynthesis).

3.1.2 Techniques for in-vivo metabolic assessment

Studying cardiac metabolism in-vivo is essential to our understanding of cardiac disease and is possible via a number of techniques [146]. Using ^{31}P-MRS we can estimate the relative concentrations of high energy phosphate metabolites within the heart to gain an understanding of prevailing energetic status, while ^{1}H-MRS gives an estimation of triglyceride content. Cellular uptake of radiolabelled glucose or FA (most commonly FDG, or ^{11}C acetate)

on the other hand can be assessed using PET. These techniques have uncovered the reductions in glucose / increases in FA uptake [147, 148], impaired energetics and elevated triglyceride content [15, 149] that characterise diabetic cardiac metabolism. They provide snapshots of metabolism but cannot however give information about downstream metabolic flux such as at the level of PDH. Furthermore in the case of PET a radiation dose is incurred, although admittedly the technique is far cheaper than DNP (at current costs). ^{13}C MRS offers this with the possibility to track the transfer of the ^{13}C nucleus from administered compound to the metabolic products via enzymatic reactions. Although attractive, conventional ^{13}C MRS suffers due to a low SNR with experiments restricted to steady state assessment and long imaging protocols at clinical field strengths, with high doses of enriched substrate needed for adequate signal [150]. Hyperpolarised MR overcomes this low sensitivity using the principle of Dynamic Nuclear Polarisation (DNP) which amplifies signal up to 10000x [53]. After injection in to a living system, real time downstream metabolism can be assessed by MRS or imaging.

3.1.3 Hyperpolarised MRS using [1-^{13}C]pyruvate

The most informative tracer to date for studying cardiac metabolism is [1-^{13}C]pyruvate, with flux through PDH easily measured by recording the resulting $H^{13}CO_3^-$ signal after injection. In these experiments, low levels of $H^{13}CO_3^-$ imply either a physiological reduction in pyruvate oxidation (a surrogate marker of glucose oxidation) due to the Randle cycle such as would be expected to occur in fasting, or hypoxia where oxidative phosphorylation is pathologically curtailed and a subsequent reduction in glucose oxidation (through PDH) occurs. This switch away from glucose as a substrate associated with fasting can be demonstrated in-vivo, with

the $H^{13}CO_3^-$ signal reduced by 74% after overnight fasting in rats [71], a similar finding is demonstrated in pigs [151]. The blunted PDH flux seen in diabetes has also been demonstrated in a variety of rodent models [71, 145, 152]. Importantly, the in-vivo PDH activity recorded using hyperpolarised MRS correlates well with that determined directly by ex-vivo measurements of PDH activity in tissue extracts, by spectrophotometric assay [153]. Similarly, Ex-vivo activity of LDH has been shown to reduce in tandem with hyperpolarised estimates of LDH activity after etoposide treatment in a mouse lymphoma model from the Brindle group in Cambridge [154].

3.1.4 Subject preparation for hyperpolarised MRS

Physiological variation in PDH flux is large and arises from the prevailing fasting status and even time of day. This is increased further in relative terms due to the heart's basal preference for FAs as an oxidative substrate. Producing robust hyperpolarised data whose primary aim is to detect regional alterations (in ischaemia), or temporal pathological global changes in flux through PDH, therefore requires a preparation strategy prior to scanning that standardises the metabolic system studied. This strategy must both ensure minimal inter-scan variation in flux through PDH (raising the power of MRS experiments studying the temporal evolution of pathological metabolism), while maximising flux at the top of the physiological range to increase the sensitivity of experiments aiming to image regional ischaemic metabolism. In both fasted rats [155] and pigs [151] infusion of glucose, insulin and potassium (GIK) is shown to successfully impose a shift in metabolism with increased flux through PDH seen. This intervention increases glucose oxidation in the heart again demonstrating the power of hyperpolarised MRS to detect real time physiological metabolic change, and provides a

rationale for why human clinical studies to date have been undertaken following an oral glucose load after an overnight fast. Preclinical studies are generally performed in overnight fed rodents, however, which approach actually yields more robust, reproducible measurements is unknown, and was the rationale for the work undertaken in this chapter.

Therefore, prior to clinical studies aiming to measure the effect of diabetes and feeding on whole heart PDH metabolism with MRS (chapter 4), and the impact of coronary artery disease on regional metabolism (chapter 7), animal experiments were needed to best decide on how metabolism should be standardised before scanning. I hypothesised that following a glucose infusion PDH flux would not only be higher, but also less variable compared to a fed state in which food was available ad-libitum overnight beforehand. Administration of high dose oral glucose is safe in humans, and is commonly undertaken during a diagnostic workup for diabetes – the oral glucose tolerance test (OGTT) [156]. As such its addition to clinical protocols is safe, cost-effective, and possibly of additional value.

Doses of glucose given intravenously (IV) to rats in these experiments equate to the same oral dose administered in the diabetic clinic (1g/kg). Experiments were undertaken in both a cohort of diabetic as well as control animals, to also investigate whether high dose glucose infusion can overcome the established pathophysiological blunting of PDH flux in the diabetic heart.

3.2 Methods

3.2.1 Ethical considerations

All animal experiments conformed to the Animals (Scientific Procedures) Act (1986) and were carried out under project licence number 30/3322. Experiments were approved by a local

ethics committee as is the national standard for research involving animals, and were carried out with the help of a personal license holder.

3.2.2 Animal handling and preparation

Twenty-four age matched (11 week old, weight 218±19g) female Wistar rats were divided in to diabetic and control groups. Diabetes was induced via a high fat diet and STZ injections (3.2.3). Rats in this group with a fasting blood sugar > 14mM were excluded (3) due to a more type 1, insulin dependent phenotype. Those animals remaining had insulin resistance profiles more akin to the type two phenotype, encountered in clinical research. All rats received intravenous glucose tolerance testing (3.2.4) at week 8 of the high fat diet to quantify levels of insulin resistance in both cohorts. 9 rats (fasting glucose between 8 and 14mM) were included in the diabetes group; all 12 control animals were scanned. Animal preparation prior to the hyperpolarised scans is summarised in Figure 20. Experiments were performed between 0700 and 1300. Each animal received two hyperpolarised scans (3.2.5) separated by a rest day; one in the fed state (food and water available ab libitum), and one 30 minutes after an infusion of 1mg/kg intravenous glucose following an overnight fast. During scanning animals were anaesthetized with 2% isoflurane and medical oxygen, blood glucose was recorded immediately following anaesthesia induction via an accu-chek glucometer from a saphenous vein prick. Following the second hyperpolarised scan animals were euthanised without recovery from anesthesia, by excision of the heart.

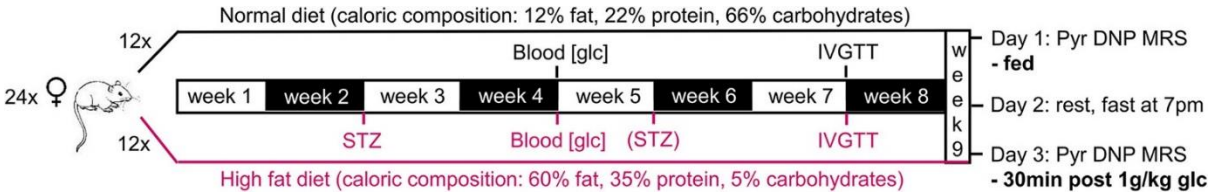


Figure 20: Rodent preparation

Study protocol. A type two diabetic phenotype was induced with a combination of STZ injections and a high fat diet beginning from 11 weeks old. At week nine, all rats had two hyperpolarised [1-^{13}C]pyruvate studies – one in the fed state, one in the fasted / glucose loaded state (separated by a rest day).

3.2.3 Streptozotocin high fat diet diabetic model

The type two diabetes model used in this chapter was induced via STZ injections and a high fat diet Figure 20. Rats were fed a high fat diet for 9 weeks (60% calories from fat). After two weeks of this diet, rats then received an injection of 25mg/kg intraperitoneal STZ to induce type 2 diabetes [73]. Two weeks after this injection, fasting blood sugar was checked (AccuCheck monitor, overnight, mild 2% isoflurane anaesthesia), if this did not exceed 8mM a further dose of STZ (25mg/kg) was administered a week later.

3.2.4 Intravenous glucose tolerance testing

At week 8 of the high fat diet (the week before scanning), as previously described [157] IV glucose tolerance testing (1g / kg) was performed on all rats (under 2% isoflurane anaesthesia) to quantify levels of insulin resistance in both normal and diabetic cohorts. Glucose solution was administered as a bolus via the tail vein (1 g/kg at a concentration of

0.5 mg/mL in sterile water). Blood glucose levels were measured at time 0, 2, 5, 10, 15 and 30 minutes with an ACCU-CHECK glucometer.

3.2.5 Hyperpolarised [1-^{13}C]pyruvate production and MRS protocol

Hyperpolarised [1-^{13}C]pyruvic acid (Sigma-Aldrich, Gillingham, UK) for injection was prepared with approximately 40mg of [1-^{13}C]pyruvic acid, mixed with 15mM of a trityl radical and 3µl dotarem (1:50 dilution). The sample was then hyperpolarised in a prototype polarizer (Alpha system, Oxford instruments) for approximately 30 minutes with microwave irradiation at 3.35T and ~1K. Anaesthetized rats were placed inside a 7T MR spectrometer (Varian, Santa Clara, CA, USA). Dissolution was performed using a superheated alkaline solution, prepared with 2.4g/L sodium hydroxide and 100mg/L EDTA at 180^{0}C, yielding an 80mM solution of hyperpolarised [1-^{13}C]pyruvate with physiological pH and temperature, 1mL was injected in to the tail vein over 10 seconds. Hyperpolarised ^{13}C MR spectra were recorded over a 1cm axial slab every second for 120 seconds using a dual tuned birdcage ^{1}H / ^{13}C coil (Rapid Biomedical, Germany) for transmission and a two-channel 13C surface coil for reception (Rapid Biomedical, Germany), and a 15^0 RF pulse and 13KHz bandwidth. These steps in sequence are shown in Figure 21.

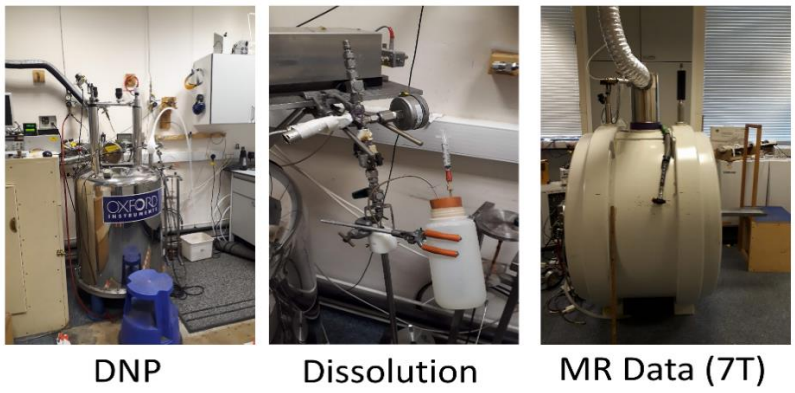


Figure 21: The preclinical DNP workflow

The dissolution process, from left to right. The sample underwent DNP in an alpha prototype polariser (3.35T Oxford instruments). Dissolution was undertaken by manually pushing the dissolution stick containing superheated NaOH into the sample cup at the bottom of the polariser. The resulting [1-13C] pyruvate solution was rapidly conveyed to the MR scanner containing the anaesthetised prepared rodent (7T Varian scanner). Following injection, ^{13}C - MRS was recorded.

3.2.6 Data handling and statistical analysis

Calculation of metabolite ratios was done using spectra summed in phase from the 30 seconds following first appearance of injected pyruvate. The cardiac multicoil ^{13}C MR Spectra were analysed using the advanced method for accurate, robust and efficient spectral fitting (AMARES) algorithm in the jMRUI software package as previously described [158]. Peaks corresponding to pyruvate and its metabolites were fitted with prior knowledge [136]. Metabolite ratios were calculated from summed spectra, an example is shown in Figure 22.

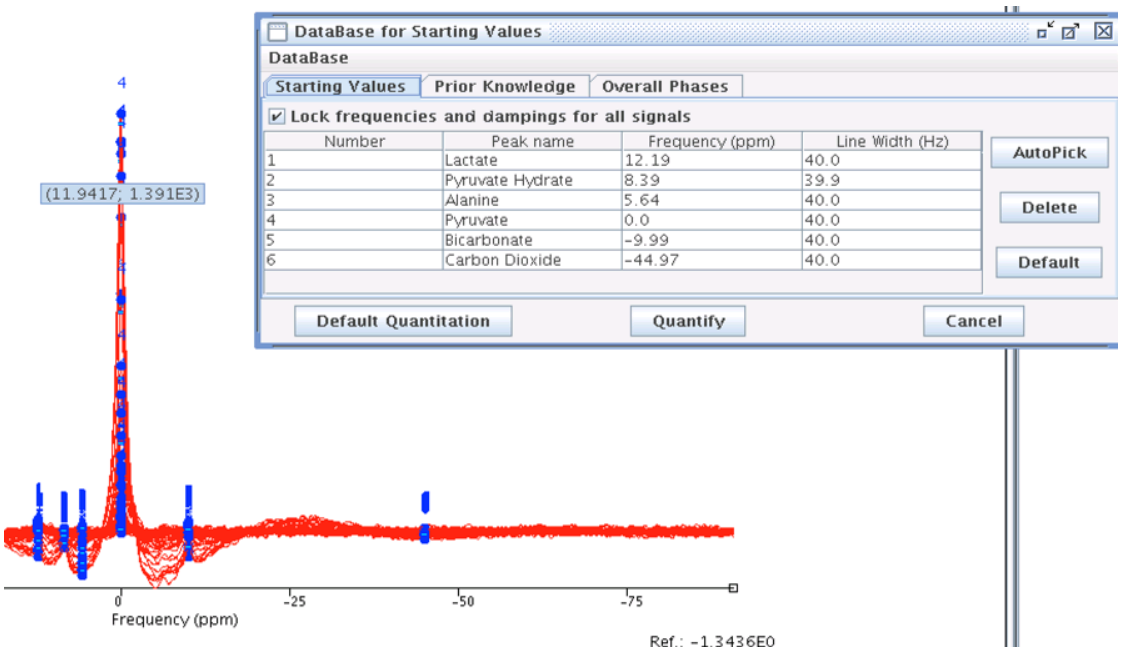


Figure 22: Summed spectra analysis in JMRUI

Using jMRUI Summed spectra were generated from the first 30 seconds of MRS data taken from the moment the [1-^{13}C]pyruvate resonance was seen. These were used to calculate metabolite ratios indicative of enzymatic flux.

Insulin concentrations from the IV glucose tolerance test were measured using a rat ELISA kit (mercodia), these were analysed at 450nm on a spectrophotometric plate reader. Due to the number of plates available, insulin concentrations were analysed for six of the diabetic rats, and four of the controls. Using a paired fasting blood sugar, homeostatic model assessment of insulin resistance (HOMA-IR) was calculated as a measure of insulin resistance:

$$HOMA - IR = \frac{[glc] \times [insulin]}{22.5mM \times mU/L}$$

Using the continuous variable insulin resistance, instead of an arbitrary cut off in fasting sugar that defines diabetes, allows a more detailed analysis of how progressive insulin resistance affects flux through PDH, and its variability.

3.2.7 Statistical methodology

Plasma glucose data was tested for normality using the Shapiro-Wilk test and T-tests assuming unequal variance then subsequently used to analyse differences between groups. This analysis was performed using GraphPad Prism v6.01 (GraphPad software, La Jolla, CA, USA), and significance considered at $p \leq 0.05$. Following confirmation of normality using kolmogorov/smirnov, comparison of metabolite ratios was undertaken with a linear mixed effect model using the lme4 package in R with metabolic state and disease state considered fixed effects and rat ID considered a random effect. Linear mixed effect models are a

generalization of ANOVA that are better placed to function well in the presence of missing observations. Unlike ANOVA which assumes equal weighting, mixed effect models calculate the variance associated with each parameter. Modelling of the individual subject variables effectively allows for the accommodation of multiple missing data points. The same approach was used to analyse metabolic data presented in the subsequent clinical translation chapter. Differences in variance were assessed with the non-parametric Fligner-Killeen test [159]. Where applicable, Bonferroni correction was used for multiple comparisons.

3.3 Results

3.3.1 Validating the STZ diabetic model

The STZ and high fat feeding diet successfully led to type two diabetes. The type II diabetic rats (T2DM) showed significantly increased fasting blood glucose levels (9.5±0.7 vs. 5.5±0.1 mmol/L [$p<0.01$], Figure 23A), fasting HOMA-IR was correspondingly significantly raised (5.6±2.9 vs. 1.5±0.2 mmol/L [$p=0.03$], Figure 23B), all rats in the control group had HOMA-IR <2, levels of insulin resistance in the diabetic group showed a large variation (range 2.5-9.8).

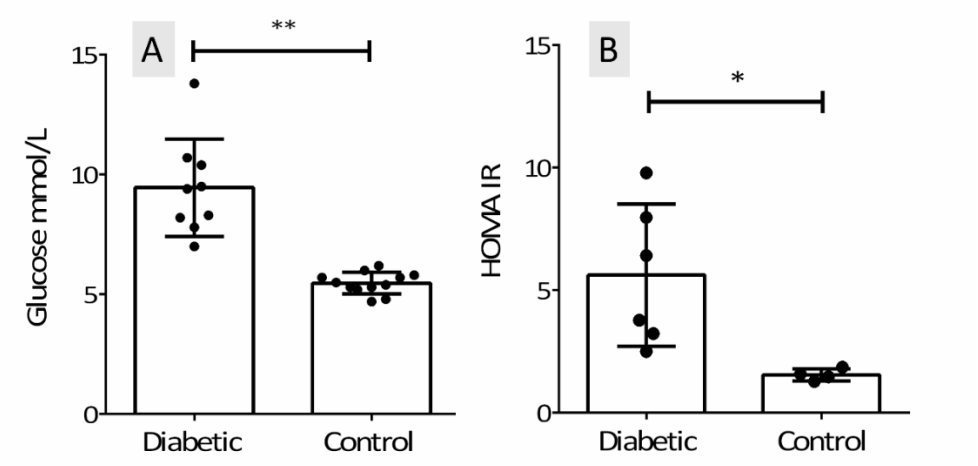


Figure 23: validating the diabetes rat model

*Diabetic rats had significantly higher fasting glucose (A), and HOMA IR (B) than control animals indicating significant insulin resistance. Data is expressed as mean±standard deviation (SD), * = p<0.05, ** = p<0.001.*

Diabetic animals had significantly impaired glucose tolerance at all time points measured following IV glucose administration compared to their age-matched controls (Figure 24A). Insulin was significantly higher at time 0, but only numerically higher (no significance) at other time points Figure 24B. At the time of the final scan (20 weeks old), the weight of diabetic animals was no different to the controls (271±30g vs. 262±17g [p=0.50]).

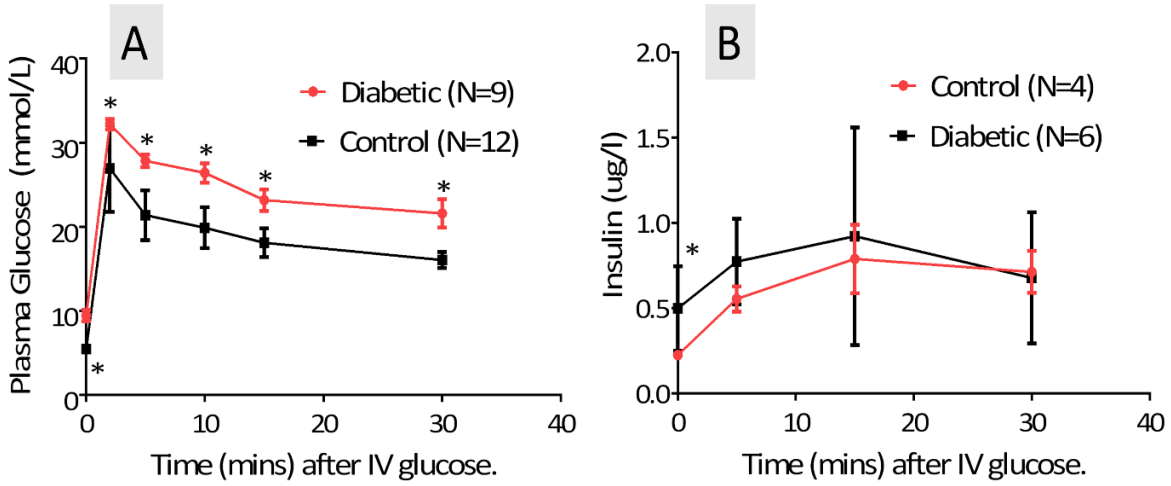


Figure 24: IV glucose tolerance testing in diabetic and control rats

*Plasma glucose, (A, mean ± SD) and insulin (B, mean ± SEM) response to IV glucose in both diabetic (Red) and control (black) animals. Comparisons using unpaired unequal-variance t-test, * = p<0.05.*

3.3.2 In-vivo metabolic data.

I compared the in-vivo metabolism of [1-^{13}C]pyruvate in the diabetic model, with control animals, in the fed state and 30 minutes after an intravenous glucose challenge (delivered to

a fasted animal). Spectra were summed over the 30 seconds following appearance of the pyruvate peak. Example summed spectra generated in AMARES (of the four possible combinations) are shown in Figure 25.

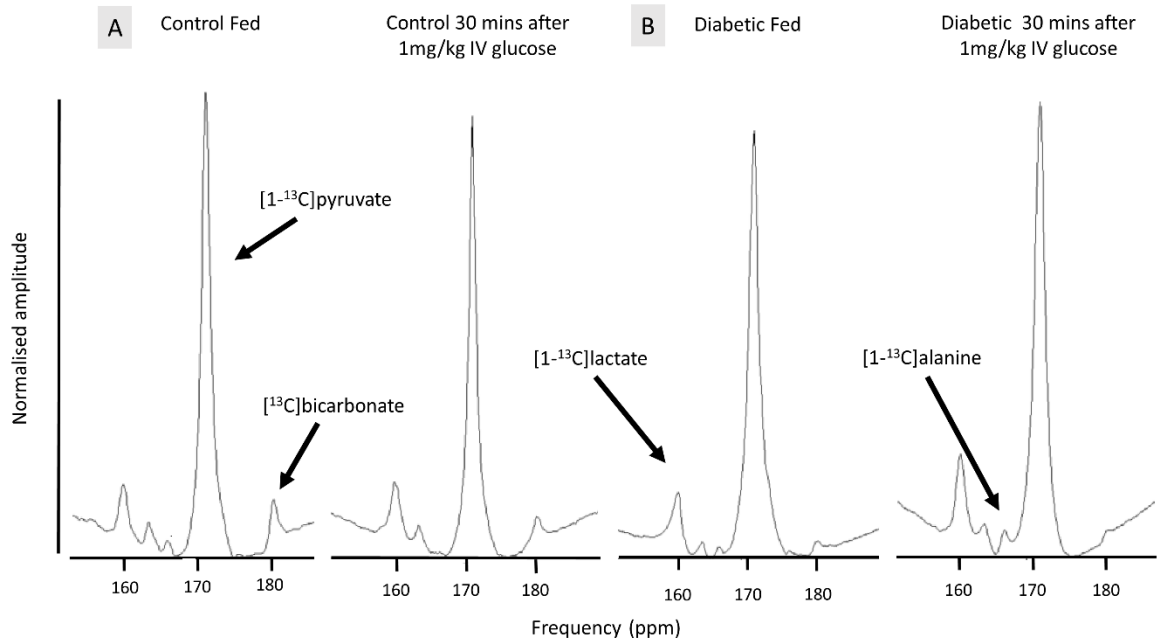


Figure 25 Typical ^{13}C rat spectra highlighting [1-^{13}C]pyruvate and its metabolites

Hyperpolarised [1-^{13}C]pyruvate MRS in the heart. Spectra from a 10mm slab covering the heart from a representative control (A) and diabetic (B) rat in the fed state and 30 minutes after an IV glucose bolus (1g/kg) following an overnight fast.

From these summed spectra, peaks were identified and computed in AMARES using prior knowledge. Ratios were taken of the peaks corresponding to the metabolites [1-^{13}C]lactate, $H^{13}CO_3^-$ and [1-^{13}C]alanine, these are normalised to the pyruvate peak to account for differences in polarisation.

3.3.3 The impact of Animal preparation strategy on metabolic Flux changes.

The first aim of the experiment was to assess how two different preparation strategies (glucose infusion on a background of fasting, or free feeding overnight) affected the metabolite ratios. Metabolite ratios (mean ± SD) can be found in Table 2, with p-values calculated using a linear mixed effect model (with preparation strategy and disease status considered as fixed effects, and rat ID considered a random effect). There was no evidence to suggest that fasting followed by glucose-loading altered cardiac metabolite levels compared to leaving the rats in the fed state in either control or diabetic rats. The bicarbonate to [1-^{13}C]pyruvate ratio, reflecting PDH flux, did not differ by preparation strategy (fed or fasted / glucose infused) in either control (0.091 ± 0.041 [fed] vs. 0.074 ± 0.044 [glucose]) or diabetic (0.032 ± 0.010 [Fed] vs. 0.021 ± 0.018 [glucose]) rats (p=0.08, Figure 26A). Preparation strategy also had no significant effect on [1-^{13}C]lactate / [1-^{13}C]pyruvate (p=0.91, Figure 26B) or [1-^{13}C]alanine / [1-^{13}C]pyruvate (p=0.99).

Table 2: Metabolite ratios of control and diabetic rats

	CONTROL (N=12)		**DIABETIC (N=9)**		**P-VALUE**	
	Fed	Fast/IVG	Fed	Fast/IVG	Preparation	Diseased state
BIC/PYR	0.091± 0.041	0.074± 0.044	0.032± 0.010	0.021± 0.018	0.08	0.00016
LAC/PYR	0.132± 0.063	0.108± 0.078	0.126± 0.044	0.165± 0.048	0.91	0.41
ALA/PYR	0.027± 0.027	0.012± 0.012	0.032± 0.022	0.029± 0.034	0.99	0.24

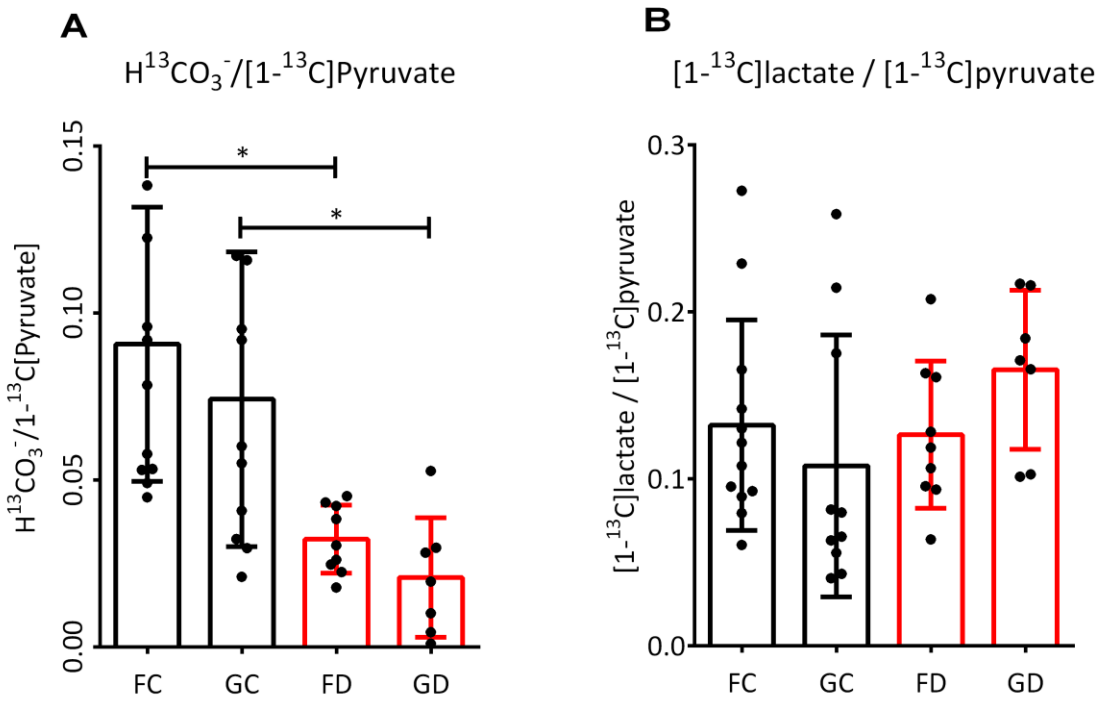


Figure 26: Metabolite ratios in diabetic and control rats

*C=Control, D=diabetic, F=fed, G=fasted then glucose loaded. Mean (±SD) metabolite ratios calculated from summed spectra. Preparation strategy made no significant impact to flux through PDH at the time course of glucose infusion studied. Glucose infusion did not overcome the blunted PDH flux seen in diabetes (*p<0.01). Only data points successfully fitted by AMARES are included: $H^{13}CO_3^-$ / [1-^{13}C]pyruvate (CF 12, CG 11, DF 9, DG7), [1-^{13}C]lactate / [1-^{13}C]pyruvate (CF 12, CG 10, DF 9, DG 7), * denotes p<0.05.*

3.3.4 Overcoming pathological PDH flux with intravenous glucose

In the T2DM rats PDH flux, as expected, was significantly reduced (control vs diabetic, 0.091±0.041 vs. 0.074±0.044 [fed] vs 0.074±0.044 vs. 0.021±0.018 [Glucose], p<0.01, Figure 26). PDH flux was fairly uniformly reduced by any degree of insulin resistance in the diabetic rats; with increasing degrees of resistance conferring no incremental depression in flux. Put

another way, PDH flux seems highly sensitive to any degree of insulin resistance. This is demonstrated in Figure 27 below (note HOMA-IR was only available for the rats in which insulin concentrations were recorded with ELISA).

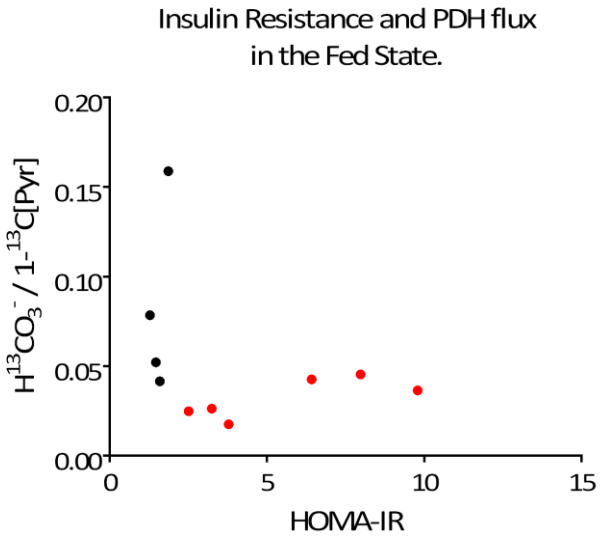


Figure 27: PDH flux vs HOMA-IR in all rats

The effect of increasing degrees of Insulin resistance had no effect of further increasing the reduction in PDH flux seen. PDH flux is depressed early in the course of insulin resistance. Red dots denote diabetic animals.

Although non-significant, a trend toward higher [1-^{13}C]lactate / [1-^{13}C]pyruvate in diabetic rats was seen (control vs diabetic 0.132±0.063 vs 0.126±0.044 [fed] vs 0.108±0.078 vs. 0.165±0.048 [glucose], p=0.41). This finding is discussed in more detail in chapter 4. Previous experiments [71] establishing the blunted PDH flux that typifies diabetes, undertook experiments in overnight fed rats. The second aim here was to determine whether or not glucose loading intravenously before scanning, could overcome this impairment in PDH flux. This is important to establish as If it did so it would suggest hyperpolarised MR experiments

in humans with diabetes would be much easier in the glucose loaded state. Using unpaired t-tests PDH is seen to be significantly reduced in the fed state (0.091 ± 0.041 [control] vs. 0.032 ± 0.010 [diabetic], $p<0.01$), and this was not overcome by glucose infusion (0.074 ± 0.044 [control] vs. 0.021 ± 0.018 [diabetic], $P<0.01$, Figure 26.

3.3.5 Preparation strategy and variability in metabolic flux between animals

Finally, I aimed in this chapter to investigate the hypothesis that scanning 30 minutes after a glucose infusion (given fasted) may reduce the variability of PDH flux recorded. It is hypothesised that the optimal strategy for minimal variability (yet maximal flux) would be giving a glucose load to an animal after an overnight fast (and therefore in a fairly metabolically standardised state), with feeding likely to be a heterogeneous state. Reducing variability in metabolic data is desirable if hyperpolarised MR is to reliably pick-up temporal changes in substrate handling as a disease progresses. Reassuringly $H^{13}CO_3^-$ / [1-^{13}C]pyruvate in the fed state correlated positively with the fasted / glucose infused state (Figure 28 A) excluding biological variation in response to glucose as a major contributor to variation between strategies. However recorded $H^{13}CO_3^-$/ [1-^{13}C]Pyruvate ratios in individual diabetic and control rats demonstrated that the PDH response to glucose infusion was highly variable in magnitude and direction, with some animals demonstrating marked increases and some marked decreases (Figure 28 B) There was no evidence to suggest that the variance in data acquired was significantly reduced by fasting followed by glucose infusion compared to scanning fed animals. Using the non-parametric (unpaired) Fligner-Killeen test for the homogeneity of variance, results show no difference in variation in any of the metabolite ratios, in either control or diabetic animals (bicarbonate/pyruvate, lactate/pyruvate,

alanine/pyruvate: $p = 0.63, 0.90, 0.69$ for the control group; $p = 0.96, 0.75, 0.35$ for the diabetic group). This would suggest that glucose loading does not reduce the variability of PDH measurement above simply scanning in the fed state.

Another unaccounted for potential source of variation is the signal derived from the pyruvate which varies in hyperpolarised experiments according to the total dose, venous transit time, and polarisation levels. Plotting $H^{13}CO_3^-$ / [1-^{13}C]pyruvate against total pyruvate signal however gives no correlation (Figure 28 C) suggesting that the ratio observed is independent of initial pyruvate signal strength. Normalising $H^{13}CO_3^-$ to another metabolic product [1-^{13}C]lactate would also help exclude such a source of variability, this however had no impact on reducing the observed variability; $p = 0.73$ (control) and $p = 0.94$ (diabetic), (Figure 28 D). Here, once again the ratios were significantly reduced in both fed (p=0.02) and glucose infused (p<0.01) diabetic animals compared to controls. Here the decrease in the ratio in diabetic animals on glucose infusion was significant (p=0.03, paired).

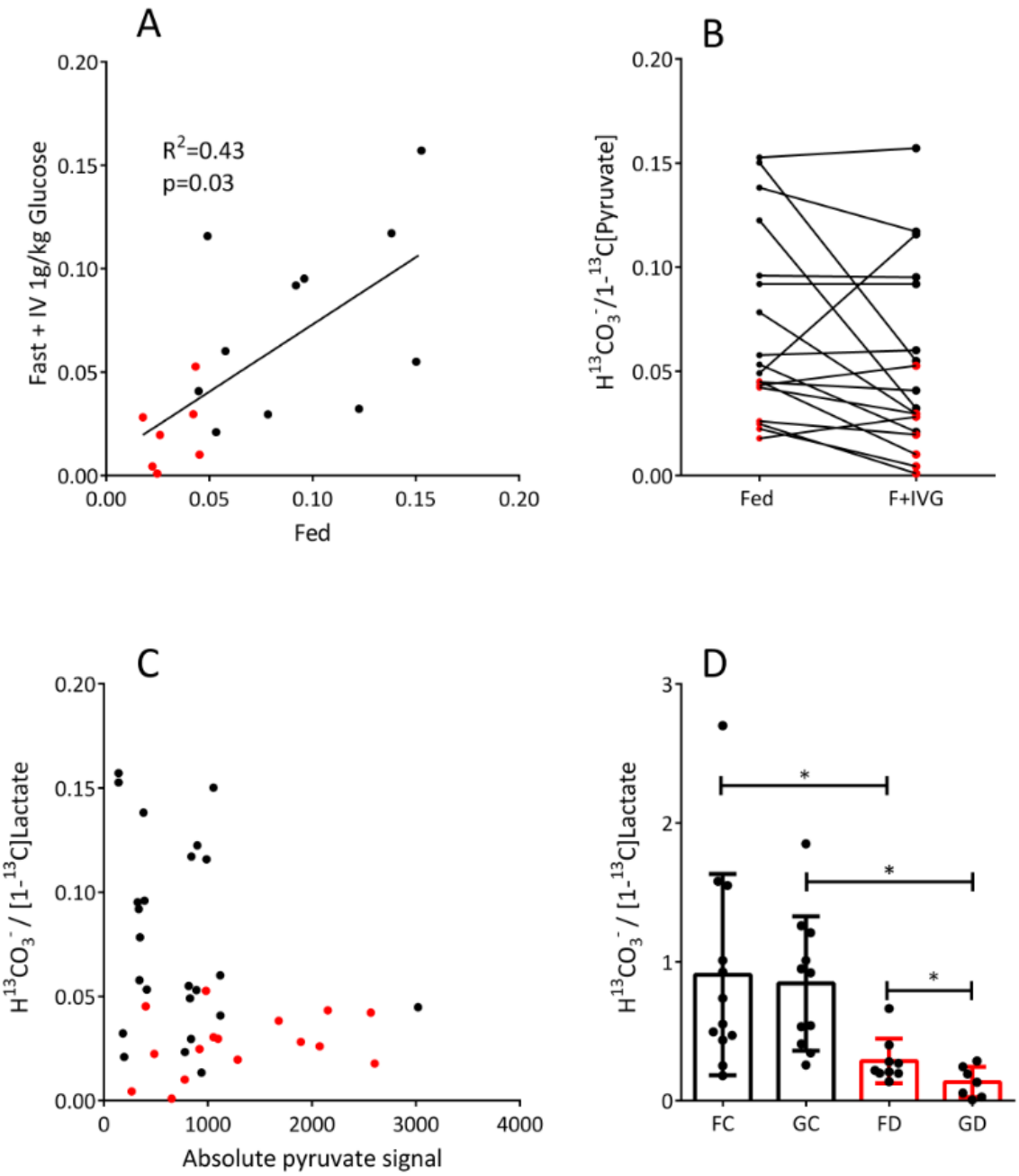


Figure 28: Preparation strategy and metabolic flux in diabetic and control rats

PDH flux in the glucose loaded state correlated with that seen in the fed state (A), but the magnitude of change and direction varied greatly between individuals (B). Polarisation level was not correlated to the signal metabolic products signal seen (C). A significant reduction in PDH flux in diabetes is still seen when $H^{13}CO_3^-$ is normalised to [1-^{13}C]lactate, and had no impact on reducing variability. Red denotes diabetics.

3.4 Discussion

DNP of ^{13}C containing compounds makes MRS of carbon containing compounds practical such that their in-vivo metabolism can be recorded in real time. Animal work eluding to the potential of the technology for clinical translation is extensive [160]. Relevant to this work, the switch away from glucose as a substrate associated with fasting has been demonstrated in-vivo, with the $H^{13}CO_3^-$ signal reduced by 74% after overnight fasting in rats [71], a similar finding is demonstrated in pigs [151]. The animal work presented in this first results chapter aimed to answer some key questions that needed to be addressed prior to onward human hyperpolarised MR experimentation with [1-^{13}C]pyruvate. The ideal preparation routine prior to hyperpolarised MR experiments seeking to detect changes in flux through PDH either regionally within the same heart (by imaging studies), or over the whole heart with time (with MRS studies), must ensure maximal basal flux through PDH prior to scanning, and minimal temporal variation. This ensures the maximal chance that any deviation in metabolism away from baseline can be detected. In pre-clinical studies, animals are generally in the fed state (food available ad-libitum), whereas human studies have used glucose loading (orally 75g) following an overnight period of fasting. Here I compared both these strategies by substituting an IV dose of glucose prior to scanning for the oral dose given to humans.

3.4.1 Effect of glucose administration on cardiac metabolism

No significant difference in PDH flux in either control or diabetic animals was demonstrated between the metabolic states studied. This does suggest however that the glucose infusion was successful in overcoming the blunted PDH flux that characterises fasting (reduced by up to 74% in fasted Wistar rats [71]). Other metabolite ratios were similarly unaffected. Glucose

infusion prior to scanning was also not able to overcome the pathological PDH flux that characterises diabetes demonstrated here and by others models [71, 145, 152]. Finally, variation in metabolite ratios was not significantly reduced by administering glucose on the background of a standardised fasted state. This was disappointing since the glucose loading regime was hypothesised to reduce variability before scanning, thus potentially increasing the power of repeated experimentation over time to detect real change. Glucose infusion did not however increase the variation recorded.

3.4.2 Metabolic variation is likely multifactorial

This chapter reports a high variation in PDH flux whose source is likely multifactorial, variation was seen in each of the metabolic states studied, and in the response to glucose by individuals. A lack of correlation between $H^{13}CO_3^-$ / [1-^{13}C]pyruvate and absolute pyruvate signal, and the absence of reduced variation when instead normalising $H^{13}CO_3^-$ to [1-^{13}C]lactate, together exclude variation in pyruvate delivery, availability and polarisation as a source, suggesting what is seen is genuine biological variation. Variation from within the free feeding state may be expected as animals had food available ad-libitum, hence PDH flux at the moment of scanning can be expected to be heterogeneous. Glucose infusion however failed to reduce variability in metabolic flux. Perhaps the time delay of 30 minutes from glucose infusion to scanning was insufficient to curtail the fatty acid β-oxidation which would have been marked in the fasted state, with Randall signalling events leading to maximal PDH flux and reducing intra-individual variability, requiring a longer period of time to occur. No increase in $H^{13}CO_3^-$ / [1-^{13}C]pyruvate was seen after glucose administration and is supportive of this theory, but admittedly the comparator here was the fed state, not the fasted state, so

any increase would likely be smaller than that seen in the studies mentioned earlier which directly compared the fasted and fed states [71, 151]. Indeed, perhaps in the fed state PDH flux was nearly maximal so the lack of variation in metabolic flux, and lack of increment after IV glucose administration may simply reflect a like-with-like comparison. Serial DNP scanning of the same animal after glucose infusion would help to define how long PDH flux takes to maximally increase in response to the glucose load, however this is not practical since each scan takes about 30 minutes to set up with only one polariser, however varying the timing of the glucose prior to scanning on different days could be undertaken.

The fasted state was not studied here given the hypotheses pertain to preparation of human subjects for DNP scanning, with the two possible options being fasted then glucose loaded or fed. However, a third permutation of fed then glucose loaded may be informative to study since baseline PDH flux in the fed state is minimally suppressed with PDH flux potentially more receptive to high dose glucose. Such a strategy however would obviously increase the risk of hyperglycaemic episodes in diabetic patients. These experiments studied inter-individual variation, no assessment of intra-individual variation within the population was made. Assessing the magnitude of this by undertaking repeated hyperpolarised scans on different days but using the same preparation strategy and animal would allow me to answer which preparation strategy minimises intra-individual variation, which is important for studies measuring temporal changes in flux as disease progresses.

3.4.3 Confounding factors in the present study

Other factors can easily impact metabolic flux and are harder to account for. Firstly, levels of circulating free fatty acids impact glycolytic flux – with higher levels curtailing glucose

oxidation as a source of Acetyl-CoA [8]. Secondly the anaesthetic agent itself, isoflurane, is shown to reduce oxidative phosphorylation and glycolytic flux, reducing $H^{13}CO_3^-$ and increasing the [1-^{13}C]lactate detectable in hyperpolarised MRS [161]. This effect was likely minimal however given a highly standardised anaesthetic protocol. On the strength of the data presented here, although the possibility remains that this small animal study was simply underpowered, the null hypotheses must be accepted. Although it did return flux to the level seen in the fed state, IV high dose glucose administered after fasting did not augment PDH flux over a free feeding baseline, and no reduction in inter-individual metabolic variation was seen. The reduced PDH flux seen in diabetes was not presumably overcome by IV glucose as the complex is in the phosphorylated state due to PDH kinase overexpression, with insulin resistance meaning signalling to the corresponding phosphatase is ineffective. The phosphorylation status of the PDH complex in diabetes is thus likely fairly insensitive to feeding.

3.4.4 Implications for human translation

The first report of hyperpolarised MR in the human heart prepared patients by loading with a 75g oral dose of glucose (orally) 1 hour prior to pyruvate injection on the baseline of the fed state [133]. This strategy is hoped to augment physiological PDH flux, and thus the power of metabolic experiments to change away from this baseline. Animal studies are however carried out on overnight fed animals. This work would suggest that, at least in the preclinical setting, glucose infusion prior to scanning would add only complexity to hyperpolarised experiments, and casts doubt on whether such preparation of clinical patients is necessary, especially given that fasting followed by high dose oral glucose solution is not a zero-risk

intervention to diabetic patients. However, given that PDH flux increases during feeding when compared to the fasted state, and the possibility that this work was underpowered, it would not seem sensible to suggest changes to the clinical protocol for the time being, other than to scan 45 minutes after oral administration (as opposed to the 30 here). In rats, biological variation in PDH flux and the response to feeding were much larger than anticipated. In humans, variation in flux is likely to be even greater given that the food available to the rats is highly standardised, which is not the case for human subjects, strengthening the argument for fasting and glucose loading prior to human scans.

3.5 Conclusion

Here, I have demonstrated that glucose loading prior to hyperpolarised [1-^{13}C]pyruvate measurements of $H^{13}CO_3^-$ / [1-^{13}C]pyruvate make no impact on variation or maximal flux, with the pathological reduction due to diabetes unaffected. Further animal work varying the timing of glucose delivery prior to scanning on different days to ascertain the time course of Randall cycle changes following glucose administration would be useful. Similarly, scanning the same protocol on the same animal on multiple occasions would allow me to assess the impact of different preparation strategies on intra-individual variation, which needs to be minimized to detect temporal changes associated with disease progression or onset. A small human study measuring PDH flux and variability in each of three permutations (fed with glucose, fasted with glucose, or simply fed) would be informative in planning future studies. This being said, hyperpolarised SFPs are in demand, and costly, with a list of desired human experimentation planned. As such, I chose to continue human experiments unchanged in a glucose loaded

state after an overnight fast, but extended the time between glucose and scanning to 45 minutes.

Chapter 4. Substrate handling in the human diabetic heart; a multi-nuclear approach to diabetic cardiac metabolism

The work in this chapter is published in the following journal:

O Rider*, Apps A*, Miller J et al. Non-invasive In Vivo Assessment of Cardiac Metabolism in the Healthy and Diabetic Human Heart Using Hyperpolarized ^{13}C MRI. *Circ Res* 2020;126(6):725-736.

*First two authors contributed equally to this work.

4.1 Introduction

This chapter aimed to

1) Confirm the presence of Randle cycle associated changes in [1-^{13}C]pyruvate metabolism in the healthy human heart to inform the optimal patient preparation strategy in future human imaging studies.
2) Assess changes in fasting cardiac substrate selection in diabetes, and any relationship this may have with diastolic dysfunction or abnormal myocardial energetics, with a comparison of the effect size of diabetes on each of these parameters.
3) Confirm that metabolic flexibility and Randle cycle associated changes in cardiac substrate selection can still be appreciated in the diabetic heart, so that glucose loading prior to hyperpolarised experiments can be justified in diabetic patients.
4) Assess for any changes in LDH or ALT flux occurring during feeding and in diabetes.

4.1.1 Substrate handling in the diabetic heart

Despite diabetes being characterised by an abundance of circulating FAs and glucose, the diabetic heart almost exclusively oxidises FAs as a substrate, this is mediated by an upregulation of signalling through PPARα driven by myocardial steatosis [75]. The metabolic flexibility of the heart to turn towards glucose as a substrate is markedly reduced [115]. Decreased glucose *uptake* in the human diabetic heart has been demonstrated with [^{18}F] FDG PET [76], but *oxidation* changes cannot be studied with this technique.

4.1.2 Hyperpolarised MRS offers mechanistic insight into substrate selection

By measuring PDH flux using hyperpolarised [1-^{13}C]pyruvate MRS, the contribution of glucose (via glycolysis) to the acetyl-CoA pool (and thus ATP generation) at the moment of imaging can be assessed. In a number of murine diabetes models including streptozotocin induced [71, 152, 162], and also in a βVM59 mouse model [145], hyperpolarised MRS has confirmed the central role that impairment of PDH flux plays in the pathological substrate handling seen. In the βVM59 model, diabetes is induced by a K^+_{ATP} channel mutation which impairs glucose stimulated insulin secretion and induces diabetes in the absence of obesity or insulin resistance. Diabetes here can rapidly be reversed by treatment with a sulphonylurea, and restoration of PDH flux is correspondingly seen [145]. A high fat diet alone also induces mild insulin resistance and depresses PDH flux in rats [153]. Using Western blotting techniques from myocardial extracts, PDH flux reduction here is shown to be mediated largely by overexpression of PDH kinase 4 [73]. Dichloroacetate (DCA, a potent PDK inhibitor) restores PDH flux, and normalises diastolic function [152]. This important finding suggests pathological substrate handling could be central to the pathogenesis of diabetic cardiomyopathy and offers a potential therapeutic target. The diabetic heart is also characterised by progressive energetic impairment with a reduced PCr/ATP consistently seen [15]. Combined with steatosis (measured by ^{1}H MRS [74]), this drives concentric remodelling, and ultimately diabetic cardiomyopathy [163, 164]. The interaction between impaired energetics and structural impairment is discussed and explored in more detail in chapter 6 by seeking to gain a better insight in to any alterations in ΔG_{ATP} that may occur in the condition. Measuring PDH flux, if this can be recorded in the human heart, provides the opportunity to track global alterations in substrate preference and glucose handling that accompany the progression of cardiac diseases not limited to diabetes. For example progressive reduction in PDH flux is seen

as DCM develops in response to chronic cardiac pacing [67], and increases during hypertensive stress [165] in porcine models.

4.2.3 Hyperpolarised MRS to assess the Randle cycle in real time

Physiological changes such as the substrate switch described by Randle [8] can also be demonstrated (Figure 19), with increased PDH flux demonstrated in both rats [71] and pigs [151] following glucose infusion. Measuring real time change in metabolic flux is yet to be achieved in the human heart, but the confirmation of Randle cycle changes, and an idea of their magnitude, is necessary to guide participant preparation for hyperpolarised MR experiments seeking to detect changes in [1-^{13}C]pyruvate handling. The effect of diabetes should also be quantified given results from the previous chapter. The primary aim of chapter 4 was therefore to provide the first non-invasive *in vivo* demonstration that physiological (Randle cycle associated changes seen during feeding) and pathological (in diabetes) changes in PDH flux can be detected in the human heart using hyperpolarised [1-^{13}C]pyruvate MRS. Ensuring PDH flux is indeed discernible in the context of diabetes was also essential prior to imaging studies whose aim will be to detect regional cardiac differences in the handling of [1-^{13}C]pyruvate in those with coronary artery disease, given diabetes is a significant vascular risk factor. The observation of reduced PDH flux in the diabetic human heart would also confirm it as a potential therapeutic target for diabetic cardiomyopathy. By assessing the other hallmarks of diabetic heart disease (impaired energetics, myocardial steatosis, and diastolic impairment), I further aimed to determine additional metabolic information, for effect size comparison to any pathological change in PDH flux recorded during the hyperpolarised [1-^{13}C]pyruvate technique.

4.2 Methods

4.2.1 Ethical considerations

Research undertaken at 3T using hyperpolarised MR to investigate diabetic cardiac metabolism was approved by the Exeter Research Ethics Committee (REC) Centre (Reference 13/SW/0108, IRAS ID 111881), and conducted in accordance with the declaration of Helsinki and the Caldicott principles. All participants gave written informed consent.

4.2.2 Eligibility criteria

4.2.2.1 Inclusion criteria

All participants recruited to this chapter were healthy controls or patients with diabetes, and fulfilled the eligibility criteria below:

Healthy controls

- Aged over 18 years
- Able and willing to provide informed consent
- Asymptomatic, with no significant medical history and no regular medications
- Normal ECG and cardiovascular examination

Patients with stable Type 2 diabetes

- Aged over 18 years
- Not on insulin therapy
- No change in medication for 3 months
- HbA1c of between 6 and 9%
- Normal ECG and cardiovascular examination

4.2.2.2 Exclusion criteria

- Any history of cardiovascular, endocrine or neurological disease, pregnancy, uncontrolled hypertension, chronic renal impairment (estimated glomerular filtration rate < 30ml/min/1.73m^2) or undiagnosed chest pain.
- General MR exclusion criteria outlined in appendix 9.3

4.2.3 Study population

This is the first clinical study using hyperpolarised MR, and dealing with a novel technique posed novel problems to the whole team, thus, data presented in this chapter was collected over a full three-year period. All participants provided written informed consent. Thirteen people with type 2 diabetes (age 55.2±5.8 years, 2 female (F) and 12 controls (age 50.3±11.4 years, 4F) were recruited from local advertisements, all participants were aged >18 yrs. Patients with diabetes taking the oral anti-hyperglycaemic drug Metformin, were asked to refrain from taking their medication for 24 hours before the study visit given its potential effect on the cardiac redox state [166]. No patients with diabetes were taking sodium-glucose cotransporter-2 (SGLT2) antagonists.

4.2.4 Study visit

Sterile fluid pathways were loaded into the polariser to begin the process of hyperpolarisation at 5am, with the participant arriving at 7 am following an overnight fast lasting at least 9 hours. Patients with diabetes were asked to withhold taking any diabetic medications. Fasting cholesterol, glucose and HbA1c were taken. Spot creatinine was recorded using a point of care device if one was not available recorded within the last 6 months. Firstly, a resting ECG

was recorded along with height and weight, and echocardiographic assessment of diastolic function was undertaken. Myocardial ^{31}P MRS was undertaken to record PCr/ATP using a non-gated, free breathing, 3D acquisition–weighted CSI sequence, followed by ^{1}H MRS to assess myocardial lipid content, both undertaken in the fasted state. Additionally, hyperpolarised [1-^{13}C]pyruvate MRS was undertaken immediately before and 45 minutes after a standardized oral glucose dose consisting of a 75g (the dose used during the OGTT) glucose dose taken in under 5 minutes. During the first half of the study this was given as Lucozade®, however the sugar content of the product was reduced during the study mandating a different method to deliver the required amount. The study was amended so that Rapilose® (Penlan healthcare, UK) could be used. Details of SFP preparation, the acquisition and processing of hyperpolarised data, as well as the analysis workflow for ^{31}P and ^{1}H spectra are found in chapter 2. All scanning was undertaken at 3T (Tim Trio MR system, Siemens Healthineers, Erlangen, Germany). The outline of the study visit is summarised in Figure 29.

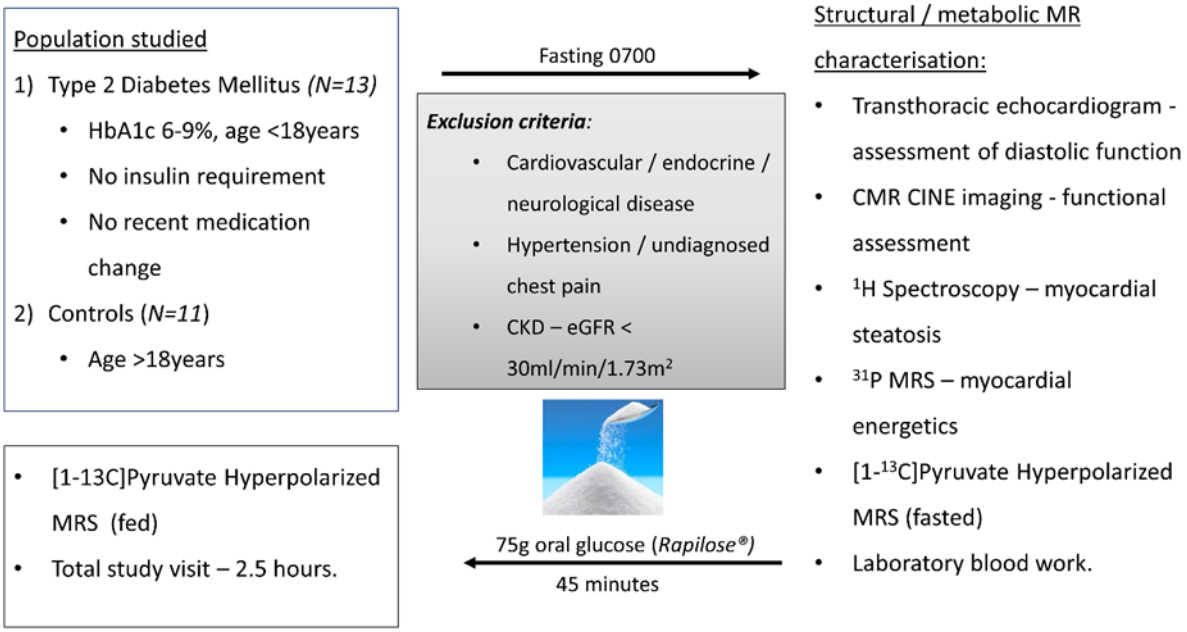


Figure 29: Diabetes and cardiac metabolism study visit

Structure of a typical study visit using hyperpolarised MRS to assess the impact of diabetes on PDH flux in both the fasted and fed states.

My study was the first to report results from three nuclei (^{31}P, ^{1}H, and ^{13}C) in a cardiac MRS study. Alongside this, an assessment of LV structure and diastolic function was made, to characterise the diabetic phenotype in some detail. Examples of the data collected, providing an overview of the breadth, can be seen in Figure 30.

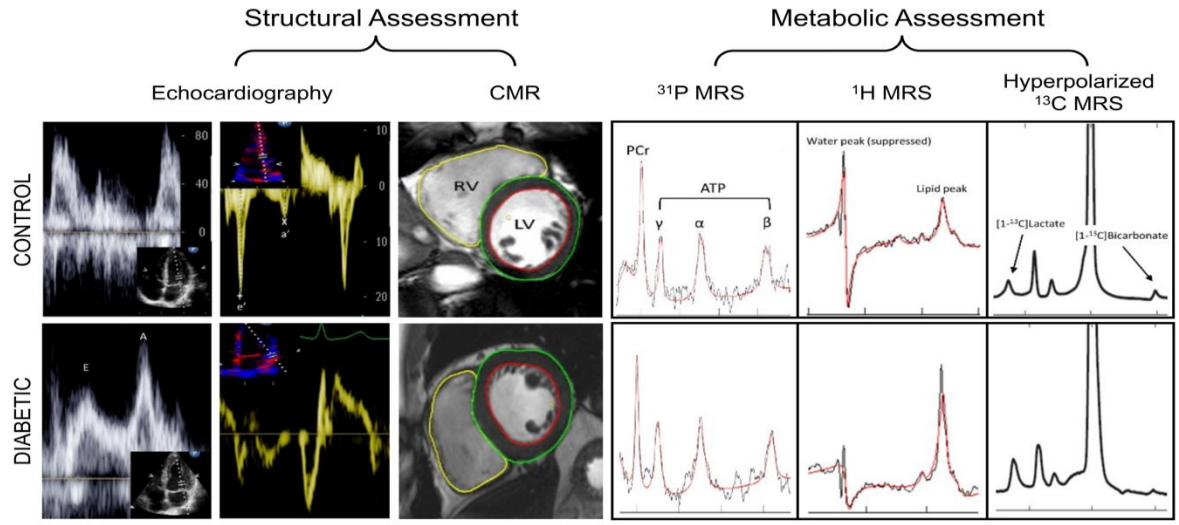


Figure 30: Comprehensive structural and metabolic assessment of diabetes

4.2.5 Data and statistical analysis

As in the previous chapter, linear mixed effect models were used to analyse the hyperpolarised data, which are a powerful generalisation of repeated measures ANOVA methods and are effectively able to use repeated measurements even if data is missing [167].

Hyperpolarised datasets were analysed in R by this method (v3.6.0, R Foundation for Statistical Computing, Vienna, Austria), with metabolic state and disease status considered as fixed effects, and subject ID considered as a random effect, and an ANOVA table computed. Data were subject to a Shapiro-Wilk normality test. One outlier corresponding to the [^{13}C]bicarbonate to [1-^{13}C]pyruvate ratio for an unpaired fasted subject with type 2 diabetes with a Z-score of 9.4, was identified (Grubb's test p = .003), suggesting that point was an outlier. Data derived from this participant were excluded from subsequent analysis. All other analyses were performed in GraphPad Prism (GraphPad Software, San Diego, California, USA) via simple unpaired unequal-variance *t*-tests with the canonical p<0.05 threshold for statistical significance. To compare the effect of diabetes on each metabolic parameter recorded, a simple post hoc estimation of effect sizes was calculated for each, using Hedges G (g) statistic which is given by:

$$g = \frac{\bar{x}_1 - \bar{x}_2}{s_p}$$

Where $\bar{x}$ represents the mean of samples 1 and 2, and S_p is the pooled standard deviation, which is in turn given by:

$$Sp = \sqrt{\frac{(n_1 - 1)s_1^2 + (n_2 - 1)s_2^2}{(n_1 - 1) + (n_2 - 1)}}$$

With n and s representing the number and standard deviation within each individual sample. Post Hoc power calculations were subsequently performed using G* power 3.1.9.4.

4.3 Results

4.3.1 Baseline population characteristics

Patients with diabetes were confirmed to be more insulin resistant than the controls (HOMA-IR 4.3±2.5 vs. 1.3±0.8, p=0.005), with higher fasting blood sugar (7.9±2.7 vs. 4.8±0.7, p=0.006). These baseline characteristics, as well as the medications the diabetic group were taking can be found in Table 3.

Table 3: Baseline population characteristics

Study Population	**Control (n=12)**	**Diabetic (n=13)**	**p-Value**
Age (years)	50.3±11.4	55.2±5.8	0.190
Weight (kg)	68.0±13.1	93.7±17.7	<0.001
BMI (kg/m^2)	22.6±3.0	29.7±6.8	0.003
HbA1c (%)	4.9±0.3	6.9±1.0	<0.001
HOMA IR	1.3±0.8	4.3±2.5	0.005
Fasting Glucose (mmol/l)	4.8±0.7	7.9±2.7	0.006
Medication (Cardiovascular)			
ACE* Inhibitor	0	6 (46%)	-
Statin	0	9 (69%)	-
Sulfonylurea	0	5 (38%)	-
Calcium channel blocker	0	2 (15%)	-
Thiazide	0	2 (15%)	-
Aspirin	0	2 (15%)	-
Medication (for diabetes)			
Metformin	0	11 (85%)	-
Liraglutide	0	1 (8%)	-
Sitagliptin	0	1 (8%)	-
SGLT-2 Inhibitor	0	0 (0%)	

**Angiotensin converting enzyme*

4.3.2 Baseline structural characteristics and MRS

Indexed left ventricular end-diastolic volume (LVEDVi) was no different between controls and patients with diabetes (82±12 ml/m^2 vs. 79±15 ml/m^2, p=.58) neither was myocardial mass index (64±10 g/m^2 vs. 62±11 g/m^2, p=.66), or the mass to volume ratio (0.79±0.17 vs. 0.81±0.16, p=0.83). Similarly, no difference in ejection fraction of either the left (60±4% vs. 57±6%, p=.23), or right (54±4 vs. 54±6, p=0.93) ventricles was apparent. As expected, diastolic function differed between the two groups; with a higher mean E/e' seen in diabetes (7.2±1.4 vs 5.7±1.7 p=0.04), recorded values still lay however within the normal range. Structural characteristics as measured with CMR and echocardiographic data is presented below in Table 4.

Table 4: Table of baseline structural and MRS characteristics

	Control (n=12)	Diabetic (n=13)	p
CMR			
LVEF (%)	60 ± 4	57 ± 6	0.228
LVEDV	149±21	169±30	0.085
LVEDV Index (ml/m^2)	82±12	79±15	0.577
LV mass (g)	118±27	133±25	0.169
LV Mass Index (g/m^2)	64±10	62±11	0.659
LV mass / LVEDV (g/ml)	0.79±0.17	0.81±0.16	0.830
RVEF (%)	54 ± 4	54 ± 6	0.934
RVEDV Index (ml/m^2)	93 ± 8	84 ± 16	0.095
Echocardiography			
E/A	1.3 ± 0.4	1.0 ± 0.3	0.127
E/e' (medial)	6.3 ± 2.0	8.1 ± 1.4	0.025
E/e' (lateral)	5.1 ± 1.8	6.3 ± 1.8	0.149
E/e' (mean)	5.7 ± 1.7	7.2 ± 1.4	0.040
Spectroscopy			
PCr/ATP	1.94 ± 0.21	1.71 ± 0.30	0.042
Myocardial Lipid Content (% of water)	1.59 ± 0.88	3.05 ± 1.96	0.026

As was expected diabetes significantly impaired myocardial energetics (PCr/ATP 1.71±0.30 vs 1.94±0.21 p=0.042, Figure 31A). Myocardial triglyceride content was almost two fold higher in diabetes (3.05±1.96% vs. 1.59±0.88% p=0.026, Figure 31B.

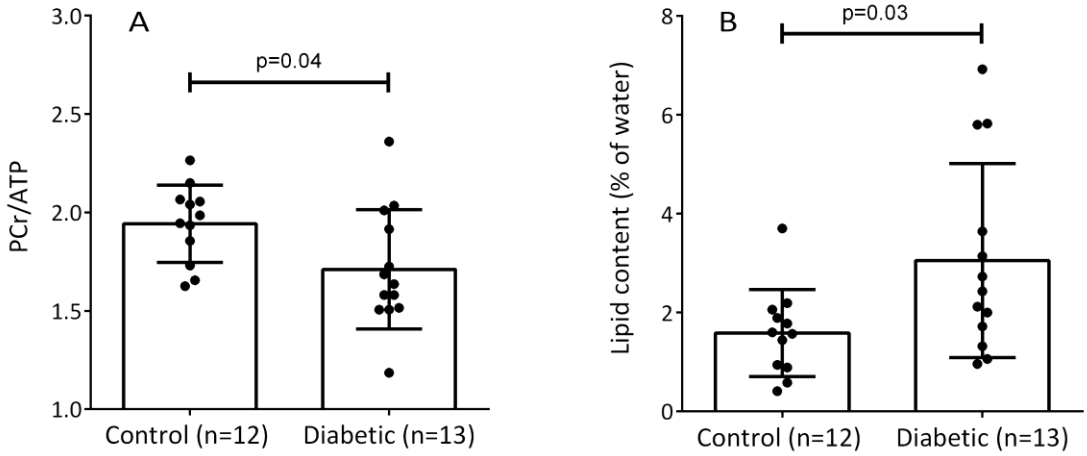


Figure 31: Myocardial PCr/ATP and lipid content in diabetics and controls

Myocardial PCr/ATP (A) was significantly reduced, and lipid content significantly increased (B) in diabetics.

Diastolic dysfunction in these patients is often ascribed to progressive myocardial hypertrophy and concentric remodelling. Diastolic function however as measured by E/e' bore no relationship to either LV mass (Figure 32A) or the mass to volume ratio (Figure 32C). Indeed, rather unexpectedly, when LV mass was indexed to BMI, a significant inverse correlation to E/e' was seen (R = 0.51, R^2=0.26, p=0.02, Figure 32B). No correlation was found between cardiac energetics and either of LV mass (Figure 32D), LV mass index (Figure 32E), or the mass to volume ratio (Figure 32F).

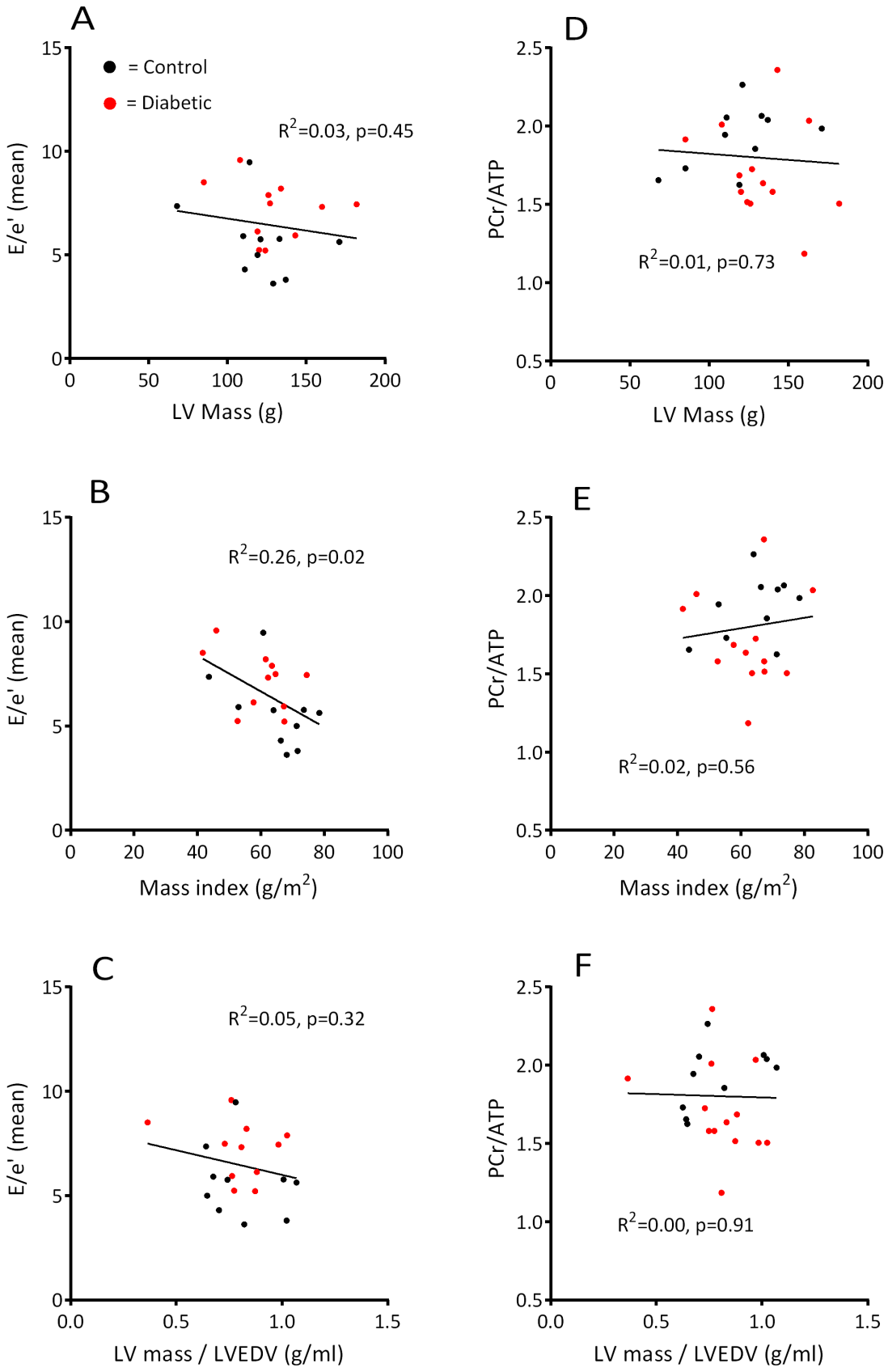


Figure 32: LV characteristics and relationships to diastolic function and energetics

Aside from a significant inverse correlation between diastolic function and LV mass index (B), no significant correlations were found between structural LV characteristics and either diastolic function, or cardiac energetics. Red denotes patients with diabetes (in this and all subsequent graphs).

Insulin resistance (HOMA-IR) showed a non-significant positive correlation with myocardial lipid content (Figure 33A), however lipid content bore no relation to any structural characteristics of the left ventricle recorded, including mass (Figure 33B), mass index (Figure 33C) and the mass to volume ratio (Figure 33D).

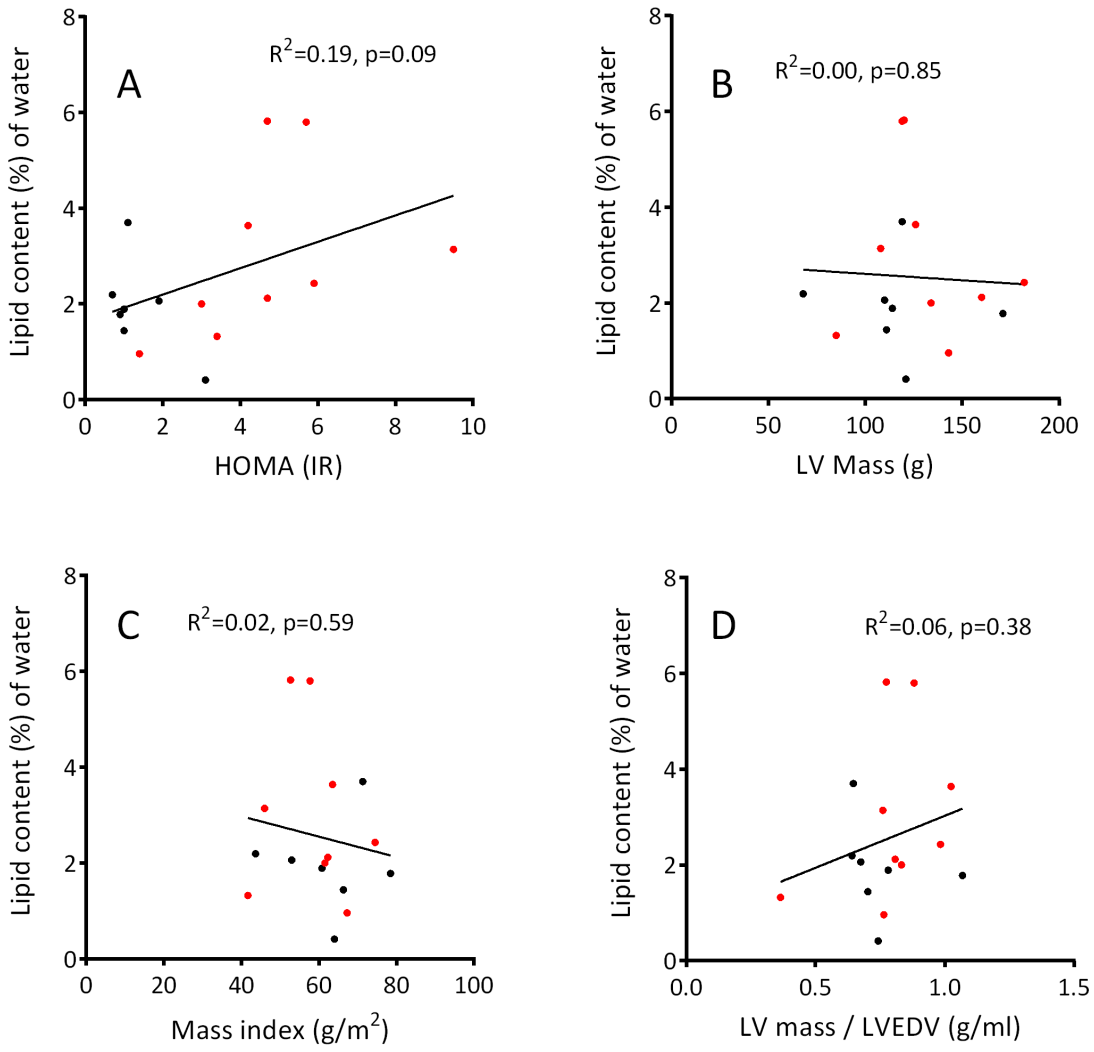


Figure 33: Myocardial lipid content and its relations to insulin sensitivity and LV characteristics

Myocardial lipid accumulation is thought to be a contributing factor, in the development of the pathological changes in substrate handling and abnormal energetics seen in patients with diabetes. A significant inverse correlation between lipid content and PCr/ATP was seen (Figure 34A), but not with E/e' (Figure 34B). The lack of any relation between diastolic function and lipid content seen in this group is perhaps not surprising given that diastolic function was relatively normal with E/e' on the upper limit of normal in the patients with diabetes.

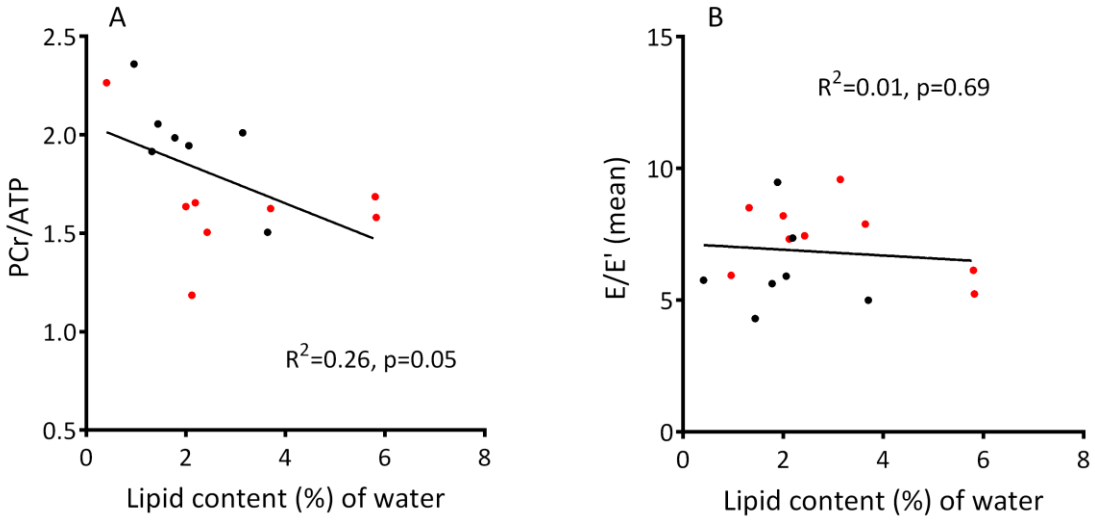


Figure 34: Myocardial lipid content, energetics, and diastolic function

Myocardial lipid content adversely affected myocardial energetics (A) with an inverse correlation seen between lipid content and PCr/ATP. No such association was seen in diastolic function (B).

4.3.3 Injected [1-^{13}C]pyruvate specifications, and population injected

5 controls and 5 patients with diabetes from within the cohort described above then went on to have fasting [1-^{13}C]pyruvate hyperpolarised MRS, with 5 (2 control, 3 diabetic) then receiving successful repeat [1-^{13}C]pyruvate hyperpolarised MRS 45 minutes after glucose ingestion. As in the wider group, the BMI was again significantly higher in the diabetics. The quality of the solutions generated after polarisation were highly standardised; mean (±SD)

pyruvate concentration was 239.6±8mM, residual EPA 1.1±0.7μM, pH 7.7±0.4, temperature 34±1°C and polarization 34.5±13%. Mean polarization time was 150±30minutes and dissolution to injection times were all less than 90 seconds, with injected volumes ranging from 21 to 45mls, (0.4 mls/kg). Hyperpolarised [1-^{13}C]pyruvate solution injections were well tolerated with no side effects reported. This smaller group had similar age and myocardial structural characteristics. Although diastolic function remained significantly different amongst the diabetics in this smaller group, significance was lost for the ^{1}H and ^{31}P MRS data (Table 5). The magnitude of change in this was however similar in both groups, with a 12% reduction in PCr/ATP seen in the diabetics in the wider group vs. a 14% reduction in the ^{13}C MRS group, and a ~doubling of myocardial lipid content in the diabetics in both groups. ^{31}P and ^{1}H MRS results are summarised in Table 5.

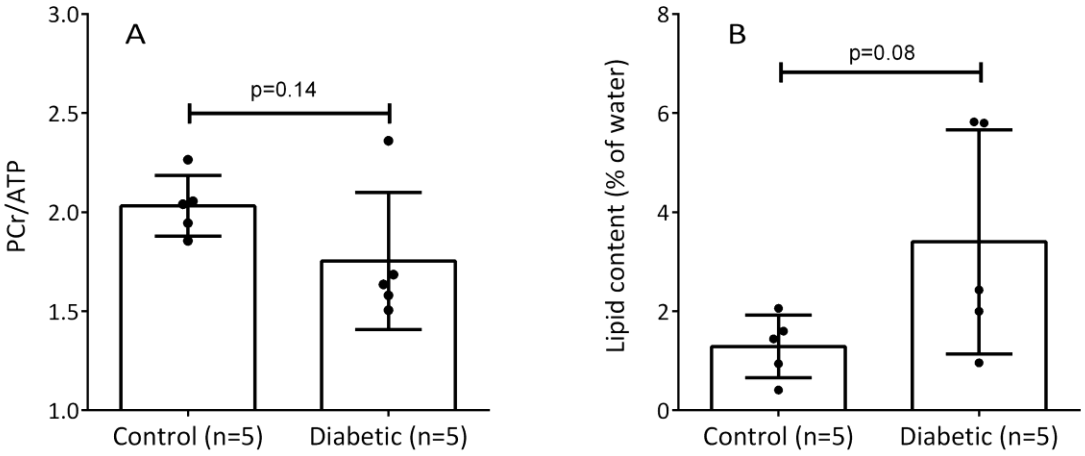


Table 5: Characteristics of the group receiving hyperpolarised MRS

^{13}C MRS Only Group	Control (n=5)	Diabetic (n=5)	p
Age (years)	49.2 ± 13.1	52 ± 5.2	0.668
Weight (Kg)	72.1 ± 7.4	99.2 ± 13.9	0.005
BMI (Kg/m^2)	22.6 ± 1.7	31.1 ± 6.1	0.017
E/e' (mean)	4.7 ± 1.1	6.6 ± 1.2	0.030
PCr/ATP	2.03 ± 0.15	1.75 ± 0.35	0.138

Myocardial Lipid Content (% of water)	1.29 ± 0.63	3.40 ± 2.26	0.079

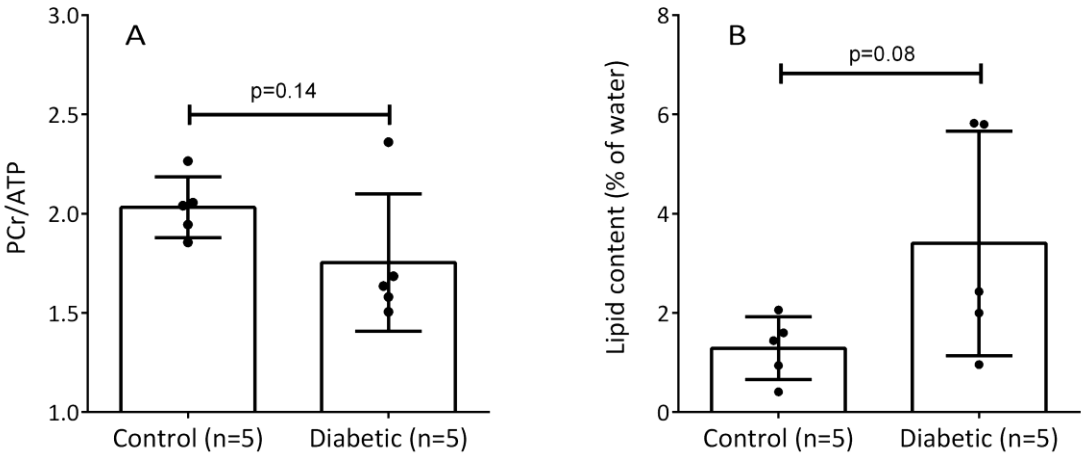


Figure 35: PCr/ATP and lipid content in [1-^{13}C]pyruvate injected subgroup

In the group who went on to receive ^{13}C MRS assessment of metabolic flux, significance was lost for the differences between the groups in ^{31}P-MRS (A) and ^{1}H data (B), but the magnitude of change was preserved suggesting the smaller group was representative.

4.3.4 Hyperpolarised ^{13}C MRS

Acquired hyperpolarised spectra were of high quality with peaks corresponding to $H^{13}CO_3^-$, [1-^{13}C]lactate and [1-^{13}C]alanine (the downstream metabolites of [1-^{13}C]pyruvate), clearly visible and appearing as expected 2-3 seconds after the ventricular [1-^{13}C]pyruvate resonance. Example summed spectra from both a control and a patient with diabetes, and the typical time course of substrate and metabolite signal intensities for a control and a subject with type 2 diabetes are shown in Figure 36. Integrated ratios for each of the three metabolic products of [1-^{13}C]pyruvate for all successful patients is seen in Table 6.

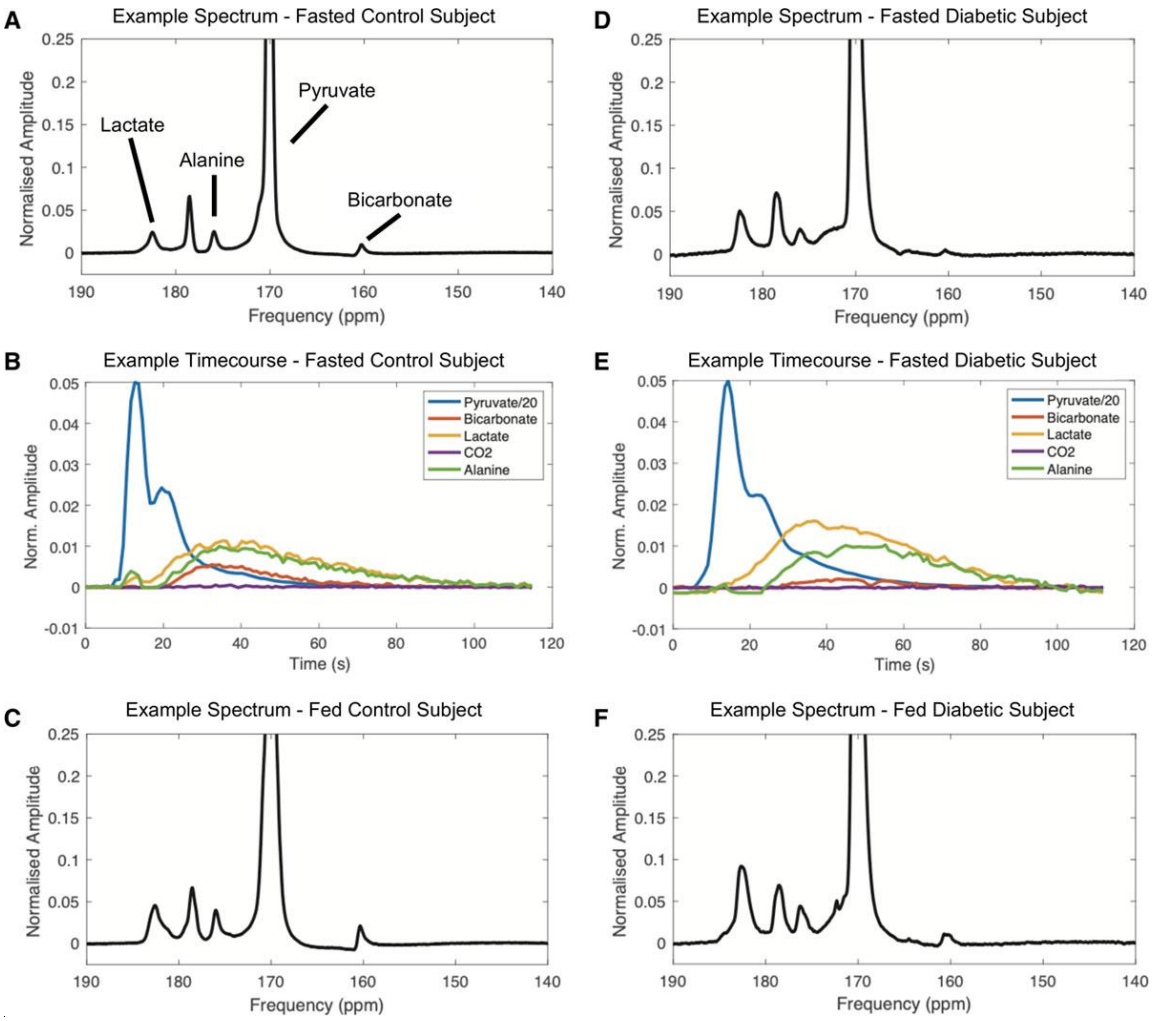


Figure 36: Representative spectra from healthy and diabetic participants

The $H^{13}CO_3^-$, resonance is visibly reduced in the subject with type 2 diabetes (A, D) with increases seen during feeding in both controls and diabetics (C, F). Time courses of appearance of downstream ^{13}C metabolic products are shown (B, E).

Table 6: Integrated ratios for each of the three metabolic products of [1-^{13}C]pyruvate

Controls	**$H^{13}CO_3^-$ / [1-^{13}C]pyruvate**		**1-^{13}C Lac / [1-^{13}C]pyruvate**		**1-^{13}C Ala / [1-^{13}C]pyruvate**	
	Fast	Fed	Fast	Fed	Fast	Fed
1	0.013	0.026	0.045	0.074	0.037	0.051
2	0.004	0.011	0.059	0.045	0.022	0.023
3	0.003		0.043		0.023	

4	0.003		0.037		0.028	
5	0.018		0.075		0.049	
Diabetic						
1	0.000	0.003	0.084	0.104	0.029	0.044
2	0.003	0.002	0.087	0.093	0.043	0.055
3	0.001	0.010	0.071	0.120	0.054	0.044
4	0.001		0.107		0.030	
5	0.004		0.076		0.035	

The $H^{13}CO_3^-$ to [1-^{13}C]pyruvate ratio reflecting PDH flux was significantly reduced by diabetes both in the fasted (5.3-fold) and fed (3.5-fold) states (p=0.013, Figure 37A). Conversely, the [1-^{13}C]lactate to [1-^{13}C]pyruvate ratio reflecting exchange through LDH, was increased in diabetes (1.6-fold increase fasted, 1.8-fold increase fed, p<0.001, Figure 37B). Combining these individual results in to the $H^{13}CO_3^-$ to [1-^{13}C]lactate ratio gives a direct ratio between glycolytic and oxidative carbohydrate metabolism, and has been used before to measure the return of oxidative metabolism during reperfusion [168]. The ratio was significantly reduced in diabetes in both fasted (7.5-fold) and fed (6-fold) states **(**p<.001, Figure 37C). Transamination of [1-^{13}C]pyruvate to [1-^{13}C]alanine was not different between subjects with type 2 diabetes and controls (p=.257).

Hyperpolarised MRS also successfully demonstrated Randle cycle associated increases in PDH flux after feeding with flux significantly increased 45 minutes after the oral administration of 75 g of glucose (p<.001, Figure 37A). Importantly significance was driven by discernible changes in the diabetic group (3.3-fold), as well as controls (2.2-fold increase), in spite of the impaired basal PDH flux demonstrated in this disease. No statistically significant differences in LDH flux (p=.072) or the rate of pyruvate transamination (p=.077) between the

fasted and fed states was seen. Straight forward analysis of the data in a simple two-way ANOVA, despite the 5 missing data points gave significance in the same manner. Mean time-integrated metabolite to substrate ratios derived from hyperpolarised ^{13}C MR data can be found in Table 7.

Table 7: Time integrated metabolite ratios for successful scans

	CONTROL (N=5)		**DIABETIC (N=5)**		**P-VALUE**	
	Fast (n=5)	Fed (n=2)	Fast (n=5)	Fed (n=3)	Metabolic state	Diseased state
BIC/PYR (10^{-2})	0.84 ± 0.67	1.84 ± 1.09	0.16 ± 0.14	0.53 ± 0.41	*<.001*	*0.013*
LAC/PYR (10^{-2})	5.16 ± 1.52	5.94 ± 2.01	8.51 ± 1.38	10.53 ± 1.38	0.072	*<.001*
BIC / LAC	0.15 ± 0.10	0.30 ± 0.08	0.02 ± 0.02	0.05 ± 0.03	*<.001*	*<.001*
ALA/PYR (10^{-2})	3.17 ± 1.11	3.70 ± 2.03	3.82 ± 1.05	4.74 ± 0.66	0.077	0.257

Time integrated metabolite to substrate ratios, p-values refer to individual assessment for the effect of metabolic or disease state and are calculated via a linear mixed effect model extension of a traditional 2-way ANOVA.

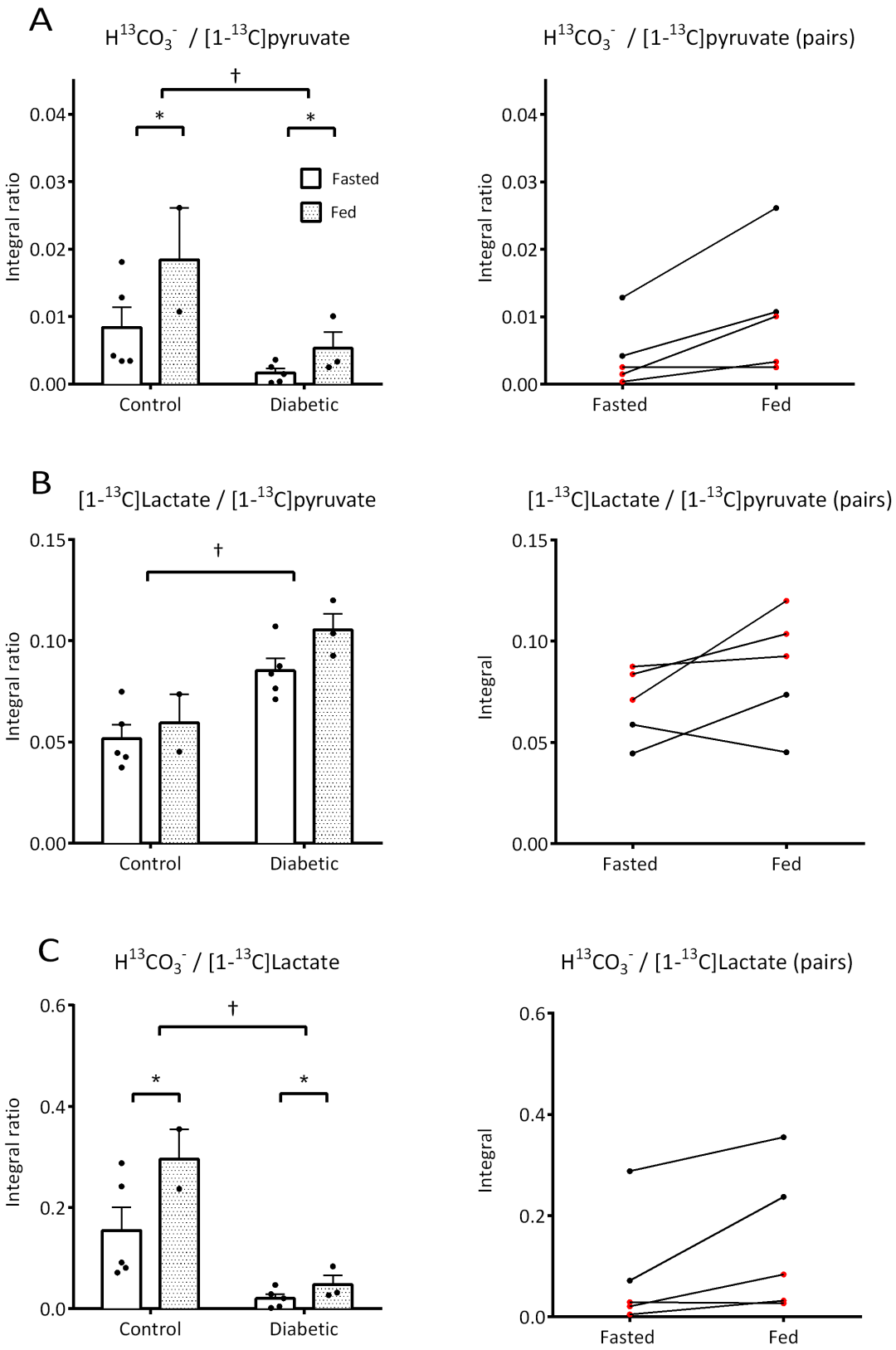


Figure 37: Effect of diabetes and feeding on cardiac metabolic flux

*Diabetes significantly reduced PDH flux (A, p=0.013), with increases seen in both controls and diabetics during feeding (p<0.01). LDH flux was significantly increased in the diabetic heart (B, p<0.01). The ratio of bicarbonate to lactate was significantly decreased in diabetics (C, p<0.01), with significant increases seen during feeding (p<0.01). † denotes p<0.05 in subjects with diabetes compared to controls, * denotes p<0.05 in fed compared to fasted states. Available paired results are shown in the right panels (red denotes patients with diabetes).*

4.3.5 Substrate metabolism, energetics, insulin resistance and LV characteristics

Non-significant correlations were observed between the PCr/ATP ratio and the fasted metabolite ratios recorded during hyperpolarised MRS. These were positive for bicarbonate/pyruvate and bicarbonate/lactate and Plots can be seen in Figure 38.

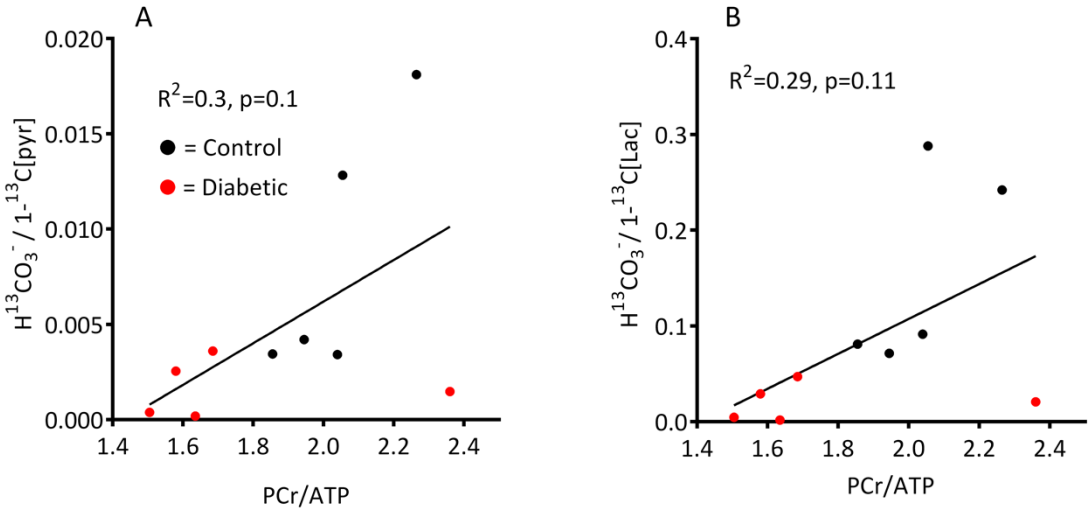


Figure 38: Metabolic flux data and PCr/ATP

A non-significant positive correlation was seen between PCr/ATP and both PDH flux ($H^{13}CO_3^-$ / [1-^{13}C]pyruvate, (A) and $H^{13}CO_3^-$ / [1-^{13}C]lactate (B).

Relationships between fasting metabolic flux and metrics of LV structure, function and insulin resistance can be found in Figure 39. An inverse correlation was seen between LV mass index and PDH flux (as measured by $H^{13}CO_3^-$ / [1-^{13}C]pyruvate, Figure 39A). When $H^{13}CO_3^-$ was normalised instead to another metabolic product [1-^{13}C]lactate, this inverse correlation gained significance ($R = -0.74$, R^2 0.56, $p=0.01$, Figure 39B). There was no correlation between PDH flux and LVEDVi (Figure 39C), or E/e' (Figure 39D). This later finding again needs to be taken in the context of the only mild diastolic dysfunction displayed in this cohort, with recorded E/e' (mean) on the upper limit of normal [143]. Weight loss as an intervention has been shown to improve diastolic function [169], with one possible explanation being normalisation of cardiac substrate handling. A non-significant but inverse correlation was seen between BMI and PDH flux (Figure 39E), which was unrelated to the underlying grade of insulin resistance (Figure 39F).

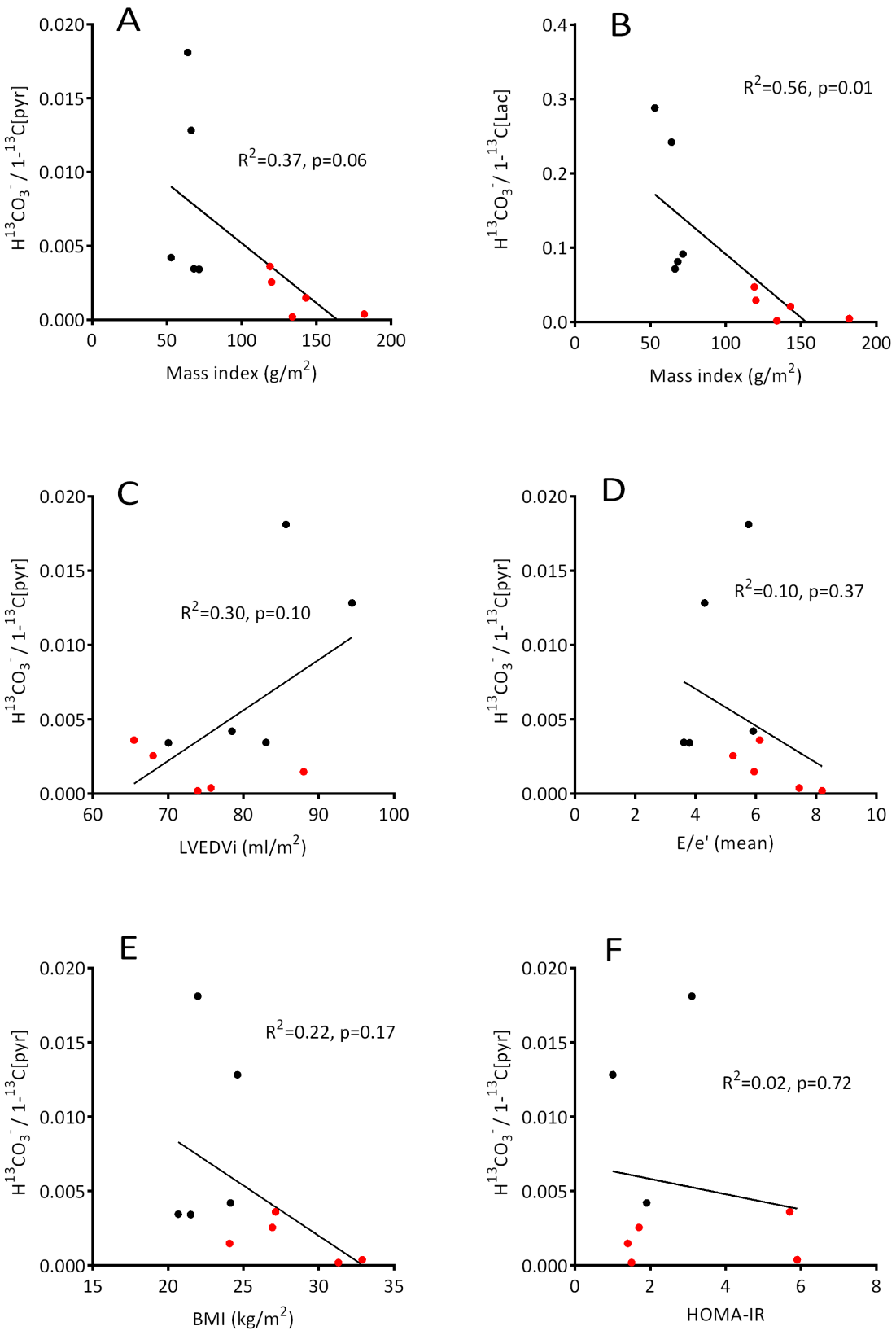


Figure 39: Metabolic flux and its correlations to other structural characteristics

Left ventricular mass index correlated inversely with both PDH flux (A), and $H^{13}CO_3^-$ / [1-^{13}C]lactate (B). However no correlation was seen with LVEDVi, (C), diastolic function (D), BMI (E) or HOMA-IR (F).

4.3.6 Effect size and power comparisons

Calculated with Hedges' G statistic using the SDs and means calculated in both the diabetic and control groups, the effect size for ^{31}P-MRS was 0.886, 0.950 for ^{1}H-MRS, and 0.993 for E/e' (average). Taking these in to a retrospective power calculation, and assuming independent T-Tests, gives expected total sample sizes of 56 (^{31}P-MRS), 50 (^{1}H-MRS), and 46 (E/e') to achieve significance (p=0.05) with 90% power in a simple unpaired students t-test. The effect size of diabetes on the observed metabolite ratios (calculated on fasted data points) was much larger; 1.390 (bicarbonate/pyruvate), 2.311 (lactate/pyruvate), and 1.826 (bicarbonate/lactate). Subsequent expected total sample sizes to achieve significance are therefore smaller (24, 12 and 16 respectively).

4.4 Discussion

In this study, using a hyperpolarised [1-^{13}C]pyruvate tracer, changes in flux through the key regulatory enzyme PDH have been demonstrated, observing increased myocardial pyruvate oxidation following glucose ingestion, as described by Randle [8]. Further, a reduction in PDH flux in patients with type 2 diabetes was demonstrated, confirming the observations in various rodent models of the disease [71, 145, 152], including in the previous chapter. This finding is extremely important given an increasing prevalence of obesity and diabetes, and the recognised complication of metabolic cardiomyopathy. This work was the first in man to demonstrate the real time ability of hyperpolarised MR to measure short-term physiological

changes in cardiac metabolism, and detect the impact of pathology on such changes. It confirms the potential of the technique for application in a number of cardiac metabolism studies. The study made a comprehensive assessment of diabetic cardiac metabolism, and using a multi-nuclear spectroscopic approach confirmed that in the presence of reduced PDH flux, impaired myocardial energetics (reduced PCr/ATP) and increased myocardial triglyceride content are also seen. The relative difference in triglyceride content seen here is similar in magnitude to that reported in prior studies using the same ^{1}H MRS sequence [119]. Values reported here however appear higher in both controls and patients with diabetes which is without explanation. All the metabolic changes demonstrated in the patients with diabetes may potentially make a contribution toward diabetic cardiomyopathy [163].

4.4.1 The Randle cycle in the healthy and diabetic heart

As was hypothesised, this chapter confirmed an increase in PDH flux following feeding, consistent with a switch in metabolic substrate preference toward glucose and away from FAs. This finding confirms hyperpolarised MR experiments in mice [70] rats [71] and pigs [72] and is consistent with the Randle cycle. The diabetic heart loses metabolic flexibility, becoming almost exclusively reliant upon FAs as its main catabolic substrate. This is underpinned by both an impaired ability to uptake glucose, and also to oxidise the glycolysis derived pyruvate produced, with impaired flux through PDH. Reduced PDH flux in diabetes has been seen both ex-vivo [170] and in-vivo in various rodent models of the disease [71, 145, 152].

Only a small number of patients with diabetes, (all of whom were on oral medications only and can be considered to have a mild phenotype with HOMA-IR 4.1 and borderline

impairment of diastolic function) were needed to demonstrate significantly impaired PDH flux. The disease had a greater effect size on this variable compared to energetics and diastolic function. The result supports the findings from the animal study which demonstrated how sensitive PDH flux was to any degree of insulin resistance (Figure 27). Although minimal, discernible PDH flux was recorded in the fasted diabetic state, and a significant increase maintained following feeding, suggesting metabolic flexibility is not lost completely. However, the diabetic phenotype studied here was mild and as such it cannot be confirmed that this would not also be lost with higher grades of insulin resistance.

Restoration of PDH flux using DCA is shown to improve diastolic function in a rat model of diabetes [152], and the conformation of reduced PDH flux in human patients with diabetes here raises the question of whether this could represent a viable therapeutic target in patients with diabetic cardiomyopathy. Although the observation will make hyperpolarised [1-^{13}C]pyruvate experiments aiming to detect changes in PDH flux (either regionally or temporally) more difficult in diabetic patients, it does suggest that such experiments remain feasible, as discernible metabolic flux was recorded.

4.4.2 Confirmation of glucose optimisation protocol

The result seen here confirms that standardising myocardial substrate metabolism in humans by delivery of an oral glucose load prior to scanning increases basal PDH flux, and thus may increase the power of experiments aiming to detect pathological changes in PDH flux [55]. Furthermore, cardiac PDH flux also significantly increased during feeding in the diabetics, indicating that metabolic flexibility is maintained to an extent that glucose loading this group prior to such hyperpolarised experiments is indeed justified. Ideal standardisation not only

increases pre-scan PDH flux (while still rendering it sensitive to change – i.e. at the top of the physiological range), but minimises intra-individual variation such that temporal changes in metabolism seen as disease progresses can specifically be ascribed to disease progression, and not day-to-day changes.

Significant intra-individual variation in metabolite ratios, equal in magnitude between the fed and glucose infused (scanned 30 minutes after glucose loading of a fasted animal) states were demonstrated in the previous chapter [162]. The same variability is also shown when comparing fasted and fed pigs [72]. Large variation in metabolism was also seen here in both fasted and fed scans. Together these results do not provide any evidence to suggest that inter-individual variability in metabolic flux differs significantly across the three physiological states, fasted, fed, and glucose infused. With clear evidence that feeding increases PDH flux, glucose loading should be considered standard, and it would be logical and safer to continue to deliver this on a background of the fasted state since delivering it fed would increase the risk of hyperglycaemia. There is a possibility that the injected pyruvate dose from the first scan may also have played a part in the increased PDH flux observed. However, it is unlikely that a 1 g dose of pyruvate given systemically some 50 minutes prior to the second scan (during the fasted scan), would have had a significant impact on top of the 75g of glucose provided between scans. Increasing heart rate and myocardial work would feasibly increase flux through PDH, however, all scans were undertaken in the resting state, such that myocardial work showed little variation between participants. Such small differences likely were no different between groups, and would not have biased results.

4.4.3 Lactate dehydrogenase and alanine aminotransferase flux

Incorporation of the ^{13}C label in to [1-^{13}C]lactate was significantly higher in patients with diabetes in both fasted and fed states suggesting raised LDH flux in this group. This finding is in keeping with chapter 3 in which a trend to elevated [1-^{13}C]lactate / [1-^{13}C]pyruvate was observed in diabetic rats. A simple suggestion to explain this finding could be that with lower flux through PDH, [1-^{13}C]pyruvate is diverted through LDH which is reciprocally increased. Such an argument is however likely too simplistic. The myocardial [1-^{13}C]lactate signal has proven much more diffuse in hyperpolarised short axis images of the both the human [133] and pig heart [171] with a large contribution from the blood pool. This suggests [1-^{13}C]lactate generated In the liver may be contaminating cardiac readouts [172]. As such, there must be caution in interpreting the exact derivation of the increased lactate signal in non-localised spectra. Metabolic imaging studies, now possible in the human heart [133] are needed to further localise this lactate signal to the myocardium. Finally, the anti-hyperglycaemic agent metformin has been shown to have an effect on cardiac redox, with increased lactate seen [166]. Patients with diabetes taking metformin omitted this drug for the 24 hours leading up to the study visit, however, it is possible that a chronic effect of this medication may have contributed to the elevated lactate signal seen.

The relative stability of [1-^{13}C]alanine / [1-^{13}C]pyruvate in this study is reassuring. In ex-vivo models the rate of this transamination is shown to increase proportionally as perfusate pyruvate concentration increases, with increased transfer of a ^{13}C [173] or ^{14}C [174] label in to alanine. Labelled alanine is thus a direct measure of the intra-cellular availability of labelled pyruvate such that its peak has been suggested as an alternative normalisation standard (as opposed to the pyruvate peak used in most hyperpolarised studies) [153].

Relative stability in this study, and lack of difference between patients with diabetes and controls suggests cellular bioavailability of administered [1-^{13}C]pyruvate was fairly uniform and not a potential confounder of the variation of enzymatic flux seen. The result is also consistent with the non-rate limiting passive movement of [1-^{13}C]pyruvate across the myocyte cell membrane mediated by the monocarboxylate transporter [175], unaffected by hormonal regulation or diabetes. Recently in pigs, however, pyruvate transamination was increased alongside flux through PDH after feeding (although to nowhere near the same extent – 76% vs 176%) [72].

4.4.4 Impact of insulin resistance on global cardiac metabolism

Given the fasting stipulation, recruitment was restricted to patients with diabetes on oral medications only, and the diabetic phenotype recruited in this study can be considered mild (HOMA-IR 4.3±2.5). Indeed, the nominal value of E/e' in the patients with diabetes (7.2±.1.4) although significantly higher than the controls lies within the upper limit of normal (<10, [143]). The CMR characteristics of the recruited patients also showed no evidence of hypertrophy, with recorded LVEDVi and LV mass index no different to the control group, and lying within normal limits. Collectively these structural observations suggest that although these diabetic hearts were tending towards filling impairment the typical structural diabetic cardiomyopathy phenotype was by no means emerging. Significant differences in ^{31}P, ^{1}H and, in an even smaller cohort, ^{13}C MRS data were clearly demonstrated in patients with diabetes, however, emerging prior to typical phenotypic CMR structural characteristics, or profound diastolic dysfunction. There is no evidence that structural cardiac dysfunction (either diastolic or systolic) is related to metabolism in diabetes, but this is not evidence that such

relationships do not exist. A significant negative correlation was seen between LV mass index and $H^{13}CO_3^-$ / [1-^{13}C]lactate (R = -0.74, R^2 0.56, p=0.01, (Figure 38B) suggesting cardiac pyruvate handling may occur early in the hypertrophy process. Causation is not demonstrated but as was shown in chapter three in which the sensitivity of PDH flux to insulin resistance was demonstrated, cardiac metabolism is highly sensitive to insulin resistance and its pathological alteration remains a candidate requisite precursor.

Obesity, the common precursor to type two diabetes in humans is shown to also impair diastolic function and myocardial energetics, and a paradoxical worsening of LV function and increase in myocardial lipid content occur during the early stages of weight loss, despite increases in peripheral insulin sensitivity (Figure 40) [169]. As in diabetes, cardiac FA uptake and oxidation, and oxygen uptake are increased in obese humans [176]. PDK overexpression is seen early in a rat model of obesity as blood sugar rises [116], again due to increased PPARα signalling [177]. Early results from ongoing work (unpublished, Figure 40E) suggest that PDH flux falls in obese human volunteers during the early stages of weight loss (alongside the increase in myocardial fat content). Studies serially measuring PDH flux through the weight loss process, and investigating relationships to changes in ventricular performance are ongoing and important, given the early paradoxical relationships thus far uncovered between an initial worsening of the cardiac metabolic status as peripheral insulin sensitivity improves.

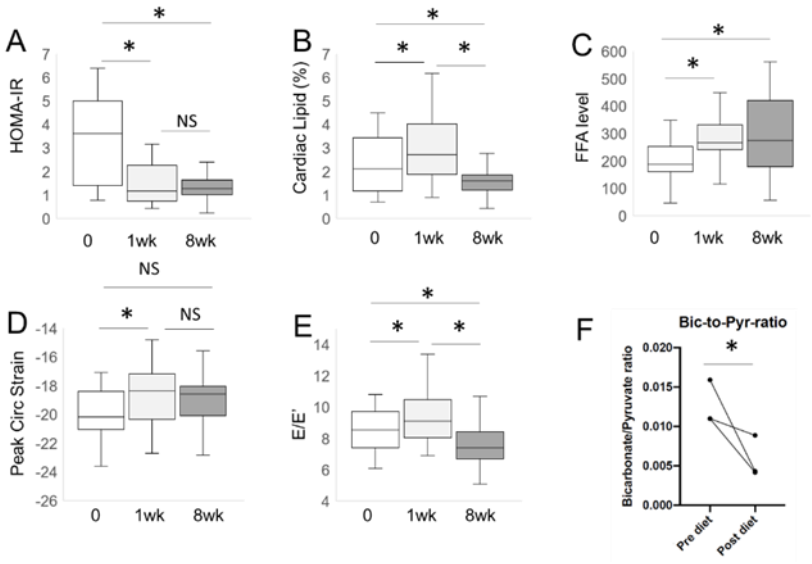


Figure 40: Cardiac changes during very low energy diet

At 1 and 8 weeks following institution of very low energy diet significant insulin re-sensitisation occurs (A), however this is accompanied by significant increases in cardiac lipid content (B), and circulating FFA level (C). Significant further impairment of systolic strain (D) and diastolic function (E) occur, and reduction in PDH flux (F). Taken from Rayner et al [169] (A-E), F with permission from Rider et al.

4.4.5 Difficulties in human translation of hyperpolarised MR, limitations of the present study

Human application of dissolution DNP is in its infancy. The first demonstration of clinical translation was published in 2013 using a prototype polariser located inside a cleanroom to prepare sterile injections for prostate cancer patients [122]. The SPINlab is the second generation of polariser suitable for preparing sterile injections outside of a controlled pharmaceutical facility. Sterility assurance in SPINLab preparations is achieved by enclosing the chemical constituents within single-use E-beam irradiated plastic kits that can be assembled and sealed in a certified compounding facility prior to being inserted into the SPINLab polariser. During rapid dissolution, these plastic kits must withstand a nearly

instantaneous temperature change of over 400°C under 250 psi of pressure. Due to the specialised nature of these plastic kits, there is currently a limited supply worldwide and a proportion fail when subjected to the extreme conditions of the dissolution process. Failed dissolutions account for just one of the many technical challenges of translating this technology. Indeed, 87 dissolutions were attempted (giving a failure rate of 87%), over the course of 43 study visits to collect the data presented in this chapter. However, the large effect size of metabolic dysregulation in diabetes was still exposed with hyperpolarised MRS despite the small ^{13}C dataset, and alludes to the importance of attempting to measure metabolism in human cardiac disease.

Other challenges to hyperpolarised ^{13}C MRS are harder to overcome. The signal from the hyperpolarised tracer rapidly decays according to the T1 of the tracer used (in the case of pyruvate 67±3s [178]) meaning the SPINlab must be in close proximity to the MR scanner with a clinical team ready to quality control the released product and undertake intravenous injection as rapidly as possible. The T1 time of the tracer also limits the number of metabolic conversions that can be studied, to those that occur sufficiently rapidly enough to produce enough product prior to full relaxation. This chapter suggests that such speed and connectivity of the dissolution process are however achievable.

Hyperpolarised MR requires a higher dose of tracer to produce measurable signal compared to PET systems, which are capable of measuring the handling of picomolar amounts of radiolabelled molecules, doses required have led some to argue that the pyruvate dose per second could alter the steady state of the metabolic system studied. In a rat model [153], infusion of 1ml of an 80mM pyruvate solution increased systemic pyruvate levels from 60 to 250μM, with similar maximal concentrations seen in humans after high dose pyruvate

infusion (13.9mmol / 1.73m^2) [179]. These doses are similar to that used here. Given that the pyruvate concentration recorded during exercise increases in humans to >400µM [180], it is unlikely that the dose of pyruvate administered in this study perturbs the metabolic state encountered to a significant extent.

4.5 Conclusions and future perspectives

The work presented in this chapter confirms the power of hyperpolarised MR to measure metabolism in humans, and makes a multinuclear assessment of the diabetic metabolic phenotype. Having confirmed, as expected, a reduced myocardial PCr/ATP and raised triglyceride content in the diabetic cohort studied, using hyperpolarised MR it has also been demonstrated that there is reduced, increased and stable flux through PDH, LDH and ALT respectively. During a glucose challenge Randle associated changes in substrate preference were documented in-vivo for the first time, and although flux through PDH was depressed in the diabetic heart, the metabolic flexibility to respond to a glucose challenge was not lost. I do not report any correlation with any of these data to the significantly raised E/e' (mean) found in the diabetics. However, in nominal terms this was only on the upper limit of normal, rendering this not surprising. The observation of depressed PDH flux in diabetes, demonstrated in only a small cohort with a mild phenotype of the disease, confirms it as a potential therapeutic target to improve pathological substrate handling.

Chapter 5. Quantifying the effect of stress on myocardial Pi and pH in healthy volunteers; ^{31}P-MRS at 7T.

The work in this chapter is published in the following journal:

Apps A, Valkovic L, Lau J et al. Quantifying the effect of dobutamine stress on myocardial Pi and pH in healthy volunteers; a 31P MRS study at 7T. Magnetic resonance in medicine, 2020 Sep 14. doi: 10.1002/mrm.28494.

5.1 Introduction

This chapter aimed to:

1) Test the ability of STEAM-^{31}P-MRS at high field strength to provide quantification of cardiac Pi free from 2,3-DPG blood pool obstruction, and assess the repeatability of Pi/PCr and cardiac pH across different scans.
2) Test the hypothesis that Pi increases in response to increasing cardiac work in the healthy heart, stimulating mitochondrial oxidative phosphorylation and increasing ATP production.
3) Examine the response of myocardial pH to an increase in cardiac work.

^{31}P-MRS is widely used for the non-invasive study of the cellular energetic state. Clinical studies report PCr/ATP, which is typically shown to be depressed in heart failure [83, 85, 86]. Reasons cited for this perturbation include an early fall in creatine [88, 91], a later fall in ATP and the total purine pool [91, 92, 93], and impairment of flux through CK [42] (as previously discussed in section 1.5.3). A reduction in this ratio however is not specific to heart failure with reduced ejection fraction (HFrEF), and is also seen in those considered at risk of developing a cardiomyopathy such as obesity [77], hypertension [87], heart failure with preserved ejection fraction (HFpEF) and diabetes [15], (shown in chapter 4). As such a reduction is not 100% sensitive to HFrEF [86].

Pathological energy metabolism upstream of systolic (or diastolic) dysfunction, combined with the finding that this biomarker is prognostic [83] does raise the possibility that this may in part have a causal association to mechanical cardiac dysfunction rather than being purely associative. As such there is a pressing need to develop further tools that are more sensitive and specific for the detection of meaningful pathological changes in energy

metabolism. To illustrate the problem with PCr/ATP, Figure 41 shows 300 recordings with wide variation in absolute values seen, and, similar reductions seen across a variety of pathological groups.

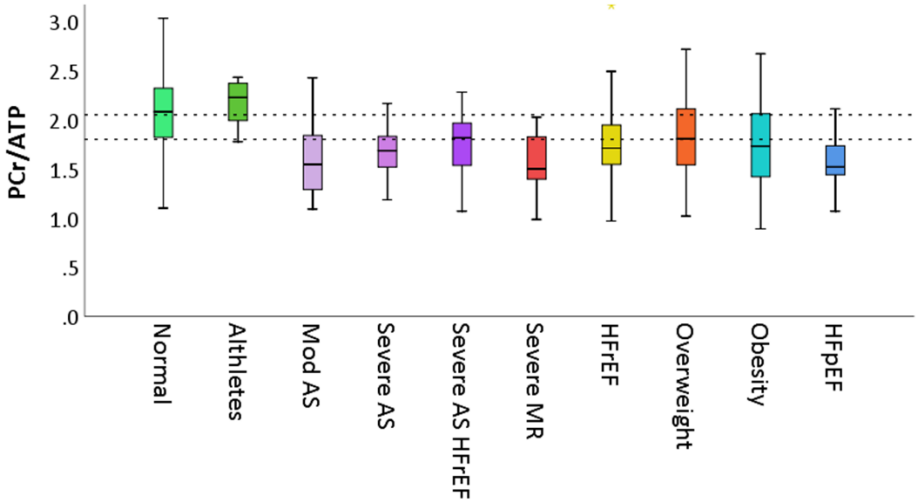


Figure 41: Box Whisker plot of 300 PCr/ATP recordings from OCMR across groups

This figure has been produced from data across a variety of research groups; and I thank Drs Peterzan, Rayner, Watson, Green, Abdesselam and Rider for access to the data.

5.1.1 Myocardial ΔG_{ATP} requires measurement of [Pi]

The bioavailability of ATP at sites of hydrolysis is maintained at the expense of the cytosolic PCr pool by CK, and for any reduction in PCr/ATP to have a meaningful negative energetic consequence it must result in an increase in the value of ΔG_{ATP}, (becoming less negative). It follows then that the computation of $\Delta G_{ATP,}$ is important, and is given by the following equation.

$$\Delta G_{ATP} = \Delta G^{\circ}{}_{ATP} - \mathrm{RT} \ln \frac{[ATP]}{[ADP][Pi]}$$

Pi is integral to the computation of ΔG_{ATP}, and any rise in [Pi] would reduce its value. Pi is an attractive candidate for assessing energy metabolism in-vivo for a number of reasons, alongside its role in determination of ΔG_{ATP}. Pi/PCr can be hypothesised to be a more sensitive marker of energetic dysfunction; in heart failure PCr/ATP may underestimate energetic dysfunction due to reductions in both metabolites [91, 181], to the extent that a normal (pseudonormal) ratio has been shown in some cohorts [86]. Pi is shown to be elevated in the hypertrophied rat heart [65] and also in humans with a combination of hypertension, LVH and diastolic function (as estimated with ^{31}P-MRS by comparing the size of the resonance within the 2,3-DPG region with controls) [87]. Impairment of CK flux in heart failure results in impaired phospho-transfer [42, 88]. Although traditionally measured using saturation transfer techniques, a rise in [Pi] (but not ADP) has recently been suggested to follow a reduction in K_f [50]. Measuring Pi in the human heart may thus represent a proxy through which CK flux can be investigated. PCr and ATP have been shown to be remarkably stable in healthy controls during incremental cardiac work [15, 16, 17, 86, 182], and Pi is thought to be integral to this homeostasis by linking rates of ATP hydrolysis with production, feeding back to increase mitochondrial oxidative phosphorylation [9, 23, 25]. Studying the control of oxidative phosphorylation may thus be possible by examining changes in [Pi] during pharmacological stress, and I investigated this in healthy control subjects in this chapter.

Pi plays several other important cellular signalling roles which are of interest. It is a potent stimulator of glycogen phosphorylase (its K_M renders the enzyme highly sensitive to small changes in the concentration of this substrate) which breaks down glycogen and thus increases the bioavailability of glucose as a substrate, [94, 96] and simulates glycolysis through activation of phosphofructokinase [65, 94, 183]. These roles mean small changes in myocardial Pi alter the heart's ability to oxidise glucose as a substrate. Indeed the rise seen in

hypertrophy makes Pi a potential candidate through which the increased glucose oxidation seen in early compensated heart failure (characterised by normal PCr/ATP) [12, 65] is effected. Furthermore, during incremental stress Pi/PCr is shown to rise earlier and more markedly in animals with hypertrophy than controls, and at lower degrees of stress than that required to trigger any fall in PCr/ATP [12, 184]. Such rises in the hypertrophied myocardium both at rest and during stress would have the concerted effect of increasing glucose oxidation (via glycolysis and glycogenolysis) and stimulating oxidative phosphorylation at the cost of a small reduction in the magnitude of ΔG_{ATP}. Changes to Pi/PCr prior to PCr/ATP during pharmacological stress demonstrate the importance of developing protocols for measuring Pi/PCr which are short enough to be tolerated by patients during stress.

5.1.2 Techniques to measure cardiac Pi

Data on human cardiac Pi assessment are scarce because overlap from blood pool 2,3-DPG makes it challenging to quantify reliably with the Pi resonance obscured by 2,3-DPG (Figure 42A). The large voxel sizes required for adequate SNR during ^{31}P-MRS experiments make resolving heart muscle tissue from blood difficult, however two approaches have been assessed. Recently Pi was estimated using a 45 minute CSI sequence with adiabatic excitation at high field strength [109]. Here, using a long T_R allows Pi to recover more (since it has a long T1) between excitations, maximising the Pi signal. However, the problem of contamination remains, making resolution imprecise, and the long scan duration (45 minutes) makes stress studies impractical (Figure 42B). Another approach using the technique of ^{1}H-decoupling has been reported at the lower field strength of 1.5T [111], this attempts to reduce Pi and 2,3-DPG linewidths and produce separate peaks (Figure 42C). However, using this method, Pi was

only reported in less than half of healthy participants (4/9), and the scan still took 30 minutes. The technique also necessarily corrupts Pi signal amplitudes due to magnetization transfer and nuclear Overhauser effects. Such an approach is also not feasible at the higher field strength of 7T due to the decoupling power breaching limits of acceptable specific absorption rate (SAR) safety guidelines for body radio frequency power absorption. Finally, given 2,3-DPG and Pi overlap, the approach of simply subtracting the resonance appearing in the region of 2,3-DPG from pairs of spectra (rest – stress or control [Figure 42D] vs pathology) also is suggested to give a semi-quantitative estimate of Pi [185]. Results from these strategies to quantify Pi can be seen in Figure 42.

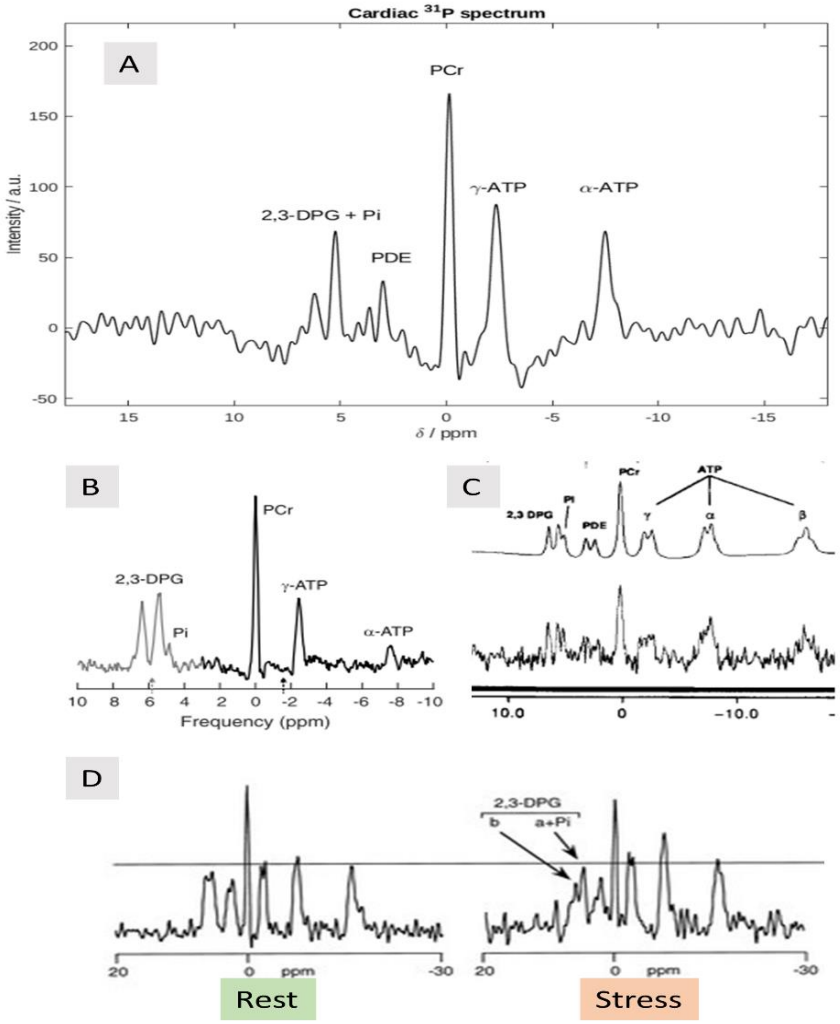


Figure 42: Comparing recent techniques for the quantification of cardiac Pi

Typical cardiac ^{31}P MRS CSI spectra (A) demonstrating 2,3-DPG completely obscuring the Pi peak. Published solutions to this problem such as using long TR adiabatic excitation (B, 40 minute scan) [109], and ^{1}H decoupling techniques (C, 30 minutes) [111] to increase separation still do not resolve the problem of Pi peak contamination. Assuming 2,3-DPG contamination as a constant, has led some to make estimates of myocardial Pi changes during stress by simply subtracting the resonance appearing in the DPG range within two spectra (D) [185].

5.1.3 Pi and the control of oxidative phosphorylation

Energy homeostasis requires ATP (and ΔG_{ATP}) stability during incremental cardiac work. This is achieved by a rapid increase in the rate of mitochondrial oxidative phosphorylation as ATP hydrolysis rates increase. A rise in cellular Pi and ADP secondary to increased hydrolysis are implicated in this control, feeding back to increase production [10]. Experimental observations from the human upper limb using NMR indeed demonstrate Pi/PCr increasing in a hyperbolic fashion from 0.1 to 1 as work increases [13]. Such a rise however, incurs an energetic cost given the associated rise in ΔG_{ATP}. In tissues with a higher capacity for oxidative metabolism, such as the myocardium, experimental observations are more variable. In canine open chest models, Pi/PCr is shown to be stable during incremental cardiac pacing [18], with significant changes in this ratio only seen during excessive chronotropic and inotropic stress [11, 12, 13]. Such rises may themselves represent a loss of the steady state rather than representing physiological control. One study reports gross increases in Pi during high grade stress in the healthy heart [185]. However, here Pi was estimated using the subtraction method noted in Figure 42, and synchronous falls in PCr/ATP were noted over a three-fold increase in the RPP. This finding is at odds to the stability of PCr/ATP during dobutamine stress in the healthy control arms of a number of subsequent clinical studies [15, 16, 17].

5.1.4 STEAM-^{31}P-MRS at high field strength for myocardial Pi

STEAM generates dark blood contrast during ^{1}H-MRI [112, 113]. Harnessing this property for spectroscopy, I hoped to (unlike the techniques outlined in 5.1.2) achieve stand-alone, robust Pi resolution, completely free from contaminating signals, within a scan time rendering stress studies in a new steady state possible. The first aim of this chapter was to test the feasibility

of whether STEAM-^{31}P-MRS, together with the strategy of undertaking a custom shim and generation of individual voltage reference maps for each participant, could indeed fulfil this requirement and produce spectra containing a standalone Pi peak in under 15 minutes. Given the potential impact of T_M on the susceptibility from various factors such as SNR, heart rate and myocardial deformation to impact the recorded Pi/PCr, intra-exam repeatability experiments were first undertaken. Given my aim was to go on and test the response of pH and Pi/PCr to stress, I then conducted repeatability experiments to test the ability of the protocol to produce stable measurements within the same individual under the same (rest) conditions [186]. The second aim of this chapter was to test the hypothesis that significant changes in Pi/PCr (as seen in human skeletal muscle), and/or pH, occur during incremental workloads in the healthy human heart, in order to maintain energy homeostasis.

5.2 Methods

5.2.1 Ethical considerations

Work in this chapter was approved by the Bristol Research Ethics Committee Centre (Reference 13/SC/0736, IRAS ID 128163). All participants gave written informed consent.

5.2.2 Eligibility criteria

All participants recruited for the work presented in this chapter were healthy controls fulfilling the criterial below:

Inclusion:

- Aged over 18 years

- Able and willing to provide informed consent
- Asymptomatic, with no significant medical history and no regular medications.
- Normal resting ECG and cardiovascular examination.

Exclusion:

- Any contraindications to dobutamine infusion such as severe outflow tract obstruction, recent history of arrhythmia, severe hypertension (>200/100), or active infection.
- Any of the general exclusion criteria outlined in appendix 9.3

5.2.3 Study population and visit

Nine healthy volunteers (2F, age 37±9), >18 years of age and able to give written informed consent were recruited for repeatability experiments to test the stability of results prior to onward dobutamine stress studies. Height and weight were recorded before scanning. In these studies, STEAM-^{31}P-MRS was simply repeated twice during the same scanning session under identical conditions. A separate cohort of 21 healthy volunteers (8F, age 39±15, BMI 23±2 kg/m^2) were recruited for the stress studies to test the hypothesis that large movements in Pi are needed for the physiological control of aerobic respiration. The structure of the typical study visits for both the repeatability and stress in healthy controls studies is found in Figure 43. Green boxes represent activities undertaken in the Oxford centre for Clinical MR Research (OCMR), blue boxes represent activities undertaken in the Oxford Centre for Functional MR of the Brain (FMRIB).

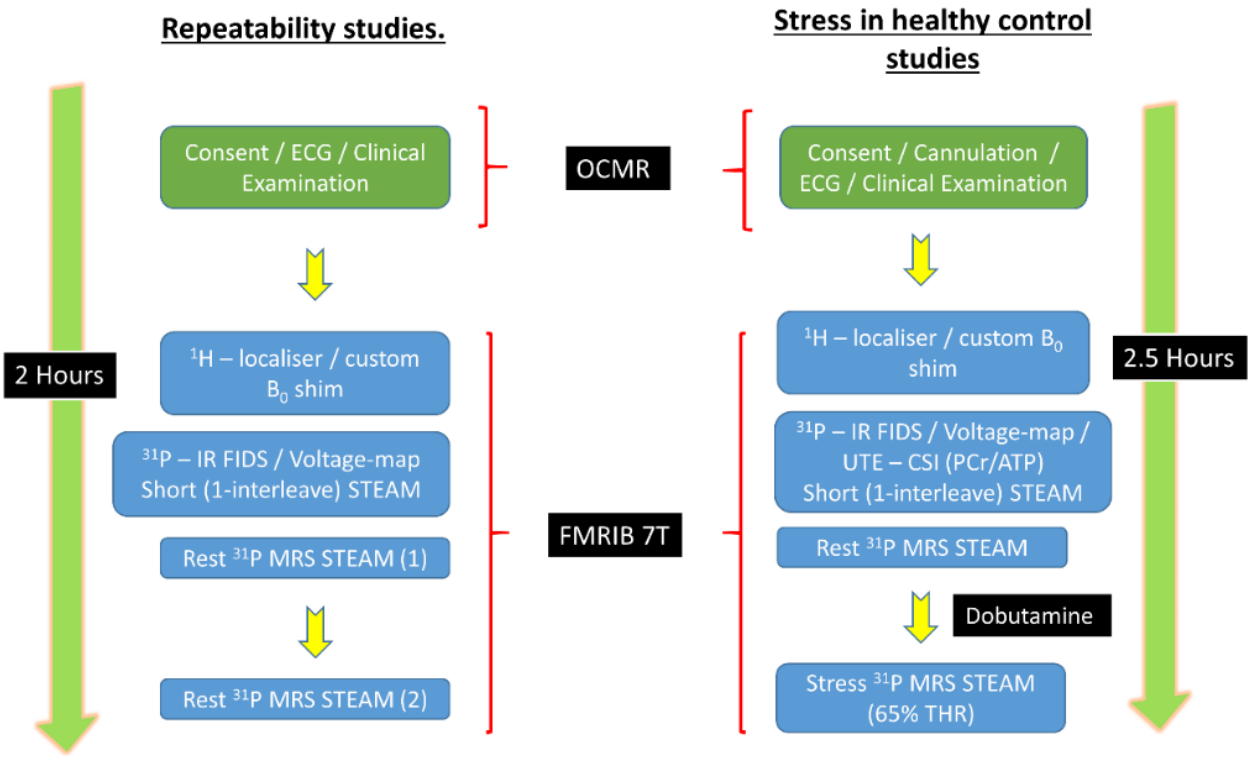


Figure 43: Outline of the studies to record Pi using STEAM-^{31}P-MRS in healthy controls

All MRS scans were undertaken using a Magnetom whole-body 7T MRI scanner (Siemens, Erlangen, Germany). Localisers were acquired using a standard 10cm ^{1}H transmit/receive loop (Rapid Biomedical, Rimpar, Germany), these were taken at end expiration in the main cardiac orientations. Subject-specific B_0-shimming was performed on all subjects in order to prevent high intensity signals of the chest wall from dominating the shim calculations. The coil was then changed for a 16-element array ^{31}P coil for ^{31}P-MRS (Rapid Biomedical, Rimpar, Germany). ^{31}P-FLASH localisers were acquired from the fiducial markers mounted on the coil corners to determine the coil position, then a set of IR-FIDs acquired to measure the flip angle experienced by a fiducial marker centrally housed within the coil. Following these, recruits to the stress studies then underwent UTE-CSI to compute PCr/γATP at rest.

During the CSI sequence, a subject specific voltage map was generated in Matlab using the acquired IR-FIDs. This was used to calculate the voltage required through the coil, to produce the 90° flip angles used in the STEAM acquisition at the voxel of interest. An initial (short) PCr only STEAM-^{31}P-MRS scan was then undertaken to ensure the excitation pulse was centred exactly on PCr (T_E 13 ms, T_M 7ms, T_R 3s [minimum], 48 averages, 3-4 minutes). This step was repeated until the excitation pulse resulted in the PCr peak being exactly on resonance (assigned 0ppm). The scan with two interleaves (Pi: T_E 13ms, T_M 60 ms 4.8 ppm relative to PCr, PCr as above, 148 averages, T_R 3s) was then acquired at rest (14-15 minutes), and repeated at rest after a short interval (repeatability cohort), or when the target heart rate had been reached during intravenous dobutamine infusion (stress cohort see 2.4.5). Further details of the ^{31}P-MRS protocols employed in this and the subsequent chapter can be found in section 2.3.2.

5.2.5 MRS analysis

Fitting was performed using the open-source Matlab-based Oxford Spectroscopy Analysis (OXSA) toolbox's implementation of AMARES [136, 187]. To fit STEAM-^{31}P-MRS spectra, first the 'PCr-interleaf' spectrum was fitted, then the 'Pi-interleaf' spectrum was fitted using 4 Lorentzian peaks at PCr, Pi and two phosphodiester frequencies, signals typically found in these spectra. The algorithm fitting the Pi frequency was constrained to search between +4.2 and +5.8 ppm relative to PCr, and the PCr linewidth and phase were used as starting points for the Pi parameter fitting. All peak amplitudes were corrected for the effect of T1 partial saturation using literature values [81, 188]. A typical pair of STEAM-^{31}P-MRS spectra can be seen in Figure 44.

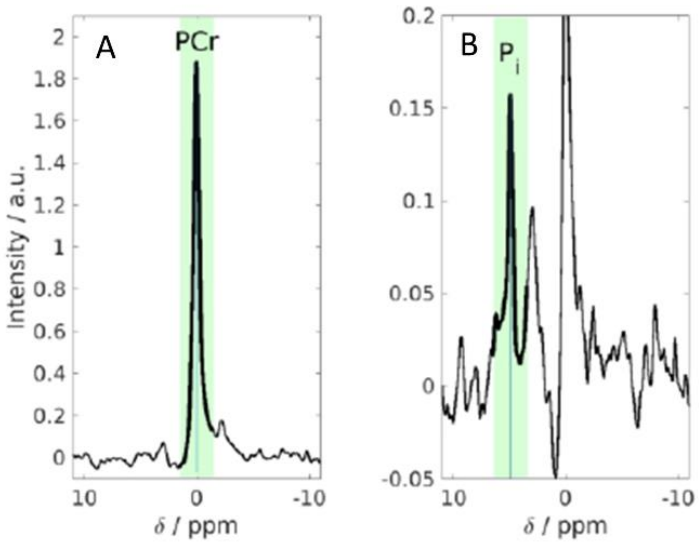


Figure 44: Typical STEAM-^{31}P-MRS spectra showing PCr (A) and Pi (B) interleaves

In each interleaf, the spectral region to be trusted is that immediately surrounding the metabolite excited marked by bolder lines and green background. Other parts of the spectrum arise from different spatial locations due to strong chemical shift displacement effects and cannot be taken as cardiac. Pi can clearly be resolved with little or no contaminating 2,3-DPG.

pH was computed from the chemical shift of Pi relative to PCr (taken from the PCr interleaf), using a modified Henderson-Hasselbalch relationship:

$$\mathrm{pH}(\delta) = 6.77 + \log_{10}\frac{\delta - 3.23}{5.70 - \delta}$$ [107].

UTE-CSI spectra were fitted as previously described [81] using prior knowledge of 12 Lorentzian peaks for ATP, PCr, and DPG with literature values for scalar couplings and initial frequency estimates. Peak amplitudes were corrected for partial saturation and blood contamination [81, 188].

5.2.6 Statistical analysis

To test repeatability of cardiac Pi/PCr quantification and pH calculation, Bland-Altman analysis of agreement was used to compare the two measurements - the coefficient of repeatability was calculated, as described by Bartlett and is given by the following equation:

$$CR = 1.96 \times \sqrt{2} \times \text{within subject SD} \quad [186]$$

All statistical analysis was performed in GraphPad Prism v6.01 (GraphPad, La Jolla, CA, USA). Results are given as mean ± SD. Comparisons between rest and stress values (where available) for pH and Pi/PCr were undertaken using paired Student's *t*-tests.

5.2.7 Signal to noise (SNR) changes during stress; dealing with unpaired results

I sought to undertake a paired analysis of the effect of stress on Pi/PCr. Myocardial [Pi] is extremely low, thus any small loss of SNR during the stress scan may impact my ability to quantify it. Loss of SNR during stress (such as that which would occur with coil displacement) can be assumed to affect both interleaves equally. Restricting stress data to only pairs with clear evidence of the Pi peak (defined as SNR >2.5 and visually obvious), may thus bias a result toward underreporting lower Pi/PCr values, missing any changes from or to un-recordable levels. To avoid this, in the event of only one of the two data points (stress / rest) containing an easily defined Pi peak (defined as SNR >2.5 and visually obvious), a maximal Pi amplitude that would still not be determined above the noise floor was estimated and used to compute Pi/PCr, if the overall scan SNR (judged using an arbitrary PCr SNR threshold of > 35) warranted this. This would avoid missing a change, but would also prevent the reporting of an exaggerated change as a maximal estimate for Pi/PCr is used. This estimate was always taken from the fit generated in AMARES within the resonance frequency of interest. Such

estimations cannot provide Pi resonance frequency with adequate certainty and are hence not used for pH computation.

5.3 Results

5.3.1 Repeatability

Intra-subject repeatability was assessed in 9 healthy volunteers (2 female, age 37±9). Of the 18 scans undertaken, Pi was clearly resolved (defined using the above criteria) in 17. In the one scan without unequivocal Pi resolution, overall scan SNR was sufficient to justify Pi/PCr upper bound estimation (as per the above criteria – PCr SNR in this case was 58). This pair of scans was not included in the pH repeatability analysis given uncertainty of the chemical shift of the Pi resonance. A table of results for the repeatability studies is shown in Table 8. No significant differences were seen between scans one and two for Pi/PCr (0.100±0.035 vs. 0.099±0.029 p=0.93 [n=9]) or pH (7.06±0.05 vs 7.04±0.06 p=0.52 [n=8]).

Table 8: Repeatability results in healthy volunteers

Participant		**Measurement 1**				**Measurement 2**			
Sex/Age	BMI	Pi Amp*	PCr Amp	Pi/PCr	pH	Pi Amp	PCr Amp	Pi/PCr	pH
♂ (52)	24.9	15.9 (18.8)	133.6	0.142	6.99	12.9 (4.8)	131.6	0.117	7.02
♂ (35)	22.3	6.4 (12.0)	88.9	0.086	7.05	6.0 (7.8)	94.0	0.076	7.00
♂ (29)	28.1	5.2 (5.8)	93.6	0.066	7.04	6.4 (7.0)	108.4	0.070	7.10
♂ (32)	23.8	3.9 (2.2)**	57.8	0.079	*6.92#*	6.5 (5.2)	64.4	0.121	7.03
♂ (37)	24.5	13.3 (10.6)	151.7	0.104	7.06	13.3 (13.8)	154.9	0.102	7.11
♂ (35)	24.0	6.2 (11.0)	118.4	0.062	7.01	5.8 (9.7)	114.2	0.060	7.06
♀ (25)	22.1	8.3 (9.3)	72.3	0.137	7.15	8.9 (8.0)	68.9	0.154	7.11
♂ (48)	24.0	6.5 (8.7)	105.9	0.073	7.12	8.8 (9.3)	105.5	0.099	6.94
♀ (45)	19.5	8.8 (5.4)	68.5	0.152	7.05	5.6 (8.7)	71.8	0.092	6.98
Mean				0.100±0.035	7.06±0.05			0.099±0.029	7.04±0.06

**Pi amplitude (amp) is given with corresponding SNR given in brackets. ** Pi peak not robustly resolved, # pH estimate drops out of the subsequent calculations due to uncertainty in the chemical shift of the Pi resonance.*

The 95% limits of agreement were ±0.058 (Pi/PCr) and ±0.16 (pH). The coefficient of repeatability for Pi/PCr was 0.041 and that for pH 0.12. Results are demonstrated in a Bland-Altman plot in Figure 45; solid lines demonstrate the bias from 0 (scan 1 – scan 2), dashed lines represent limits of agreement representing ± 1.96SD. A typical pair of spectra is shown in Figure 46.

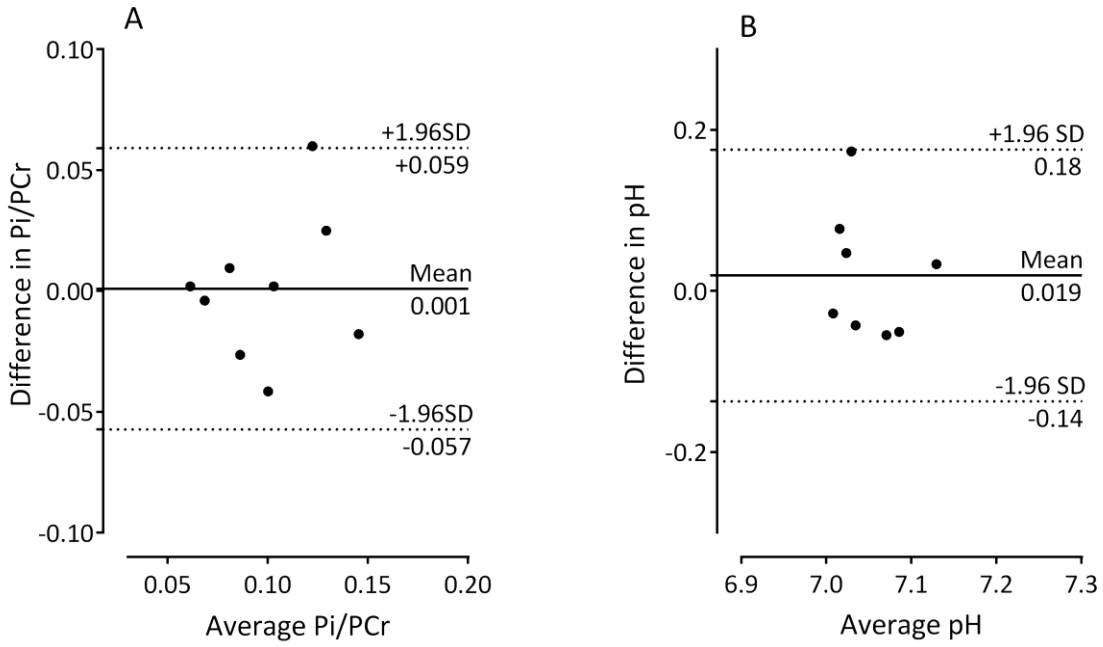


Figure 45: Bland Altman plots for repeatability of Pi/PCr and pH

Solid lines demonstrate bias (scan 1 – scan 2, ideally 0). Dashed lines represent the limits of agreement that is, representing ± 1.96SD. The coefficient of repeatability for Pi/PCr was 0.41, and was for pH 0.12.

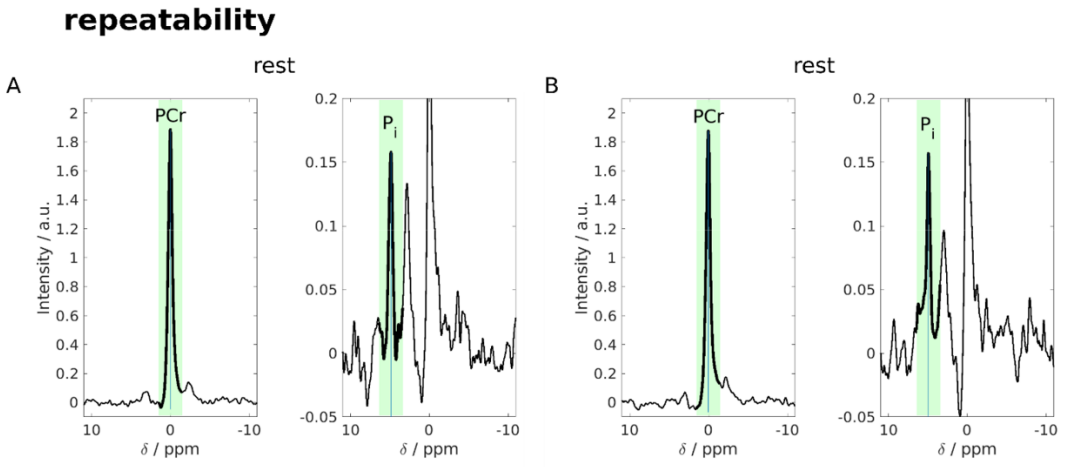


Figure 46: Pair of STEAM-^{31}P MRS spectra from the repeatability study

STEAM-^{31}P-MRS data from a healthy volunteer in the repeatability. The STEAM acquisition was repeated at rest after a short interval. Again, the spectral region to be trusted is that immediately surrounding the metabolite excited marked by bolder lines and green background.

5.3.2 Resting myocardial energetics and pH in healthy controls

21 healthy volunteers (8 female, age 39±15, BMI 23±2 kg/m^2) were recruited. Mean blood and saturation-corrected PCr/γ-ATP was recorded successfully in 19/21 of this group and was 2.13±0.45. All participants underwent STEAM-^{31}P-MRS at rest. Mean PCr SNR was recorded as 74±42. Pi had a lower signal, as expected, due its lower myocardial concentration. I was able to robustly resolve the Pi peak (by visual inspection and SNR >2.5 – as per the above criteria) in 18/21 (86%) of subjects, mean SNR for these Pi peaks was 6.3±3.8. Average acquisition duration was 15.2±0.9 minutes, 2,3-DPG was not visible in any of the STEAM-^{31}P-MRS spectra (including in the three rest scans without adequate Pi resolution). Considering the 18 spectra with unambiguous Pi peak quantification, mean resting Pi/PCr was

0.095±0.030 and myocardial pH 7.07±0.08. In this healthy population Pi/PCr showed a significant positive correlation, with resting PCr/γ-ATP (R=0.52, R^2 0.27, p = 0.04, Figure 47).

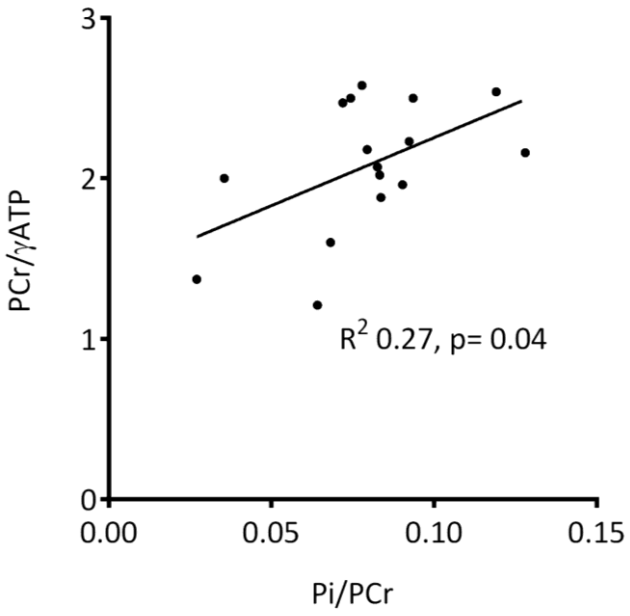


Figure 47: Correlation between markers of resting energetics

In this healthy population resting Pi/PCr (0.095±0.030) showed a significant positive correlation with resting PCr/γ-ATP (2.13±0.45, R^2 0.27, p = 0.04).

5.3.2 Dobutamine stress in healthy controls

20 of the 21 healthy controls underwent successful STEAM-^{31}P-MRS at stress (one scan was aborted due to a failure of the blood pressure monitoring system mid-way through the scan). All patients irrespective of Pi resolution at rest were given intravenous dobutamine since the hypothesis was testing whether [Pi] may rise during stress as part of the metabolic control of oxidative phosphorylation. This is the first report of the administration of dobutamine at high field strength, and all dobutamine infusions were well tolerated without incident. During stress, mean RPP [mmHg/min] rose over 2-fold (from 7,337±1,470 to 15,775±2,052, p<0.001),

with mean heart rate (min^{-1}) increasing from 61±10 to 105±10 ($p<0.001$). Individual values for each participant can be seen in Table 9, with RPP changes demonstrated Figure 48A, and HR changes shown in Figure 48B.

Table 9: RPP and HR changes during dobutamine infusion

Participant	Rest		Stress	
	RPP (mmHg.BPM)	HR (bpm)	RPP (mmHg.BPM)	HR (bpm)
1	6477	53	15435	111
2	7320	62	17953	127
3	10332	82	17006	123
4	8001	60	18238	118
5	8928	70	20179	110
6	5418	44	16632	92
7	5280	50	16095	96
8	6148	52	15534	103
9	9472	71	-	-
10	6400	61	17057	100
11	8400	70	15153	101
12	8960	80	13552	110
13	6018	50	11734	100
14	7015	64	15694	98
15	6850	53	14070	110
16	6900	62	16828	95
17	6380	64	15314	102
18	6960	60	12048	86
19	9940	71	17624	110
20	6820	55	14544	100
21	6055	52	14805	98
Group Mean	**7337 ± 1470**	**61 ± 10**	**15775 ± 2052**	**105 ± 10**

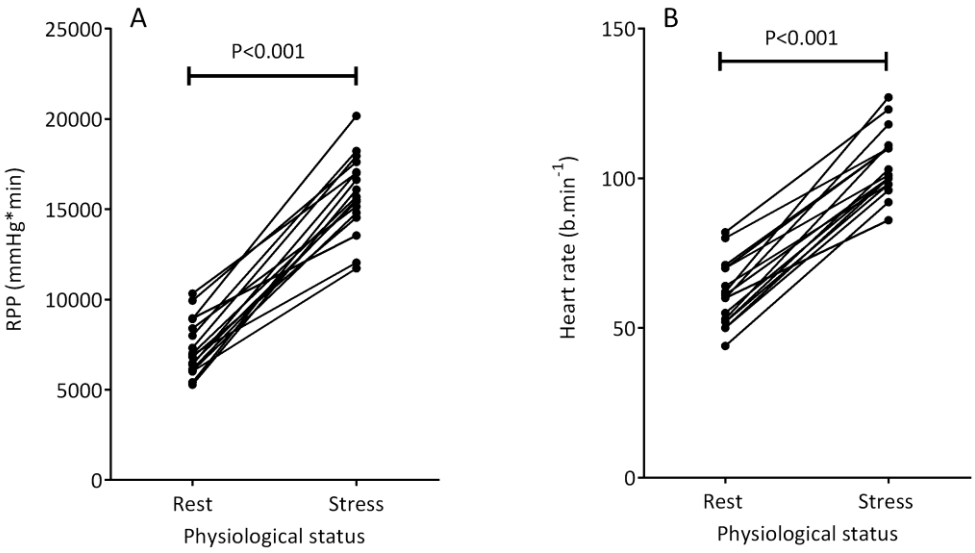


Figure 48: RPP changes during stress in a healthy cohort

As was expected, dobutamine resulted in a significant increase in both the RPP (A) and heart rate (B)

Using the above-described criteria for the resting state spectra, Pi was adequately identified in 16 of the 20 stress scans (stress Pi/PCr 0.094±0.031, pH 7.08±0.11). A typical pair of rest (Figure 49A) and stress (Figure 49B) spectra are also shown. Of the four stress scans that I was unable to resolve Pi robustly, two had correspondingly poor SNR in the rest scan, in the other two Pi could not be seen during stress despite clear resolution at rest. However, in both these cases SNR loss during stress was catastrophic (such as can occur during coil movement) and as such upper bound estimation for Pi was not justified as per our defined criteria of PCr SNR (in both these PCr SNR was reduced to < 14 during stress).

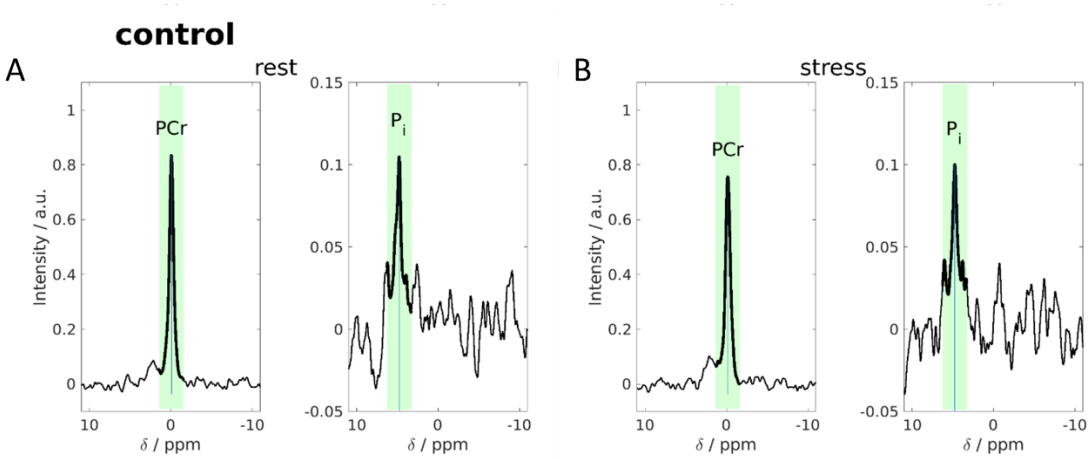


Figure 49: Typical spectra from stress studies

STEAM-^{31}P-MRS data from a healthy volunteer during rest (A) and during dobutamine stress (B). Again, the spectral region to be trusted is that immediately surrounding the metabolite excited marked by bolder lines and green background.

In one case Pi was resolved during stress, but not clearly during rest, here however PCr SNR justified upper bound estimation (SNR 37); this was computed in AMARES and the corresponding Pi/PCr ratio pair included. More details of the data included in each analysis for both the results sections of this chapter can be found in the appendix.

5.3.4 Effect of dobutamine on myocardial Pi/PCr and pH

In this healthy cohort, Pi/PCr was not significantly different during stress (0.093±0.032 [rest] vs 0.094±0.031 [stress], p=0.79,

Figure *50*A, C). As expected, pH did not change (7.09±0.07 [rest] vs 7.08±0.11 [stress], p=0.96,

Figure *50*B, D). The red dot denotes Pi/PCr derived from an upper bound estimate (above the noise floor) for Pi computed in AMARES, given sufficient overall scan SNR (PCr SNR > 35). Data handling in this chapter can be found in the appendix.

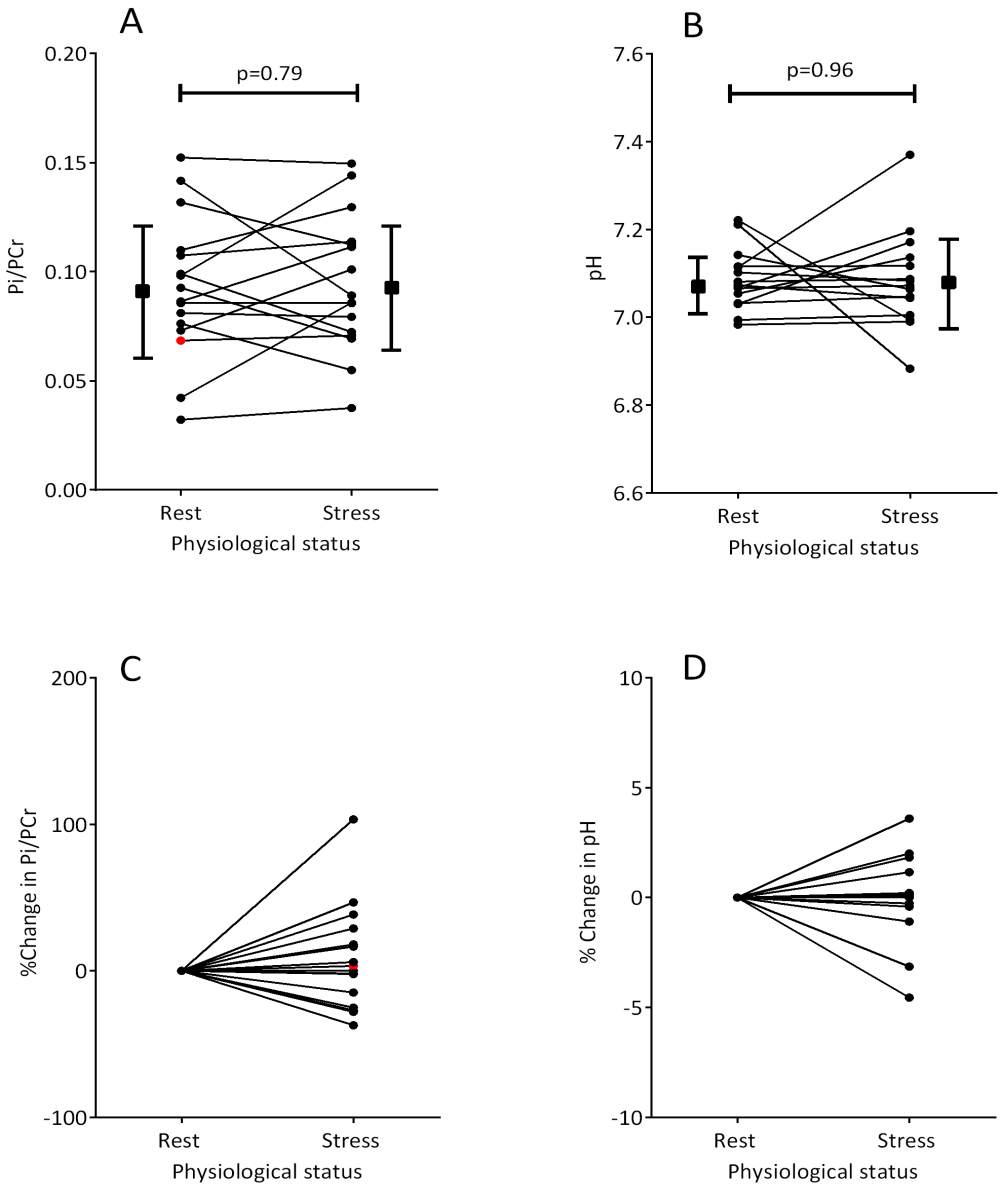


Figure 50: Myocardial Pi/PCr and pH during stress in healthy controls

Myocardial Pi/PCr did not change during dobutamine stress in this healthy cohort (A,C), similarly pH also did not change (B,D). The red data point (A), denotes an upper bound estimate for Pi/PCr as computed in AMARES, justified here given good overall scan SNR (PCR SNR > 35).

5.4 Discussion

STEAM-^{31}P-MRS at 7T generated dark-blood contrast with sufficient SNR to allow Pi peak resolution and quantification. In contrast to the methods previously described (Figure 42) this is the first study to report a human, cardiac in vivo Pi peak, with minimal 2,3-DPG contamination. The scan length (14.8±1.3 minutes) also meant that Pi/PCr estimation was also uniquely feasible during dobutamine stress; this study was the first to perform catecholamine stress during MR examinations at 7T.

5.4.1 Resting energetics and pH

The resting state PCr/γ-ATP I recorded in those recruited to the stress study (2.1±0.5) is not different to recently published values in controls at the 7T field strength of 2.1±0.2 [109] and 1.9±0.4 [82], confirming the population studied to have myocardial energetics in the normal range (as defined by this method). With STEAM-^{31}P-MRS, I recorded myocardial pH (7.07±0.08) to be more acidic than blood (7.35-7.45) [189]. This is consistent with the pH recorded employing both UTE-CSI with long T_R [7.12±0.04; [109]], and ^{1}H decoupling techniques [7.08±0.03 [110]] to record the Pi resonance and its chemical shift with respect to PCr (experiments at 7T and 1.5T respectively). Similarly Pi/PCr recorded by STEAM-^{31}P-MRS in this healthy cohort (0.095±0.030) agrees with that reported using these techniques (0.097±0.072 [110] / 0.11±0.02 [109]).

5.4.2 Resolution of Pi with STEAM-^{31}P-MRS

Unlike PCr and ATP which have estimated free cellular concentrations of 11±2.7 µmol/g and 6.9±1.6 µmol/g (3-5mM) wet weight respectively in resting muscle [2, 37], [Pi] is much lower,

in the range of ~0.8 µmol/g wet weight [19, 37]. Anatomic variability in cardiac ^{31}P-MRS experiments leads to a wide variation in SNR between individuals, thus despite 2,3-DPG suppression in some cases Pi could not be defined due to low SNR. This was the case in 4 of the total 39 rest scans done in this study (~10%). These four cases had lower PCr SNR (29, 37, 35, 41) compared to the group average of 92. Any significant loss of SNR during stress, further hampered my ability to define Pi especially in those with poor SNR at baseline, since no significant rise in Pi/PCr during stress was seen. A fall in SNR during stress was seen in some volunteers which was likely to be due to extra motion (cardio-respiratory and possibly participant restlessness). Pi/PCr however was not affected by this phenomenon, given both interleaves can be presumed to be equally affected. The chemical shift of the peak and thus pH is also unaffected. In the present study, with no change in Pi/PCr seen during stress, any small change in scan SNR in some cases had a large impact. It should be noted, however, that assessment during stress may uncover latent energetic deficits which manifest in very large movements at higher workloads. In these cases, clear-cut resolution of Pi may be obvious only during stress (previously unachievable due to the scan duration of existing methods). In the rare event of Pi not being demonstrable in the corresponding rest scan due to low SNR, a maximum estimate for Pi/PCr generated in AMARES (given adequate PCr SNR) allows the stress response to be quantified but not overestimated. In short, SNR insufficient to robustly resolve Pi may become irrelevant when it matters most; when pathology is encountered which can be hypothesised to cause a rise in resting Pi/PCr and clear-cut increases during stress. This is explored further in chapter 6.

5.4.3 Stress Pi/PCr, and the control of oxidative respiration

Control of oxidative respiration is tight and maintains ATP concentrations through huge variations in cardiac work. Such homeostasis requires the bio-availability of oxygen, reducing equivalents (NADH), and ADP/Pi [10]. Studying Pi thus gives a new insight into the control of respiration and as far as I am aware this is the first reported direct measurement of myocardial Pi/PCr as workload increases in the healthy human heart. The stability reported during incremental cardiac work is similar to the conservation of PCr/ATP seen in healthy human subjects during dobutamine stress [15, 16, 17, 86]. Some may argue that this stability challenges the hypothesis that changes in intracellular Pi are necessary to convey a change in the energy requirement of the myocardium to the mitochondria, to upregulate oxidative phosphorylation. Indeed, an early ^{31}P-MRS experiment in healthy humans in which myocardial Pi was estimated semi-quantitatively by assuming any change to the spectral resonance in the region of 2,3-DPG during stress represents a change in Pi, demonstrated an increase in Pi by some 33% during a 3-fold increase in the RPP [14]. This study (in contrast to those above) also reported a concomitant fall in PCr/ATP. My result is consistent with preclinical work (in open chest dogs) demonstrating stability of Pi as myocardial work was increased by differential cardiac pacing [12, 18]. In these models however, when much higher levels of cardiac stress are induced by high dose noradrenaline combined with pacing, or uncoupling agents of oxidative phosphorylation, detectable rises in Pi begin to occur [11, 12, 184]. In this context, however, instead of representing the physiological control of oxidative phosphorylation, increases in Pi likely represent loss of the steady state as CK flux becomes rate limiting, not surprising at such extreme levels of cardiac work, in an open chest model. This level of cardiac stress is clearly not possible to induce in human studies with healthy volunteers. Open chest animal models also demonstrate the point of stress at which Pi begins

to rise is lowered in conditions such as hypertrophy and heart failure [12, 184]. Consistent with this is a model of human HCM, predicting a three-fold increase in Pi during work in this condition [190]. It is likely that this technique is simply not sensitive enough to detect the small change in [Pi] responsible for energy homeostasis over a physiological range of work, but it may be able to pick up larger changes in Pi that may be seen in patients with impaired energetics during stress. I go on to explore this in the next chapter.

Some have suggested that ADP regeneration by cytosolic CK, not Pi, is the primary effector of increased mitochondrial respiration [37]. However, free ADP is too low to be quantified non-invasively (<1mM [79]), and regardless, Pi (the other product of ATP hydrolysis) can be considered a good proxy. Nevertheless, various recent in-silico models harnessing all available data as their inputs, agree that together, Pi and ADP feedback to convey alterations in the rate of ATP hydrolysis to the mitochondria, increasing the rate of oxidative phosphorylation [23, 25, 191]. The magnitude of these changes over a physiological work load, in-vivo, are likely out of the realms of detection by ^{31}P-MRS. Corroborating this idea, isolated mitochondria are highly sensitive to extremely small changes in Pi around the cardiac intracellular concentration [10], changes too small to detect by in vivo ^{31}P-MRS under physiological conditions. I have shown in this chapter however that Pi/PCr is stable during a doubling of the RPP in healthy controls indicating that oxidative metabolism is not limiting over this range of work, and that gross changes in Pi/PCr (which would incur a change in cellular ΔG_{ATP}), as seen in skeletal muscle [13], are not implicated in matching ATP production with disposal. Rather unexpectedly in this group, I found a significant positive ($R=0.52, R^2=0.27$, $p=0.04$, Figure 47) correlation between resting PCr/γ-ATP and Pi/PCr. The interpretation of this finding however must not be clouded with the expectation that in pathology Pi/PCr may rise as PCr/ATP falls. These hearts are healthy, at a steady state without

cellular loss of metabolites, and as such a simple explanation would suffice: in health, higher resting Pi levels achieve higher resting PCr concentrations through a higher rate of basal oxidative phosphorylation.

5.4.4 Myocardial pH during dobutamine stress

As we would expect, myocardial pH was demonstrated to be stable during dobutamine stress in this healthy cohort. This was an expected finding during low intensity work in a healthy cohort without coronary artery disease. Independently of Pi/PCr, the non-invasive assessment of pH has huge value given that a fall not only negatively impacts $\Delta G_{ATP,}$ but also results in contractile dysfunction and dysrhythmia [101]. This could prove useful (especially during the transition to stress) to detect the switch to anaerobic metabolism that defines ischaemia. Regional detection of such metabolic changes within the heart in distinct myocardial segments could be possible when combining the technique with a ^{31}P-MRS body coil which gives circumferential ventricular signal [192].

5.4.5 Pi, CK flux and glucose metabolism

With animal evidence that impaired CK flux raises Pi [50], and recent observations that CK flux itself becomes impaired in heart failure [42, 100], this technique may be convenient to measure latent energetic deficits in CK which may only be exposed during stress (with a loss of the steady state early during exertion). Various observations also suggest that Pi/PCr could be a more sensitive marker of early energetic dysfunction, preceding any changes in PCr/ATP. In canine models of ventricular hypertrophy, Pi/PCr changes earlier and with greater magnitude than PCr/ATP during incremental work induced by pacing and/or dobutamine [12,

193]. Similarly in a porcine model of hypertrophy, increasing the rate of oxygen consumption using the decoupling agent Dinitrophenol quickly increases Pi/PCr in the face of early PCr/ATP stability [184]. Resting Pi has been observed to be raised in the hypertrophied ex-vivo perfused rat heart [65], and thus it could be hypothesised to directly signal the increased glucose oxidation seen in early heart failure [1] given that Pi activates the glycolytic enzyme phosphofructokinase and glycogenolysis [65, 194]. Furthermore, with cellular loss of PCr *and* ATP as seen as heart failure progresses [93, 195], Pi/PCr may be more closely aligned to the degree of energetic dysfunction in more advanced disease, underestimated by (a potentially pseudo-normal) PCr/ATP.

5.4.6 Comparison with other techniques and limitations

Recently, Pi was demonstrated using a long-T_R CSI protocol [109] giving a favourable balance of myocardial Pi to blood 2,3-DPG signal intensity. Here, unlike with STEAM in which any residual 2,3-DPG was indistinguishable from the noise floor, 2,3-DPG peaks (as in ^{1}H decoupling techniques in the 1990s) are still present and obscure Pi. Having said this, suppression is difficult in MRS with nothing ever 100% suppressed, but with 2,3-DPG being an almost exclusively blood born red cell metabolite, STEAM suppresses 2,3-DPG better than existing techniques and its use represents progress in in-vivo Pi quantification. Further potential drawbacks of STEAM-^{31}P-MRS should also be considered. The approach was unique in suppressing signals from moving compartments, making it susceptible to some diffusion weighting. With a b-value of 30 s/mm^2 this, however, would lead to less than 5% proton signal attenuation given the myocardial diffusivity of 1.43 x 10^{-3}mm^2/s [196], which would be lower for intracellular Pi and PCr. STEAM also has an inherently lower SNR than other techniques as

the signal is formed from a stimulated echo rather than a spin echo. Spoiling gradients are an essential part of STEAM to remove residual unwanted magnetization (spurious FIDs and spin echoes) and were employed after each of the three pulses. These introduce motion sensitivity, and further adjustment of the spoilers could potentially improve SNR in future work.

Although corrected for the effect of T1 partial saturation, this Pi data is not corrected for T2 relaxation as to date this has not been measured in the heart. However if this is assumed to be similar to skeletal muscle [197], only a very small underestimate in the ratios would result. Some considerations also arise with the large single voxel used for STEAM-^{31}P-MRS. Despite estimating transmit efficiency and adjusting coil voltages for each participant, inevitably some variation in flip angle (20-30%) will result over the voxel, this is however a constant and impossible to avoid.

STEAM-^{31}P-MRS was free breathing, but the large voxel makes uniform coverage of the septum more likely throughout the respiratory cycle. Contamination by surrounding structures is also more likely however, but retrospectively collecting only spectra acquired at the end of expiration would increase scan time to such an extent that studies during stress would no longer be feasible (this was attempted in preparatory work). Similarly, improving Pi SNR at rest by adding averages to reduce the observed failure rate from 10% would increase the scan time and thus patient dropout rate for paired studies.

5.6 Conclusion

7T STEAM-^{31}P-MRS can measure cardiac Pi/PCr and pH, at rest and during catecholamine stress, clearly resolving the Pi peak with suppression of 2-3 DPG. I have demonstrated stability of myocardial Pi/PCr and pH during stress, and will use the sequence to investigate cardiac energetics in more detail in a range of pathologies in chapter 6, as part of a broader strategy to build toward computation of ΔG_{ATP}.

Chapter 6. Investigating Pi metabolism in the diabetic and cardiomyopathic heart; a step closer to ΔG_{ATP}

Work in this chapter was presented at SCMR 2020, and shortlisted for the young investigator award. The work has also been presented orally at ISMRM 2020, and won the magna cum laude merit award. The work is in preparation for publication.

6.1 Introduction

This chapter aimed to:

1) Record myocardial pH and Pi/PCr at rest in both diabetics and patients with DCM and compare these values to controls.
2) Record the response of Pi/PCr to dobutamine stress in both diabetics and DCM, and compare this to controls.
3) Explore correlations between abnormal resting diastolic function in diabetes and resting Pi/PCr. An inverse relationship can be hypothesised since higher Pi reduces ΔG_{ATP}.
4) Explore any relationships between the degree of structural abnormality in the DCM cohort and the Pi/PCr response to stress.

The utility of STEAM ^{31}P-MRS as a technique to quantify Pi and myocardial pH was demonstrated in chapter 5. This chapter aimed to use the technique to gain a deeper understanding of the reduced PCr/ATP and impaired cardiac energetics demonstrated in the diabetic cohort in chapter 4, which has also been demonstrated by other groups [15, 149]. I go on to use the technique to study both rest/stress Pi/PCr in a group of patients with DCM. I chose this group for further study since the condition is typified by not only a reduced PCr/ATP [85, 86] but also impairment of CK flux as recorded by various saturation transfer studies [42, 88]. With an increase in Pi modelled to be a consequence of impaired CK flux [50], studying a condition typified by abnormal CK flux with this technique seemed scientifically valid.

6.1.1 The emergence of diabetic cardiomyopathy

Diabetes is a global health emergency and the myocardial consequences of chronic diabetes are numerous with risk extending beyond its well-established role as a vascular risk factor. The diabetic heart is subject to a variety of structural changes with progressive concentric remodelling and interstitial fibrosis occurring in the absence of hypertension [119, 198]. Progression is almost ubiquitously through an asymptomatic phase of diastolic dysfunction [120] which culminates in diabetic cardiomyopathy defined as the onset of systolic heart failure in the absence of causative coronary artery disease, hypertension, or valvular heart disease [198]. There is a pressing need to understand the molecular mechanisms contributing to these processes [15]. The presence of diastolic dysfunction doubles the five year risk of heart failure in diabetes [199]. Impaired relaxation is a common finding as the heart ages, and is reported in 15% of those over the age of 65 with no significant medical history or symptoms [200]. Unlike in such controls however, in subjects with diabetes the finding confers a significant prognostic disadvantage [201]. The expansion of the extracellular volume and fibrosis resulting from adverse concentric remodelling has been quantified by CMR and is shown to correlate directly with increased mortality and hospitalisation events [202, 203].

6.1.2 Progression toward cardiomyopathy is likely multifactorial

Concomitant to the evolution of structural heart disease in diabetes there is an increasingly characterised pathological metabolic and biochemical phenotype. Elevated circulating free fatty acids leads to fat deposition within the myocardium, as was demonstrated using ^{1}H spectroscopy in chapter 4. Lipotoxicity and glucotoxicity lead to oxidative stress and generation of reactive oxygen species, with a subsequent reduction in nitric oxide

bioavailability resulting in reduced signalling through protein kinase G and impaired relaxation. Secondly, microvascular inflammation is triggered with recruitment and activation of macrophages which in turn activate fibroblasts through production of Transforming growth factor-β. Fibrosis and adverse concentric remodelling result, which drive progression toward diabetic cardiomyopathy. These pathways are extensively reviewed [204]. Signalling through PPAR-α [75] is also upregulated mediating a pathological switch in substrate preference, upregulating the Beta-oxidation of fatty acids and reducing myocardial uptake and oxidation of glucose [78, 205]. Blunted flux through PDH in the diabetic heart was the primary outcome of the hyperpolarised experiments in chapter 4 [206], this is discussed in more detail in 4.1.2. Reductions in PCr/ATP, exacerbated by cardiac work also characterises the disease [15, 149]. The degree of energetic impairment correlates with circulating free fatty acid concentrations and systolic strain [149]. Mechanistic causation between pathological energetics, substrate preference, and progressive diastolic impairment is however lacking. Indeed, the exact role and contribution of all of the changes described above in driving the evolution of diabetic cardiomyopathy is unknown.

6.1.3 Impaired energetics and diabetic cardiomyopathy

Various observations in the rat heart challenge the notion that changes in HEP metabolism may be a precursor to meaningful functional changes. Tissue extracts from the diabetic rat heart have shown normal [PCr] and [ATP] with heart failure impairment being rescued with DCA suggesting primarily substrate level changes playing a key role in the pathogenesis of the contractile dysfunction [207]. K_f in the diabetic rat heart has been shown to be increased [208] such that CK flux and ATP delivery is maintained perhaps compensating for the reduction in

PCr/ATP, and loss of CK isoenzymes [209]. However, in compensated human severe aortic stenosis in patients with preserved left ventricular systolic function, a significant reduction in CK flux is seen, no different to that recorded in patients in whom ventricular function was reduced [210]. A similar reduction is seen in humans with only a mild degree of heart failure [42], suggesting that the CK system may at least contribute to heart failure progression. Invasive quantification of cardiac PCr, ATP, CK, and data on CK flux in humans with diabetes is not available. However, these observations make the search for any direct causation between impaired energetics and diabetic cardiomyopathy more pressing. Fundamental to understanding how impaired energetics may lead to mechanical dysfunction in the diabetic heart is computation of ΔG_{ATP}, with correlation between PCr/ATP and ΔG_{ATP} unproven. In the healthy heart ΔG_{ATP} is ~-60kJmol^{-1}, and each ATPase within the cell has a unique value of ΔG_{ATP} above which the reaction becomes thermodynamically unfavourable and halts. These values are -52 and -46 for SERCA2A (calcium handling) and the myofibrillar ATPases respectively [211], thus it is calcium handling which is the most susceptible to any reduction in ΔG_{ATP} [212]. With active calcium sequestration in the sarcoplasmic reticulum during diastole a requirement for ventricular relaxation, and the myofibrillar ATPase required for systolic contraction, it could be hypothesised then that a progressive drop in absolute ΔG_{ATP} could account for the stepwise progression from diastolic to systolic dysfunction. Three measured components (ATP, ADP and Pi) are needed to calculate ΔG_{ATP}, alongside ΔG^0_{ATP} at standard conditions (-32.2 kJ/mol), the gas constant, R (8.3 J/mol/K), and the temperature in Kelvin, T. The equation is given as:

$$\Delta G_{ATP} = \Delta G^\circ_{ATP} - \mathrm{RT} \ln \frac{[ATP]}{[ADP][Pi]}$$

Free ADP concentration is too low to be estimated from ^{31}P-MRS. It can however be estimated by rearranging the CK equilibrium reaction, using a creatine concentration recorded during ^{1}H spectroscopy [213] and CK velocities measured during saturation transfer experiments [42].

6.1.4 Impairment of CK flux in DCM, and the potential impact on Pi and ΔG_{ATP}

The energetic metabolic phenotype of DCM is better characterised than that of diabetes with cellular loss of creatine, adenine nucleotides [91], and impairment of CK flux [42] demonstrated. A rise in Pi under resting conditions has been modelled to follow this impairment of CK flux [50], and with recent evidence that CK flux is adaptive to exercise in health [40], explosive rises can be hypothesised to occur during stress in this condition, deleterious to ΔG_{ATP}. Pi is predicted to increase over 3x during exercise in hypertrophic cardiomyopathy (compared to a 1x rise in ADP) by a biophysical model of high energy phosphate metabolism used to predict the energetic response to the inefficient sarcomeric ATP utilisation which characterises the condition. These increases were exacerbated by creatine loss and would increase ΔG_{ATP} by up to 3kJmol^{-1} [190].

With stereotyped progression of diabetic heart disease from initial diastolic to systolic dysfunction, in this chapter I investigated the relationship of Pi, to echocardiographic metrics of diastolic function in these patients. Given further falls in (the already depressed) PCr/ATP demonstrated during stress in the human diabetic heart [15], I also investigated the response of Pi/PCr to stress. With this result in mind, I went on to investigate the response of myocardial Pi/PCr to stress in DCM; a condition characterised by impaired CK flux, here I

aimed to correlate any change in the ratio during stress with the degree of left ventricular systolic impairment as assessed by ^{1}H CMR scanning.

6.2 Methods

6.2.1 Ethical considerations

All scanning and research visits in this chapter were approved by the Bristol Research Ethics Committee (Reference 13/SC/0736), IRAS ID 128163). All participants gave written informed consent to participate had a normal resting 12-lead ECG and normal cardiovascular clinical examination.

6.2.2 Eligibility criteria

Three groups were recruited to this chapter; healthy controls, patients with type two diabetes, and patients with DCM. Specific eligibility criteria are given below.

Healthy controls:

- Aged over 18 years, able to provide informed consent.
- Asymptomatic, with no significant medical history and no regular medications.
- Normal resting ECG and cardiovascular examination.

Patients with stable Type 2 diabetes:

- Aged over 18 years, able to provide informed consent.
- Not on insulin therapy.
- No change in medication for 3 months.
- HbA1c of between 6 and 9%.

- Were excluded if there was a history of cardiovascular, endocrine or neurological disease, pregnancy, uncontrolled hypertension, chronic renal impairment (estimated glomerular filtration rate < 30ml/min/1.73m^2) or undiagnosed chest pain.

Patients with dilated cardiomyopathy:

- Aged over 18 years, able to provide informed consent.
- Patients with known non-ischaemic cardiomyopathy diagnosed by either CMR or an echocardiogram (LVEF < 50%).
- No significant coronary artery disease on perfusion CMR, myocardial perfusion scanning or CT coronary angiography that would increase the risk of dobutamine infusion.

General exclusion criteria (all participants):

- Any contraindications to dobutamine infusion such as severe outflow tract obstruction, recent history of arrhythmia, severe hypertension (>200/100), or active infection.
- Any of the general exclusion criteria outlined in appendix 9.3.

6.2.3 Study population and visits

17 patients with type 2 diabetes (3 female, age 61±7) were recruited to the study. In these patients, an echocardiogram was undertaken for assessment of diastolic and systolic left ventricular function before MRS (see 2.5.3). None of these patients were on SGLT2 inhibitors at the time of enrolment, although this was not a specific exclusion criterion. 22 patients with an established diagnosis of DCM (1 female, age 58.8±15.9 years) were recruited, all of whom received ^{1}H MRI for assessment of left ventricular ejection fraction and mass (at 3T, 2.4.2).

These patients were asked to stop their beta-blockers 48 hours prior to attending for dobutamine stress studies. The healthy volunteers studied in the previous chapter form the basis of the control group used here. Four extra controls were recruited to bring the age of the group up, the two controls that gave no usable data (Pi 18 and Pi 3) are excluded; thus the comparator control group comprises 23 individuals (9 Female, age 43±16). The 7T MRS protocol for all participants in this study was the same as that described in the previous chapter for the healthy controls during stress. UTE-CSI was undertaken for calculation of PCr/ATP, followed by STEAM-^{31}P-MRS at rest and then during dobutamine stress. Details of the dobutamine infusion protocol can be found in section 2.4.5. A study visit flow diagram can be seen in Figure 51.

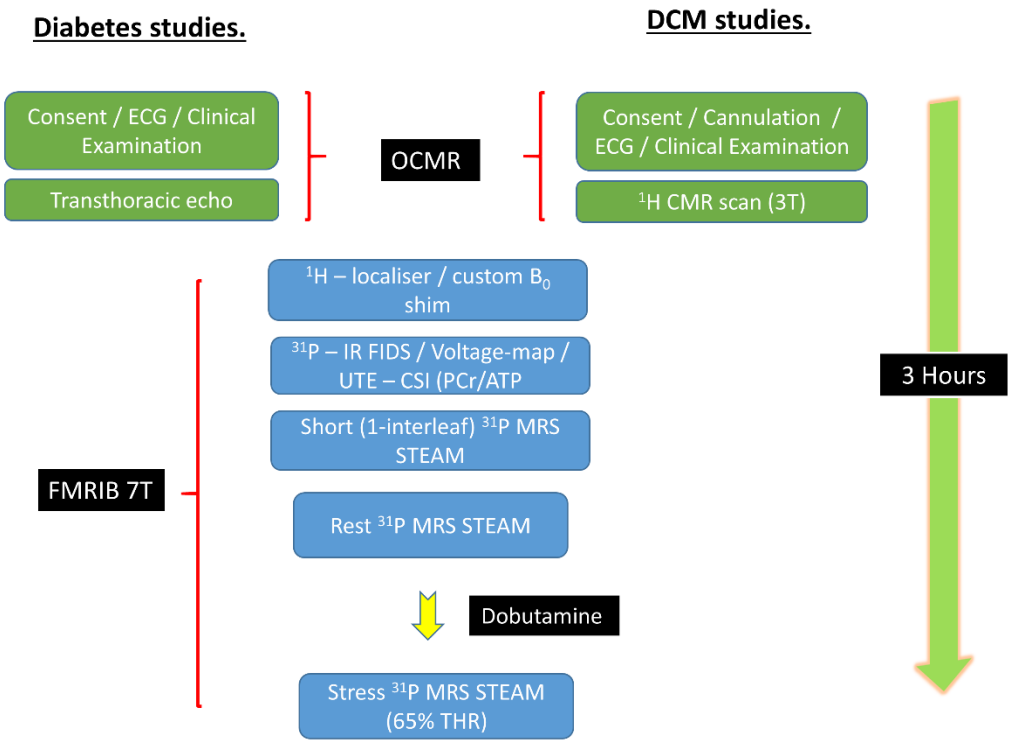


Figure 51: Myocardial Pi/PCr and pH during stress in patients with diabetes and DCM

6.2.4 Data analysis

SNR encountered during MRS is often poorer in patients than controls, and rules described in the previous chapter (5.2.6) for data inclusion in the event of only one of the scans (rest or stress) containing a visually robust Pi peak were again followed. This was important here, as restricting the data to only pairs with clear evidence of the Pi peak (defined as SNR >2.5 *and* visually obvious), may bias a result toward underreporting lower Pi/PCr values, missing any changes from or to un-recordable levels in patients. The method employed ensures a change (in either direction during stress), can be quantified but not overestimated as a maximal estimate for Pi/PCr is used. Spectral fitting and pH calculation are as described previously in 5.2.4.

6.2.5 Statistical analysis

Statistical analysis was performed in GraphPad Prism v6.01 (GraphPad, La Jolla, CA, USA). Results are given as mean ± SD. Paired Student's *t*-tests with equal variance were used to test for significance of change during dobutamine stress after passing testing for normality using the Shapiro-Wilk test, and for between-group homogeneity of variance using Levene's test.

6.3 Results

6.3.1 Baseline population characteristics

Baseline characteristics of all diabetic and DCM patients recruited are shown in Table 10. CMR was not undertaken on diabetic patients or controls. This was not possible at 7T, and the COVID 19 pandemic prevented me from bringing back these patients for an LV stack at 3T.

Table 10: Baseline characteristics of DCM and diabetic patients

	T2DM	DCM	Control	P-value*
Number	17 (3F)	22 (1F)	23 (9F)	
Age (years)	61.4±6.8	58.8±15.9	43±16.4	<0.01
BMI (kg/m^2)	27.1±4.2	25.8±3.7	24.1±2.6	<0.01
HOMA-IR	9.2±3.8 (2.5-3.5)	-	-	
HBA1c (%)	7.2±1.2	-	-	
Total Cholesterol (mmol/l)	3.7±0.9	-	-	
LDL Cholesterol (mmol/l)	2.2±0.6	-	-	
Medication History				
Metformin	17 (100%)	0	0	
Sulfonylurea	5 (29%)	0	0	
SGLT-2 inhibitor	1 (6%)	0	0	
ACE inhibitor	5 (29%)	19 (90%)	0	
Mineralocorticoid antagonist	0	3 (14%)	0	
Statin ± Ezetemibe	11 (65%)	7 (33%)	0	
Aspirin	3 (18%)	3 (14%)	0	
Beta blocker	0	12 (57%)	0	
Calcium channel blocker	0	2 (10%)	0	
Echocardiography				
LVEF (%)	59.3±4.2	-	-	
E/A	0.9±0.2	-	-	
E/e' (medial)	7.8±2.3	-	-	
E/e' (lateral)	5.9±1.9	-	-	
E/e' (average)	6.9±2.0	-	-	
CMR Findings				
LVEF (%)	-	38.7±10.2	-	
LVEDV (mls)	-	249.8±76.3	-	
LVEDVi (mls/m^2)	-	124.2±38.9	-	
LV Mass (gm)	-	158.5±39.8	-	
LV Mass index (g/m^2)	-	80.7±21.3	-	
RVEF (%)	-	54.2±12.2	-	
CAD Exclusion test				
CTCA	-	10	-	
ICA	-	8	-	
CMR	-	4	-	

**group p-value by one way ANOVA.*

6.3.2 Resting Energetics and resting pH

Metrics of resting energetics across all groups studied are shown in tabular form in Table 11, and graphically in Figure 52. As expected, resting PCr/γ-ATP was significantly lower in diabetics compared to controls (1.70±0.31 vs. 2.07±0.39, p<0.01, Figure 52A). In the opposite direction, resting Pi/PCr was significantly higher (0.127±0.050 vs. 0.096±0.028, p=0.03, Figure 52B). Similarly, but not reaching significance in the DCM cohort, PCr/γ-ATP was lower (1.91±0.34 vs. 2.07±0.39, p=0.18), and Pi/PCr higher (0.102±0.034 vs 0.096±0.028, p=0.19) at rest. Resting myocardial intracellular pH was no different across all three groups (7.1±0.12 [controls], 7.14±0.12 [diabetics], 7.04±0.12 [DCM]).

Table 11: Resting energetics in diabetic and DCM patients

	Control	Diabetic	P
PCr/γ-ATP	2.07±0.39	1.70±0.31	<0.01
Pi/PCr	0.096±0.028	0.127±0.050	0.03
pH	7.10±0.12	7.14±0.12	0.31

	Control	DCM	P
PCr/γ-ATP	2.07±0.39	1.91±0.34	0.18
Pi/PCr	0.096±0.028	0.102±0.034	0.19
pH	7.10±0.12	7.04±0.12	0.11

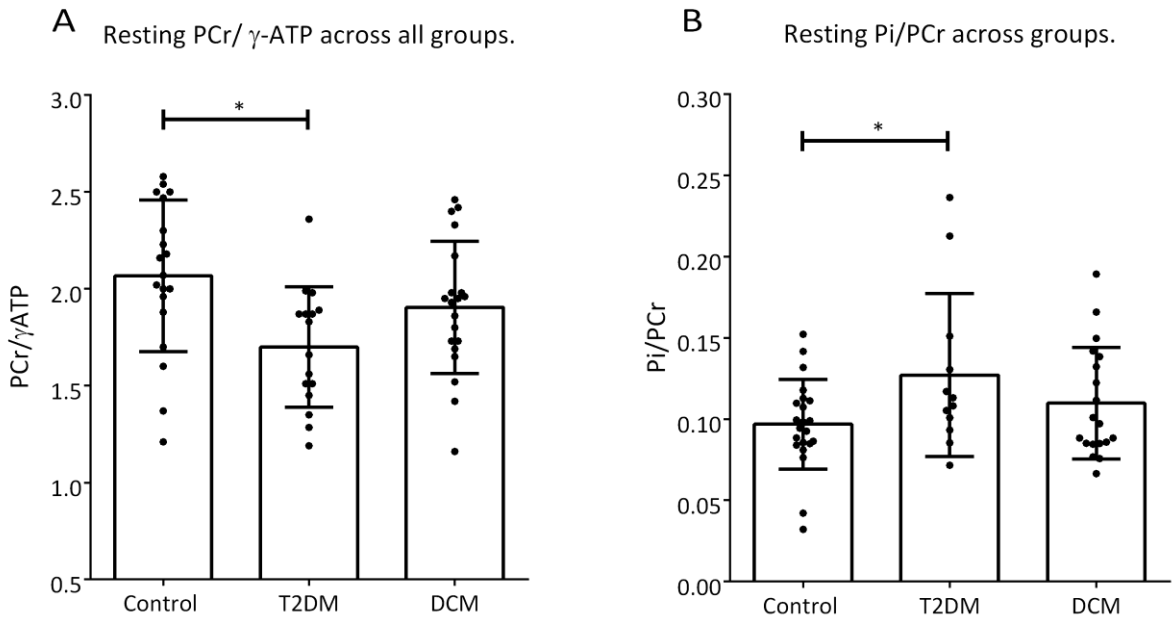


Figure 52: Resting energetics in all participants

Resting PCr/γ-ATP was significantly lower in diabetics (1.70±0.31 vs. 2.07±0.39, p<0.01), and lower in DCM (1.91±0.34 vs. 2.07±0.39, p=0.18) compared to controls (A). Conversely, Pi/PCr was significantly raised in patients with diabetes (0.127±0.050 vs. 0.096±0.028, p=0.03, B)

6.3.3 Dobutamine stress at 7T in a patient population

Rate pressure product changes during dobutamine infusion for all groups can be found in Table 12. In all groups RPP significantly rose during stress. The degree of this rise varied with groups, the rise was no different between controls and patients with DCM, but was lower in patients with diabetes compared to controls. RPP changes for all participants can be seen in Figure 53. Three DCM patients (14%), and five diabetics (29%), did not undergo stress, 1 DCM and 2 diabetics opted to not have dobutamine administered during the consent process, the others stopped the scan due to needing the bathroom or anxiety. Every patient who was commenced on dobutamine safely finished the infusion. One diabetic patient had an ST

segment elevation myocardial infarction 48 hours following study visit, and was successfully revascularized. This was unrelated to the study visit.

Table 12: RPP changes during dobutamine stress in patient studies

	RPP (mmHg/min x 10^2)				
	Rest	Stress	Δ (%)	P (rest vs stress)	P (vs control)
Control	76±17	160±21	111	<0.01	N/A
T2DM	91±12	154±18	70	<0.01	<0.01
DCM	84±23	161±26	92	<0.01	0.32

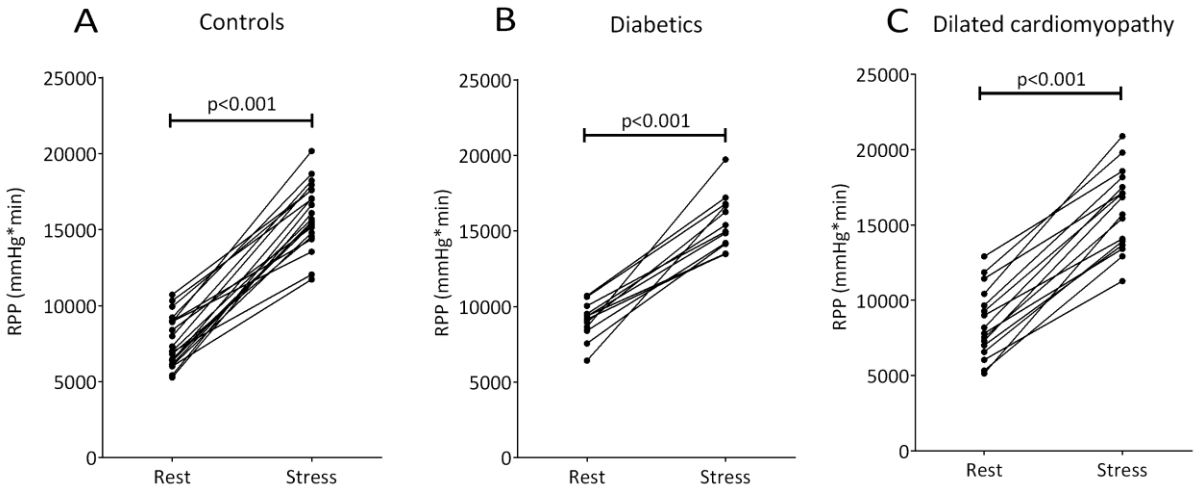


Figure 53: Changes in RPP during stress at 7T in patients

During dobutamine infusion, the rate pressure product significantly increased in controls (A), patients with diabetes (B) and patients with dilated cardiomyopathy (C).

6.3.4 Pi/PCr during dobutamine stress in DCM and diabetes

In this extended control group again no change in Pi/PCr occurred during stress (0.095±0.028 [rest] vs 0.096±0.031 [stress], p=0.95, Figure 54A). During dobutamine stress, Pi/PCr was unchanged in patients with diabetes (0.121±0.049 [rest] vs 0.109±0.046 [stress], p=0.50,

Figure 54B), but rose significantly in patients with dilated cardiomyopathy (0.092±0.031 [rest] vs 0.132±0.076 [stress], p=0.04, Figure 54C).

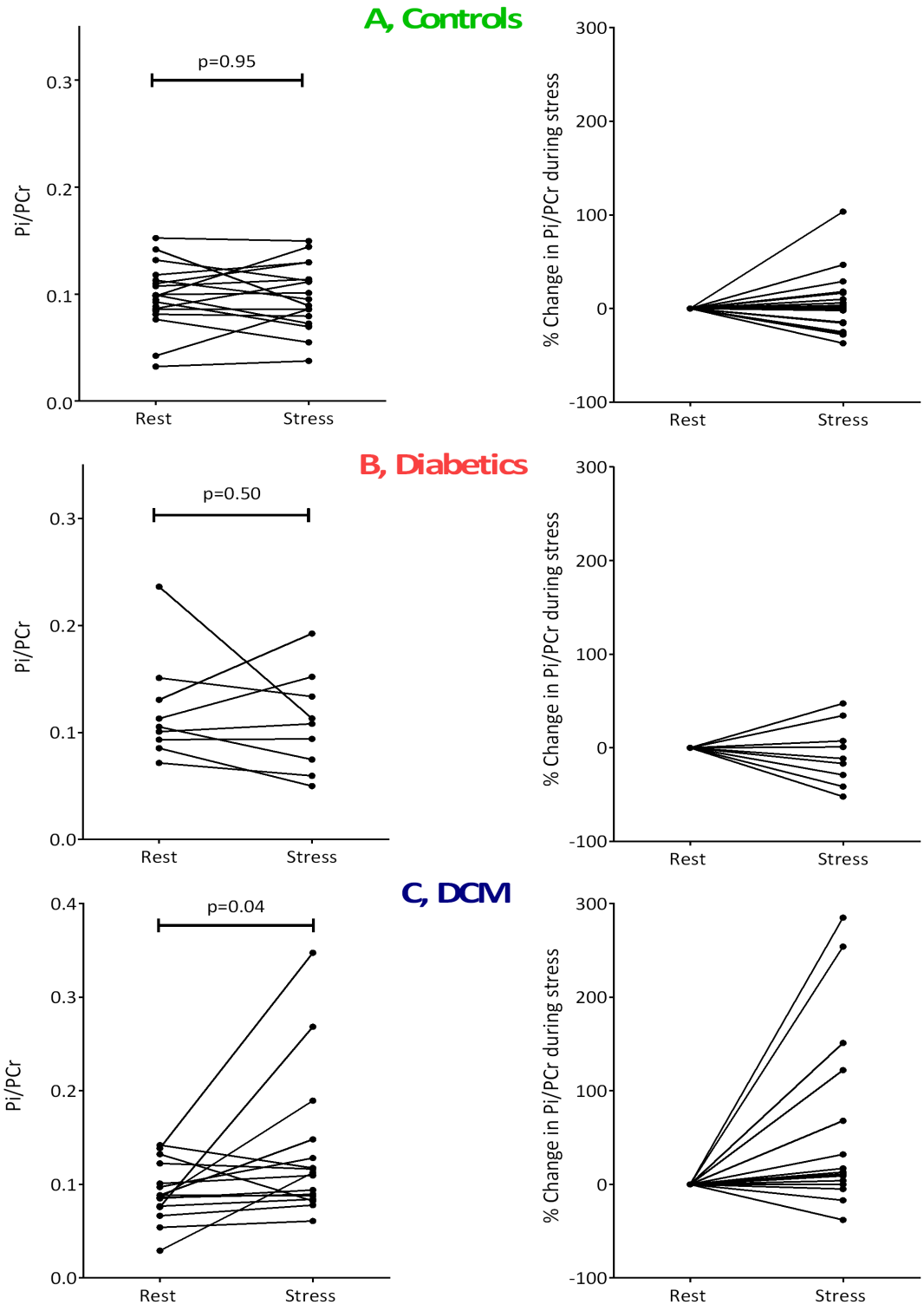


Figure 54: Pi/PCr changes during dobutamine stress

During dobutamine stress, Pi/PCr was stable in controls (0.095±0.028 [rest] vs 0.096±0.031 [stress], p=0.95 [A]), and also in patients with diabetes (0.121±0.049 [rest] vs 0.109±0.046 [stress], p=0.50 [B]), however in the DCM group a significant rise (0.092±0.031 [rest] vs 0.132±0.076 [stress], p=0.04 [C]) was observed.

6.3.5 Intracellular pH during dobutamine stress in DCM and diabetes

As was demonstrated for the healthy controls, myocardial pH was stable during dobutamine stress in patients with diabetes (7.10±0.07 [rest] vs 7.09±0.07 [stress], p=0.77, (Figure *55* A), and DCM (7.06±0.07 [rest] vs 7.08±0.16 [stress], p=0.65, (Figure *55* B). One patient in the DCM group had a marked decrease in pH during stress, although all patients had either a negative functional test or no significant coronary disease at coronary angiography (invasive or CT), it is plausible that this patient may have had undiagnosed ischaemia such as microvascular disease, although there were no reported symptoms suggestive of angina during the dobutamine infusion.

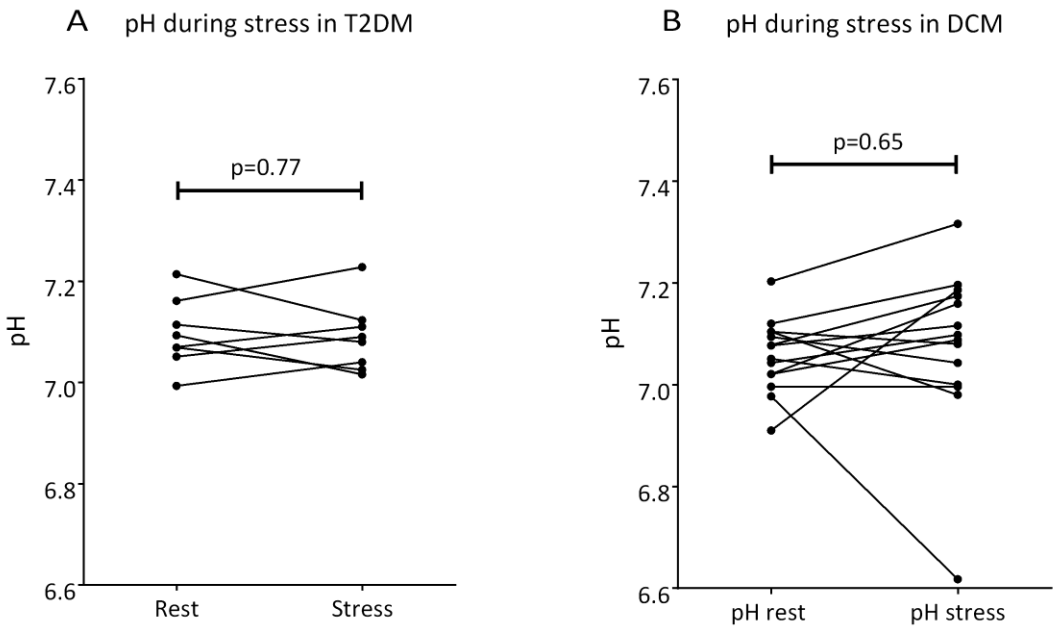


Figure 55: Intracellular pH during stress in diabetic and DCM patients

Myocardial pH was stable during dobutamine stress in patients with diabetes (7.10±0.07 [rest] vs 7.09±0.07 [stress], p=0.77 A), and DCM (7.06±0.07 [rest] vs 7.08±0.16 [stress], p=0.65 B).

6.3.6 Resting energetics and diastolic dysfunction in diabetes

In chapter 5, the normal group demonstrated a positive correlation between Pi/PCr and PCr/γ-ATP (Figure 47), in patients with diabetes no correlation was seen between these (Figure 56A). When plotted against the control group however, diabetic patients can be seen as shifted to higher resting Pi/PCr values, and lower PCr/γ-ATP values (Figure 56B).

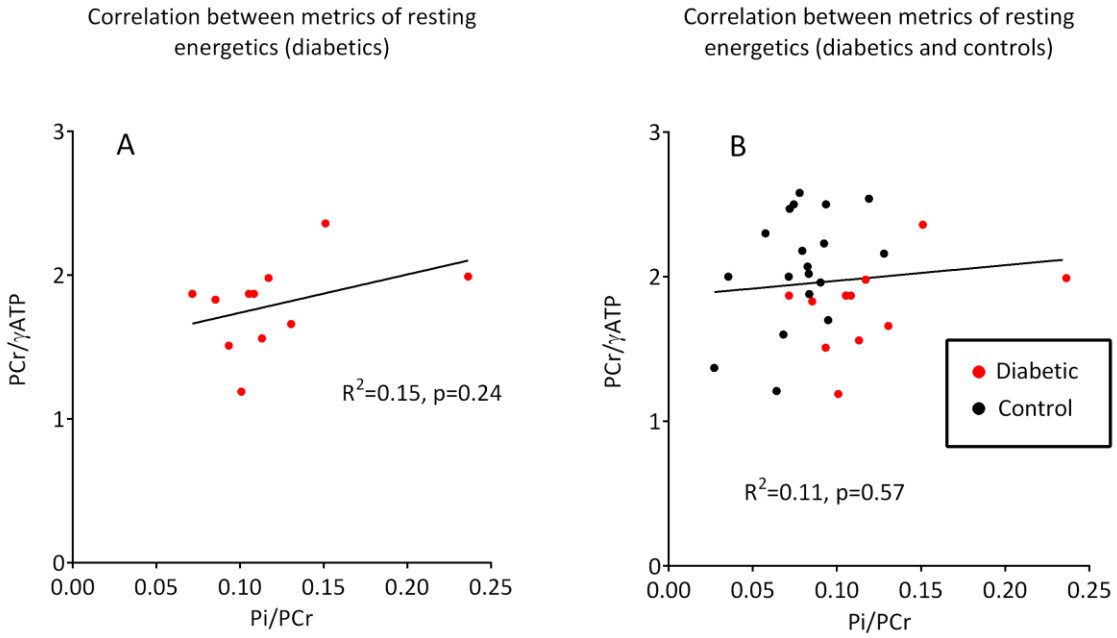


Figure 56: Relationship between metrics of rest energetics in diabetics

In patients with diabetes no correlation was seen between PCr/γ-ATP, and Pi/PCr (A). When plotted against the control group however (B), diabetic patients can be seen as shifted to higher resting Pi/PCr values and lower PCr/γ-ATP values.

Patients with diabetes also underwent echocardiography, the results are shown in Table 10. There was no correlation between Pi/PCr and E/e' $_{mean}$ (R^2 0.08, p=0.43, Figure 57A), but a significant inverse correlation was seen between PCr/γ-ATP and E/e' $_{mean}$ (R^2 0.33, p=0.02, Figure 57B). PCr is not a term in the equation for $\Delta G_{ATP,}$ Pi/γ-ATP may offer a more sensitive marker of the prevailing energetic status over both Pi/PCr and PCr/ATP. Pi/γ-ATP plotted against E/e' $_{mean}$ can be seen in Figure 57C, a weak inverse correlation was seen R^2 0.26, p = 0.12).

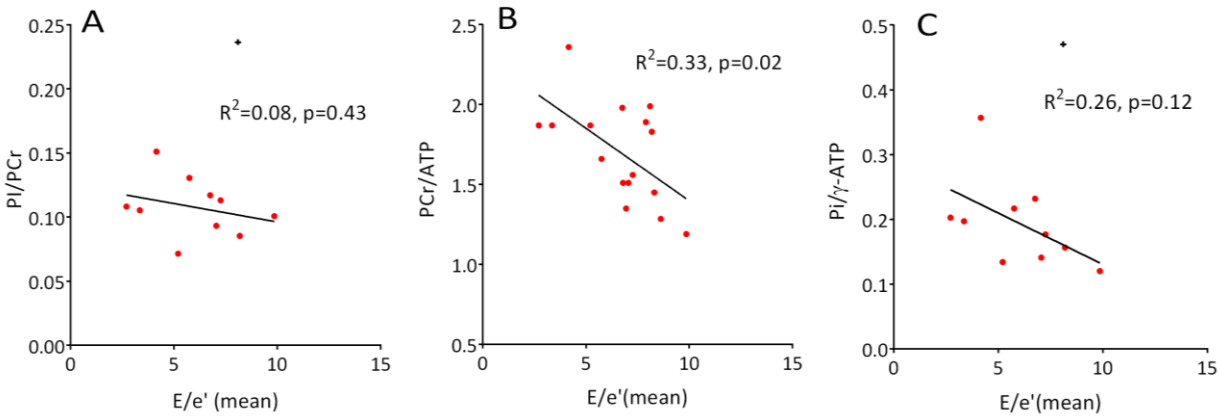


Figure 57: Correlation of diastolic function with energetics in diabetics

Pi/PCr did not correlate with E/e' (A), PCr/γ-ATP however did correlate inversely with E/e' (B). Pi and ATP are both terms in the equation for $\Delta G_{ATP,}$ however this also showed no correlation with E/e' (C). A black cross represents an excluded outlier (Grubbs test p<0.05).

6.3.7 Energetics and Structural heart disease in dilated cardiomyopathy

Grade of systolic dysfunction showed no correlation with resting energetics; LVEF showed no association to either resting PCr/γ-ATP (Figure 58A) or Pi/PCr (Figure 58B), suggesting neither parameter is mechanistically implicated with the functional impairment seen in this disease. The abnormal stress response and pathological rise in Pi/PCr demonstrated was also not

predicted by underlying ejection fraction (Figure 58C), suggesting the mechanism underlying this (a possible candidate being abnormal CK flux) is independent to that driving mechanical dysfunction. Indeed, the two patients with the poorest baseline LVEF recruited to the study (EF<20%) demonstrated no change in Pi/PCr during stress. Correlations between underlying LVEF and Pi/PCr at rest or the magnitude of its change during stress may strengthen if control data is added to these graphs, however neither echo nor CMR was undertaken in the normal cohort so these data are not available. Details of data handling in this chapter can be found in the appendix.

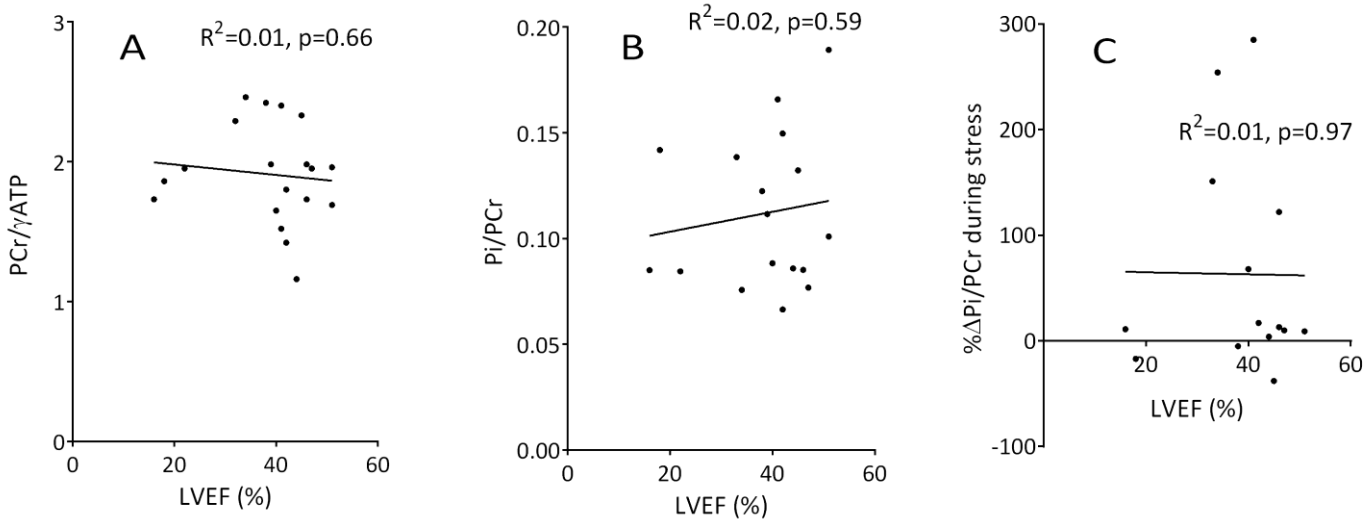


Figure 58: Energetics and stress response according to baseline LVEF in DCM

6.4 Discussion

During chapter five STEAM ^{31}P-MRS was successfully used to measure the Pi resonance with minimal 2,3-DPG contamination. In this chapter, I used this sequence to explore [Pi] both at rest and its response to dobutamine stress in patients with myocardial energetic deficits. As demonstrated in the diabetic cohort in chapter 3, I have again confirmed a reduced resting

PCr/γ-ATP in a type two diabetic cohort, (1.70±0.31 vs. 2.07±0.39, p<0.01) but here I also demonstrated an opposing significant increase in Pi/PCr (0.127±0.050 vs. 0.096±0.028, p=0.03). Diastolic function was recorded in this diabetic cohort and found to be borderline as opposed to frankly abnormal with mean E/e' of 6.9±2.0 (normal range < 8) and E/A of 0.9±0.2 (normal range 1-2). Despite this, PCr/γ-ATP was significantly inversely correlated with E/e' (R^2 0.33, p=0.02), no significant correlation was seen with either Pi/PCr or Pi/γ-ATP. In patients with DCM, I identified a change in both ratios in similar directions to those with diabetes but not reaching significance; Pi/PCr was increased (0.102±0.034 [DCM] vs 0.096±0. 028 [C], p=0.19) and PCr/γ-ATP lower (1.91±0.34 [DCM] vs. 2.07±0.39 [C], p=0.18). The stress response was markedly different in those with DCM; the Pi/PCr ratio significantly rose during stress (0.092±0.031 [rest] vs 0.132±0.076 [stress], p=0.04), this response was not however predicted by the degree of underlying LV systolic dysfunction. Like the control group, in patients with diabetes the ratio did not change during stress (0.121±0.049 [rest] vs 0.109±0.046 [stress], p=0.50).

6.4.1 Pi/PCr in the diabetic heart

Corroborating the findings of others [15, 149], I have confirmed here at 7T, (and in chapter 4 at 3T [206]) that diabetes is characterised by a pathological reduction in the PCr/ATP ratio. This finding has been shown to correlate negatively with plasma FFAs [149], and in these patients may thus be related to the pathological substrate handling in diabetes, with increased FA and reduced glucose oxidation (and transport) [148, 214]. The mechanism behind the reduction in PCr/ATP seen in diabetes is different for that seen in heart failure, where a cellular loss of creatine (and PCr) occurs [91] followed by a loss of adenine

nucleotides [92] which may in some cases pseudo-normalise the ratio. However, it should be noted that such direct metabolic analysis of human diabetic myocardium by chemical assay and high performance liquid chromatography is not available in a similar way to DCM, where biopsy tissue is available during transplant or diagnostic biopsy [89, 92]. The energetic deficit in the diabetic heart is shown to be exacerbated as cardiac work increases [15], an observation that supports the notion that the energetic impairment is likely due to an impairment of cardiac substrate handling.

In diabetes, the increase in PPARα signalling stimulates fatty acid metabolism. On the other hand glucose oxidation is curtailed with reduced flux through PDH (chapter 4) due to both increased levels of citrate and an increase in PDK4 [215, 216]. Despite lower expression of glucose transporters, cellular glucose is maintained due to systemic hyperglycaemia [217], and glycolytic intermediates accumulate as pyruvate oxidation uncouples from glycolysis. Metabolic inflexibility with an impaired ability to augment glucose oxidation (as is physiological) during exercise may thus account for the PCr/ATP fall during stress seen in diabetics, compounded by a more fundamental impairment of oxidative phosphorylation at the mitochondria itself [218]. PCr/ATP was not recorded during stress in this study, Pi/PCr remained stable during dobutamine stress however, and resting PCr/γ-ATP showed no correlation with Pi/PCr. Taken together this suggests the rise in Pi seen at rest may be mechanistically independent to the fall in PCr/ATP, and not related to the substrate inflexibility seen in diabetes. Indeed, given the profound levels of PDH inhibition demonstrated in the diabetic heart in chapter 4 (in a cohort with a fairly mild phenotype), it is unlikely that substrate level changes in diabetes account for the rise in resting Pi/PCr seen, especially in the context of stability during stress.

One candidate for the rise in resting Pi would be impaired CK flux [50], although not reported in the human diabetic heart, evidence would suggest this would be highly unlikely. Pi/PCr was stable during stress, and K_f has been shown to be increased in obese humans (who may be considered insulin resistant) [41]. Furthermore in a rat model of diabetes (high fat diet) K_f is not only shown to be increased at rest, but increases further during stress [208] in a similar way to the controls, and indeed in the healthy human heart [40]. An increase in K_f in insulin resistant states may actually compensate for a reduction in PCr/ATP, maintaining CK flux, and rates of ATP delivery. Such changes may be expected to reduce intracellular Pi not increase it, given evidence that a reduction in flux through MtCK specifically, or though both isoforms equally would result in an increase in Pi [50]. Renal cellular Pi uptake is well characterised as it is responsible to overall systemic phosphate homeostasis; Na-Pi co-transport occurs and is under the hormonal regulation of Parathyroid hormone [219]. Myocyte Pi uptake is thought to occur similarly with sodium symport, but the regulation of this has not been studied [220]. It is however likely to be extremely tightly regulated given its profound impact on high energy phosphate metabolism.

Glucose oxidation is however highly sensitive to small changes in cellular Pi. It stimulates phosphofructokinase (a key glycolytic regulatory enzyme) and is a key substrate for glycogen phosphorylase which is non-saturating during basal conditions (as recorded in skeletal muscle) [94, 96]. As such, small rises in Pi in the diabetic heart in concert increase both the glycolytic rate (with associated ATP production and increased LDH flux as seen in chapter 4 despite PDH flux being fairly inhibited [206]) and glucose mobilisation from glycogen stores (although these are admittedly small in the myocardium). In support of the notion that the increase in Pi seen in diabetics (with a negligible effect on ΔG_{ATP}) could represent an adaptation, Pi is shown to be significantly elevated in a rodent (aortic banding)

model of hypertension [65] although this could also be due to increased AMPK activation and a secondary rise in Pi. In a canine model of LVH (open chest), Pi was shown to increase markedly during cardiac pacing but not in controls [12]. It may be tempting to suggest such rises would augment glucose provision to the hypertrophied heart during stress by increasing PKA mediated glycogenolysis during stress. Such rises are of a magnitude to meaningfully increase ΔG_{ATP} however, and thus are likely truly pathological representing loss of the CK flux steady state.

6.4.2 Pi/PCr and its relation to diastolic function

In this cohort of diabetics, Pi/PCr showed no correlation to diastolic dysfunction. Admittedly mitral annular tissue Doppler assessment is an insensitive marker of low grade diastolic dysfunction (with grade two diastolic dysfunction only likely with E/e' > 10 [143]), but with mean E/A of 0.9±0.2 and mean E/e' of 6.2±2.0 in the patients with diabetes, the grade of diastolic dysfunction recorded was mild. This may reflect the excellent glucose control seen in these patients (HbA1C 7.2±1.2%). Pi/γ-ATP, a more sensitive marker of energetic status than Pi/PCr indeed actually showed a weakly *negative* correlation (Figure 57). This supports the notion that the observed change is adaptive, stimulating oxidative phosphorylation and improving substrate flexibility, resulting in improved diastolic function. Further investigation of the relationship between Pi and diastolic dysfunction would be aided by recruiting a group with a diagnosis of diabetic cardiomyopathy, or indeed heart failure with preserved ejection fraction (HFpEF), the hallmark of which is high grade diastolic dysfunction.

6.4.3 Pi/PCr and pH in DCM

The metabolic phenotype associated with heart failure is distinct to that seen in diabetes. Oxidative metabolism is reduced in heart failure [221]. Early in the disease, the heart turns to a more foetal like phenotype preferentially increasing oxidation of glucose which is more oxygen efficient per mole of ATP generated. An increase in glycolysis [65] is seen, and possibly glucose transport / uptake [57, 222]. As disease progresses both FA metabolism [57] and glucose oxidation [1, 62] are curtailed, likening the situation to an 'engine running out of fuel' [1]. With this in mind pharmacologically altering substrate preference in heart failure toward glucose oxidation (indirectly by downregulating FA oxidation with compounds such as perhexiline or trimetazedine, or directly by increasing PDH flux with dichloroacetate) have shown promise [221]. Reduced PCr/ATP in DCM is multifactorial in origin with global metabolite loss seen – firstly of creatine [88, 91], then of the adenine nucleotide pool [93]. A trend toward lower PCr/γ-ATP and higher Pi/PCr was seen in the DCM cohort, which perhaps would have met significance if the study was more highly powered. As in the diabetics however, these varied independently from one another.

Although PCr/ATP in both diabetes and DCM is shown to behave in a similar way during stress (with further falls seen over and above the reduction seen at rest), the Pi/PCr response to stress in these two pathologies differed greatly in my study. In the DCM group a significant 40% increase in Pi/PCr was seen ($p=0.04$), and this abnormal response was not predicted by underlying LVEF; In the 5 cases in which I observed a Pi/PCr rise >50% (range 68 – 285%) the mean EF was (38.8%) - no different to those in which a less marked rise in Pi/PCr (<50%) was seen (38.6%). The CK pseudo-first order rate constant K_F has been consistently observed to be reduced in human heart failure [42, 88], and a rise in Pi has been modelled to

be consistent with this [50]. Similarly, a three-fold rise in Pi during work is modelled to occur in human hypertrophic cardiomyopathy [190].

The response of myocardial Pi to stress has previously been experimentally studied in open chest canine models with the coil directly sutured to the left ventricle. These by design cannot be considered physiological, but results are supportive for the explanation that large rises seen in my DCM group likely result from an underlying impairment of CK flux. In these open chest models, large rises in Pi are only recorded in the otherwise healthy heart when exposed to extremely high degrees of exogenous stress (high concentrations of dobutamine and dopamine, or dinitrophenol). This likely reflects the point at which a healthy CK system loses the steady state, and is supported by observations that such rises are brought forward to lower degrees of stress in hearts with impaired CK reserve (such as in ventricular hypertrophy) [12, 184]. My result here is very different to the healthy controls; Pi changes considered physiological and mediating control of oxidative phosphorylation are too small to be detected with this technique, but large changes occurring in the context of reduced K_f can clearly be appreciated. Formally measuring K_f at rest using saturation transfer techniques in each patient, then plotting this against the rise in Pi/PCr seen during stress is needed to further prove this hypothesis. Although myocardial pH did not change during stress in either patients with DCM, one patient saw a drop in pH from 7.0 to 6.6. Myocardial pH falls to this level in the ex-vivo rat heart within 2 minutes of global ischaemia from a starting value of 7.1, [223], and within 20 minutes following balloon occlusion of the left anterior descending artery (LAD) in-vivo in the dog heart [224]. Contractility although reduced at this pH is still meaningful [225]. With this in mind perhaps the pH drop observed in this patient is plausible, especially given the good quality spectra underlying this result.

6.4.4 Energetic consequences of the changes in Pi seen

Taking typical values of phosphorus containing metabolites measured in the isolated rat heart using both extracts and ^{31}P NMR [79], and assuming a constant PCr, the significant rise in Pi/PCr seen in the diabetic patients, although nominally impressive at 32%, only increases ΔG_{ATP} by 0.6kJ/mol (from -61.1 to -60.5). Such a small rise (less negative ΔG_{ATP}) suggests this rise in Pi would have little consequence for the cell in terms of energetic requiring processes. Although I only report a trend toward higher resting Pi/PCr in human heart failure, large increases were seen in some patients during low grade work. In 13% of the patients providing paired data (2/16), a 2-3 fold increase in Pi/PCr was seen during stress. Using the same inputs to the equation for ΔG_{ATP} [79] this equates to an increase in ΔG_{ATP} from a baseline value of -61.1kJ/mol to between 58.5 and 57.8 (i.e. between a 4% and 5.4% change) in these patients during only modest exertion. At first glance, again this still puts the value below (more favourable) than the most vulnerable ATPases (e.g the SERCA2A Ca ATPase at -52kJ/mol) [211]. However, these estimations make assumptions of stability of the other HEP metabolites. ATP availability at sites of hydrolysis is substantially lower in the failing heart with reduced absolute concentrations [93] compounded by impaired phosphotransfer, causing a further unfavourable change in ΔG_{ATP}. Changes in [ADP] are less clear; its concentration is extremely small but can be estimated by rearranging the CK equilibrium reaction:

$$K_{Eq} = \frac{[ATP][Cr]}{[PCr][ADP][H^+]} \qquad \text{To} \qquad [ADP] = \frac{[ATP][Cr]}{[PCr][K_{Eq}][H^+]}$$

Creatine can be estimated from ^{1}H MRS in human heart failure [226], and using an equilibrium constant (K_{Eq}) of 1.66 x 10^9 liters $/$mol estimated from rat heart data [227], neutral pH, and

^{31}P-MRS data in human heart failure [42], ADP is suggested to fall in heart failure by up to 50% [42]. The magnitude and directionality of changes in ADP in heart failure is however controversial. Estimates in porcine models of heart failure (using the same methods but importantly with all measurements made in the same animal) following either myocardial infarction [228], or aortic banding [229] suggest an increase. On balance despite this uncertainty, my estimate for thermodynamically unfavourable changes in ΔG_{ATP} due to the observed rise in Pi during exertion in these patients is likely an underestimate.

6.4.6 Limitations of the present study

The RPP increase in the diabetics was significantly lower than the control group. This is hard to control in practice, especially since the patients were older, meaning the target heart rate increases were lower. The stress result in the diabetic group was sufficiently negative however, such that marginally higher RPP would unlikely change it in my opinion. The control group presented here (in its entirety) is significantly younger than the patients recruited. Toward the end of the study, I was unable to finish recruitment of older controls due to the prevailing COVID-19 public health emergency. I see no reason for phosphate to vary with age, and reassuringly when plotting resting Pi/PCr against age for all controls recruited (including those used for the repeatability studies) no association is seen Figure 59.

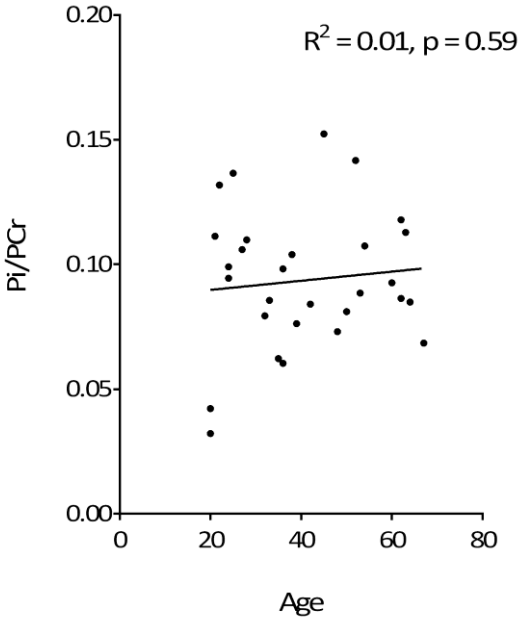


Figure 59: Pi/PCr variation with age in healthy controls

6.5 Conclusion and future perspectives

Any rise in ΔG_{ATP} does not necessarily need to cross an arbitrary estimated threshold at which various ATPases are estimated to halt, to have a cellular thermodynamic consequence. Some heart failure patients have a clear discrepancy between their NYHA heart failure status (a measure of how symptomatic they are) and underlying LV ejection fraction. My result is supportive of the notion that in such patients, exertional symptoms could arise due to a marked reduction in absolute ΔG_{ATP}. Such changes may contribute to a deterioration in diastolic and/or systolic function during exercise; measuring these two metrics during stress and correlating any changes with the Pi/PCr stress response would be useful to test this hypothesis. Further work needs to move toward computation of ΔG_{ATP} at 7T which is discussed in detail in chapter 7. Testing the hypothesis that the observed ΔPi/PCr seen in DCM is related to the degree of impairment of CK flux is worthy of investigation; and could be achieved by investigating its relationship with CK K_F, or ΔK_F if rest / stress TRiST is undertaken

during a separate dobutamine infusion. The significant signal to noise increase achieved using a commercially available ^{31}P-MRS body coil [192], would also be welcomed in future experiments.

Recording NYHA class and undertaking a formal assessment of functional capacity with a 6-minute walk test in the DCM patients, would also allow me to investigate how stress ΔPi and estimated $\Delta\Delta G_{ATP}$ is related to functional capacity, and underling ejection fraction. In 1997, work by Stefan Neubauer uncovered the prognostic importance of underlying energetic dysfunction (a reduced PCr/ATP) in DCM, independent to LVEF [83]. Ion transportation, to maintain gradients essential to normal excitation contraction coupling, is an active process. Changes in ΔG_{ATP} during exertion may therefore increase susceptibility to electrical instability, and may even increase the risk of sudden cardiac death (SCD). The next step would be to follow up a cohort of patients with an abnormal energetic stress response and comparing survival with an age and LVEF matched group, to investigate whether this finding confers a poorer prognosis. If shown to be the case, perhaps a metric of abnormal energy metabolism may prove useful in assessing the risk of SCD and aid risk stratification for implantation of a primary prevention cardiac defibrillator.

The detection of regional ischaemic metabolism during stress (the hallmark of which is a drop in pH associated with lactate production) in distinct myocardial segments using the technique and a ^{31}P-MRS body coil may be possible, providing a completely novel approach to the non-invasive detection of physiologically significant coronary disease (in a population with undiagnosed chest pain). This is likely a bridge too far for the technique.

Chapter 7. Imaging myocardial ischaemic metabolism using hyperpolarised MR

Work in this chapter has been presented in abstract form (ISMRM 2020) and the following manuscript is in press at the Journals of the America College of Cardiology: Cardiovascular imaging.

Apps A, Lau J, Miller J et al. Proof of Principle Demonstration of Direct Metabolic Imaging Following Myocardial Infarction Using Hyperpolarized ^{13}C MRI

7.1 Introduction

The hyperpolarised MRS study in chapter 4 successfully tracked the metabolism of hyperpolarised [1-^{13}C]pyruvate within the heart. Moving from spectroscopy to imaging the metabolism of this tracer opens the door to a variety of clinical applications since it sits at an important crossroads in metabolism, with its fate reflecting not only substrate preference, but also oxygen availability. The imaging of $H^{13}CO_3^-$ production in healthy human myocardium representing the aerobic metabolism of [1-^{13}C]pyruvate by the PDH complex has recently been reported [133], and one use of hyperpolarised imaging with potentially large clinical impact is within the field of coronary artery disease.

Ischaemic burden from stable coronary artery disease confers risk [127] and revascularisation restores myocardial contractility if deemed viable by CMR [128], yet the clinical impact of revascularisation procedures aimed at these targets is variable. The quest to accurately record ischaemia has evolved from the non-invasive to the invasive arena, harnessing intracoronary physiology to record the fractional flow reserve (FFR) [230]. However, despite this procedure which carries a risk of iatrogenic myocardial infarction stroke and death, no reduction in myocardial infarction or death has been demonstrated compared to medical therapy when using FFR to guide PCI in stable disease [129, 130]. Either measuring intracoronary flow changes mediated by stable disease is not measuring ischaemia, or we are overestimating the prognostic benefits of relieving ischaemia downstream of stable disease. There is a pressing need to resolve this; a weak mandate for a procedure carrying a procedural risk of death, and accounting for an annual spend in the USA alone of over $30 billion is, clearly, unacceptable and unsustainable. Directly measuring the hallmarks of ischaemia and viability (lactate production and respiration) using hyperpolarised MR rather than their

surrogates (flow, perfusion, and LGE) may allow more effective guidance of revascularisation procedures to these targets and help to answer this question.

Preclinical work with hyperpolarised MR demonstrates the power of the technique to offer such ischaemic metabolic phenotyping. Under ischaemic conditions the ^{13}C label is transferred from [1-^{13}C]pyruvate via LDH to [1-^{13}C]lactate, with reduced conversion to $H^{13}CO_3^-$. These findings were first confirmed in a rodent ex-vivo infarct model [231], and subsequently in-vivo in a pig model using a balloon to undertake transient LAD [131], or LCx [132] occlusion. As ischaemic time is prolonged in these models, heterogenous infarcts develop displaying varying viability [171]. Non-viable infarcts displayed transmural late enhancement, with myocardium remaining metabolically inactive one-week post infarct (denoted by an absence of $H^{13}CO_3^-$) and with no functional recovery. Conversely, wall motion returns when HCO_3^- signal normalized after reperfusion and no late enhancement was seen (Figure 60).

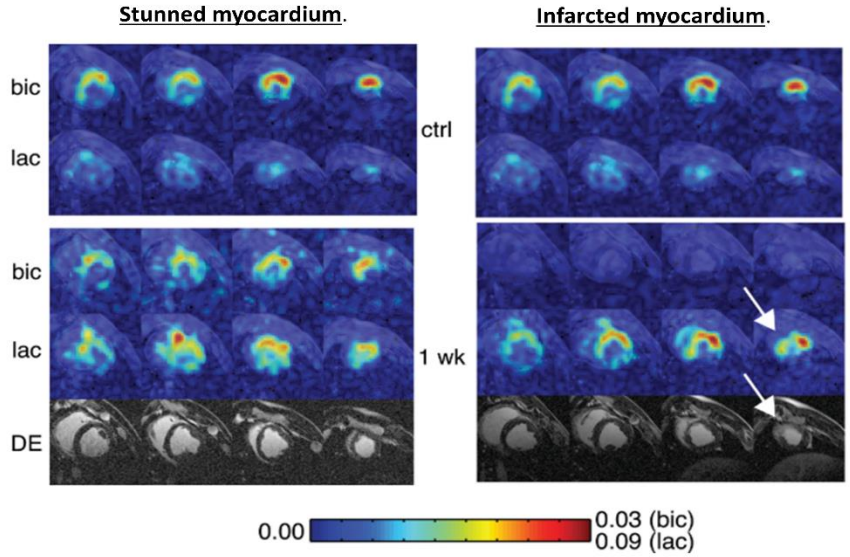


Figure 60: Ischaemia imaging in the pig heart using Hyperpolarised MR

Short axis hyperpolarised imaging after a 60 min left anterior descending artery (LAD) occlusion in pigs, at baseline and 1-week post-reperfusion. Colour intensity is normalised to LV pyruvate, stunned myocardium (shown on the left) demonstrated normalisation of HCO_3^-, absence of delayed enhancement, and normalisation of function at 1 week. In infarcted myocardium (right) HCO_3^- production remained absent at 1-week delayed enhancement denotes infarction. (Magn Reson Med Apr;69:1063–71 - [171]).

Admittedly, these porcine models involve binary vessel occlusion followed by reperfusion and as such hyperpolarised imaging is taken in the context of an acute coronary syndrome model. Despite this, the idea of imaging ischaemia in those with stable coronary artery disease, and viability in those with ischaemic left ventricular systolic dysfunction by determining the fate of an administered hyperpolarised [1-^{13}C]pyruvate tracer in humans is extremely intriguing. Preliminary work attempting to image the differential metabolic handling of a hyperpolarised [1-^{13}C]pyruvate tracer in the hearts of those with coronary artery disease is presented here.

7.2 Methods

7.2.1 Ethical considerations

Research described below to investigate the effect of Ischaemic heart disease on cardiac metabolism were approved by the South Birmingham Research Ethics Committee (Reference 17/WM/0200, IRAS ID 135913). All participants gave written informed consent to participant, and all had an ECG recorded, and a cardiovascular examination undertaken, prior to enrolment.

7.2.2 Human ^{13}C Hybrid-Shot Spiral for hyperpolarised Imaging

Imaging was acquired using a novel hybrid spiral shot sequence (HYSS) to achieve hyperpolarised ^{13}C metabolic imaging in patients with coronary artery disease, which was developed by my colleagues in OCMR Dr. Justin Lau, Dr. Jack Miller and Mr Andrew Tyler [232]. Using a spiral trajectory, the high signal central K-space is sampled first, thus SNR is maximised (Figure 61). Three spirals are combined (each slightly rotated with respect to each other, and oversampling the centre of k-space) for the high spatial resolution image, with each spiral corresponding to a different time point. Three slices (basal, mid, apical) were encoded per heartbeat. The centre frequency was interleaved such that the pyruvate, bicarbonate, and lactate resonances were excited in three consecutive heartbeats. A set of images of 3 slices and 3 metabolites was obtained every 3 heartbeats. The spiral trajectory was then rotated for the next set of 3 heartbeats. Three spiral rotation angles were acquired to give a full set of spiral rotations in 9 heartbeats. Readouts can be processed retrospectively at the time of reconstruction depending on whether high spatial or temporal resolution is desired. By combining time points (and spiral rotations) of the HYSS acquisition, temporal resolution can be traded for spatial resolution, whereas by only considering the central K-space sampling of each spiral high temporal resolution information can be acquired. The sequence is cardiac gated, and the order of excitation can be varied for different primary scan objectives (Bicarb-lac-pyr for viability studies, pyr-lac-bicarb for ischaemia studies). In each case, data were acquired for three short axis slices (basal, mid and apical) of 20mm thickness each with nominal 10mm in-plane resolution, with the intention that myocardium can be analysed in the typical American Heart Association model. Imaging was performed over two expiratory breath holds started 22s after injection, each 18 heart beats approximately 5s apart. 2D and 3D implementations of the sequence were used (Figure 61).

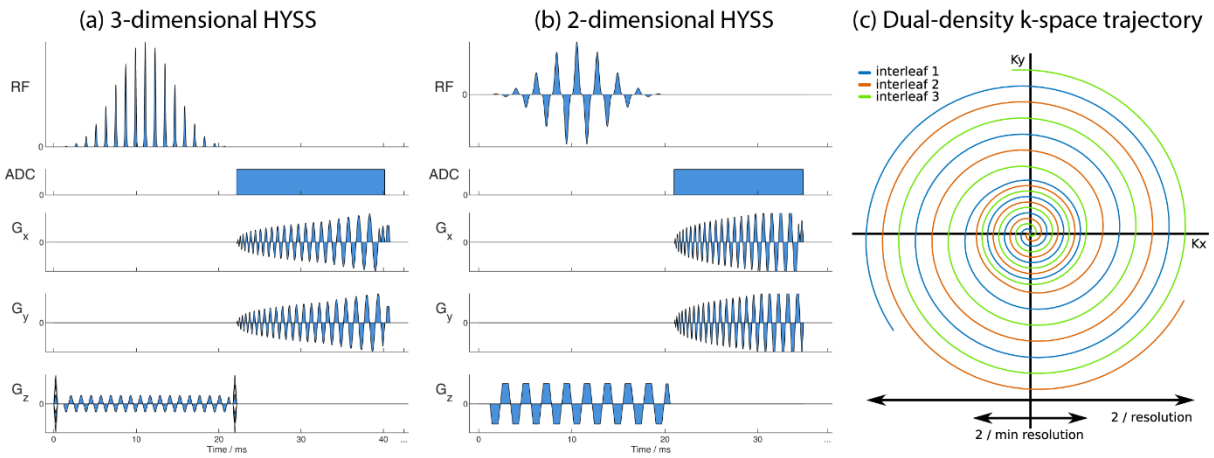


Figure 61: Hybrid-Shot Spiral sequence for hyperpolarised imaging

7.2.3 Pilot work; ischaemia study design and eligibility

The study underway aims to metabolically define both ischaemia and viability in a population of patients with stable coronary artery disease who are suggested to display these by contemporary testing. As such the study has two main arms. The ischaemia arm recruits patients with symptoms typical of stable angina who have documented inducible regional myocardial ischaemia on a routine clinical myocardial nuclear perfusion scan, stress echocardiogram, or CMR study, and who are planned for coronary angiography. Here the aim is to illicit regional [1-^{13}C]lactate production during dobutamine stress in the territory deemed ischaemic (Figure 62), with adenosine perfusion performed during the same study visit. Exclusion criteria include acute coronary syndrome, unstable symptoms (at rest) and impaired ventricular function (LVEF < 50%).

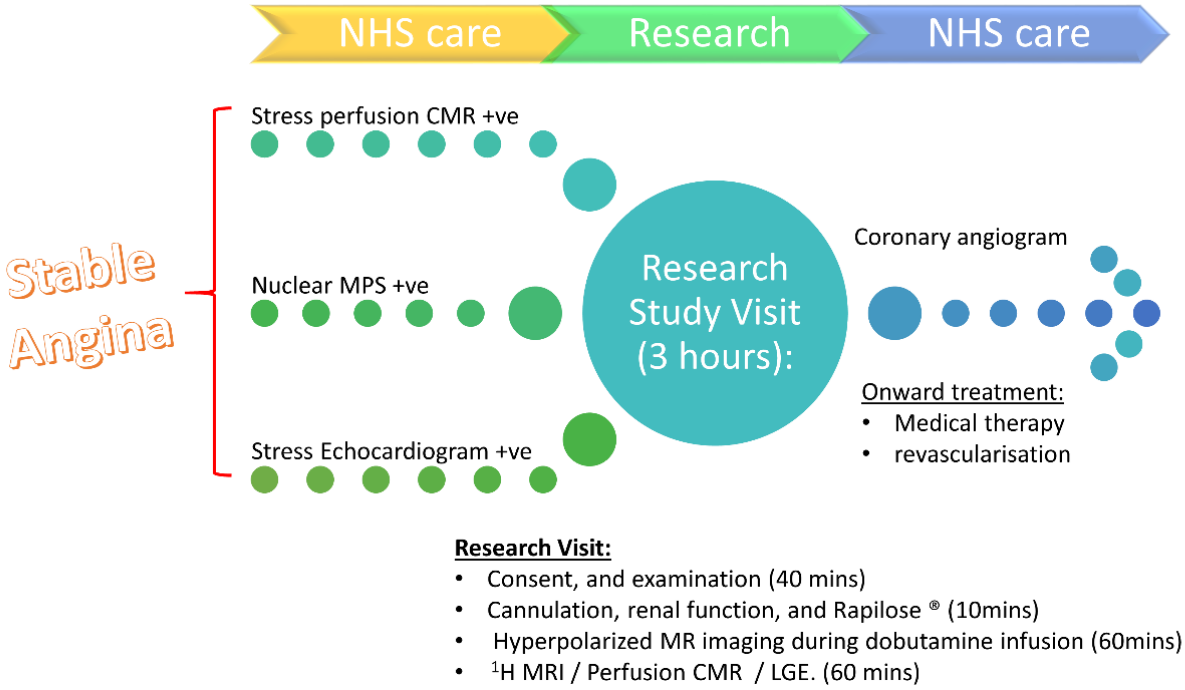


Figure 62: Hyperpolarised imaging in CAD; ischaemia sub-study

7.2.4 Pilot work; viability study design and eligibility

The viability arm recruits those with a regional myocardial wall motion abnormality on a routine clinical echocardiography or CMR study in the territory subtended by a coronary artery containing a flow limiting lesion, to be treated (surgically or percutaneously) with the aim of restoring contractility. Here the aim is to assess the ability of $H^{13}CO_3^-$ imaging to act as a marker of viability and compare this with late gadolinium enhancement for predicting recovery of function after revascularisation of hibernating myocardium (a second visit) Figure 63. Exclusion criteria include within two days of an acute coronary syndrome, LVEF < 35%, and awaiting inpatient staged percutaneous revascularisation. SFP preparation is identical to chapter 4, and further technical details can be found in 2.2.1. All patients were again prepared with a 70 gram Rapilose© solution 45 minutes prior to injection.

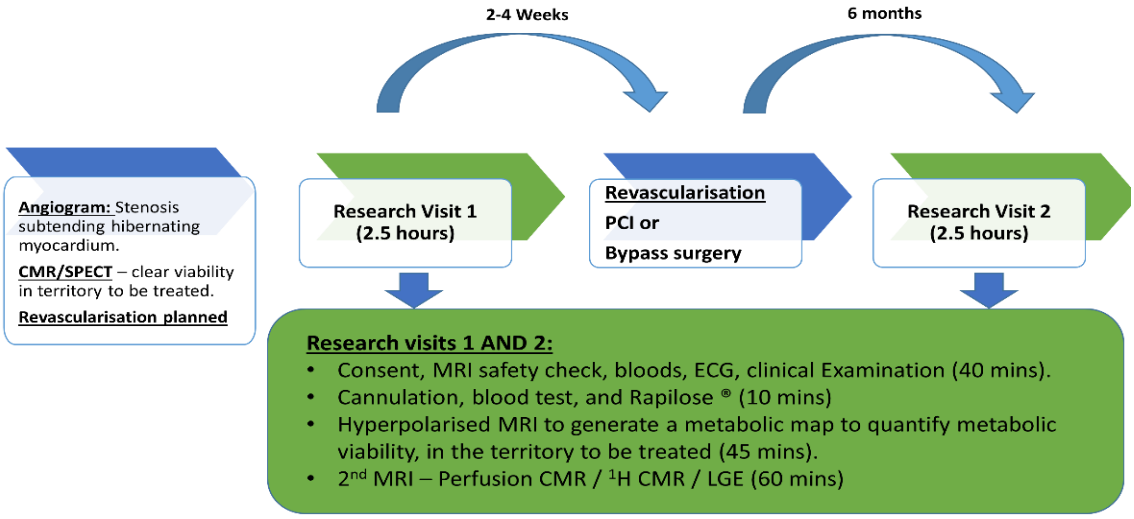


Figure 63: Hyperpolarised imaging in CAD; viability sub-study

7.3 Results

Preliminary example results from two patients are presented, I cannot include quantitative details of results here, but include examples of images. Firstly, a 76-year-old female presented with ST segment elevation MI. Pain had resolved and anterior Q waves were evident on the ECG, and with little motion seen on echocardiography viability testing with CMR was undertaken prior to coronary angiography. Transmural enhancement and significant microvascular obstruction were seen in the anterior and antero-lateral walls during CMR suggesting the infarcted territory was non-viable (Figure 64A). A non-invasive medical course of therapy was thus pursued. Metabolic imaging (Figure 64B) was performed using the 3D implementation of HYSS with nominal flip angles of 6° on pyruvate and 30° on lactate and bicarbonate. Signals from [1-^{13}C]lactate and ^{13}C-bicarbonate were absent from the territory of transmural infarction, but a strong [1-^{13}C]lactate signal was observed localising to the peri-

infarct region corresponding to the infero-lateral and inferior walls. [1-^{13}C]pyruvate was seen clearly within the ventricular cavity, reflecting delivery.

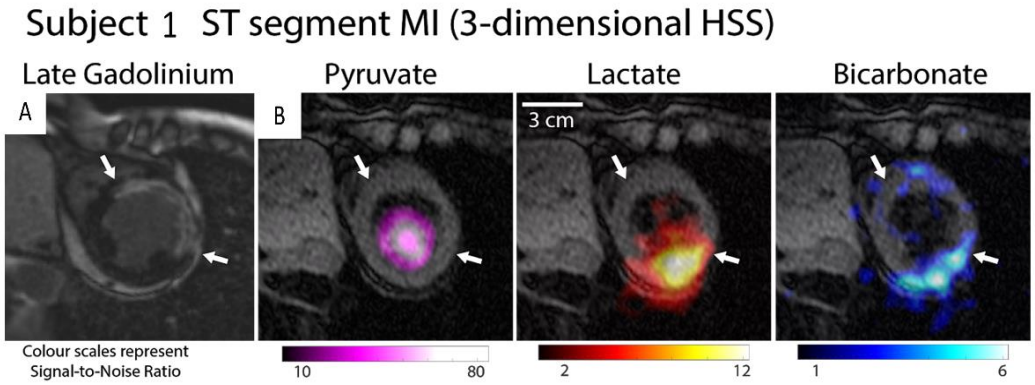


Figure 64: Hyperpolarised imaging following STEMI

Secondly, a 67-year-old male presented with non-ST elevated MI and ECG evidence of anterior territory ischaemia. Relevant medical history included type 2 diabetes, and a recent admission for urinary sepsis. Coronary angiography revealed disease of the distal left main and proximal left anterior descending coronary arteries with right coronary artery chronic occlusion. CMR demonstrated a hypokinetic anterior wall with evidence of subendocardial enhancement suggesting limited infarction. The infero-septum was akinetic with transmural (non-viable) infarction (Figure 65A). On this basis, the patient was referred for LAD bypass grafting. Metabolic imaging with 2D HYSS (Figure 65B) correlated to CMR findings with absence of ^{13}C-bicarbonate signals in the infarcted infero-septum. ^{13}C-bicarbonate signals were, however, preserved in the region of anterior wall subendocardial infarction. Signals from [1-^{13}C]lactate were similarly absent in the area of old (inferior) MI but seen elsewhere in the myocardium, most avidly in the ischaemic anterior wall. An Intense splenic [1-^{13}C]lactate signal was also seen.

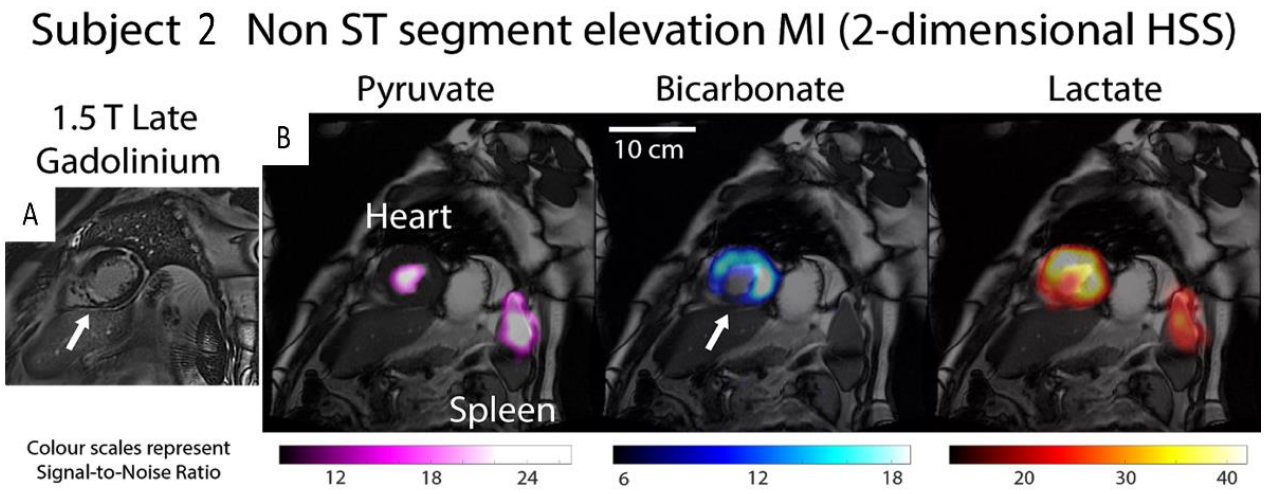


Figure 65: Hyperpolarised imaging following NSTEMI

7.4 Discussion

These results demonstrate the potential for hyperpolarised imaging to reveal the various metabolic sequalae seen with coronary artery disease. I have demonstrated the PDH-catalysed conversion of [1-^{13}C]pyruvate to ^{13}C-bicarbonate in perfused viable myocardium. Encouragingly for the detection of regional ischaemia, the lactate signal was localised to myocardium remote to infarction, as opposed to the ventricular blood pool, somewhat alleviating concerns from chapter 4 that the observed lactate signal may have been contamination from the blood pool, hepatic in origin [172].

Using hyperpolarised imaging, glycolytic [1-^{13}C]lactate production is increased within infarcted myocardial segments in rodent and porcine models following myocardial infarction, correlating to macrophage infiltration on histological assessment, and reversed after macrophage depletion [233]. PET demonstrates this inflammation to be widespread with ^{18}FDG-PET uptake increased in all remote myocardial segments up to 10 days after ischaemia in a mouse model of myocardial infarction [234]. Hyperpolarised [1-^{13}C]lactate also

demarcates neuro-inflammation in a murine model of multiple sclerosis [235], and taken together such findings suggest that the lactate signal seen in these patients likely reflects an an inflammatory cell infiltrate, with both patients being scanned following (fairly) recent myocardial infarction. Conclusions about the ability to image ischaemic myocardial metabolism cannot be drawn thus far, but the ability to demonstrate regional variation in [1-^{13}C]lactate production is encouraging.

The second patient discussed had a recent admission for urinary infection with a recorded C-reactive protein of 140, here a high [1-^{13}C]lactate signal was also seen in the spleen. This finding is consistent with macrophage activation in the spleen, which become increasingly glycolytic and anaerobic during a systemic inflammatory response [236, 237]. Imaging the burden of inflammation following myocardial infarction and in other conditions typified by inflammation such as myocarditis or sarcoidosis, may have utility in its own right since this finding portends fibrosis and adverse remodelling. The technique may be more specific for inflammation than other techniques such as T1 which reflects oedema, and PET (glucose uptake), and may as such prove useful in targeting patients for immunomodulatory therapy such as canakinumab – the IL1β inhibitor shown to reduce cardiovascular events in those with established coronary artery disease, but at the cost of increased infections [238].

Being metabolically inert, hyperpolarised [^{13}C] urea has been demonstrated for use as a marker of cardiac perfusion, with a linear signal response to concentration [239]. Co-polarisation with [1-^{13}C]pyruvate thus theoretically adds perfusion data to metabolic data without an increase in scan time, should it be desired in a clinical MR protocol. Simultaneous metabolic / perfusion data has been demonstrated in rats with increased [^{13}C] urea signal seen during adenosine induced coronary vasodilatation simultaneous to an increase in $H^{13}CO_3^-$ after DCA [240]. This would obviate the need for a 1st pass gadolinium assessment of

perfusion if desired. Onward referral for invasive delineation of coronary anatomy is only justified on demonstration of a substantial burden of ischaemia, with intention to treat.

Chapter 8. Conclusions and further work.

8.1 Summary of main findings

In preparation for human studies using hyperpolarised MR, this work began with a rodent study designed to investigate the optimal preparation strategy for hyperpolarised studies. I hypothesised that glucose administration given to fasted animals would reduce variation in, while increasing flux through, the PDH complex compared to the fed state. Whether flux is responsive to glucose loading in diabetes which is characterised by a reduction in PDH flux, was also investigated. Intravenous glucose administration however did not reduce variation in metabolic flux (estimated via metabolite ratios), nor did it normalise PDH flux in diabetes which was still significantly lower compared to controls.

Chapter 4 presented the human translation of hyperpolarised MR and makes a multi-nuclear assessment of the diabetic metabolic phenotype. Having confirmed a reduced myocardial PCr/ATP and raised triglyceride content in the diabetic cohort studied, using hyperpolarised MR, I demonstrated reduced / increased flux through PDH / LDH. These changes were documented in a group of diabetics displaying only mild insulin resistance, demonstrating metabolic change as a sensitive biomarker of early disease. During a glucose challenge, Randle-cycle associated changes in substrate preference were documented in-vivo for the first time in humans, and although flux through PDH was depressed in the diabetic heart, the metabolic flexibility to respond to a glucose challenge was not lost.

Substrate changes and alterations in PCr/ATP ultimately impact ΔG_{ATP} and its computation in the heart human heart is yet to be achieved. One problem in achieving this

goal has been measurement of Pi and I turned to this for the remainder of my work. In chapter 5, I demonstrated the utility of STEAM-^{31}P-MRS at 7T to measure Pi free from blood pool contamination, and demonstrated stability of Pi/PCr, and cardiac pH, during a doubling of the rate pressure product in the healthy human heart. The finding does not refute the hypothesis that Pi is a feedback regulator involved in the control of oxidative respiration, but that such changes are small and likely simply not within a range detectable by ^{31}PMRS. This is perhaps not surprising; relative stability in Pi during incremental work means cardiac ΔG_{ATP} is maintained during physiological workloads, a different situation to skeletal muscle in which gross changes in Pi/PCr occur [13]. In chapter 6, I went on to explore the response of Pi/PCr to stress in two diseases typified by abnormal energetics; diabetes, and DCM. Rest Pi/PCr was higher in diabetics compared to controls but showed no change during dobutamine stress, which was in contrast to DCM where resting Pi/PCr was no different to controls but a significant rise during stress was seen. Such differences may be accounted for by the differing mechanisms underpinning impaired energetics in both conditions, with pathological substrate handling and CK flux impairment taking primacy in diabetes and DCM respectively.

8.2 Subject preparation prior to hyperpolarised studies

Following chapter 3, further rat studies, varying the timing of glucose delivery prior to scanning (on different days) would allow me to ascertain the time course of Randle cycle changes following feeding. At the time course of 30 minutes following glucose administration fasting inhibition was overcome and PDH flux was already back at the level seen in the fed state. Scanning the same protocol on the same animal on multiple occasions would also allow me to assess the impact of different preparation strategies on intra-individual variation, which

needs to be minimized in order to detect temporal changes associated with disease progression or onset. A small human study measuring PDH flux and variability in each of three permutations (fed with glucose, fasted with glucose, or simply fed) would also be informative in planning future studies.

8.3 Hyperpolarised MRS to assess disease progression

The ability to pinpoint temporal changes in substrate preference in the human heart may be a useful marker of risk as disease progresses. Substrate preference changes during progression toward heart failure with an initial shift toward glucose as a substrate, demonstrated using hyperpolarised MR with increasing PDH flux seen during progression of hypertrophy in rodent models [63, 66]. Having confirmed the ability of hyperpolarised MRS to detect pathological metabolic change in the human heart, it would be logical to extend such studies into humans. For example, such change could be hypothesised to precede ventricular decompensation in those with valvular heart disease graded as severe by imaging but who remain asymptomatic, and as such inform the optimal timing of surgery in such patients prior to ventricular decompensation. Measuring PDH metabolism in an obese population, with serial measurements during weight loss, would also be interesting given it is a precursor to diabetes in most cases, and can also result in a cardiomyopathy supposedly independent of diabetes [241]. Such studies would strengthen the argument that PDH may represent a therapeutic target for those suffering from diabetic or obesity related heart failure. However, I have clearly demonstrated throughout my DNP work that metabolic flux is hypervariable and as such temporal changes not related to disease, may hide the emergence of pathological metabolism within the boundaries of normal variation.

8.4 Hyperpolarised imaging for diagnosis and treatment planning in coronary disease

At present the clinical impact of revascularisation procedures treating stable coronary artery disease in those with angina is highly variable. In the early 1990s, the prognostic impact of treating stable lesions with stents was not definitively demonstrated in the landmark COURAGE trial [242, 243]. Ischaemic burden as assessed by nuclear perfusion scintigraphy, however, clearly conferred risk [127]. In the decades since, functional testing has evolved in an effort to measure just this. Testing has moved in to the catheter lab with the advent of the pressure wire to measure the Fractional Flow Reserve (FFR) during hyperaemia, of a stable coronary stenosis. Treating lesions with low (positive) FFR was however shown to simply reduce the risk of a further procedure (for chest pain), and not reduce subsequent myocardial infarction or death [230]. More recently in the ORBITA trial [129] a sham procedure was introduced to remove the placebo effect of the PCI procedure itself, and reported no difference in exercise capacity after PCI. The highly anticipated $100million ISCHAEMIA trial [130] reporting in April 2020, was the first trial to reserve coronary angiography for those in the invasive arm (vs. medical therapy) only. Such a design thus tested whether invasive management of a high ischaemia burden (as assessed by perfusion CMR, FFR, or SPECT) can be safely differed. The primary endpoint of myocardial infarction, death, or hospitalisation for chest pain was not met (although high grade angina and left main coronary disease were excluded).

A weak mandate for a procedure carrying a procedural risk of stroke or death is unacceptable, even ignoring the huge annual spend on these procedures. Revascularisation for myocardial viability is in similar need. Stents or bypass grafts relieve coronary lesions subtending myocardium said to be in a chronic metabolically downregulated state (hibernating) due to chronic low-grade hypoxia. Revascularisation is shown to restore

myocardial contractility [128], with the chance of recovery inversely related to late gadolinium enhancement. RCT data again disappoints, with surgical revascularisation offering no clear survival benefit [244, 245], or improvement in function [245] over medical therapy alone. It may be that by including, and treating, patients without ischaemia or viability, our evidence base is misguided and not giving these procedures a fighting chance to prove themselves. Ischaemia and viability are *metabolic* phenomena. Local regional ischaemic myocardial metabolism in response to coronary occlusion has been demonstrated using hyperpolarised MR and a [1-^{13}C]Pyruvate tracer in porcine ischaemic reperfusion models, [131, 132] with ischaemic time demonstrably impacting myocardial viability [171]. Chapter 7 extends whole heart MRS in humans to imaging regional changes within the hearts of those with coronary artery disease and changes in metabolism following myocardial infarction are demonstrated. Studies are currently recruiting using the technique to directly measure both myocardial viability and ischaemia, comparing the technique's performance against LGE CMR to predict recovery of function of hibernating myocardium following revascularisation, and perfusion imaging to predict coronary anatomy and the results of intracoronary pressure wire assessment. Directly measuring metabolism rather than surrogate markers (flow, perfusion, and late gadolinium enhancement [246, 247]), may allow more effective guidance of revascularisation procedures [55], substantially reducing overtreatment, cost, and unnecessary procedural risk.

8.5 Hyperpolarised imaging for regional cardiac pH assessment

Following infusion of hyperpolarised [1-^{13}C]pyruvate in the isolated rat heart, cardiac pH_i can be estimated before and immediately after ischaemia by recording the $H^{13}CO_3^-/^{13}CO_2$ ratio and using the Henderson-Hasselbalch equation [248]. Values agree well with that estimated

using ^{31}P-MRS to estimate the chemical shift of the Pi peak discussed earlier. Assuming non rate limiting carbonic anhydrase flux (not a given during extreme acidosis), imaging the distribution between hyperpolarised bicarbonate and CO_2 could provide a pH map of the heart, useful to predict contractile recovery after myocardial infarction given that severe acidosis implies cellular death. This would provide complementary information to the regional production of [1-^{13}C]lactate by measuring associated regional change in myocardial pH. To test such a potential utility, a selection of patients could be recruited and scanned following myocardial infarction and displaying regional wall motion abnormality. However, this all requires imaging ^{13}CO2 which to date has proved difficult.

8.6 Measuring ΔG_{ATP} in the human heart and its pathological alterations

Although measurement of Pi provides an important step toward ΔG_{ATP}, other parameters are required and the collection of all these parameters in one group of patients will be the focus of future studies. Free ADP at rest and stress can be estimated by a rearrangement of the CK equilibrium using a creatine measured from ^{1}H MRS and taking the CK equilibrium constant previously recorded [227]. Adding a third interleaf to the STEAM sequence to excite γ-ATP would allow its measurement without a CSI sequence. A significant increase in SNR achieved from the use of a commercially available ^{31}P-MRS body coil [192], would allow this by reducing the number of averages needed to keep the stress scan time down to within acceptable limits. Combining all this with measuring rest / stress CK flux by TRIST in the same patients would allow me to determine the impact of abnormalities of CK flux on ΔG_{ATP}, and directly confirm the involvement of movements in Pi. With estimates for $\Delta\Delta G_{ATP}$ in heart failure, cohort studies could then help understand whether such patients are indeed at increased risk of adverse outcomes including death and exertional ventricular arrhythmia, which could in turn inform

selection for a primary prevention cardiac defibrillator. Indeed an adverse prognosis by a reduction in either ΔG_{ATP} at rest, or significant $\Delta\Delta G_{ATP}$ during exertion may offers an explanation for the finding that a reduction in PCr/ATP confers a poorer prognosis [49].

8.5 Post face narrative

In 1987 the Business author Tom Peters wrote "under-promise and over-deliver" with reference to communication with stake holders. Hyperpolarised MR has definitely not read this script. Scale up and human translation has been extremely difficult because of the extremes of temperature involved in the DNP process, coupled with the need to carefully balance a clinical grade safe product with the rapid return of the tracer to thermal equilibrium following dissolution. Such difficulty is evidenced by the fact that data in chapter 4 of this thesis was collected over a four-year period. Only a handful of diabetics were needed to demonstrate dramatic reductions in PDH flux however, understating how opportunities for new treatments and diagnostic strategies may lie in uncovering the metabolic foundation of disease, and the ability of hyperpolarised MR to help do this.

The potential clinical benefit of studying phosphotransfer and the CK system is less immediately apparent compared to using hyperpolarised MR to image ischaemia from coronary artery disease. Without cheating the laws of thermodynamics, phosphorus spectroscopy experiments take sometimes hours as opposed the minutes DNP allows. Using the technique in my work, I uncovered a rise in Pi during stress in DCM patients, and suggest this may result in a significant fall in ΔG_{ATP} during exertion. This would result in a further "hit", with deterioration of mechanics accounting in part for exertional symptomatology. As a research tool ^{31}P MRS is central to investigate any theory of heart failure whose underlying

thesis is energetic dysfunction, and in uncovering new mechanisms of disease (or symptoms), which in turn presents a panoply of novel therapeutic targets. It is my hope that the scientific communities working on the techniques developed within this thesis, and those working on complementary techniques such as PET, can work together to exploit the synergism that these techniques offer, toward the goal of delivering clinically relevant metabolic imaging. Recent healthcare consumption has largely been driven by an insatiable desire for, and pre-occupation with, new treatments. However, marginal improvements in hard patient outcomes (for example in death or hospitalization) often offered by such treatments do not keep pace with their associated rapidly escalating cost of delivery. It is my hope that this work has contributed to the development of techniques that may ultimately have paradigm shifting implications in the way we diagnose and select patients for treatments, with an associated meaningful reduction in the morbidity and mortality associated with cardiovascular disease.

Chapter 9. Appendix

9.1 Data handling chapter 5

Table 13: Data handling chapter 5 healthy controls

Repeatability participant ID	Scan 1 Pi	Scan 2 Pi	Pi/PCr (paired analysis)	pH (paired analysis)
01	✓	✓	✓	✓
02	✓	✓	✓	✓
03	✓	✓	✓	✓
04	✓	✓	✓	✓
05	✓	✓	✓	✓
06	✓	✓	✓	✓
07	✓	✓	✓	✓
08	×*	✓	✓	×
09	✓	✓	✓	✓

Stress Study participant ID	Rest Pi	Stress Pi	Pi/PCr (paired analysis)	pH (paired analysis)
01 (Pi1)	✓	✓	✓	✓
02 (Pi2)	✓	✓	✓	✓
03 (Pi3)	×	×	×	×
04 (Pi4)	✓	✓	✓	✓
05 (Pi5)	✓	✓	✓	✓
06 (Pi6)	✓	✓	✓	✓
07 (Pi7)	✓	✓	✓	✓
08 (Pi6)	✓	✓	✓	✓
09 (Pi9)	✓	N/A	N/A	N/A
10 (Pi10)	✓	✓	✓	✓
11 (Pi11)	×*	✓	✓	×
12 (PI12)	✓	✓	✓	✓
13 (Pi13)	✓	✓	✓	✓
14 (Pi14)	✓	✓	✓	✓
15 (Pi15)	✓	×	×	×
16 (Pi16)	✓	×	×	×
17 (Pi 18)	×	×	×	×
18 (Pi 19)	✓	✓	✓	✓
19 (Pi 48)	✓	✓	✓	✓
20 (Pi 59)	✓	✓	✓	✓
21 (Pi 63)	✓	✓	✓	✓

Data from all volunteers in this chapter. Myocardial [Pi] is low, and in rare cases could not be seen with confidence. I therefore used a method for data inclusion in to the analysis of pairs, to ensure no bias. ✓ Denotes robust Pi peak (visually obvious and SNR>2.5), × denotes no Pi resonance seen, in some cases (× *) overall scan SNR (PCr SNR>35) was sufficient to justify an upper bound estimation for Pi/PCr using AMARES (Id 8 and 11). Such cases do not provide Pi resonance frequency and are not used for pH computation

9.2 Data handling chapter 6

Table 14: Data collection dilated cardiomyopathy

DCM (ID)	Rest Pi	Stress Pi	Pi/Pcr (paired analysis)	pH (paired analysis)
01 (24)	✓	✓	✓	✓
02 (28)	✓	N/A	N/A	N/A
03 (30)	✓	N/A	N/A	N/A
04 (31)	✓	✓	✓	✓
05 (33)	✓	✓	✓	✓
06 (35)	✓	✓	✓	✓
07 (36)	✓	✓	✓	✓
08 (37)	✓	✓	✓	✓
09 (39)	✓	✓	✓	✓
10 (38)	×*	✓	✓	×
11 (39)	✓	✓	✓	✓
12 (44)	✓	N/A	N/A	N/A
13 (45)	✓	✓	✓	✓
14 (47)	×*	✓	✓	×
15 (49)	✓	✓	✓	✓
16 (50)	✓	×	×	×
17 (51)	✓	✓	✓	✓
18 (52)	✓	N/A	N/A	N/A
19 (54)	✓	✓	✓	✓
20 (56)	✓	✓	✓	✓
21 (58)	✓	✓	✓	✓
22 (61)	✓	✓	✓	✓

Data from all DCM patients recruited to this study. N/A represents patient did not undergo dobutamine stress – in two cases the patient only consented to rest ^{31}P-MRS-STEAM, in the other two the stress scan was abandoned (one for the toilet and one due to a failure of the Blood pressure recording equipment).

Table 15: Data collection type two diabetics

Diabetic Participant (ID)	Rest Pi	Stress Pi	Pi/PCr (paired analysis)	pH (paired analysis)
1 (Pi 17)	✓	✓*	✓	×
2 (Pi 20)	✓	✓	✓	✓
3 (Pi 21)	×	N/A	N/A	N/A
4 (PI 22)	✓	N/A	N/A	N/A
5 (Pi 23)	✓	N/A	N/A	N/A
6 (PI 25)	×	×	×	×
7 (PI 26)	×	N/A	N/A	N/A
8 (PI 27)	✓	✓	✓	✓
9 (Pi 32)	✓	✓	✓	✓
10 (Pi 34)	×	×	×	×
11 (Pi 40)	×	×	×	×
12 (Pi 41)	✓	✓	✓	✓
13 (Pi 42)	✓	✓	✓	✓
14 (Pi 43)	✓	✓	✓	✓
15 (Pi 46)	✓	✓	✓	✓
16 (Pi 53)	✓	N/A	N/A	N/A
17 (PI 60)	✓	✓	✓	✓

Data from all diabetics recruited to this study. Four patients did not tolerate the length of time in the magnet beyond the rest STEAM ^{31}P MRS scan, and hence did not undergo stress. One patient did not tolerate dobutamine infusion and asked to stop.

Table 16: Extended control group chapter 6

Control participant (ID)	Rest Pi	Stress Pi	Pi/PCr (paired analysis)	pH (paired analysis)
01 (Pi1)	✓	✓	✓	✓
02 (Pi2)	✓	✓	✓	✓
03 (Pi4)	✓	✓	✓	✓
04 (Pi5)	✓	✓	✓	✓
05 (Pi6)	✓	✓	✓	✓
06 (Pi7)	✓	✓	✓	✓
07 (Pi6)	✓	✓	✓	✓
08 (Pi9)	✓	N/A	N/A	N/A
09 (Pi10)	✓	✓	✓	✓
10 (Pi11)	× *	✓	✓	×
11 (PI12)	✓	✓	✓	✓
12 (Pi13)	✓	✓	✓	✓
13 (Pi14)	✓	✓	✓	✓
14 (Pi15)	✓	×	×	×
15 (Pi16)	✓	×	×	×
16 (Pi 19)	✓	✓	✓	✓
17 (Pi 48	✓	✓	✓	✓
18 (Pi 59)	✓	✓	✓	✓
19 (Pi 63)	✓	✓	✓	✓
20 (Pi 64)	✓	✓	✓	✓
21 (Pi 65)	✓	×	×	×
22 (Pi 66)	✓	✓	✓	✓
23 (Pi 67)	✓	×	×	×

9.3 General MR exclusion criteria

General exclusion criteria:

- Contra-indications to MR studies (with stringency depending on the field strength), such as metal implants, pacemakers, defibrillators.
- Claustrophobia (relative caution rather than total exclusion).
- Uncontrolled hypertension (Systolic over 140mmHg, Diastolic over 90mmHg).

- Chronic kidney disease of a moderate or severe degree (e-GFR less than or equal to 30mls/kg/min).
- Inability or loss of ability to give informed consent.
- Current participation in another research trial.
- Pregnancy, lactation or planning pregnancy during the course of the study.
- Any significant disease or disorder which may have put the individual at risk because of participation in the study, or have affected the participants' ability to participate fully in the study.

`

References.

1 Neubauer S. The failing heart—an engine out of fuel. *New England Journal of Medicine* 2007;**356**:1140-51.

2 Bottomley PA, Hardy CJ, Roemer PB. Phosphate metabolite imaging and concentration measurements in human heart by nuclear magnetic resonance. *Magnetic resonance in medicine* 1990;**14**:425-34.

3 Ingwall JS. ATP and the Heart. *Kluwer Academic* 2002.

4 Lopaschuk GD, Ussher JR, Folmes CD, et al. Myocardial fatty acid metabolism in health and disease. *Physiological reviews* 2010;**90**:207-58.

5 Jennings RB, Reimer KA, Hill ML, et al. Total ischemia in dog hearts, in vitro. 1. Comparison of high energy phosphate production, utilization, and depletion, and of adenine nucleotide catabolism in total ischemia in vitro vs. severe ischemia in vivo. *Circulation Research* 1981;**49**:892-900.

6 Visscher MB, Mulder AG. The carbohydrate metabolism of the heart. *American Journal of Physiology-Legacy Content* 1930;**94**:630-40.

7 Bing R, Siegel A, Ungar I, et al. Metabolism of the human heart: II. Studies on fat, ketone and amino acid metabolism. *The American journal of medicine* 1954;**16**:504-15.

8 Randle P, Garland P, Hales C, et al. The glucose fatty-acid cycle its role in insulin sensitivity and the metabolic disturbances of diabetes mellitus. *The Lancet* 1963;**281**:785-9.

9 Lardy HA, Wellman H. Oxidative phosphorylations: role of inorganic phosphate and acceptor systems in control of metabolic rates. *Journal of Biological Chemistry* 1952;**195**:215-24.

10 Balaban RS. Regulation of oxidative phosphorylation in the mammalian cell. *American Journal of Physiology-Cell Physiology* 1990;**258**:C377-C89.

11 Zhang J, Gong G, Ye Y, et al. Nitric oxide regulation of myocardial O2 consumption and HEP metabolism. *American Journal of Physiology-Heart and Circulatory Physiology* 2005.

12 Bache RJ, Zhang J, Path G, et al. High-energy phosphate responses to tachycardia and inotropic stimulation in left ventricular hypertrophy. *American Journal of Physiology-Heart and Circulatory Physiology* 1994;**266**:H1959-H70.

13 Chance B, Leigh J, Clark B, et al. Control of oxidative metabolism and oxygen delivery in human skeletal muscle: a steady-state analysis of the work/energy cost transfer function. *Proceedings of the National Academy of Sciences* 1985;**82**:8384-8.

14 Lamb HJ, Beyerbacht HP, Ouwerkerk R, et al. Metabolic response of normal human myocardium to high-dose atropine-dobutamine stress studied by 31P-MRS. *Circulation* 1997;**96**:2969-77.

15 Levelt E, Rodgers CT, Clarke WT, et al. Cardiac energetics, oxygenation, and perfusion during increased workload in patients with type 2 diabetes mellitus. *European heart journal* 2015;**37**:3461-9.

16 Rider OJ, Francis JM, Ali MK, et al. Effects of catecholamine stress on diastolic function and myocardial energetics in obesity. *Circulation* 2012:CIRCULATIONAHA. 111.069518.

17 Dass S, Cochlin LE, Suttie JJ, et al. Exacerbation of cardiac energetic impairment during exercise in hypertrophic cardiomyopathy: a potential mechanism for diastolic dysfunction. *European heart journal* 2015;**36**:1547-54.

18 Katz LA, Swain JA, Portman MA, et al. Relation between phosphate metabolites and oxygen consumption of heart in vivo. *American Journal of Physiology-Heart and Circulatory Physiology* 1989;**256**:H265-H74.
19 Katz L, Swain J, Portman M, et al. Intracellular pH and inorganic phosphate content of heart in vivo: a 31P-NMR study. *American Journal of Physiology-Heart and Circulatory Physiology* 1988;**255**:H189-H96.
20 Balaban R. The application of nuclear magnetic resonance to the study of cellular physiology. *American Journal of Physiology-Cell Physiology* 1984;**246**:C10-C9.
21 LaNoue KF, Jeffries F, Radda G. Kinetic control of mitochondrial ATP synthesis. *Biochemistry* 1986;**25**:7667-75.
22 Weiss K, Bottomley PA, Weiss RG. On the theoretical limits of detecting cyclic changes in cardiac high-energy phosphates and creatine kinase reaction kinetics using in vivo 31P MRS. *NMR in biomedicine* 2015;**28**:694-705.
23 Wu F, Zhang EY, Zhang J, et al. Phosphate metabolite concentrations and ATP hydrolysis potential in normal and ischaemic hearts. *The Journal of physiology* 2008;**586**:4193-208.
24 Beard DA, Kushmerick MJ. Strong inference for systems biology. *PLoS computational biology* 2009;**5**:e1000459.
25 Tran K, Loiselle DS, Crampin EJ. Regulation of cardiac cellular bioenergetics: mechanisms and consequences. *Physiological reports* 2015;**3**.
26 Bertero E, Maack C. Calcium signaling and reactive oxygen species in mitochondria. *Circulation research* 2018;**122**:1460-78.
27 Harris DA, Das A. Control of mitochondrial ATP synthesis in the heart. *Biochemical Journal* 1991;**280**:561.
28 Baughman JM, Perocchi F, Girgis HS, et al. Integrative genomics identifies MCU as an essential component of the mitochondrial calcium uniporter. *Nature* 2011;**476**:341-5.
29 Balaban RS. Cardiac energy metabolism homeostasis: role of cytosolic calcium. *Journal of molecular and cellular cardiology* 2002;**34**:1259-71.
30 SAKS VA, CHERNOUSOVA GB, GUKOVSKY DE, et al. Studies of energy transport in heart cells: mitochondrial isoenzyme of creatine phosphokinase: kinetic properties and regulatory action of Mg2+ ions. *European journal of biochemistry* 1975;**57**:273-90.
31 Schlattner U, Tokarska-Schlattner M, Wallimann T. Mitochondrial creatine kinase in human health and disease. *Biochimica et Biophysica Acta (BBA)-Molecular Basis of Disease* 2006;**1762**:164-80.
32 Saks V, Lipina N, Smirnov V, et al. Studies of energy transport in heart cells: the functional coupling between mitochondrial creatine phosphokinase and ATP-ADP translocase: kinetic evidence. *Archives of biochemistry and biophysics* 1976;**173**:34-41.
33 Saks V, Ventura-Clapier R, Huchua Z, et al. Creatine kinase in regulation of heart function and metabolism. I. Further evidence for compartmentation of adenine nucleotides in cardiac myofibrillar and sarcolemmal coupled ATPase-creatine kinase systems. *Biochimica et Biophysica Acta (BBA)-Molecular Cell Research* 1984;**803**:254-64.
34 Yang WC, Geiger PJ, Bessman SP, et al. Formation of creatine phosphate from creatine and 32P-labelled ATP by isolated rabbit heart mitochondria. *Biochemical and biophysical research communications* 1977;**76**:882-7.
35 Kay L, Nicolay K, Wieringa B, et al. Direct evidence for the control of mitochondrial respiration by mitochondrial creatine kinase in oxidative muscle cells in situ. *Journal of biological chemistry* 2000;**275**:6937-44.

36 Saks VA, Kaambre T, Sikk P, et al. Intracellular energetic units in red muscle cells. *Biochemical Journal* 2001;**356**:643.
37 Wallimann T, Wyss M, Brdiczka D, et al. Intracellular compartmentation, structure and function of creatine kinase isoenzymes in tissues with high and fluctuating energy demands: the'phosphocreatine circuit'for cellular energy homeostasis. *Biochemical Journal* 1992;**281**:21.
38 Joubert F, Hoerter JA, Mazet J-L. Discrimination of cardiac subcellular creatine kinase fluxes by NMR spectroscopy: a new method of analysis. *Biophysical journal* 2001;**81**:2995-3004.
39 Joubert F, Mazet J-L, Mateo P, et al. 31P NMR detection of subcellular creatine kinase fluxes in the perfused rat heart contractility modifies energy transfer pathways. *Journal of Biological Chemistry* 2002;**277**:18469-76.
40 Peterzan M CW, Lygate C, Rayner J, Hundertmark M, Sayeed R, Krasopoulos G, Neubauer S, Rodgers C, Rider O. Validation of non-invasive measurement of creatine kinase flux in human myocardium and effect of acute catecholamine stress. *In proceedings of the 22nd Annual Meeting of SCMR, Seattle, USA* 2016.
41 Rayner JJ, Peterzan MA, Watson WD, et al. Myocardial Energetics in Obesity: Enhanced ATP Delivery Through Creatine Kinase with Blunted Stress Response. *Circulation* 2020.
42 Weiss RG, Gerstenblith G, Bottomley PA. ATP flux through creatine kinase in the normal, stressed, and failing human heart. *Proceedings of the National Academy of Sciences* 2005;**102**:808-13.
43 Grist T, Kneeland J, Rilling W, et al. Gated cardiac MR imaging and P-31 MR spectroscopy in humans at 1.5 T. Work in progress. *Radiology* 1989;**170**:357-61.
44 Illing B, Horn M, Urban B, et al. Changes of myocardial high-energy phosphates with the cardiac cycle during acute or chronic myocardial stress. *Magnetic resonance in medicine* 1998;**40**:727-32.
45 Honda H, Tanaka K, Akita N, et al. Cyclical changes in high-energy phosphates during the cardiac cycle by pacing-Gated 31P nuclear magnetic resonance. *Circulation journal* 2002;**66**:80-6.
46 Lygate CA, Aksentijevic D, Dawson D, et al. Living without creatine: unchanged exercise capacity and response to chronic myocardial infarction in creatine-deficient mice. *Circulation research* 2013;**112**:945-55.
47 Saupe KW, Spindler M, Hopkins JC, et al. Kinetic, thermodynamic, and developmental consequences of deleting creatine kinase isoenzymes from the heart reaction kinetics of the creatine kinase isoenzymes in the intact heart. *Journal of Biological Chemistry* 2000;**275**:19742-6.
48 Glancy B, Hartnell LM, Malide D, et al. Mitochondrial reticulum for cellular energy distribution in muscle. *Nature* 2015;**523**:617.
49 Neubauer S, Horn M, Cramer M, et al. Myocardial phosphocreatine-to-ATP ratio is a predictor of mortality in patients with dilated cardiomyopathy. *Circulation* 1997;**96**:2190-6.
50 Hettling H, van Beek JH. Analyzing the functional properties of the creatine kinase system with multiscale 'sloppy'modeling. *PLoS computational biology* 2011;**7**:e1002130.
51 Miller JJ. Myocyte Metabolic Imaging with Hyperpolarised MRI. *Protocols and Methodologies in Basic Science and Clinical Cardiac MRI* 2018:111-73.

52 Dodd MS, Atherton HJ, Carr CA, et al. Impaired In Vivo Mitochondrial Krebs Cycle Activity Following Myocardial Infarction Assessed Using Hyperpolarized Magnetic Resonance Spectroscopy. *Circulation: Cardiovascular Imaging* 2014:CIRCIMAGING. 114.001857.
53 Ardenkjær-Larsen JH, Fridlund B, Gram A, et al. Increase in signal-to-noise ratio of> 10,000 times in liquid-state NMR. *Proceedings of the National Academy of Sciences* 2003;**100**:10158-63.
54 Golman K, Thaning M. Real-time metabolic imaging. *Proceedings of the National Academy of Sciences* 2006;**103**:11270-5.
55 Apps A, Lau J, Peterzan M, et al. Hyperpolarised magnetic resonance for in vivo real-time metabolic imaging. *Heart* 2018;**104**:1484-91.
56 van Bilsen M, Smeets PJ, Gilde AJ, et al. Metabolic remodelling of the failing heart: the cardiac burn-out syndrome? *Cardiovascular research* 2004;**61**:218-26.
57 Osorio JC, Stanley WC, Linke A, et al. Impaired myocardial fatty acid oxidation and reduced protein expression of retinoid X receptor-α in pacing-induced heart failure. *Circulation* 2002;**106**:606-12.
58 Dávila-Román VG, Vedala G, Herrero P, et al. Altered myocardial fatty acid and glucose metabolism in idiopathic dilated cardiomyopathy. *Journal of the American College of Cardiology* 2002;**40**:271-7.
59 Kolwicz Jr SC, Tian R. Glucose metabolism and cardiac hypertrophy. *Cardiovascular research* 2011;**90**:194-201.
60 Ardehali H, Sabbah HN, Burke MA, et al. Targeting myocardial substrate metabolism in heart failure: potential for new therapies. *European journal of heart failure* 2012;**14**:120-9.
61 Pepin ME, Drakos S, Ha C-M, et al. DNA Methylation Reprograms Cardiac Metabolic Gene Expression in End-Stage Human Heart Failure. *American Journal of Physiology-Heart and Circulatory Physiology* 2019.
62 Taylor M, Wallhaus TR, DeGrado TR, et al. An evaluation of myocardial fatty acid and glucose uptake using PET with [18F] fluoro-6-thia-heptadecanoic acid and [18F] FDG in patients with congestive heart failure. *Journal of Nuclear Medicine* 2001;**42**:55-62.
63 Seymour A-ML, Giles L, Ball V, et al. In vivo assessment of cardiac metabolism and function in the abdominal aortic banding model of compensated cardiac hypertrophy. *Cardiovascular research* 2015;**106**:249-60.
64 Christe ME, Rodgers RL. Altered glucose and fatty acid oxidation in hearts of the spontaneously hypertensive rat. *Journal of molecular and cellular cardiology* 1994;**26**:1371-5.
65 Nascimben L, Ingwall JS, Lorell BH, et al. Mechanisms for increased glycolysis in the hypertrophied rat heart. *Hypertension* 2004;**44**:662-7.
66 Dodd MS, Ball DR, Schroeder MA, et al. In vivo alterations in cardiac metabolism and function in the spontaneously hypertensive rat heart. *Cardiovascular research* 2012;**95**:69-76.
67 Schroeder MA, Lau AZ, Chen AP, et al. Hyperpolarized 13C magnetic resonance reveals early-and late-onset changes to in vivo pyruvate metabolism in the failing heart. *European journal of heart failure* 2013;**15**:130-40.
68 Zhou X, Chen J. Is treatment with trimetazidine beneficial in patients with chronic heart failure? *PLoS One* 2014;**9**:e94660.
69 Lee L, Campbell R, Scheuermann-Freestone M, et al. Metabolic modulation with perhexiline in chronic heart failure. *Circulation* 2005;**112**:3280-8.

70 Dodd MS, Ball V, Bray R, et al. In vivo mouse cardiac hyperpolarized magnetic resonance spectroscopy. *Journal of Cardiovascular Magnetic Resonance* 2013;**15**:19.
71 Schroeder MA, Cochlin LE, Heather LC, et al. In vivo assessment of pyruvate dehydrogenase flux in the heart using hyperpolarized carbon-13 magnetic resonance. *Proceedings of the National Academy of Sciences of the United States of America* 2008;**105**:12051-6.
72 Tougaard RS, Szocska Hansen ES, Laustsen C, et al. Hyperpolarized [1-13C] pyruvate MRI can image the metabolic shift in cardiac metabolism between the fasted and fed state in a porcine model. *Magnetic resonance in medicine* 2019;**81**:2655-65.
73 Mansor LS, Gonzalez ER, Cole MA, et al. Cardiac metabolism in a new rat model of type 2 diabetes using high-fat diet with low dose streptozotocin. *Cardiovascular diabetology* 2013;**12**:136.
74 McGavock JM, Lingvay I, Zib I, et al. CLINICAL PERSPECTIVE. *Circulation* 2007;**116**:1170-5.
75 Finck BN, Lehman JJ, Leone TC, et al. The cardiac phenotype induced by PPARα overexpression mimics that caused by diabetes mellitus. *The Journal of clinical investigation* 2002;**109**:121-30.
76 Rijzewijk LJ, Jonker JT, van der Meer RW, et al. Effects of hepatic triglyceride content on myocardial metabolism in type 2 diabetes. *Journal of the American College of Cardiology* 2010;**56**:225-33.
77 Rayner J, Banerjee R, Holloway C, et al. The relative contribution of metabolic and structural abnormalities to diastolic dysfunction in obesity. *International Journal of Obesity* 2018;**42**:441.
78 Chong C-R, Clarke K, Levelt E. Metabolic remodelling in diabetic cardiomyopathy. *Cardiovascular research* 2017;**113**:422-30.
79 Ingwall JS. *ATP and the Heart*. Springer Science & Business Media 2002.
80 Bottomley PA. Noninvasive study of high-energy phosphate metabolism in human heart by depth-resolved 31P NMR spectroscopy. *Science* 1985;**229**:769-72.
81 Rodgers CT, Clarke WT, Snyder C, et al. Human cardiac 31P magnetic resonance spectroscopy at 7 Tesla. *Magnetic resonance in medicine* 2014;**72**:304-15.
82 Ellis J, Valkovič L, Purvis LA, et al. Reproducibility of human cardiac phosphorus MRS (31P-MRS) at 7 T. *NMR in biomedicine* 2019.
83 Neubauer S, Horn M, Cramer M, et al. Myocardial phosphocreatine-to-ATP ratio is a predictor of mortality in patients with dilated cardiomyopathy. *Circulation* 1997;**96**:2190-6.
84 Stoll VM, Clarke WT, Levelt E, et al. Dilated cardiomyopathy: phosphorus 31 MR spectroscopy at 7 T. *Radiology* 2016;**281**:409-17.
85 Neubauer S, Krahe T, Schindler R, et al. 31P magnetic resonance spectroscopy in dilated cardiomyopathy and coronary artery disease. Altered cardiac high-energy phosphate metabolism in heart failure. *Circulation* 1992;**86**:1810-8.
86 Schaefer S, Schwartz GG, Steinman SK, et al. Metabolic response of the human heart to inotropic stimulation: in vivo phosphorus-31 studies of normal and cardiomyopathic myocardium. *Magnetic resonance in medicine* 1992;**25**:260-72.
87 Lamb HJ, Beyerbacht HP, Van Der Laarse A, et al. Diastolic dysfunction in hypertensive heart disease is associated with altered myocardial metabolism. *Circulation* 1999;**99**:2261-7.

88 Smith CS, Bottomley PA, Schulman SP, et al. Altered creatine kinase adenosine triphosphate kinetics in failing hypertrophied human myocardium. *Circulation* 2006;**114**:1151.
89 Nascimben L, Ingwall JS, Pauletto P, et al. Creatine kinase system in failing and nonfailing human myocardium. *Circulation* 1996;**94**:1894-901.
90 Sylven C, Jansson E, Böök K. Key enzymes of myocardial energy metabolism in patients with valvular heart disease: relation to left ventricular function. *Acta physiologica scandinavica* 1988;**132**:267-70.
91 Beer M, Seyfarth T, Sandstede J, et al. Absolute concentrations of high-energy phosphate metabolites in normal, hypertrophied, and failing human myocardium measured noninvasively with 31 P-SLOOP magnetic resonance spectroscopy. *Journal of the American College of Cardiology* 2002;**40**:1267-74.
92 Starling RC, Hammer DF, Altschuld RA. Human myocardial ATP content and in vivo contractile function. *Molecular and cellular biochemistry* 1998;**180**:171-7.
93 Shen W, Asai K, Uechi M, et al. Progressive loss of myocardial ATP due to a loss of total purines during the development of heart failure in dogs: a compensatory role for the parallel loss of creatine. *Circulation* 1999;**100**:2113-8.
94 Neely JR, Morgan HE. Relationship between carbohydrate and lipid metabolism and the energy balance of heart muscle. *Annual review of physiology* 1974;**36**:413-59.
95 Cohen P. The role of cyclic-AMP-dependent protein kinase in the regulation of glycogen metabolism in mammalian skeletal muscle. *Current topics in cellular regulation* 1978;**14**:117-96.
96 Chasiotis D. The regulation of glycogen phosphorylase and glycogen breakdown in human skeletal muscle. *Acta Physiologica Scandinavica Supplementum* 1983;**518**:1-68.
97 Clarke K, Stewart LC, Neubauer S, et al. Extracellular volume and transsarcolemmal proton movement during ischemia and reperfusion: a 31P NMR spectroscopic study of the isovolumic rat heart. *NMR in biomedicine* 1993;**6**:278-86.
98 He M-X, Wang S, Downey HF. Correlation between myocardial contractile force and cytosolic inorganic phosphate during early ischemia. *American Journal of Physiology-Heart and Circulatory Physiology* 1997;**272**:H1333-H41.
99 Xiang J-Z, Kentish JC. Effects of inorganic phosphate and ADP on calcium handling by the sarcoplasmic reticulum in rat skinned cardiac muscles. *Cardiovascular research* 1995;**29**:391-400.
100 Gabr RE, El-Sharkawy A-MM, Schär M, et al. Cardiac work is related to creatine kinase energy supply in human heart failure: a cardiovascular magnetic resonance spectroscopy study. *Journal of Cardiovascular Magnetic Resonance* 2018;**20**:81.
101 Vaughan-Jones RD, Spitzer KW, Swietach P. Intracellular pH regulation in heart. *Journal of molecular and cellular cardiology* 2009;**46**:318-31.
102 Swietach P, Youm J-B, Saegusa N, et al. Coupled Ca2+/H+ transport by cytoplasmic buffers regulates local Ca2+ and H+ ion signaling. *Proceedings of the National Academy of Sciences* 2013;**110**:E2064-E73.
103 Orchard C, Kentish J. Effects of changes of pH on the contractile function of cardiac muscle. *American Journal of Physiology-Cell Physiology* 1990;**258**:C967-C81.
104 Orchard CH, Cingolani HE. Acidosis and arrhythmias in cardiac muscle. *Cardiovascular research* 1994;**28**:1312-9.
105 Moon RB, Richards JH. Determination of intracellular pH by 31P magnetic resonance. *Journal of Biological Chemistry* 1973;**248**:7276-8.

106 Meyer R, Kuchmerick M, Brown T. Application of 31P-NMR spectroscopy to the study of striated muscle metabolism. *American Journal of Physiology-Cell Physiology* 1982;**242**:C1-C11.
107 Bailey IA, Williams SR, Radda GK, et al. Activity of phosphorylase in total global ischaemia in the rat heart A phosphorus-31 nuclear-magnetic-resonance study. *Biochemical Journal* 1981;**196**:171-8.
108 Jacobus WE, TAYLOR IV GJ, HOLLIS DP, et al. Phosphorus nuclear magnetic resonance of perfused working rat hearts. *Nature* 1977;**265**:756.
109 Valkovič L, Clarke WT, Schmid AI, et al. Measuring inorganic phosphate and intracellular pH in the healthy and hypertrophic cardiomyopathy hearts by in vivo 7T 31 P-cardiovascular magnetic resonance spectroscopy. *Journal of Cardiovascular Magnetic Resonance* 2019;**21**:19.
110 Jung W-I, Sieverding L, Breuer J, et al. 31P NMR spectroscopy detects metabolic abnormalities in asymptomatic patients with hypertrophic cardiomyopathy. *Circulation* 1998;**97**:2536-42.
111 De Roos A, Doornbos J, Luyten PR, et al. Cardiac metabolism in patients with dilated and hypertrophic cardio-myopathy: Assessment with proton-decoupled P-31 MR spectroscopy. *Journal of Magnetic Resonance Imaging* 1992;**2**:711-9.
112 Karaus A, Merboldt KD, Graessner J, et al. Black-blood imaging of the human heart using rapid stimulated echo acquisition mode (STEAM) MRI. *Journal of Magnetic Resonance Imaging: An Official Journal of the International Society for Magnetic Resonance in Medicine* 2007;**26**:1666-71.
113 Fischer SE, Stuber M, Scheidegger MB, et al. Limitations of stimulated echo acquisition mode (STEAM) techniques in cardiac applications. *Magnetic resonance in medicine* 1995;**34**:80-91.
114 Valkovič L, Clarke WT, Purvis LA, et al. Adiabatic excitation for 31P MR spectroscopy in the human heart at 7 T: A feasibility study. *Magnetic resonance in medicine* 2017;**78**:1667-73.
115 Heather LC, Clarke K. Metabolism, hypoxia and the diabetic heart. *Journal of molecular and cellular cardiology* 2011;**50**:598-605.
116 Buchanan J, Mazumder PK, Hu P, et al. Reduced cardiac efficiency and altered substrate metabolism precedes the onset of hyperglycemia and contractile dysfunction in two mouse models of insulin resistance and obesity. *Endocrinology* 2005;**146**:5341-9.
117 Mazumder PK, O'Neill BT, Roberts MW, et al. Impaired cardiac efficiency and increased fatty acid oxidation in insulin-resistant ob/ob mouse hearts. *Diabetes* 2004;**53**:2366-74.
118 Seymour A-ML, Chatham JC. The effects of hypertrophy and diabetes on cardiac pyruvate dehydrogenase activity. *Journal of molecular and cellular cardiology* 1997;**29**:2771-8.
119 Levelt E, Mahmod M, Piechnik SK, et al. Relationship between left ventricular structural and metabolic remodeling in type 2 diabetes. *Diabetes* 2016;**65**:44-52.
120 Poirier P, Bogaty P, Garneau C, et al. Diastolic dysfunction in normotensive men with well-controlled type 2 diabetes: importance of maneuvers in echocardiographic screening for preclinical diabetic cardiomyopathy. *Diabetes care* 2001;**24**:5-10.
121 Rubler S, Dlugash J, Yuceoglu YZ, et al. New type of cardiomyopathy associated with diabetic glomerulosclerosis. *American Journal of Cardiology* 1972;**30**:595-602.

122 Nelson SJ, Kurhanewicz J, Vigneron DB, et al. Metabolic imaging of patients with prostate cancer using hyperpolarized [1-13C] pyruvate. *Science translational medicine* 2013;**5**:198ra08-ra08.
123 Granlund KL, Tee S-S, Vargas HA, et al. Hyperpolarized MRI of Human Prostate Cancer Reveals Increased Lactate with Tumor Grade Driven by Monocarboxylate Transporter 1. *Cell Metabolism* 2019.
124 Stødkilde-Jørgensen H, Laustsen C, Hansen ESS, et al. Pilot Study Experiences With Hyperpolarized [1-13 C] pyruvate MRI in Pancreatic Cancer Patients. *Journal of magnetic resonance imaging: JMRI* 2019.
125 Miloushev VZ, Granlund KL, Boltyanskiy R, et al. Metabolic imaging of the human brain with hyperpolarized 13C pyruvate demonstrates 13C lactate production in brain tumor patients. *Cancer research* 2018;**78**:3755-60.
126 Day SE, Kettunen MI, Gallagher FA, et al. Detecting tumor response to treatment using hyperpolarized 13C magnetic resonance imaging and spectroscopy. *Nature medicine* 2007;**13**:1382-7.
127 Hachamovitch R, Hayes SW, Friedman JD, et al. Comparison of the short-term survival benefit associated with revascularization compared with medical therapy in patients with no prior coronary artery disease undergoing stress myocardial perfusion single photon emission computed tomography. *Circulation* 2003;**107**:2900-7.
128 Kim RJ, Wu E, Rafael A, et al. The use of contrast-enhanced magnetic resonance imaging to identify reversible myocardial dysfunction. *New England Journal of Medicine* 2000;**343**:1445-53.
129 Al-Lamee R, Thompson D, Dehbi H-M, et al. Percutaneous coronary intervention in stable angina (ORBITA): a double-blind, randomised controlled trial. *The Lancet* 2017.
130 Maron DJ, Hochman JS, Reynolds HR, et al. Initial invasive or conservative strategy for stable coronary disease. *New England Journal of Medicine* 2020.
131 Aquaro GD, Frijia F, Positano V, et al. Cardiac Metabolism in a Pig Model of Ischemia–Reperfusion by Cardiac Magnetic Resonance with Hyperpolarized 13C-Pyruvate. *IJC Metabolic & Endocrine* 2015;**6**:17-23.
132 Golman K, Petersson JS, Magnusson P, et al. Cardiac metabolism measured noninvasively by hyperpolarized 13C MRI. *Magnetic Resonance in Medicine* 2008;**59**:1005-13.
133 Cunningham CH, Lau JY, Chen AP, et al. Hyperpolarized 13C metabolic MRI of the human heart: initial experience. *Circulation Research* 2016:CIRCRESAHA. 116.309769.
134 Ardenkjaer-Larsen JH, Leach AM, Clarke N, et al. Dynamic nuclear polarization polarizer for sterile use intent. *NMR in biomedicine* 2011;**24**:927-32.
135 Rodgers CT, Robson MD. Receive array magnetic resonance spectroscopy: whitened singular value decomposition (WSVD) gives optimal Bayesian solution. *Magnetic Resonance in Medicine: An Official Journal of the International Society for Magnetic Resonance in Medicine* 2010;**63**:881-91.
136 Vanhamme L, van den Boogaart A, Van Huffel S. Improved method for accurate and efficient quantification of MRS data with use of prior knowledge. *Journal of magnetic resonance* 1997;**129**:35-43.
137 Daniels CJ, McLean MA, Schulte RF, et al. A comparison of quantitative methods for clinical imaging with hyperpolarized 13C-pyruvate. *NMR in biomedicine* 2016;**29**:387-99.
138 Bottomley PA, Ouwerkerk R. Optimum flip-angles for exciting NMR with uncertain T1 values. *Magnetic resonance in medicine* 1994;**32**:137-41.

139 Biering-Sørensen T, Mogelvang R, de Knegt MC, et al. Cardiac time intervals by tissue doppler imaging M-mode: normal values and association with established echocardiographic and invasive measures of systolic and diastolic function. *PloS one* 2016;**11**.
140 Tyler D, Emmanuel Y, Cochlin L, et al. Reproducibility of 31P cardiac magnetic resonance spectroscopy at 3 T. *NMR in Biomedicine: An International Journal Devoted to the Development and Application of Magnetic Resonance In vivo* 2009;**22**:405-13.
141 Rial B, Robson MD, Neubauer S, et al. Rapid quantification of myocardial lipid content in humans using single breath-hold 1H MRS at 3 Tesla. *Magnetic resonance in medicine* 2011;**66**:619-24.
142 Hudsmith LE, Petersen SE, Francis JM, et al. Normal human left and right ventricular and left atrial dimensions using steady state free precession magnetic resonance imaging. *Journal of cardiovascular magnetic resonance* 2005;**7**:775-82.
143 Nagueh SF, Smiseth OA, Appleton CP, et al. Recommendations for the evaluation of left ventricular diastolic function by echocardiography: an update from the American Society of Echocardiography and the European Association of Cardiovascular Imaging. *European Journal of Echocardiography* 2016;**17**:1321-60.
144 Hutson N, Kerbey A, Randle P, et al. Regulation of pyruvate dehydrogenase by insulin action. *Progress in clinical and biological research* 1979;**31**:707-19.
145 Rohm M, Savic D, Ball V, et al. Cardiac dysfunction and metabolic inflexibility in a mouse model of diabetes without dyslipidemia. *Diabetes* 2018;**67**:1057-67.
146 Taegtmeyer H, Young ME, Lopaschuk GD, et al. Assessing cardiac metabolism: a scientific statement from the American Heart Association. *Circulation research* 2016;**118**:1659-701.
147 Peterson LR, Herrero P, Coggan AR, et al. Type 2 diabetes, obesity, and sex difference affect the fate of glucose in the human heart. *American Journal of Physiology-Heart and Circulatory Physiology* 2015;**308**:H1510-H6.
148 Herrero P, Peterson LR, McGill JB, et al. Increased myocardial fatty acid metabolism in patients with type 1 diabetes mellitus. *Journal of the American College of Cardiology* 2006;**47**:598-604.
149 Scheuermann-Freestone M, Madsen PL, Manners D, et al. Abnormal cardiac and skeletal muscle energy metabolism in patients with type 2 diabetes. *Circulation* 2003;**107**:3040-6.
150 Gruetter R, Adriany G, Choi IY, et al. Localized in vivo 13C NMR spectroscopy of the brain. *NMR in Biomedicine: An International Journal Devoted to the Development and Application of Magnetic Resonance In Vivo* 2003;**16**:313-38.
151 Hansen ESS, Tougaard RS, Nørlinger TS, et al. Imaging porcine cardiac substrate selection modulations by glucose, insulin and potassium intervention: a hyperpolarized [1-13C] pyruvate study. *NMR in biomedicine* 2017;**30**:e3702.
152 Le Page LM, Rider OJ, Lewis AJ, et al. Increasing pyruvate dehydrogenase flux as a treatment for diabetic cardiomyopathy: a combined 13C hyperpolarized magnetic resonance and echocardiography study. *Diabetes* 2015;**64**:2735-43.
153 Atherton HJ, Schroeder MA, Dodd MS, et al. Validation of the in vivo assessment of pyruvate dehydrogenase activity using hyperpolarised 13C MRS. *NMR in biomedicine* 2011;**24**:201-8.

154 Day SE, Kettunen MI, Gallagher FA, et al. Detecting tumor response to treatment using hyperpolarized 13 C magnetic resonance imaging and spectroscopy. *Nature medicine* 2007;**13**:1382-7.
155 Lauritzen MH, Laustsen C, Butt SA, et al. Enhancing the [13C] bicarbonate signal in cardiac hyperpolarized [1-13C] pyruvate MRS studies by infusion of glucose, insulin and potassium. *NMR in biomedicine* 2013;**26**:1496-500.
156 Stumvoll M, Mitrakou A, Pimenta W, et al. Use of the oral glucose tolerance test to assess insulin release and insulin sensitivity. *Diabetes care* 2000;**23**:295-301.
157 Frangioudakis G, Gyte AC, Loxham SJ, et al. The intravenous glucose tolerance test in cannulated Wistar rats: a robust method for the in vivo assessment of glucose-stimulated insulin secretion. *Journal of pharmacological and toxicological methods* 2008;**57**:106-13.
158 Rodgers CT, Robson MD. Coil combination for receive array spectroscopy: Are data-driven methods superior to methods using computed field maps? *Magnetic resonance in medicine* 2016;**75**:473-87.
159 Conover WJ, Johnson ME, Johnson MM. A comparative study of tests for homogeneity of variances, with applications to the outer continental shelf bidding data. *Technometrics* 1981;**23**:351-61.
160 Timm KN, Miller JJ, Henry JA, et al. Cardiac applications of hyperpolarised magnetic resonance. *Progress in nuclear magnetic resonance spectroscopy* 2018;**106**:66-87.
161 Steinhauser J, Wespi P, Kwiatkowski G, et al. Assessing the influence of isoflurane anesthesia on cardiac metabolism using hyperpolarized [1-13C] pyruvate. *NMR in biomedicine* 2018;**31**.
162 Timm KN, Apps A, Miller JJ, et al. Assessing the optimal preparation strategy to minimize the variability of cardiac pyruvate dehydrogenase flux measurements with hyperpolarized MRS. *NMR in biomedicine* 2018;**31**:e3992.
163 Levelt E, Gulsin G, Neubauer S, et al. MECHANISMS IN ENDOCRINOLOGY: Diabetic cardiomyopathy: pathophysiology and potential metabolic interventions state of the art review. *European journal of endocrinology* 2018;**178**:R127-R39.
164 Boyer JK, Thanigaraj S, Schechtman KB, et al. Prevalence of ventricular diastolic dysfunction in asymptomatic, normotensive patients with diabetes mellitus. *The American journal of cardiology* 2004;**93**:870-5.
165 Tougaard RS, Hansen ESS, Laustsen C, et al. Acute hypertensive stress imaged by cardiac hyperpolarized [1-13C] pyruvate magnetic resonance. *Magnetic resonance in medicine* 2018;**80**:2053-61.
166 Lewis AJ, Miller JJ, McCallum C, et al. Assessment of Metformin-Induced Changes in Cardiac and Hepatic Redox State Using Hyperpolarized [1-13C] Pyruvate. *Diabetes* 2016;**65**:3544-51.
167 Harrison XA, Donaldson L, Correa-Cano ME, et al. A brief introduction to mixed effects modelling and multi-model inference in ecology. *PeerJ* 2018;**6**:e4794.
168 Merritt ME, Harrison C, Storey C, et al. Inhibition of carbohydrate oxidation during the first minute of reperfusion after brief ischemia: NMR detection of hyperpolarized 13CO2 and H13CO 3−. *Magnetic resonance in medicine* 2008;**60**:1029-36.
169 Rayner JJ, Abdesselam I, Peterzan MA, et al. Very low calorie diets are associated with transient ventricular impairment before reversal of diastolic dysfunction in obesity. *International Journal of Obesity* 2018:1.
170 Wieland O, Siess E, Schulze-Wethmar F, et al. Active and inactive forms of pyruvate dehydrogenase in rat heart and kidney: effect of diabetes, fasting, and refeeding on

pyruvate dehydrogenase interconversion. *Archives of biochemistry and biophysics* 1971;**143**:593-601.
171 Lau AZ, Chen AP, Barry J, et al. Reproducibility study for free-breathing measurements of pyruvate metabolism using hyperpolarized 13C in the heart. *Magnetic resonance in medicine* 2013;**69**:1063-71.
172 Wespi P, Steinhauser J, Kwiatkowski G, et al. Overestimation of cardiac lactate production caused by liver metabolism of hyperpolarized [1-13 C] pyruvate. *Magnetic resonance in medicine* 2018;**80**:1882-90.
173 Lewandowski ED. Metabolic heterogeneity of carbon substrate utilization in mammalian heart: NMR determinations of mitochondrial versus cytosolic compartmentation. *Biochemistry* 1992;**31**:8916-23.
174 Peuhkurinen KJ, Hiltunen JK, Hassinen IE. Metabolic compartmentation of pyruvate in the isolated perfused rat heart. *Biochemical Journal* 1983;**210**:193-8.
175 Halestrap AP, PRICE NT. The proton-linked monocarboxylate transporter (MCT) family: structure, function and regulation. *Biochemical Journal* 1999;**343**:281-99.
176 Peterson LR, Herrero P, Schechtman KB, et al. Effect of obesity and insulin resistance on myocardial substrate metabolism and efficiency in young women. *Circulation* 2004;**109**:2191-6.
177 Kirchner H, Nylen C, Laber S, et al. Altered promoter methylation of PDK4, IL1 B, IL6, and TNF after Roux-en Y gastric bypass. *Surgery for Obesity and Related Diseases* 2014;**10**:671-8.
178 Wilson DM, Keshari KR, Larson PE, et al. Multi-compound polarization by DNP allows simultaneous assessment of multiple enzymatic activities in vivo. *Journal of magnetic resonance* 2010;**205**:141-7.
179 Otonkoski T, Kaminen N, Ustinov J, et al. Physical exercise-induced hyperinsulinemic hypoglycemia is an autosomal-dominant trait characterized by abnormal pyruvate-induced insulin release. *Diabetes* 2003;**52**:199-204.
180 Freund H, Marbach J, Ott C, et al. Blood pyruvate recovery curves after short heavy submaximal exercise in man. *European journal of applied physiology and occupational physiology* 1980;**43**:83-91.
181 Bashore TM, Magorien DJ, Letterio J, et al. Histologic and biochemical correlates of left ventricular chamber dynamics in man. *Journal of the American College of Cardiology* 1987;**9**:734-42.
182 Conway M, Bristow J, Blackledge M, et al. Cardiac metabolism during exercise measured by magnetic resonance spectroscopy. *The Lancet* 1988;**332**:692.
183 Passonneau JV, Lowry OH. The role of phosphofructokinase in metabolic regulation. *Advances in enzyme regulation* 1964;**2**:265-74.
184 Gong G, Liu J, Liang P, et al. Oxidative capacity in failing hearts. *American Journal of Physiology-Heart and Circulatory Physiology* 2003.
185 Lamb HJ, Beyerbacht HP, Ouwerkerk R, et al. Metabolic response of normal human myocardium to high-dose atropine-dobutamine stress studied by 31P-MRS. *Circulation* 1997;**96**:2969-77.
186 Bartlett J, Frost C. Reliability, repeatability and reproducibility: analysis of measurement errors in continuous variables. *Ultrasound in Obstetrics and Gynecology: The Official Journal of the International Society of Ultrasound in Obstetrics and Gynecology* 2008;**31**:466-75.

187 Purvis LA, Clarke WT, Biasiolli L, et al. OXSA: An open-source magnetic resonance spectroscopy analysis toolbox in MATLAB. *PloS one* 2017;**12**:e0185356.
188 Valkovič L SA, Purvis L, Ellis J, Robson MD, Neubauer S, Rodgers CT. Quantification of human cardiac inorganic phosphate content in vivo by ^{31}P-MRS at 7T. *In proceedings of the 26th Annual Meeting of ISMRM, Paris, France* 2018:3995.
189 Hamm LL, Nakhoul N, Hering-Smith KS. Acid-base homeostasis. *Clinical Journal of the American Society of Nephrology* 2015;**10**:2232-42.
190 Bakermans AJ, Bazil JN, Nederveen AJ, et al. Human cardiac 31P-MR spectroscopy at 3 tesla cannot detect failing myocardial energy homeostasis during exercise. *Frontiers in physiology* 2017;**8**:939.
191 Wu F, Zhang J, Beard DA. Experimentally observed phenomena on cardiac energetics in heart failure emerge from simulations of cardiac metabolism. *Proceedings of the National Academy of Sciences* 2009;**106**:7143-8.
192 Valkovič L, Dragonu I, Almujayyaz S, et al. Using a whole-body 31P birdcage transmit coil and 16-element receive array for human cardiac metabolic imaging at 7T. *PloS one* 2017;**12**:e0187153.
193 Zhang J, Merkle H, Hendrich K, et al. Bioenergetic abnormalities associated with severe left ventricular hypertrophy. *The Journal of clinical investigation* 1993;**92**:993-1003.
194 Wu T-FL, Davis EJ. Regulation of glycolytic flux in an energetically controlled cell-free system: the effects of adenine nucleotide ratios, inorganic phosphate, pH, and citrate. *Archives of biochemistry and biophysics* 1981;**209**:85-99.
195 Beer M, Seyfarth T, Sandstede J, et al. Absolute concentrations of high-energy phosphate metabolites in normal, hypertrophied, and failing human myocardium measured noninvasively with 31P-SLOOP magnetic resonance spectroscopy. *Journal of the American College of Cardiology* 2002;**40**:1267-74.
196 Von Deuster C, Stoeck CT, Genet M, et al. Spin echo versus stimulated echo diffusion tensor imaging of the in vivo human heart. *Magnetic resonance in medicine* 2016;**76**:862-72.
197 Bogner W, Chmelik M, Schmid A, et al. Assessment of 31P relaxation times in the human calf muscle: a comparison between 3 T and 7 T in vivo. *Magnetic Resonance in Medicine: An Official Journal of the International Society for Magnetic Resonance in Medicine* 2009;**62**:574-82.
198 Rubler S, Dlugash J, Yuceoglu YZ, et al. New type of cardiomyopathy associated with diabetic glomerulosclerosis. *The American journal of cardiology* 1972;**30**:595-602.
199 From AM, Scott CG, Chen HH. The development of heart failure in patients with diabetes mellitus and pre-clinical diastolic dysfunction: a population-based study. *Journal of the American College of Cardiology* 2010;**55**:300-5.
200 Fischer M, Baessler A, Hense H, et al. Prevalence of left ventricular diastolic dysfunction in the community: results from a Doppler echocardiographic-based survey of a population sample. *European heart journal* 2003;**24**:320-8.
201 Özbek BT. Diastolic dysfunction is a stronger predictor of cardiovascular morbidity and mortality in individuals with diabetes as compared to individuals without diabetes in the general population. *Circulation* 2018;**138**:A12554-A.
202 Sutherland C, Fisher B, Frier B, et al. Endomyocardial biopsy pathology in insulin-dependent diabetic patients with abnormal ventricular function. *Histopathology* 1989;**14**:593-602.

203 Wong TC, Piehler KM, Kang IA, et al. Myocardial extracellular volume fraction quantified by cardiovascular magnetic resonance is increased in diabetes and associated with mortality and incident heart failure admission. *European heart journal* 2014;**35**:657-64.
204 Tan Y, Zhang Z, Zheng C, et al. Mechanisms of diabetic cardiomyopathy and potential therapeutic strategies: preclinical and clinical evidence. *Nature Reviews Cardiology* 2020:1-23.
205 Ohtake T, Yokoyama I, Watanabe T, et al. Myocardial glucose metabolism in noninsulin-dependent diabetes mellitus patients evaluated by FDG-PET. *Journal of nuclear medicine: official publication, Society of Nuclear Medicine* 1995;**36**:456-63.
206 Rider OJ, Apps A, Miller JJ, et al. Non-Invasive In Vivo Assessment of Cardiac Metabolism in the Healthy and Diabetic Human Heart Using Hyperpolarized 13C MRI. *Circulation Research* 2020.
207 Nicholl TA, Lopaschuk GD, McNEILL JH. Effects of free fatty acids and dichloroacetate on isolated working diabetic rat heart. *American Journal of Physiology-Heart and Circulatory Physiology* 1991;**261**:H1053-H9.
208 Bashir A, Coggan AR, Gropler RJ. In vivo creatine kinase reaction kinetics at rest and stress in type II diabetic rat heart. *Physiological reports* 2015;**3**:e12248.
209 Savabi F, Kirsch A. Alteration of the phosphocreatine energy shuttle components in diabetic rat heart. *Journal of molecular and cellular cardiology* 1991;**23**:1323-33.
210 Peterzan MA, Clarke WT, Lygate CA, et al. Cardiac Energetics in Patients with Aortic Stenosis and Preserved versus Reduced Ejection Fraction. *Circulation* 2020.
211 Bers D. *Excitation-contraction coupling and cardiac contractile force*. Springer Science & Business Media 2001.
212 Kammermeier H. High energy phosphate of the myocardium: concentration versus free energy change. *Cardiac Energetics*: Springer 1987:31-6.
213 Bottomley PA, Weiss RG. Non-invasive magnetic-resonance detection of creatine depletion in non-viable infarcted myocardium. *The Lancet* 1998;**351**:714-8.
214 Iozzo P, Chareonthaitawee P, Rimoldi O, et al. Mismatch between insulin-mediated glucose uptake and blood flow in the heart of patients with type II diabetes. *Diabetologia* 2002;**45**:1404-9.
215 Randle PJ, Sugden P, Kerbey A, et al. Regulation of pyruvate oxidation and the conservation of glucose. *Biochemical Society Symposium* 1978:47-67.
216 Young ME, McNulty P, Taegtmeyer H. Adaptation and maladaptation of the heart in diabetes: Part II: potential mechanisms. *Circulation* 2002;**105**:1861-70.
217 Stanley WC, Lopaschuk GD, McCormack JG. Regulation of energy substrate metabolism in the diabetic heart. *Cardiovascular research* 1997;**34**:25-33.
218 Kuo TH, Moore KH, Giacomelli F, et al. Defective oxidative metabolism of heart mitochondria from genetically diabetic mice. *Diabetes* 1983;**32**:781-7.
219 Levi M, Gratton E, Forster IC, et al. Mechanisms of phosphate transport. *Nature Reviews Nephrology* 2019;**15**:482-500.
220 Jack M, Huang W, Askari A. Characterization of Na+-dependent phosphate transport in cardiac sarcolemmal vesicles. *Journal of Biological Chemistry* 1989;**264**:3904-8.
221 Lopatin Y. Metabolic therapy in heart failure. *Cardiac failure review* 2015;**1**:112.
222 Remondino A, Rosenblatt-Velin N, Montessuit C, et al. Altered expression of proteins of metabolic regulation during remodeling of the left ventricle after myocardial infarction. *Journal of molecular and cellular cardiology* 2000;**32**:2025-34.

223 Garlick PB, Radda GK, Seeley PJ. Studies of acidosis in the ischaemic heart by phosphorus nuclear magnetic resonance. *Biochemical Journal* 1979;**184**:547-54.
224 Effros R, Haider B, Ettinger P, et al. In vivo myocardial cell pH in the dog. Response to ischemia and infusion of alkali. *The Journal of clinical investigation* 1975;**55**:1100-10.
225 Steenbergen C, Deleeuw G, Rich T, et al. Effects of acidosis and ischemia on contractility and intracellular pH of rat heart. *Circulation research* 1977;**41**:849-58.
226 Nakae I, Mitsunami K, Omura T, et al. Proton magnetic resonance spectroscopy can detect creatine depletion associated with the progression of heart failure in cardiomyopathy. *Journal of the American College of Cardiology* 2003;**42**:1587-93.
227 Vinnakota KC, Bassingthwaighte JB. Myocardial density and composition: a basis for calculating intracellular metabolite concentrations. *American Journal of Physiology-Heart and Circulatory Physiology* 2004;**286**:H1742-H9.
228 Murakami Y, Zhang J, Eijgelshoven MH, et al. Myocardial creatine kinase kinetics in hearts with postinfarction left ventricular remodeling. *American Journal of Physiology-Heart and Circulatory Physiology* 1999;**276**:H892-H900.
229 Ye Y, Gong G, Ochiai K, et al. High-energy phosphate metabolism and creatine kinase in failing hearts: a new porcine model. *Circulation* 2001;**103**:1570-6.
230 De Bruyne B, Pijls NHJ, Kalesan B, et al. Fractional Flow Reserve–Guided PCI versus Medical Therapy in Stable Coronary Disease. *New England Journal of Medicine* 2012;**367**:991-1001.
231 Ball DR, Cruickshank R, Carr CA, et al. Metabolic imaging of acute and chronic infarction in the perfused rat heart using hyperpolarised [1-13C] pyruvate. *NMR in biomedicine* 2013;**26**:1441-50.
232 Tyler A, Lau JY, Ball V, et al. A 3D-Hybrid-Shot Spiral Sequence for Hyperpolarized $^{13} $ C Imaging. *arXiv preprint arXiv:200705257* 2020.
233 Lewis AJ, Miller JJ, Lau AZ, et al. Noninvasive immunometabolic cardiac inflammation imaging using hyperpolarized magnetic resonance. *Circulation research* 2018;**122**:1084-93.
234 Lee WW, Marinelli B, Van Der Laan AM, et al. PET/MRI of inflammation in myocardial infarction. *Journal of the American College of Cardiology* 2012;**59**:153-63.
235 Guglielmetti C, Najac C, Didonna A, et al. Hyperpolarized 13C MR metabolic imaging can detect neuroinflammation in vivo in a multiple sclerosis murine model. *Proceedings of the National Academy of Sciences* 2017;**114**:E6982-E91.
236 Nonnenmacher Y, Hiller K. Biochemistry of proinflammatory macrophage activation. *Cellular and Molecular Life Sciences* 2018;**75**:2093-109.
237 Newsholme P, Curi R, Gordon S, et al. Metabolism of glucose, glutamine, long-chain fatty acids and ketone bodies by murine macrophages. *Biochemical Journal* 1986;**239**:121-5.
238 Ridker PM, Everett BM, Thuren T, et al. Antiinflammatory therapy with canakinumab for atherosclerotic disease. *New England journal of medicine* 2017;**377**:1119-31.
239 Lau AZ, Miller JJ, Robson MD, et al. Cardiac perfusion imaging using hyperpolarized 13C urea using flow sensitizing gradients. *Magnetic resonance in medicine* 2016;**75**:1474-83.
240 Lau AZ, Miller JJ, Robson MD, et al. Simultaneous assessment of cardiac metabolism and perfusion using copolarized [1-13C] pyruvate and 13C-urea. *Magnetic resonance in medicine* 2017;**77**:151-8.
241 Alpert MA. Obesity cardiomyopathy: pathophysiology and evolution of the clinical syndrome. *The American journal of the medical sciences* 2001;**321**:225-36.
242 Stergiopoulos K, Boden WE, Hartigan P, et al. Percutaneous coronary intervention outcomes in patients with stable obstructive coronary artery disease and myocardial

ischemia: a collaborative meta-analysis of contemporary randomized clinical trials. *JAMA internal medicine* 2014;**174**:232-40.
243 Boden WE, O'Rourke RA, Teo KK, et al. Optimal Medical Therapy with or without PCI for Stable Coronary Disease. *New England Journal of Medicine* 2007;**356**:1503-16.
244 Bonow RO, Maurer G, Lee KL, et al. Myocardial viability and survival in ischemic left ventricular dysfunction. *New England Journal of Medicine* 2011;**364**:1617-25.
245 Panza JA, Ellis AM, Al-Khalidi HR, et al. Myocardial viability and long-term outcomes in ischemic cardiomyopathy. *New England Journal of Medicine* 2019;**381**:739-48.
246 members ATF, Windecker S, Kolh P, et al. 2014 ESC/EACTS guidelines on myocardial revascularization: the Task Force on Myocardial Revascularization of the European Society of Cardiology (ESC) and the European Association for Cardio-Thoracic Surgery (EACTS) developed with the special contribution of the European Association of Percutaneous Cardiovascular Interventions (EAPCI). *European heart journal* 2014;**35**:2541-619.
247 Rajkumar CA, Nijjer SS, Cole GD, et al. 'Faith Healing'and 'Subtraction Anxiety'in Unblinded Trials of Procedures: Lessons from DEFER and FAME-2 for End Points in the ISCHEMIA Trial. *Circulation: Cardiovascular Quality and Outcomes* 2018;**11**:e004665.
248 Schroeder MA, Swietach P, Atherton HJ, et al. Measuring intracellular pH in the heart using hyperpolarized carbon dioxide and bicarbonate: a 13C and 31P magnetic resonance spectroscopy study. *Cardiovascular research* 2010;**86**:82-91.